Organic Semiconductors: Mixing Behavior and Charge Transfer for Diindenoperylene / Dinaphthothienothiophene:Perylene Diimide-Based Binary Systems

Dissertation

der Mathematisch-Naturwissenschaftlichen Fakultät

der Eberhard Karls Universität Tübingen

zur Erlangung des Grades eines

Doktors der Naturwissenschaften

(Dr. rer. nat.)

vorgelegt von

Nadine Rußegger

aus Stuttgart

Tübingen

2022

Gedruckt mit Genehmigung der Mathematisch-Naturwissenschaftlichen Fakultät der Eberhard Karls Universität Tübingen.

Tag der mündlichen Qualifikation:	01.02.2024
Dekan:	Prof. Dr. Thilo Stehle
1. Berichterstatter:	Prof. Dr. Dr. h.c. Frank Schreiber
2. Berichterstatterin:	Jun.-Prof. Dr. Jannika Lauth

Abstract

Thin films of organic semiconductors demonstrate important optical and electrical properties and are widely used in optoelectronic devices such as organic field-effect transistors (OFETs), organic light emitting diodes (OLEDs), or organic solar cells. Organic small molecules are very promising organic semiconducting compounds that have a broad area of optoelectronic applications. The functionality and device properties depend on the structure of the organic semiconductive layer. The thin films of organic small molecules can be prepared by organic molecular beam deposition (OMBD) under vacuum conditions. The complex structure in such optoelectronic devices involves at least two different materials, the donor and the acceptor compounds, which can be deposited for the active layer in different architectures for example simultaneously resulting in bulk heterojunctions (BHJ). The central and important topic here is the mixing behavior whether the compounds phase-separate or mix with each other. One of the fundamental processes in such optoelectronic devices relies on the molecular charge transfer (CT) which takes place at the interface of donor and acceptor molecules, for example, in molecular mixed crystals. The CT has an important impact on optoelectronic devices and is therefore essential for the fundamental challenges in these fields. In this context, the morphology and intermixing on the molecular level in bulk heterojunctions have a great influence on the CT effects and therefore also on the device structure and performance. The microscopic details of the CT, in particular for the different strengths of interactions, are still not fully understood.

The present work investigates structural morphology and charge transfer effects of organic binary bulk heterojunctions. As donors the organic small molecules Diindenoperylene (DIP) and Dinaphthothienothiophene (DNTT) and as acceptors, different perylene diimide (PDI) derivatives were chosen. At first, the influences of the different *n*-alkyl side chains and cyano groups of the various PDI acceptors with the donor DIP on structural and optical properties in these thin film systems were examined. Two of the investigated systems show well-defined co-crystal formations and strong excited-state CT effects by using different X-ray scattering techniques and absorption as well as emission spectroscopy. Moreover, the molecular CT of two different PDI:DNTT thin film systems was characterized by obtaining weak ground-state and strong excited-state CT effects. The experimental results and optical properties were compared and complemented by first-principle calculations. Furthermore, the influences of various donor molecules with a synthesized PDI acceptor molecule were investigated. The structural and optical properties of the pristine acceptor based on the substrate temperature were examined and different mixing behavior as well as CT effects were obtained for two different molecule combinations in thin films. The results lead to a deeper understanding of processes being important for organic optoelectronic applications.

Zusammenfassung in deutscher Sprache

Dünne Schichten organischer Halbleiter weisen hocheffiziente optische und elektrische Eigenschaften auf und finden weitverbreitet Verwendung als aktive Schichten in organischen Feldeffekttransistoren (OFETs), organischen Leuchtdioden (OLEDs) oder organischen Photovoltaikzellen (OPVs). Durch beträchtlichen Forschungsaufwand in den letzten Jahrzehnten wurden organisch niedermolekulare Verbindungen zu vielversprechende Materialien für organische Halbleiter in den verschiedensten (opto-)elektronischen Anwendungen. Die Funktionalität und die Eigenschaften der Bauteile hängen unter anderem stark von der Struktur der organischen Halbleiterschicht ab. Die dünnen Schichten können hierbei unter anderem mittels organischer Molekularstrahldeposition (OMBD) unter Vakuum-Bedingungen hergestellt werden. Die Komplexität solcher Strukturen in den (opto-)elektronischen Bauteilen lässt sich meist auf mindestens zwei verschiedene Komponenten zurückführen, dem Donator- und dem Akzeptormaterial. Die Herstellung der Akzeptor-Donator Schicht kann durch unterschiedlichstes Filmwachstum und Entstehung verschiedener Heterostrukturen erfolgen, beispielsweise durch gleichzeitiges Aufdampfen auf ein Substrat, wobei eine „Misch-Heterostruktur“ (Bulk Heterojunction) entsteht. Der wichtigste Punkt hierbei ist das Mischverhalten beider Komponenten, wobei essenziell ist, ob sich eine Phasenseparation beider Moleküle bildet oder sie sich miteinander mischen lassen. Ein fundamentaler Prozess in solchen (opto-)elektronischen Bauteilen ist der molekulare Ladungstransfer, welcher an der Grenzfläche der Donator- und Akzeptormoleküle, beispielsweise in molekularen Mischkristallen, stattfindet. Da der Ladungstransfer signifikante Einflüsse auf (opto-)elektronische Anwendungen ausübt, ist er essenziell für die grundlegendenden Herausforderungen in diesen Forschungsbereichen. In diesem Zusammenhang haben die Morphologie und das Mischverhalten der Dünnschichten auf molekularer Ebene wichtige Auswirkungen auf den Ladungstransfer und daher ebenso auf die Struktur und die Performance der Bauteile. Die mikroskopischen Details des Ladungstransfers, im Hinblick auf die unterschiedlichen Stärken der zwischenmolekularen Wechselwirkungen, sind noch nicht vollständig erforscht.

Die strukturelle Morphologie und der molekulare Ladungstransfer in Donator-Akzeptor Heterostrukturen ist das Hauptthema dieser Arbeit. Als Donatormoleküle wurden in dieser Arbeit die prototypischen organischen Halbleiter Diindenoperylen (DIP) und Dinaphthothienothiophen (DNTT) und als Akzeptormaterial verschiedene Perylendiimid-Derivate (PDI) verwendet. Die Einflüsse verschiedener Seitenketten (n-Alkylgruppen oder Cyanogruppen) der PDI Derivate mit dem Donatormolekül DIP wurden im Hinblick auf strukturelle und optische Eigenschaften der verschiedenen Dünnschichten untersucht. Zwei Dünnschichtsysteme bilden einen wohldefinierten Cokristall und weisen einen starken Ladungstransfer in angeregtem Zustand auf. Dieser wurde mittels verschiedener Röntgenstreutechniken und der Absorption- sowie der Emissionsspektroskopie nachgewiesen. Weiterhin wurde der molekulare Ladungstransfer zwei verschiedener PDI:DNTT Dünnschichtsysteme charakterisiert und ein schwacher Ladungstransfer im Grundzustand sowie ein starker in angeregtem Zustand ermittelt. Die experimentellen Ergebnisse, darunter die optischen Eigenschaften der dünnen Schichten, wurden durch „first-principles“-Berechnungen erweitert und ergänzt. Die Einflüsse verschiedener Donatormoleküle mit einem synthetisierten PDI Akzeptor in dünnen Schichten wurden untersucht. Die strukturellen und optischen Eigenschaften des reinen Akzeptors wurden im Hinblick auf die Substrattemperatur während des Wachstums ermittelt und verschiedene Mischverhalten sowie Ladungstransfer wurden für zwei unterschiedliche Molekülkombinationen in Dünnschichten erforscht. Die Ergebnisse, die im Rahmen dieser Arbeit gewonnen wurden, führen zu einem tieferen Verständnis der Prozesse, die für organische (opto-)elektronische Anwendungen bedeutsam sind.

Contents

Part I

Fundamentals

Chapter 1

Introduction

Organic materials offer a huge diversity of different structures and many possibilities in various mechanical, optical and electrical properties. In the last three decades, strong efforts in the area of organic semiconductors and optoelectronic applications have been achieved [1–3]. Therefore, organic optoelectronic devices are an attractive alternative to their inorganic counterparts. Nowadays, fully functional devices with organic semiconductors embedded as active layers in organic field-effect transistors (OFETs) [4–7], organic light emitting diodes (OLEDs) [8, 9], and organic photovoltaic cells (OPVCs) [10–13] have been widely accepted and well-established in the consumer market. Low cost thin film fabrication, their light weight, processability, and device flexibility, to name only a few benefits achieved by using organic semiconducting materials [14–16]. High efficiencies and the advantage of involving flexible substrates are also worth mentioning in organic optoelectronic device fabrication, such as spin-coating, vacuum sublimation or inkjet-printing [17, 18]. Additionally, a wide range of organic semiconductive materials benefits from the opportunities to adjust optoelectronic properties in a controlled way because the chemical structure can be easily modified in the desired ways. The fundamentals of tuning thin film properties are the functionalization of molecule compounds [5, 19–22]. Through the precisely functionalized structures such as fluorination or incorporated electron-withdrawing groups of organic materials, structural and optoelectronic properties such as charge transport properties of the organic active layer and therefore also of the devices can be enhanced [19, 20, 23].

Organic small molecules are one broad area of organic semiconductors that opens a wide range of possibilities for optoelectronic devices. The complex structure in such devices involves at least two different materials, the donor and the acceptor compound, for various kinds of applications. A challenging field itself is the fabrication of the active semiconducting layer which can be produced by organic molecular beam deposition (OMBD) [26] and has a great impact on the functionality of the optoelectronic devices. The growth behavior of organic small molecules has important differences compared to the inorganic counterparts due to the additional degrees of freedom of the organic materials [27]. The growth of organic-organic (donor-acceptor) thin films is more complex related to issues based on the crystal structure and its quality. The evolution of the film structure as well as the various growth parameters such as the substrate temperature, the base pressure, and the deposition rate are crucial and have a strong repercussion

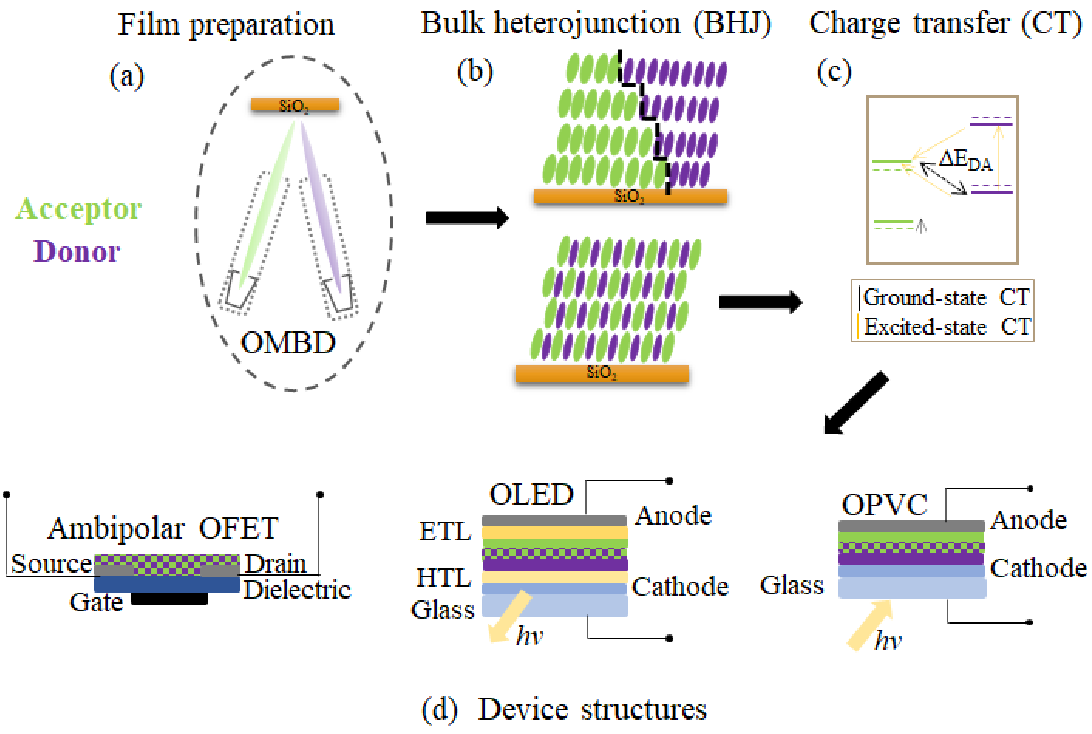

Figure 1.1: *Illustration of structures and processes relevant for organic devices: a) schematical film preparation of semiconductive (donor-acceptor) active layers by organic molecular beam deposition, b) sketches of phase-separating and mixing scenarios for binary systems in bulk heterojunctions (BHJ), c) schematical charge transfer (CT) case indicating a small ground-state CT and a strong excited-state CT and d) several simplified optoelectronic device structures consisting of an organic heterostructure as an active layer: an ambipolar organic field-effect transistor in a coplanar bottom-gate bottom-contact configuration, an organic light emitting diode with an electron (ETL) and hole transporting layer (HTL) as well as an organic photovoltaic cell. Part of the picture is modified from Refs. [24, 25].*

on the growth behavior and therefore on the device structure [28]. In Figure 1.1a the film preparation of semiconductive active layers by OMBD is schematically presented based on structures relevant for organic devices.

Possible architectures of such semiconductive layers can be organic heterostructures realized in crystalline thin films of two different donor-acceptor materials. Compositions where two compounds (A and B) are deposited simultaneously resulting in A:B heterostructures are called bulk heterojunctions (BHJ) [25, 29]. The central key is here the mixing behavior in BHJ, whether the two materials are phase-separating or efficiently mixing, which is schematically represented in Figure 1.1b. The morphology and intermixing on the molecular level in such BHJ thin films have a great impact on the device structure [25, 30–33]. For a complex device structure, exemplary an OLED or OPVC architecture in addition to the organic BHJ, electrodes, passivation layers, and blocking layers are also essential to improve the conductivity. Illustrations of the various device structures with the organic heterostructures and the required layers are shown in Figure 1.1d.

For the functionality of the optoelectronic devices, optical properties such as light absorption and emission as well as alignment of the energy levels at the interface of the heterostructure are significant. Such relevant properties of the devices are determined by the frontier molecular orbitals (FMOs) with the highest occupied molecule orbitals (HOMOs) and the lowest unoccupied molecule orbitals (LUMOs) of the respective molecule combinations [24, 34]. The important electronic processes for charge generation for example in an excitonic heterojunction photovoltaic cell can be divided in a simplified scheme into several parts. First, the light will be absorbed and excitons are generated. The excitons diffuse to the interface, they dissociate and charge carriers are formed at the interface which are then collected at the electrodes. For these relevant processes, the ideal heterostructures should exhibit low defect densities, high carrier mobilities, favorable energy level alignments at the interface and the materials should possess high absorption coefficients [12, 35]. Through the functionalization of the molecule compounds, the ionization energies, the electron affinities, the charge transport properties as well as the respective FMOs can be varied [4, 19, 20, 36].

One of the fundamental processes in such optoelectronic devices relies on the molecular charge transfer (CT) which takes place at the interface of donor and acceptor molecules, for example, in molecular mixed crystals [37, 38]. The concept of CT was first described as a mechanism of intermolecular interactions in the framework of Mulliken theory in the year 1952 with the explanation that donor-acceptor binding results on account of quantum-mechanical mixing of two states [39]. A CT transition is a large fraction of electronic charge which is transferred from one entire molecule to another one (from the donor to the acceptor molecule). The differences between partial and complete CT have to be considered. The CT interactions are quantified by the electron and hole CT integrals and depend on the nodal pattern of the relevant FMOs whose overlap should be the highest [40]. The CT has an important impact on optoelectronic devices such as OPVCs and OLEDs and is therefore essential for the associated fundamental challenges [41–44]. Thus, the processes of CT exciton formation and recombination of charge carriers and their mechanisms have to be understood. The efficiency of the CT exciton formation and their dissociation into free carriers determine the photocurrent of organic solar cells. The energy of the charge transfer state is directly proportional to the experimental open-circuit voltage V_{OC} in organic solar cells and serves therefore as a limit. This voltage is determined by the spectral properties of the CT exciton. The differences between the CT energy and the open-circuit voltage have to be reduced to optimize the V_{OC} while an efficient photocurrent generation is still available because the energy levels should still suit an efficient exciton dissociation without electron back transfer. This can be achieved by tuning the LUMO level of the acceptor molecules. The electronic coupling between the donor and acceptor molecules has also an influence on the open-circuit voltage

[43, 45, 46]. Another aspect is to minimize recombinations because CT states are efficient recombination channels for excitons [45, 47]. In this context, the morphology and intermixing on the molecular level in bulk heterojunctions have a great impact on CT effects and therefore also on the open-circuit voltage as well as on recombinations [48]. Thus, the microscopic details of CT are of crucial importance which are, in particular for the different strengths of interactions, still not fully understood. In a rather common approach, molecular CT can be roughly divided into several cases depending on how much the molecules interact with each other. For weakly bound organic molecules a partial CT on average from the donor to the acceptor is expected [41, 42, 49]. In Figure 1.1c the schematic CT case for weakly bound organic compounds is presented including a weak ground-state (GS) CT and a strong excited-state (ES) CT.

This thesis focuses on structural morphology and molecular charge transfer effects of organic binary heterojunctions. The results obtained from this thesis lead to a deeper understanding of the processes being important for organic photovoltaic devices in organic optoelectronic applications. In the first part, Chapter 2, the fundamentals of organic small molecule semiconductors, the growth behavior for thin films as well as optical and electrical properties and processes in thin films are explained. The properties of the materials used in this thesis are characterized in Chapter 3. In Chapter 4 the sample preparation for the mixed thin films is described. Furthermore, details about the different X-ray scattering characterization methods as well as the optical characterization experiments are provided. In Part II the main results of this thesis are presented which are divided into three chapters. The first part, Chapter 5, investigates the influences of the different side groups of various perylene diimide (PDI) acceptors with the donor molecule Diindenoperylene (DIP) on structural and optical properties in these mixed thin films. Thereby, two of the investigated systems show well-defined co-crystal formations and strong excited-state CT effects. Chapter 6 characterizes the molecular CT of two different donor-acceptor systems by obtaining weak ground-state and strong excited-state CT effects. The experimental results and optical properties were compared and complemented by first-principle calculations. The third part, Chapter 7, deals with the influences of various donor molecules with a synthesized PDI acceptor molecule in mixed thin films. The structural and optical properties of the pristine acceptor based on the growth temperature were examined and different mixing behavior as well as CT effects were obtained for two different molecule combinations. The thesis concludes with a summary and possible future projects (Chap. 8).

Chapter 2

Background

2.1 Organic semiconductors

Organic semiconductors are an attractive alternative to their inorganic counterparts which are widely used in organic optoelectronic devices such as organic photovoltaic cells and organic light emitting diodes [4, 5, 23]. In general and simplified, an organic semiconductor is a non-metallic solid which shows electric conductivity with increasing temperature. Considering band theory, the organic semiconductors have a band gap between the valence and the conduction band which is small enough so that it can be overcome with thermal energy. To a certain extent, they can be described as inorganic counterparts, but several concepts have to be modified.

2.1.1 Structure and properties of organic semiconductors

Organic materials have carbon and hydrogen as their essential structural elements and consist therefore of a hydrogen-carbon backbone including partly also heteroatoms such as N, O, S in the molecule structure. Organic semiconductor materials such as polymers and organic small molecules, as used in this thesis, are carbon-based compounds. Hence, to understand these materials, the electronic structure of carbon-based molecules is essential.

The electronic structure of molecules can be determined by considering the Schrödinger equation taking the Hamilton operator into account which is the sum of the kinetic and the potential energy. This is shown in Equation 2.1 with T_N and T_e the kinetic energies of the respective atomic nuclei or electrons and the total potential energy of the system V [50]:

$$\hat{H} = \hat{T}_N + \hat{T}_e + \hat{V} \tag{2.1}$$

The Born-Oppenheimer approximation separates the nuclear from the electronic part resulting in the electronic Schrödinger equation for a fixed nuclear geometry. With the approximate Hartree-Fock solution of the electronic Schrödinger equation the molecular orbitals (MOs) and their energy values can be obtained [50, 51].

The MOs and their energy values have to be considered to understand the optical and electrical processes in organic molecules. Molecule orbitals can be approximated as a linear combination of atomic orbitals (LCAO). It can be determined to which degree two orbitals, located at different centers, can overlap. The interference of these orbitals can result in bonding and anti-bonding molecule orbitals. The bonding MOs form the closed shell ground-state while the excited-states of the molecule include the anti-bonding MOs. Accordingly, it can be decided which molecule orbitals are filled with electrons, beginning with the lower lying orbitals after the Pauli principle and the Hund‘s rule [50, 51].

In the ground-state, the carbon atom consists of four valence electrons in one $2s$- and three $2p$-orbitals and can possibly establish four covalent bonds. In molecules, carbon atoms form hybridized orbitals, which are linear combinations of s- and p-orbitals, because these are energetically favorable [50, 52]. An easy and common example of an organic molecule is benzene (C_6H_6, Fig. 2.1). In the benzene molecule, each carbon atom forms three sp^2-hybridized orbitals out of one $2s$- and two $2p$-orbitals. The orbitals are hexagonal oriented in the xy-plane and the remaining p_z-orbitals are perpendicular to that plane. In a simplified scheme, a covalent bond chemical consists of two atoms that are sharing one pair of electrons. The three hybridized orbitals of the carbons in benzene (σ-bonds) are located to two other carbon atoms and one hydrogen atom and the residual electron is placed in the p_z-orbital (Fig. 2.1b). It can be paired with the other electrons in the p_z-orbitals of the carbon atoms resulting in a spatial probability density above and below the molecule axis which corresponds to the so-called π-bond, a delocalized π-system (Fig. 2.1c) [50, 52].

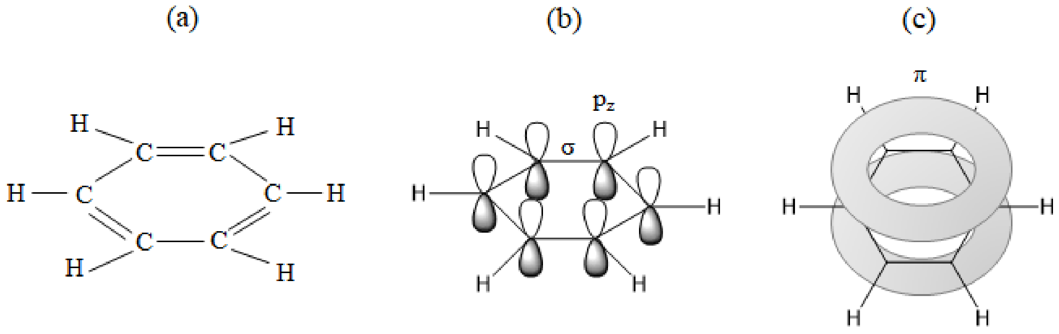

Figure 2.1: *The benzene model: a) schematic structure, b) σ-bonds and non overlapping p_z-bonds and c) σ-bonds and ring-shaped π-bonds. Picture is modified from Ref. [52].*

Organic semiconductors are aromatic compounds which consist of cyclic conjugated, delocalized π-bonds. Normally, they are planar molecules with high resonance energies. Benzene is the simplest aromatic compound, but there are also polycyclic aromatic materials with heteroatoms involved. The Hückel rule has to be fulfilled which means the molecule has to consist of $(4n + 2)$ π-electrons. Here, N is an integer and the free electron pairs of heteroatoms have also to be considered.

In aromatic compounds, the splitting of the bonding and antibonding π-orbitals is weaker than compared to the σ-bonds. This results in favorable energy levels and therefore these molecules are suitable for organic semiconductor applications. The isoenergetic highest occupied π-orbitals are called HOMOs. The HOMO and the lowest unoccupied molecular orbital are called the frontier orbitals and are separated by the energy gap whose size is depending on the nature of the respective molecule. The frontier orbitals play an important role in optical and electrical properties of the organic semiconducting compounds. Advantageous for aromatics is for example the light absorption and emission, because the $\pi \rightarrow \pi^*$ transition can take place in the visible spectral range [52, 53].

The terms of n- and p-type behavior have to be redefined for organic semiconductors. The generation of charge carriers for organic semiconductors occurs mostly by direct injection and is depending on the HOMO/LUMO level of the organic molecule and the Fermi energy of the injection electrode. P-type organic semiconductors or donors are ‘hole-transporting’ materials with high-lying HOMO levels and low ionization energies. N-type or acceptors in contrast are ‘electron-transporting’ materials with low-lying LUMO levels and high electron affinities [50, 51].

2.1.2 Solid state interactions

The structure of molecular packing in molecular organic solids is determined by inter- and intramolecular forces which have different strengths and directions.

Van der Waals forces take place between neutral and non-polar molecules. These compounds have no static dipole moments. However, there can be fluctuations in the charge distributions of one molecule which results in a fluctuating dipole moment and this can induce a dipole moment in the neighboring molecule. This leads to an attractive force and the induced dipole-dipole interaction between two molecules with distance r:

$$V_{disp} = -\frac{A}{r^6} \tag{2.2}$$

Here, A is an empirical constant and includes compound specific properties [51].

In addition to the attractive interactions, there are also repulsive forces. The interactions are based on Coulomb repulsion and stem from inner electrons and atomic nuclei to avoid a collapse of the solid structure. The forces are strong at small distances and they decrease rapidly with increasing distance. They are normally treated using approximations. The approximation is presented by the Lennard-Jones potential which is a sum of the attractive van der Waals interactions and the repulsive forces shown in Figure 2.2. The potential can be described with the following Equation 2.3

$$V = \frac{B}{r^{12}} - \frac{A}{r^6} \tag{2.3}$$

where B is again an empirical constant [51].

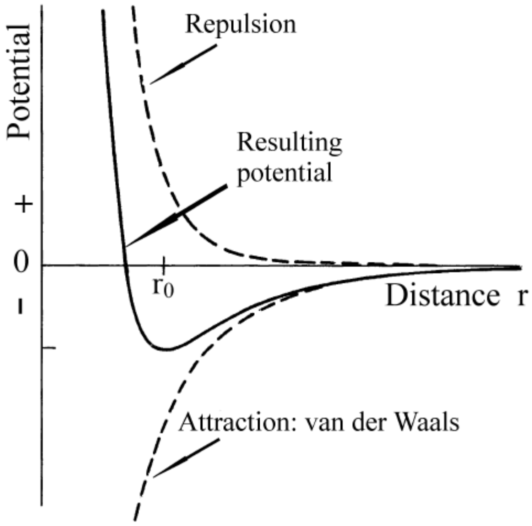

Figure 2.2: *Lennard-Jones potential curve combining van der Waals attraction contribution and repulsive forces. Picture is taken from Ref. [51].*

For organic solids which consist of molecules with polar substituents or with a permanent dipole, attractive Coulomb forces have to be taken into account as well. The intermolecular interactions are provided by a static monopole, a dipole, or a quadrupole with their long range.

Another intermolecular force is important for structure formation in organic solids, the so-called C-H/π-interaction. For the attractive interaction between π-conjugated systems electrostatic and repulsion forces are taken into account. As a prototypical aromatic compound, benzene dimers were used to study this interaction (Fig. 2.3a). In the solid and liquid phases, edge-to-face conformations are favored due to the minimization of repulsion (Fig. 2.3c). The face-to-face conformation is not so favorable for benzene dimers, which is why a more off-stacking arrangement is formed (Fig. 2.3b) [54–56].

2.1.3 Binary mixtures

In this thesis, donor-acceptor organic small molecule systems are studied. Therefore, the understanding of the mixing behavior on the molecular level in binary systems is very important. The degree of intermixing, the crystalline order, and the morphology are of sufficient interest and have a significant impact on device performance in organic optoelectronics. Here, two dissimilar materials A and B are taken into account. The mixing behavior of the organic small molecules is considered in terms of a nearest-neighbor interaction model:

$$\chi = \frac{Z}{k_B T} \cdot (W_{AA} + W_{BB} - 2W_{AB}) \tag{2.4}$$

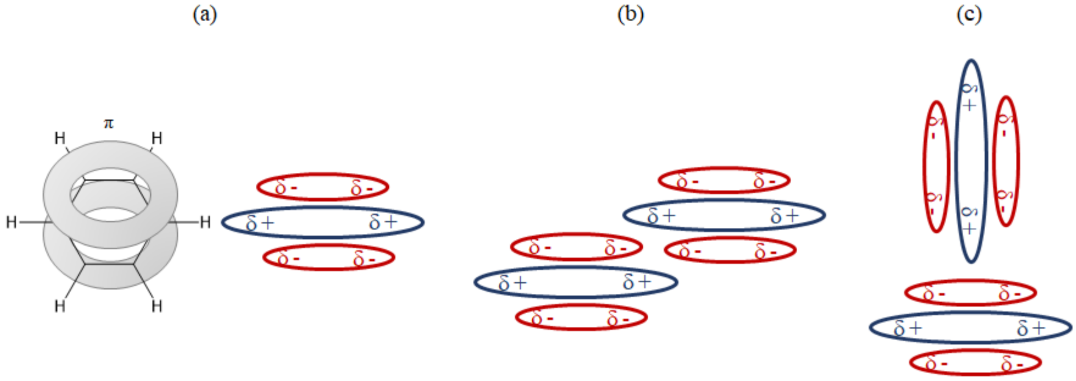

Figure 2.3: *Schematic description of aromatic electrostatic interactions: a) quadrupole moment in benzene, b) face-to-face and off-stacking conformation of benzene dimer and c) edge-to-face conformation of benzene dimer. Picture is modified from Ref. [55].*

The main driving force is the difference between the intermolecular interaction of similar (W_{AA} or W_{BB}) and dissimilar molecules (W_{AB}) [25, 57, 58]. Here, χ is the interaction parameter, Z is the coordination number, k_B is the Boltzmann constant, and T is the temperature.

The free energy of a lattice is composed of contributions from two different materials. The Helmholtz free energy of mixing F_{mix} can be described:

$$\Delta F_{mix} = k_B T \cdot [x_A ln(x_A) + x_B ln(x_B) + \chi x_A x_B] \tag{2.5}$$

The interaction and entropy terms of the system are summed up (the logarithmic-parts are the entropy terms of the system) and x_A and x_B are the respective relative concentrations of the two materials.

The mixing behavior is described in simplified scenarios in Figure 2.4. The interaction parameter is correlated to the entropy of the system. For high temperatures, the entropy term will dominate the free energy of the system. So if the interaction energy W_{AA} or W_{BB} is similar to W_{AB}, no preferred interaction occurs ($\chi \approx 0$), and a statistical mixing is formed. In this solid solution, the two materials can mix in any molar ratio (Fig. 2.4a). If the temperature is lowered, the entropy does not dominate anymore the mixing behavior. The system of A and B tend to mix ($\chi < 0$) or phase-separate into the pure components ($\chi > 2$) if one of the interaction energy terms is larger. For $\chi < 0$, the attraction forces between dissimilar molecules dominate, so the compounds A and B tend to mix and an ordered crystal can be formed of alternating A and B molecules (Fig. 2.4b). In contrast, for $\chi > 2$, the interaction forces between similar molecules are larger, so the interaction term of similar molecules is dominating and the two materials tend to phase-separate (Fig. 2.4c) [25, 57].

Binary mixtures can be formed by preparing different heterostructures. They

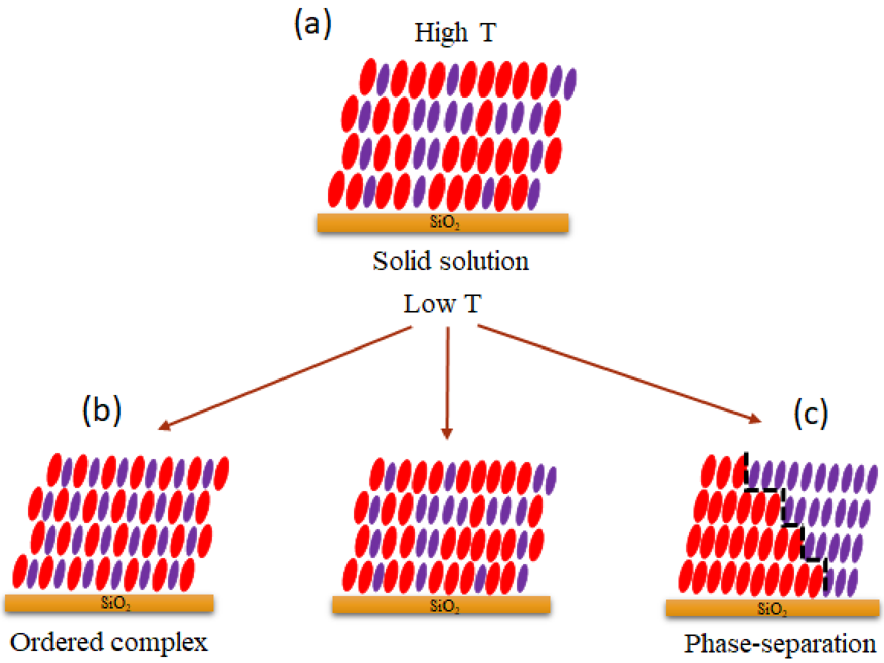

Figure 2.4: *Simplified scenarios of different binary mixing behavior for organic molecules depending on the intermolecular interactions: a) solid solution, b) ordered complex and c) phase-separation. Picture is modified from Refs. [25, 57].*

differ in properties and creation processes and are important for devices of donor and acceptor molecules used in this thesis. The different heterostructures are shown in Figure 2.5. Planar heterojunction (PHJ) is a stack of material A on top of material B (Fig. 2.5a). In this structure, a defined interface between both materials A and B is developed. The structure and morphology of the top layer are influenced by the bottom layer. A variation of this heterostructure is the graded interface. This heterostructure has, instead of a sharp boundary, a graded interface so that the materials can mix or blend at the interface (Fig. 2.5b).

The bulk heterojunction is used in this thesis to prepare thin film structures. Here, both materials are blended with each other and an homogenously mixed material results if both compounds are able to mix (Fig. 2.5c) [25, 29]. For the properties and conditions under which two materials can mix or phase-separate, see the section described above.

2.1.4 Thin film growth

Vacuum deposition techniques such as organic molecular beam deposition are an important and valuable tool to grow thin films and fabricate heterostructures in organic optoelectronic devices [25]. Organic molecules have internal degrees of freedom in contrast to their inorganic counterparts. Therefore, their self-assembly processes on surfaces are more difficult and can also influence the film growth pro-

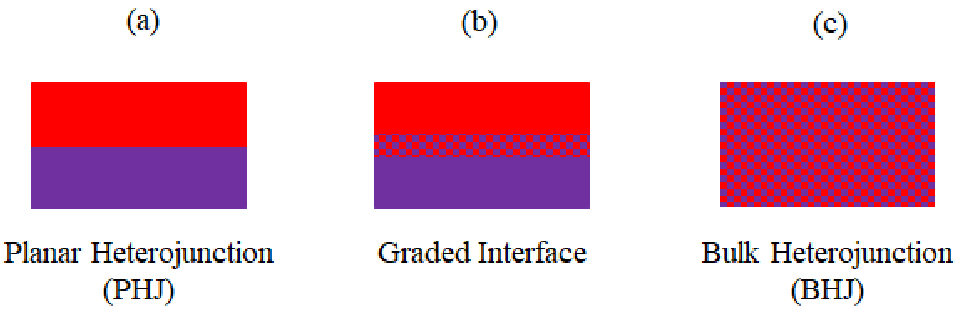

Figure 2.5: *Different schematic heterostructures of two materials A and B: a) planar heterojunction, b) graded interface and c) bulk heterojunction. Picture is modified from Ref. [25].*

cedure. Through the orientational degree of freedom, the molecular orientation in some domains can be different and the disorder in the thin films can be increased. The vibrational degrees can have impacts on the interaction of the molecule with the substrate and due to the conformational degree of freedom, some building blocks of molecules can change during the growth procedure [27]. The thin film growth and the different growth modes (Fig. 2.6) are based to some degree on the wetting theory [59] but also non-equilibrium considerations have to be taken into account. The three different growth modes of organic molecules on a respective substrate are determined by the interaction between the substrate and the adsorbate material, in this thesis, the organic molecules.

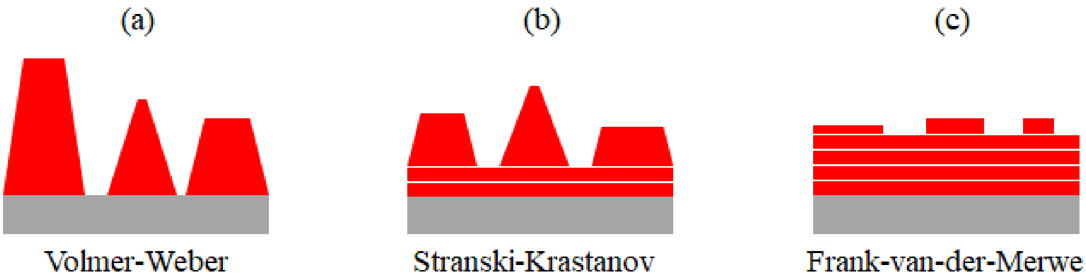

Figure 2.6: *Schematic representation of the different growth modes: a) island growth (Volmer-Weber), b) layer-by-island growth (Stranski-Krastanov) and c) layer-by-layer growth (Frank-van-der-Merwe). Picture is modified from Ref. [60].*

If stronger interaction forces are taking place within the bulk absorbate material than with the substrate, islands are formed. Here, stronger de-wetting effects have to be considered and this film growth is called Volmer-Weber growth mode (Fig. 2.6a). It is also possible that the individual islands come into contact with each other due to their lateral growth. In the Stranski-Krastanov growth mode, layer-by-layer growth is starting followed by de-wetting or roughening (Fig. 2.6b). Through the mismatch in their lattice structure, islands are formed on top of the layers which are depending on the thickness-related strain energy. Layer-by-layer are grown independent of the film thickness in the Frank-van-der-Merwe growth mode (Fig. 2.6c). The favorable interaction forces are between the substrate and the absorbate and complete wetting layers are formed [27, 60, 61].

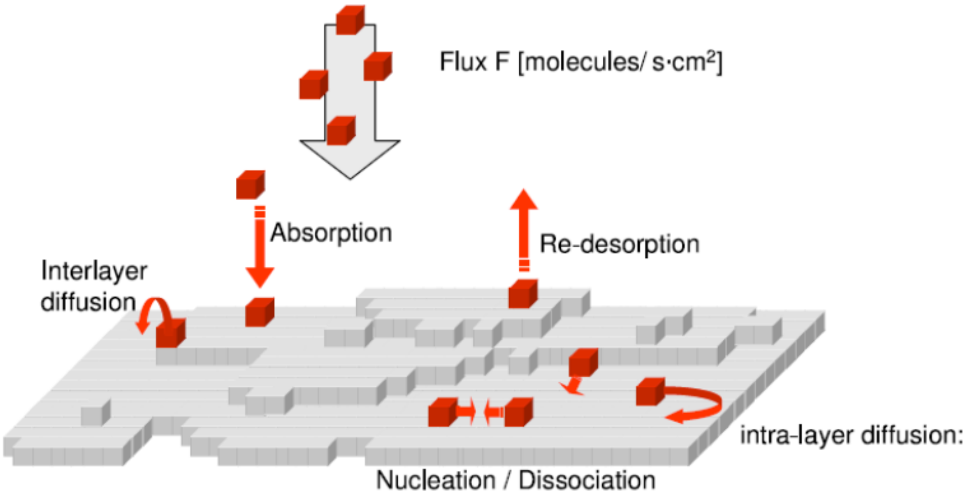

Figure 2.7: *Schematic representation of the atomistic processes of a film growth by organic molecular beam deposition. Picture is taken from Ref. [27].*

In Figure 2.7 a schematic scenario of a thin film grown by OMBD is shown with several characteristic processes. Here, the kinetic non-equilibrium processes as well as its irreversible atomic scale processes have to be considered [27]. The sublimed molecules arrive with a constant flux and a kinetic energy on a suitable surface. On this substrate surface, relevant processes like absorption, re-desorption, inter-layer diffusion, intra-layer diffusion, and nucleation take place. The nucleation is energetically favorable at steps or at defects [27, 60, 62]. Various parameters such as the growth rate, the adsorption, and re-desorption of the molecules on a respective substrate and the substrate temperature influence these processes [25].

One of the processes on the substrate surface, which can occur, is the inter-layer diffusion between growth layers. Due to the lack of nearest-neighbor interactions, an additional energy barrier exists, the so-called Ehrlich-Schwöbel barrier which is schematically shown in Figure 2.8 [62]. The molecule obtains a highly unfavorable edge position when reaching the other layer. If the Ehrlich-Schwöbel barrier is large, the inter-layer diffusion is hindered and this can lead to a wedding-cake structure. The layer coverage of such a thin film follows a Poisson distribution and a higher roughness of the thin film can be observed [59, 62–64].

The thin film properties can be adjusted by controlling and changing the different growth parameters. The shape and size of islands are determined by the kinetics of the system. For example, small islands can be formed if the deposition rate is high and the diffusion of the molecules is slow. Otherwise, bigger islands can be for example obtained when the diffusion is fast but the deposition rate is

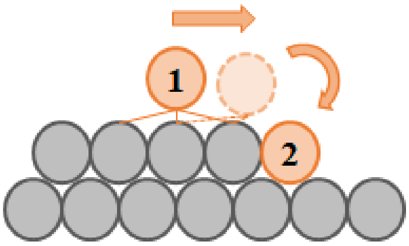

Figure 2.8: *Sketch of the inter- and intra-layer diffusion over a step edge (from position 1 to 2). Picture is modified from Ref. [62].*

lower. Another growth parameter that can be adjusted is the temperature of the substrate. If the substrate is cooled, at low temperatures, the absorbate will stay where they have arrived. At higher temperatures instead, the diffusion is more facile which can lead to a more ordered structure [59, 62, 63].

2.2 Optical response of materials

Another very important aspect especially for optoelectronic applications are the optical properties of a semiconducting material. Therefore, some basic concepts such as Fresnel coefficients at the interface and the Franck-Condon principle have to be discussed.

The dielectric function $\tilde{\epsilon}$ is an intrinsic material property and characterizes the optical behavior of a material, for instance, the interaction with electromagnetic radiation. This material property is a complex function ($\tilde{\epsilon} = \epsilon_1 - i\epsilon_2$) and related to the refractive index $\tilde{n}$ of the material through the following

$$\tilde{n} = \sqrt{\tilde{\epsilon}} \quad ; \quad \tilde{n} = n + ik \tag{2.6}$$

with k as the extinction coefficient [65, 66].

2.2.1 Fresnel coefficients at interfaces

The reflection or transmission properties of a material are depending on the dielectric function and are described in the following section. For more details, it is referred to Refs. [65, 66]. The transition of an electromagnetic wave traveling from one medium through the second one with the respective complex refractive index is schematically shown in Figure 2.9a.

Exemplary, two homogenous and isotropic media with different optical properties are presented. The transition results in a reflected wave traveling back in the first medium and a wave transmitted in the second medium. To calculate the reflection coefficients for the transition from the first to the second medium, the

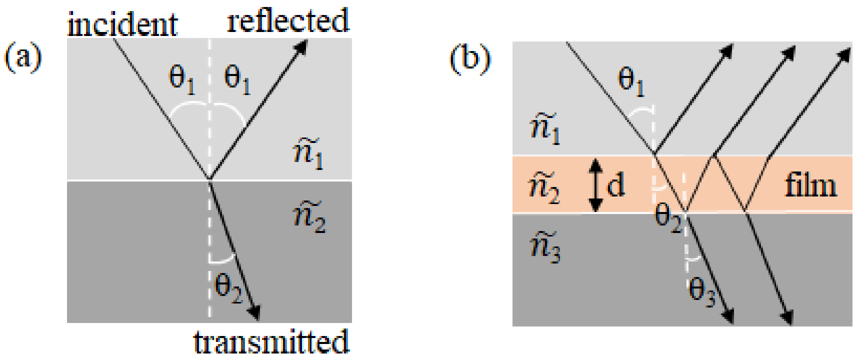

Figure 2.9: *Sketch for the Fresnel coefficient calculation: a) single interface with medium* $\tilde{n}_1$ *and* $\tilde{n}_2$ *and b) double interface with film layer and therefore medium* $\tilde{n}_1$*,* $\tilde{n}_2$*, and* $\tilde{n}_3$ *and the respective angles. Picture is modified from Refs. [65, 66].*

Maxwell relation has to be considered and Snell's law (Eq. 2.7) has to be fulfilled.

$$\frac{sin\ \theta_1}{sin\ \theta_2} = \frac{n_2}{n_1} \tag{2.7}$$

The Fresnel coefficients can be described as follows:

$$\tilde{r}_p = \frac{\tilde{E}_p^{refl}}{\tilde{E}_p^{inc}} = \frac{\tilde{n}_2\ cos\ \theta_1\ -\ \tilde{n}_1\ cos\ \theta_2}{\tilde{n}_2\ cos\ \theta_1\ +\ \tilde{n}_1\ cos\ \theta_2} \tag{2.8}$$

$$\tilde{r}_s = \frac{\tilde{E}_s^{refl}}{\tilde{E}_s^{inc}} = \frac{\tilde{n}_1\ cos\ \theta_1\ -\ \tilde{n}_2\ cos\ \theta_2}{\tilde{n}_1\ cos\ \theta_1\ +\ \tilde{n}_2\ cos\ \theta_2} \tag{2.9}$$

The indices s and p indicate the parallel polarization of the electromagnetic field to the interface plane and the polarization perpendicular to it. To determine the total reflectivity, the square of the Fresnel reflection coefficients has to be taken into account.

If the plane of an electromagnetic wave is traveling through a thin film medium (homogenous dielectric film with thickness d, Fig. 2.9b, medium 2) the Fresnel coefficients have to be redefined to the pseudo-Fresnel coefficients. On each side of the thin film, semi-finite and homogenous media are assumed. The pseudo-Fresnel coefficients are described with the phase thickness β of the film and the wavelength λ_0 of the incident radiation:

$$\tilde{r} = \frac{\tilde{r}_{12}\ +\ \tilde{r}_{23}\ e^{2i\beta}}{1\ +\ \tilde{r}_{12}\ \tilde{r}_{23}\ e^{2i\beta}} \quad ; \quad \beta = \frac{2\pi}{\lambda_0}\ \tilde{n}_2\ d\ cos\ \theta_2 \tag{2.10}$$

The boundary between the film and the air is r_{12} and r_{23} is the boundary between the film and the substrate.

2.2.2 The Franck-Condon principle

Molecule spectra are electronic spectra of organic solids where changes in the electronic as well as in the vibrational state can appear. These transitions between the energy levels of the molecule can occur with emission or absorption of radiation [67]. For a quantum-mechanical description of absorption or emission, the wavefunction can be divided into a vibronic, an electronic, and a spin state (Eq. 2.11). For real molecules, the nuclei are not stationary, instead, they oscillate with a certain vibration frequency and this can be described as a separate part of the wavefunction Ψ_{vib} according to [50]:

$$\Psi_{total} = \Psi_{el} \cdot \Psi_{spin} \cdot \Psi_{vib} \tag{2.11}$$

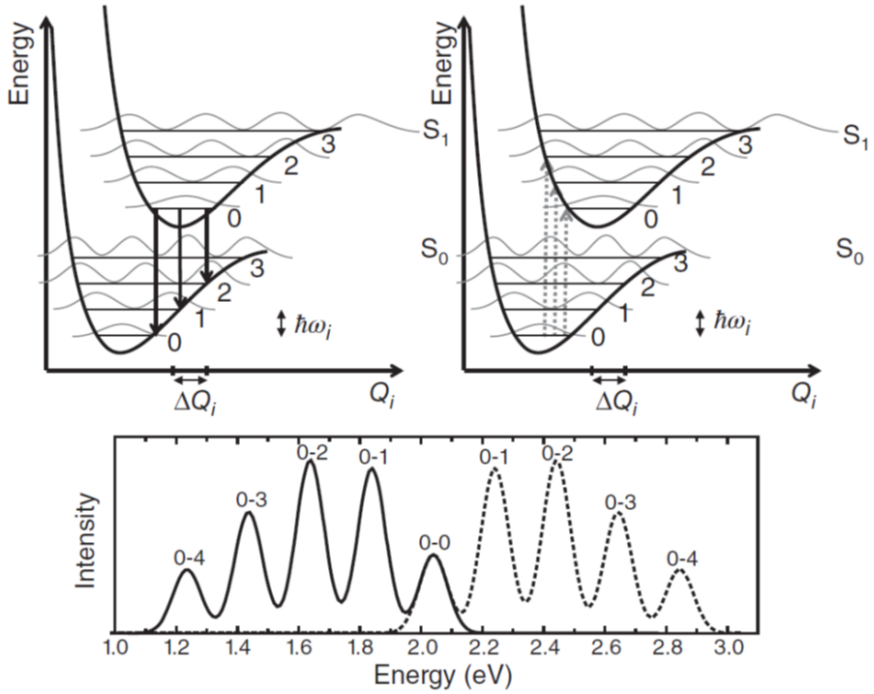

Figure 2.10: *Schematic representation of the Franck-Condon principle with simplified potential energy curves, vibrational wavefunctions, and the respective emission and absorption spectra. Picture is taken from Ref. [50].*

Due to the larger mass of the nuclei, changes are at a much larger timescale as the electronic motion [67]. Figure 2.10 shows the simplified potential energy curves and vibrational wavefunction of two electronic states. Vertical lines are representing the transitions between the two states with constant internuclear separation. The transitions are vertical because of the Franck-Condon principle which reveals that the reaction of the nuclei on changes in the electronic structure is much slower than the electronic transition [50, 68, 69]. The offset in nuclear coordination, also called the normal mode coordinate ΔQ_i between the two states, influences the maximum of the vibronic wavefunction. The square of the product of the vibrational wavefunction $|\langle\Psi_{vib,f}|\Psi_{vib,i}\rangle|^2$ is also known as the Franck-Condon factor F and indicates the probability of the transition from the lowest (0th) vibrational ground-state level to the higher vibrational level m in the excited state. The transitions have a Poisson distribution and can be described with the Huang-Rhys parameter S (Eq. 2.12):

$$I_{0-m} = |\langle\Psi_{vib,f}|\Psi_{vib,i}\rangle|^2 = \frac{S^m}{m!}e^{-S} \tag{2.12}$$

If the overlap integral, the Franck-Condon factor, is large then the transitions are most intense [50, 67, 70]. The absorption and emission transitions in an ideal case are mirror symmetric (Fig. 2.10) and the differences between their maxima are defined as Stokes-shift [50, 69, 70].

2.3 Excitons in molecular solids

In the following section, excitations and interaction processes in organic small molecule semiconducting materials will be described. In organic solids, electronic excitations from the ground-state to the excited-state lead to electron-hole pairs which are coulombically bound and called excitons. An ideal exciton is electrically neutral but contains an electronic excitation energy that can move through the periodic crystal structure [40, 51, 71]. For excitons, there are three different cases that can be distinguished, shown in Figure 2.11.

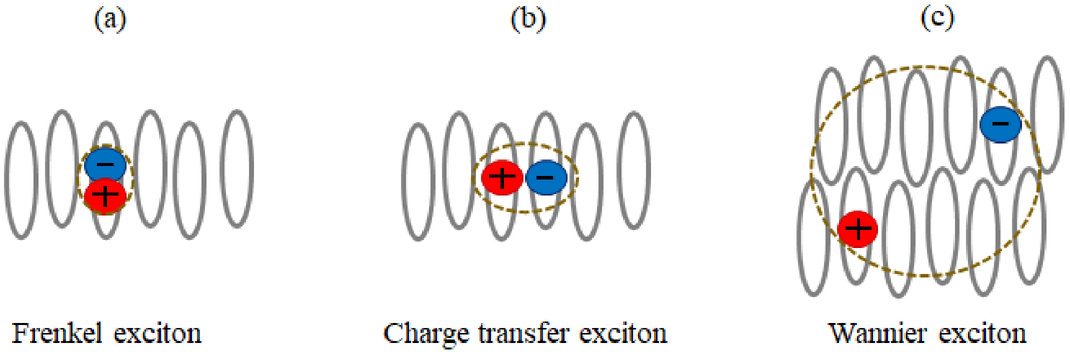

Figure 2.11: *Graphical illustration of excitons with different radii: a) a Frenkel exciton, b) a charge transfer exciton and c) a Wannier exciton. Picture is modified from Refs. [40, 51].*

A Frenkel exciton is a localized excitation on one molecule which can move through the lattice via dipole interactions (Fig. 2.11a). If the excitation takes place from one molecule to another nearest-neighbor molecule, it is called a CT exciton (Fig. 2.11b). The electron-hole pair is delocalized on two molecular units. The large Coloumb binding energies (0.2 - 0.4 eV) prohibit in organic small molecules electron and hole separation with longer distances. Normally, the electron-hole distance is one or two times larger than the distance of the molecular structural units [40, 51, 71]. For monomolecular crystals, the Frenkel exciton energy is smaller than the CT exciton energy ($E_{FE} < E_{CT}$), whereas in mixed crystal, as studied in this thesis, the Frenkel exciton is similar or larger than the CT energy ($E_{FE} \gtrsim E_{CT}$). For the Wannier exciton, the electron and hole are also localized on two different molecules, but the distance between the charges is an order of magnitude larger than the lattice structural units (about 40 - 100 Å, Fig. 2.11c). This leads to a delocalization over a large area and this type of exciton is more common for inorganic semiconductors. Wannier excitons are difficult to obtain in molecular organic solids [51, 72]. In the next section, the CT exciton and therefore also CT effects are described in more detail.

2.3.1 Charge transfer effects

A charge transfer transition is a large fraction of electronic charge which is transferred from one entire molecule to another one (from the donor to the acceptor molecule). CT can take place between two different materials for example in molecular mixtures of organic semiconductors which are investigated in this thesis [38, 41, 42, 73]. CT was first described by Mulliken in the year 1952 with the explanation that donor-acceptor binding results on account of quantum-mechanical mixing of two states [39]. CT excitations and CT excitons are the predominant lowest excitation states and cause therefore the lowest-energy transitions in singlet systems [51].

It can be distinguished between partial and complete CT. In Figure 2.12b it is schematically shown that for a partial CT only a fraction of an electron is transferred from the donor to the acceptor molecule whereas for a complete CT one electron is transmitted completely from one molecule to the other one (Fig. 2.12a).

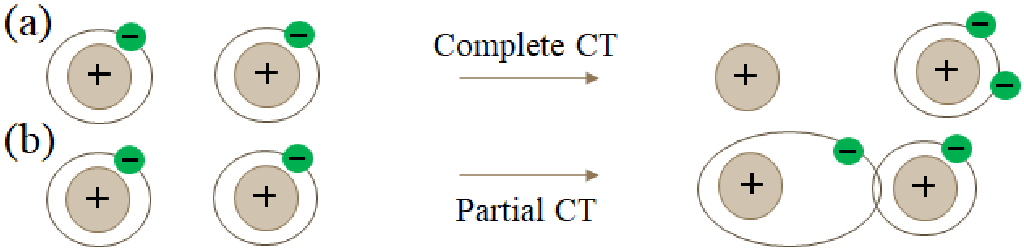

Figure 2.12: *Schematic illustration of a) complete charge transfer and b) partial charge transfer.*

The CT effects are depending on the structural morphology and the molecular packing of the respective donor-acceptor system. For a suitable CT effect, a suitable mixing of the donor and acceptor molecule is of high importance (Section 2.1.3). The CT interactions are quantified by the electron and hole CT integrals and are depending on the nodal pattern of the relevant FMOs whose overlap should be the highest [40]. There are several conditions which are defining the CT energy: the overlap of the FMOs, the Coulomb binding energy between the molecules, and the delocalization of the CT exciton [41]. The CT effects of organic molecules in thin films can have an anisotropic nature which implies that the CT transition takes mainly place in the $\pi-\pi$-direction [49]. The optical and electronic properties of such thin film systems can be determined by the CT effects [40].

Important for these effects is the distinction between ground-state CT (GS-CT) and excited-state CT (ES-CT). A GS-CT is a charge transfer state which is related to the ground-state by a CT transition and where no external stimulation is required. An ES-CT, in contrast, is a charge transfer transition that is induced by excitation with light. If the excited CT decays, a neutral ground-state and an emission of a photon are received with an energy below the optical gap of both pure acceptor and donor compounds. New emission or absorption bands can be detected which can not be assigned to the individual compounds. The existence of a CT emission also involves a CT absorption band within the optical gap of both pure materials [41, 73]. By definition, a CT complex is a donor-acceptor complex where an excited-state CT has occurred. An ES-CT of organic solids has mainly a low extinction coefficient, but therefore a high emission intensity [41, 74]. Lifetimes of CT which originate via exciton dissociation are about two magnitudes shorter than those which are formed directly from the GS [38]. For the detection and investigation of ES-CT effects, optical spectroscopy methods such as absorption, ellipsometry, and photoluminescence are used which are also carried out and explored in detail in this thesis.

There are different methods to investigate the GS-CT. One suitable method is the photoelectron spectroscopy where GS-CT is distinguishable through the shifted ground-state level and depending on the strength of the associated electric field [75]. X-ray diffraction and X-ray standing waves are used for example to detect GS-CT with a reasonable substrate through the different adsorption lengths [76]. Another method is the infrared spectroscopy, which is also performed in this thesis. Here, the GS-CT is examined through a shift of intramolecular vibration frequencies [77–79], which is described in detail in Sec. 4.4.3 (FTIR method) and in the results in Sec. 6.2.

In a rather common approach, molecular CT can be divided roughly into three different cases depending on the degree the molecules interact with each other (Figure 2.13) [41, 42, 49]. A distinction is shown between systems that form only excited-state CT effects, weak GS-CT and strong ES-CT effects, and strong GS-CT effects with the formation of hybridized molecular orbitals. For the various studied system in this thesis, the different cases will be described and discussed in detail in the results in Sec. 6.7.

Charge transfer states are intermediates in interesting optoelectronic processes such as charge separation and recombination in thin film organic photovoltaic devices [41]. The CT energy E_{CT} for example limits the open-circuit voltage and the overall power conversion efficiency [73]. CT can decay into the ground-state

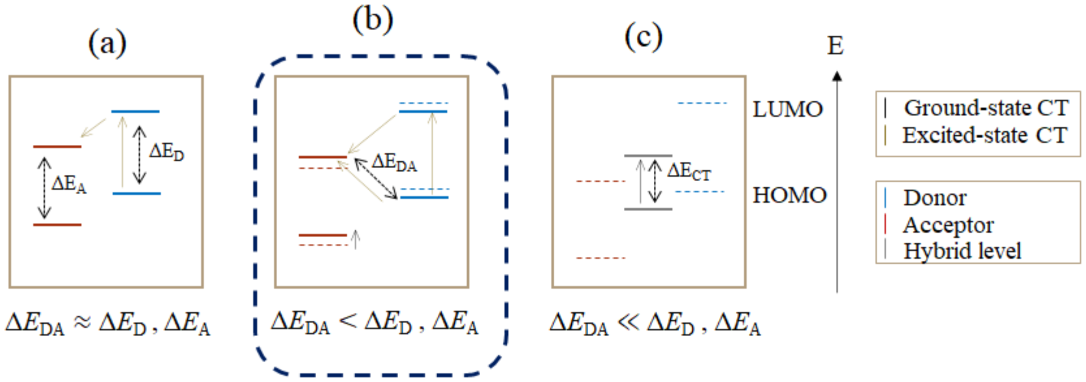

Figure 2.13: *Schematic scenarios of different charge transfer cases: a) only ES-CT effects, b) weak GS-CT and strong ES-CT effects and c) strong ES-CT effects with hybridized MOs formation.*

or it can produce the charge-separated (CS) state also desired for some processes. Therefore, it has to be distinguished between the CT and the CS state. In the CT state, the charges are bound and CT effects can take place spontaneously whereas CS needs a driving force. The dissociation into free carriers appears via the manifold of CS states. The free charges have to overcome the Coulomb binding forces and can freely move in the respective active layer. The dissociation of CT into free charge carriers can be very efficient and can increase the conductivity of the material but nevertheless, energy losses have to be considered [38, 41, 42]. In the equilibrium, the different processes such as CS, CT, and recombination are all balanced [41].

2.3.2 Jablonski diagram

Excited-states and transitions in organic small molecules can be investigated using optical spectroscopy. The following section is based on Refs. [51, 52, 80].

Light can be absorbed by an organic molecule resulting in excited singlet or triplet states. Singlet states are electronic states where the electronic spins are coupled pairwise to a total spin quantum number of $S = 0$. The ground-state of a molecule with an even number of electrons is a singlet state and is called S_0 (Fig. 2.14). In this state, the organic crystal is diamagnetic. In contrast, triplet states are electronic states where the spins of two electrons are parallel to each other and which results in a total spin quantum number of $S = 1$. The respective organic solids have paramagnetic properties.

Figure 2.14 shows the Jablonski diagram with the relevant processes for a molecule of absorption and emission by light and relaxation. Absorption occurs from the GS to the higher excited-states. Organic solids exhibit absorption coefficients in the range of 10^5 cm^{-1}. The non-radiative transitions from the higher

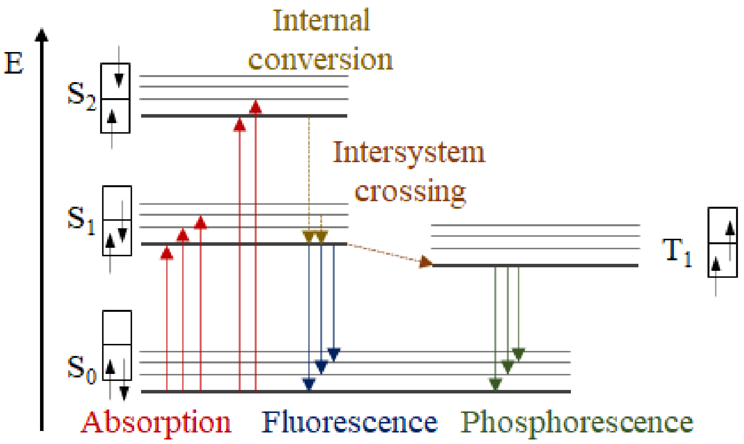

Figure 2.14: *Jablonski diagram with the relevant processes of absorption and emission and the different electronic singlet states* S_0*,* S_1*,* S_2*, and triplet state* T_1 *of a molecule. Picture is modified from Ref. [51].*

excited-states which have short lifetimes to the respectively first excited singlet or triplet state S_1 or T_1 are called internal conversion (IC). They are one magnitude faster than emissions from higher excited-states. The excited-state S_1 has lifetimes between 10^{-9} s - 10^{-4} s. Fluorescence is the radiative transition from $S_1 \rightarrow S_0$ and phosphorescence is the radiative transition from $T_1 \rightarrow T_0$. As defined by the Kasha rule, the emission takes place from the lowest excited-state of the respective multiplicity. The forbidden transitions between the singlet and triplet systems, called intersystem crossing (ISC), are non-radiative and depend on spin-orbit coupling. For organic solids which consist mainly of C and H (plus N and O) this coupling is relatively weak. The probability of the ISC is increasing if heavier atoms such as Br or I are incorporated in the molecule structure or by the influences of strong electric or magnetic fields.

2.3.3 Davydov splitting

The exciton model in dimers, which is important for organic semiconductors with two inequivalent molecules, is described in detail in Refs. [81, 82]. This model applies to crystals with several molecules per unit cell or molecule dimers that are not translationally equivalent. In the absorption spectra, several exciton bands are observed for these materials. The two molecules where the respective transition dipole moments (TDM) have different orientations reveal independent excited-state formation resulting in two energetically different states. This is the so-called Davydov splitting with the exciton splitting energy ΔE_{DS} (Eq. 2.13)

$$\Delta E_{DS} = \frac{2\,|\mu^2|}{r_{12}^3} \cdot (cos\ \alpha + 3\ cos^2\ \theta) \tag{2.13}$$

with μ as the transition dipole moment for the singlet-singlet transition of the monomer, and r_{12} is the center-to-center distance between the molecules. The angles α and θ are shown in Figure 2.15a and are described by the polarization axes of both compounds [82].

In Figure 2.15b the Davydov splitting and the exciton formation in a molecular dimer is shown. Due to the van der Waals binding contribution, the excited-state of the monomer is slightly at lower energy (red-shifted). For the dimer, the Davydov splitting into the two energy bands E' and E'' takes place. The in-phase arrangement of the transition dipole moments results in E' and the out-of-phase arrangement in E''. The larger intensity of light absorption of one molecular unit leads to larger Davydov splitting.

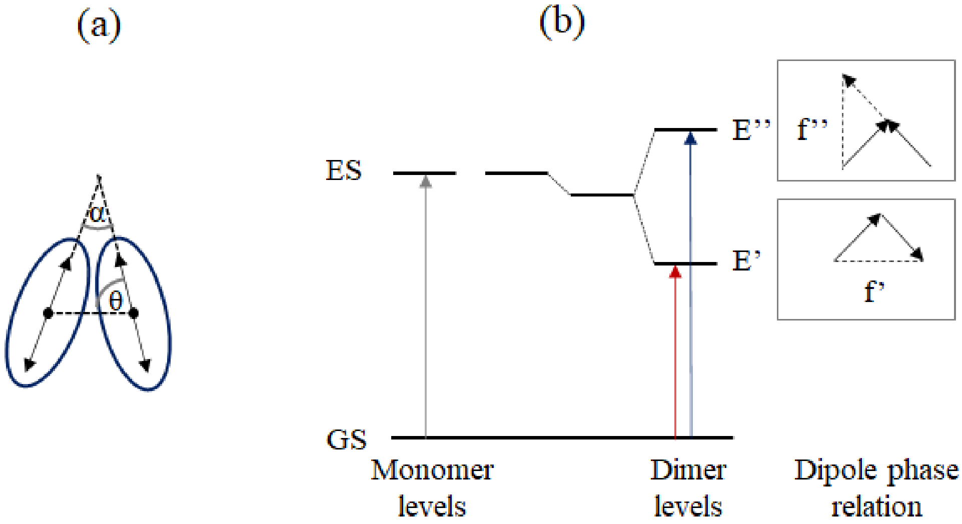

Figure 2.15: *Davydov splitting and exciton formation in a molecular dimer: a) schematic oblique orientation of the respective transition dipole moments and b) representation of the Davydov splitting with the respective energy levels and the dipole phase relation f of the two TDMs. Picture is modified from Ref. [82].*

Optical properties of thin films are depending on the molecular environment [83, 84]. Absorption and emission spectra for thin films differ from the monomer spectra due to intermolecular interactions. One effect is the so-called gas-to-crystal shift, a red-shift of the absorption thin film spectra compared to the monomer spectra because of the polarizability changes of the molecular environment [85, 86].

For dimers with strong Coulomb interactions and parallel oriented TDMs, which result in Davydov splitting as described above, a blue- or red-shift in absorption (H- or J-aggregations) can occur compared to the isolated molecules defined by Kasha et al. [82, 87]. For ideal J-aggregates, the 0-0 vibronic peak is increased compared to 0-1 or lower energy transitions in the absorption spectra (away from a Poisson distribution) and the 0-0 emission is allowed. In contrast, for ideal H-aggregates, it is the opposite case in absorption and the 0-0 emission is denied

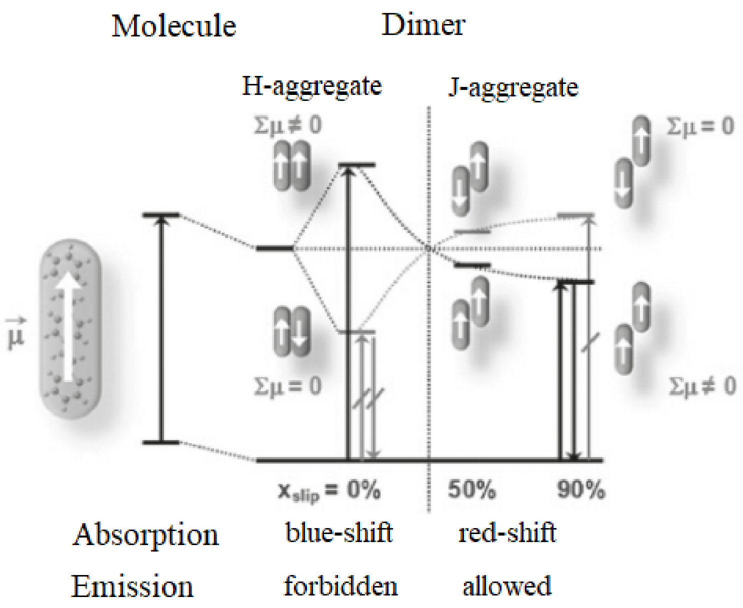

Figure 2.16: *The exciton model with the schematic representation of J- and H-aggregates and their respective influence on absorption and emission processes. Picture is taken from Ref. [90].*

[86, 88, 89]. If the TDMs of the dimers are oriented 'side-by-side', the dimers are identified as *H*-aggregates and 'head-to-tail' orientations as *J*-aggregates (Fig. 2.16) [88].

Chapter 3

Materials

3.1 Acceptor molecules: Perylene diimide derivatives

Perylene diimide (PDI) derivatives are organic small molecules that are widely used as electron donors and acceptors in organic electronic devices especially for organic field effect transistors [4, 5, 91–94]. Due to their relatively strong electron affinities, they are very promising and most investigated n-type organic materials [20]. They show excellent chemical and thermal stabilities, high light absorption capabilities, and high fluorescence quantum yields [23, 95]. PDI derivatives consist of a perylene diimide backbone responsible for strong intermolecular π - π interaction forces (Fig. 3.1). Through the incorporation of different side groups, they can easily be chemically modified to suit solubility, photophysical, or electron-bearing demands and to be very suitable for organic electronic applications [20, 95, 96]. They are structurally well-defined and due to the tailoring of the charge-transport properties upon changing the substituents on the imide or the bay position of the perylene backbone (Fig. 3.1) [4, 19, 20, 36], they can therefore serve as an acceptor model system.

The alkyl, branched, and fluorinated side chains and the electron-withdrawing side groups can alter molecular packing and morphology of the deposited thin films [19, 20, 23]. The symmetric anhydride substitution at the imide position of PDI derivatives, to achieve alkyl, branched, or fluorinated side chains, has influences on the different optical and structural properties of the thin film growth. For example, flexible long alkyl side chains can lead to several crystalline phases in thin film growth. Branched side chains can decrease the π - π interaction of the respective PDI derivatives due to the steric hindrance of the groups. This leads also to charge carrier traps and increases the solubility of these molecules [19, 20]. Through the electron-withdrawing groups and rigid behavior of fluorinated side chains, the LUMO level can be lowered compared to the respective counterparts. This will also allow dense and face-to-face packing [19, 20, 23].

Through the difunctionalized core substitution at the bay position of the PDI derivatives cyano groups, Br, F or Cl atoms can be incorporated. Fluorinated and also brominated PDIs are more complicated to synthesize and the molecules can decompose during sublimation [20]. Through chlorinated and especially cyanted PDIs, the LUMO level can be lowered, the solubility of these molecules is increased

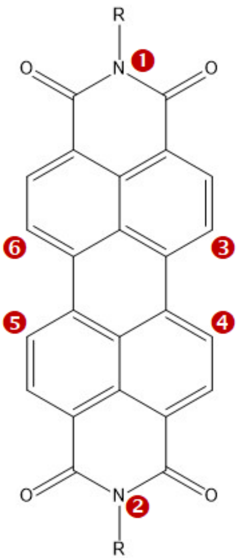

Figure 3.1: *Schematic structure of a generic PDI derivative with two side chains (R) at the imide positions (marked with numbers 1 and 2) and marked bay positions by the numbers 3, 4, 5, and 6.*

and they demonstrate superior electrical transport properties [21, 22].

By varying the side chains and incorporating the cyano groups of the PDI derivatives, the various growth and mixing behavior with a donor molecule as well as the influence on possible CT effects can be investigated in such systems. There are only few publications on donor-acceptor thin film systems of PDI derivatives with organic small donor molecules [97–99]. In this thesis, the focus is on several PDI derivatives as acceptors which differ in the side chains in the imide position and in the cyano groups in the bay position as well as on two different donor molecules.

3.1.1 PDI derivatives with n-alkyl side chains

The following PDI derivatives shown in Figure 3.2 belong to the perylene alkyldiimide class and are used in this thesis as acceptor molecules. They consist of a perylene diimide core with different *n*-alkyl side chains in the imide position and have therefore different properties regarding thin film growth. These different PDI derivatives are used in organic electronic applications, but only PTCDI-C_8 is structurally well investigated [91, 98, 100, 101].

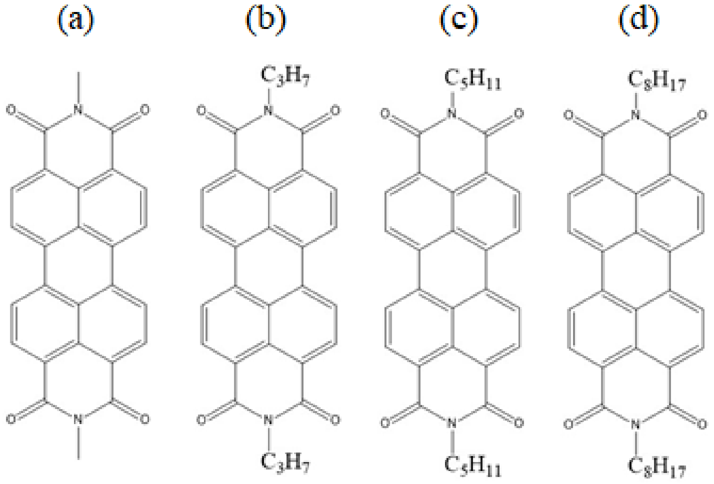

Figure 3.2: *Schematic structure of the PDI acceptor molecules: a) PDIC*$_1$*, b) PDIC*$_3$*, c) PDIC*$_5$ *and d) PDIC*$_8$*.*

Table 3.1: *Calculated thin film unit cell parameters of pristine PDI derivatives with* n*-alkyl side chains in the imide position.*

	a [Å]	b [Å]	c [Å]	α [°]	β [°]	γ [°]
PDIC$_1$ [102]	3.867	15.571	14.587	90	97.71	90
PDIC$_3$ [102]	4.689	18.077	14.258	104.24	89.93	111.30
PDIC$_5$ Polymorph A [103]	4.754	8.479	16.30	86.88	93.50	83.68
PDIC$_5$ Polymorph B [103]	11.624	11.617	17.415	98.21	71.25	116.06
PDIC$_5$ Polymorph C [1]	-	7.35	18.4	80.5	90	90
PDIC$_8$ [1]	8.45	4.77	21.49	99.7	106.4	97.8

[1] calculated in the results in Sec. 5.1.1

PTCDI-C$_1$ (PDIC$_1$) is short for N,N'-dimethyl-3,4:9,10-perylenedicarboxyimide and has only a methyl group in the imide position (Fig. 3.2a). PDIC$_1$ grows in thin smooth films with small spherical crystallites and the crystallinity can strongly increase with higher substrate temperature [104, 105]. The molecules are oriented in thin films in a herringbone arrangement and parallel to the substrate surface when grown under suitable conditions on SiO$_2$ substrates [104]. The unit cell parameters for the various PDI derivatives are depicted in Table 3.1.

The PDI acceptor molecule with n-propyl side chains in the imide position is PTCDI-C$_3$ (PDIC$_3$), which is short for 2,9-Dipropylanthra[2,1,9-def:6,5,10-d'e'f'] diisoquinoline-1,3,8,10(2H,9H)tetrone (Fig. 3.2b). These molecules are oriented in thin films in an edge-on configuration and also a more offset-stacked orientation is created [106].

In contrast, PTCDI-C_5 (PDIC_5) molecules, which is short for N,N'-dipentyl-3,4:9,10-perylenedicarboxyimide (Fig. 3.2c), are arranged in thin films in an offset-stacked packing. A tilted but more standing-up orientation is established when deposited under suitable conditions on SiO_2 substrates. The growth modes of the PDIC_5 molecules with an *n*-pentyl side chain in the imide position are changing from a layer-by-layer growth followed by an island growth to a 3D growth with increasing thickness. Better crystallinity and electronic thin film device characteristics are achieved at higher growth temperatures [107, 108]. PDIC_5 molecules create numerous polymorphs when deposited at high substrate temperatures (Table 3.1) [103] which are explained in detail in the result Section 5.1.

PTCDI-C_8 (PDIC_8) is short for N,N'-dioctyl-3,4:9,10-perylenedicarboxyimide and consists of a perylene diimide core with *n*-octyl side chains in the imide position (Fig. 3.2d). Thin film devices of PDIC_8 have outstanding optical and electrical properties, high electron mobility, and high photosensitivity [91, 98]. PDIC_8 grows in smooth films with needle-like features and is coherently ordered across the entire film thickness. As the other PDI derivatives, the layer-by-layer growth is changing to a 3D crystalline structure with increasing film thickness [91, 109]. The PDIC_8 molecules are oriented standing upright with a tilt angle to the surface of 67° and are arranged in an offset-stacked orientation. The TDM is along the long molecule axis [101, 110]. All four PDI derivatives are purchased from Sigma Aldrich with a purity of 98 % and used as received.

3.1.2 PTCDI-C_8-CN_2 and PDIF-CN_2

Figure 3.3a shows the molecule structure of PTCDI-C_8-CN_2 (PDIC_8-CN_2), which is short for N,N'-bis(n-octyl)-dicyanoperylene-3,4:9,10-bis-(dicarboxyimide), with its respective HOMO and LUMO levels. PDIC_8-CN_2 consists of a perylene diimide core with *n*-octyl side groups in the imide position and two incorporated cyano groups at the bay position (Fig. 3.3a). Thin films of PDIC_8-CN_2 are structurally well investigated and organic electronic devices can be prepared with this PDI derivative demonstrating high charge carrier mobilities between 0.1 and 1 cm^2/Vs and efficient electron injection from gold electrodes [4, 111]. PDIC_8-CN_2 grows in smooth thin films without forming polymorphic phases [112]. Thin films of this molecule show quasi 2D layer-by-layer growth. This changes to 3D spiral growth which means a Stransky-Krastanov mode, a layer-plus-island growth, with increasing film thickness [113–115]. The PDIC_8-CN_2 molecules are oriented in thin films with the longest axis normal to the surface and the π - π overlap is in the substrate plane [4, 111, 116]. The TDM is along the long molecule axis. The unit cell parameters for PDIC_8-CN_2 and PDIF-CN_2 are depicted in Table 3.2.

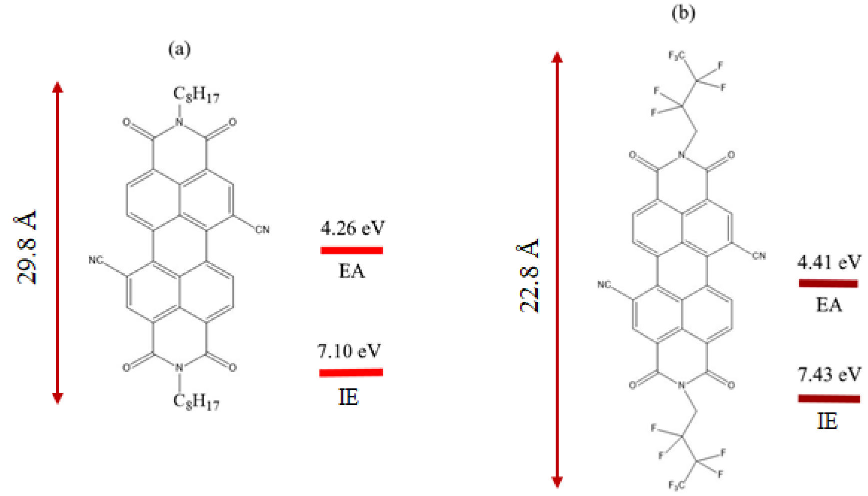

Figure 3.3: *Schematic structure of the PDI acceptor molecules with the different electron affinities (EA) and ionization energies (IE) [113, 117]: a) PDIC$_8$-CN$_2$ and b) PDIF-CN$_2$.*

Table 3.2: *Calculated thin film unit cell parameters of pristine PDIC$_8$-CN$_2$ and PDIF-CN$_2$.*

	a [Å]	b [Å]	c [Å]	α [°]	β [°]	γ [°]
PDIC$_8$-CN$_2$ [1]	5.0	8.7	20.3	100.78	96.94	100.1
PDIF-CN$_2$ [49]	5.53	7.52	20.4	87.12	101.5	106.3

[1] calculated in the results in Sec. 5.1.1

PDIF-CN$_2$ is short for N,N'-1H,1H-perfluorobutyl-dicyanoperylene-3,4:9,10-bis-(dicarboxyimide) and consists of a perylene diimide core with perfluorobutyl which means there are fluorinated side groups in the imide position and two incorporated cyano groups at the bay position (Fig. 3.3b). Thin film organic electronic devices with this PDI derivative show high charge carrier mobilities, low threshold voltages, and high I_{on}/I_{off} ratios [36, 93]. Enhanced electron mobility can also be achieved through depositing thin films of PDIF-CN$_2$ on hydrophobic surfaces which can be surfaces treated with Hexamethyldisilazane (HMDS) [118]. PDIF-CN$_2$ grows amorphous on an untreated SiO$_2$ substrate when deposited at room substrate temperature. Crystalline PDIF-CN$_2$ films can be observed at growth temperatures higher than 403 K. The molecules are oriented almost standing upright and the TDM is along the long molecule axis [117]. PDIC$_8$-CN$_2$ and PDIF-CN$_2$ were bought from Flexterra.

3.1.3 $PDIC_2F_3$

$PDIC_2F_3$ is short for N,N'-bis(2,2,2-Trisfluoroethyl)-perylene-3,4:9,10-bis (dicarboxyimide), a PDI derivative with two fluorinated ethyl side chains in the imide position. Its molecular weight is 554 g mol^{-1} and $PDIC_2F_3$ has a molecule volume of 548 $Å^3$ calculated for normal pressure and temperature. $PDIC_2F_3$ is thermally stable against polymerization and decomposition and starts to sublime at $T > 603$ K at a pressure in the range of 10^{-6} mbar. The molecule structure and its synthesis are depicted in Figure 3.4. The acceptor molecule $PDIC_2F_3$ is synthesized according to previously reported imidization procedures [36, 119, 120]. The reaction mechanism is a rather simple and straightforward condensation reaction where a primary amine reacts with carbon acid anhydride to a secondary carbon acid amide (Fig 3.5).

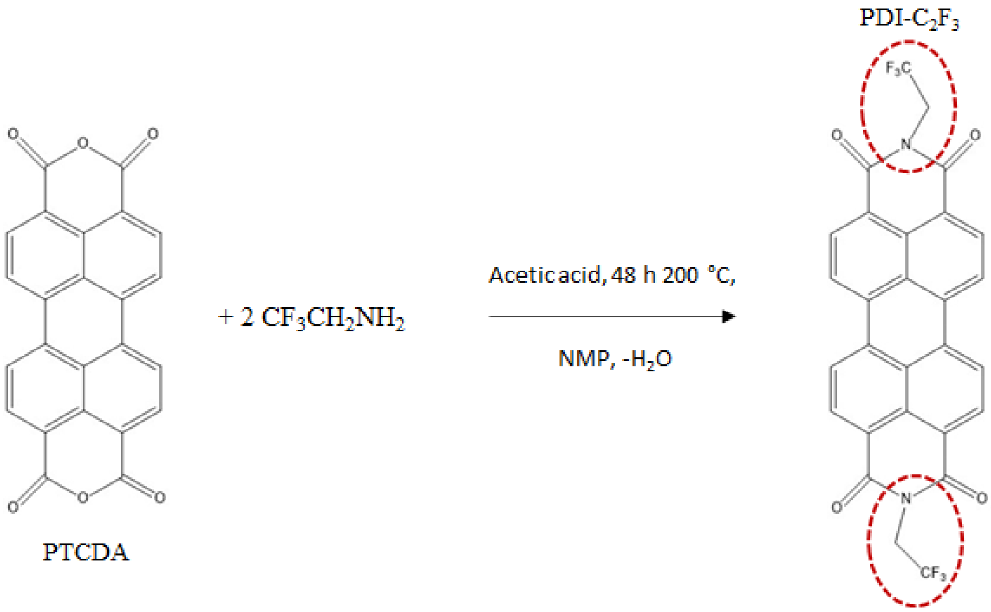

Figure 3.4: *Schematic structure of the acceptor molecule* $PDIC_2F_3$ *and its reaction mechanism starting from the educt PTCDA.*

All of the reagents are bought from Sigma Aldrich and used as received. Perylene tetracarboxylic dianhydride (PTCDA) (0.82 g, 2.09 mmol) is dispersed in dried N-methyl-2-pyrrolidone (NMP, 8.2 ml) with a catalytic amount of Acetic Acid (0.82 ml) under Argon atmosphere. To the reaction mixture, Trifluoroethylamine (1.1 ml, 14.014 mmol) is added slowly within a period of 0.5 h and stirred at 200 °C for 48 h. The reaction mixture is cooled to room temperature and slowly poured into 2N HCl (20 ml). The precipitate is filtered, washed, and dried in vacuum. The crude product is purified by recrystallization first with 2 % $NaHCO_3$ solution and afterwards with Toluene to obtain the product as a brown solid (1.07 g, 86 %). Before film preparation, the material was purified

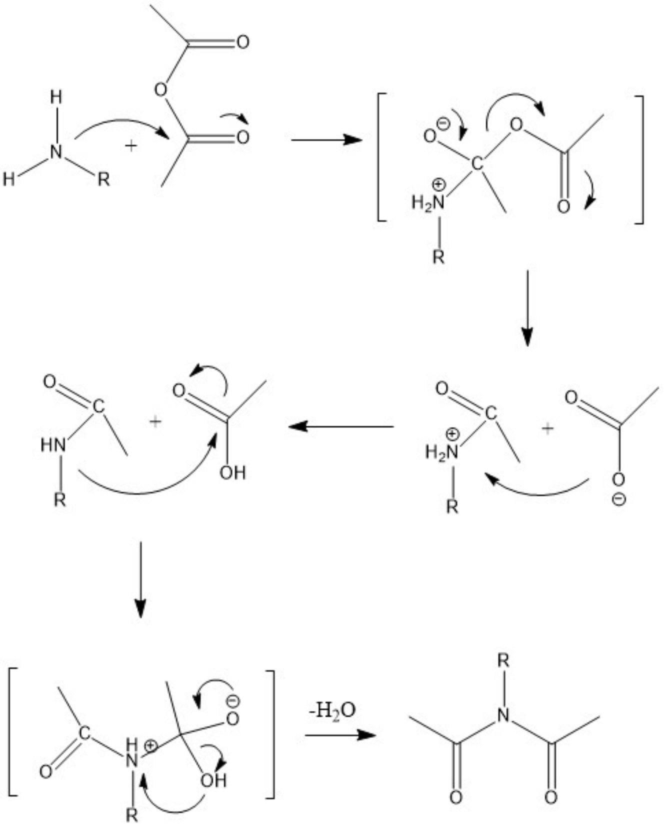

Figure 3.5: *Reaction mechanism of the condensation reaction simplified for the* $PDIC_2F_3$ *molecule.*

twice by gradient sublimation by Stephan Hirschmann, University of Stuttgart [121].

The growth behavior of $PDIC_2F_3$ in thin films (on substrates as for instance SiO_2) is not established yet [122]. The comprehensive structural and optical characterization of thin films with this acceptor molecule was not done before, only similar molecules were yet synthesized and structurally investigated [119, 120, 122]. In this thesis, the focus is also on the structural and optical characterization of the pure compound in thin films at different substrate temperatures.

3.2 Donor molecules: Dinaphthothienothiophene and Diindenoperylene

The two donor molecules are Diindenoperylene (DIP) and Dinaphthothienothiophene (DNTT) which are both well known for their applications in organic electronics, in particular, as donor molecules in OPV devices and as p-type organic semiconductors in OFETs [123–127].

DIP is a planar perylene derivative with the same perylene core as the PDI acceptor molecules and has two indeno-groups located at the opposite sites of this core along the long molecular axis. The schematic molecule structure with its energy levels is shown in Figure 3.6a. The specific name for this molecule is Diindeno[1,2,3-c,d:1',2',3'-lm]perylene with the chemical formula $C_{32}H_{16}$. The growth behavior of DIP in thin films is well established [83, 128–130]. DIP crystallizes in a herringbone structure motif (Fig. 3.6b) and is arranged in a standing-up orientation if grown under suitable conditions ($T > 300$ K) on SiO_2 substrates [27, 83, 129]. Under these conditions, DIP exhibits a nearly perfect initial layer-by-layer growth (up to 7-8 monolayers). Afterwards, due to a layer-dependent Ehrlich-Schwöbel barrier, a morphological transition to rapid surface roughening occurs which reveals terrace-like structures and is also observed in large film thicknesses [27, 129, 131]. The unit cell parameters of DIP are shown in Table 3.3. The TDM of DIP is oriented along the long molecular axis.

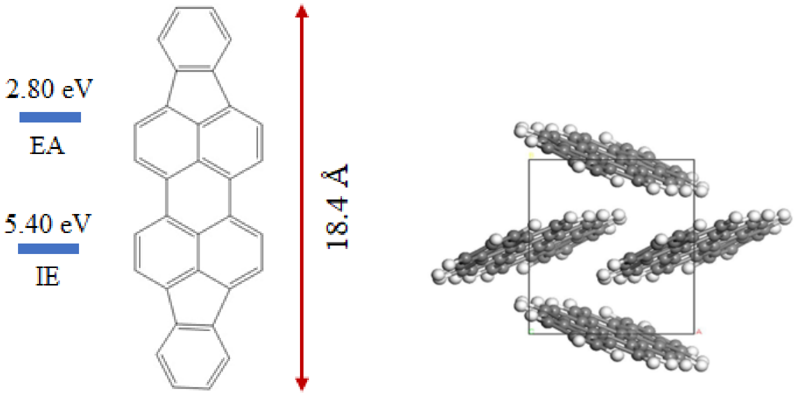

(a) (b)

Figure 3.6: *a) Schematic structure of the donor molecule DIP with the electron affinity (EA) and ionization energy (IE) [117] and b) herringbone structure. Picture is taken from Ref. [132].*

Table 3.3: *Calculated thin film unit cell parameters of pristine DIP and DNTT.*

	a [Å]	b [Å]	c [Å]	α [°]	β [°]	γ [°]
DIP [133]	7.171	8.550	16.798	90	92.416	90
DNTT [134]	6.187	7.622	16.211	90	92.49	90

DNTT is short for Dinaphtho[2,3-b:2',3'-f]thieno[3,2-b]thiophene and its thin film structure and organic electronic applications are comparable with pentacene (PEN) [135, 136]. DNTT has the chemical formula of $C_{22}H_{12}S_2$ and compared to the structure of PEN, the middle of the five benzol rings in PEN is replaced through two anti-thiophene groups (Fig. 3.7). In contrast to PEN, the advantages of DNTT are superior air stability due to the large ionization potential, high charge carrier mobility, and thiophene containing aromatics being more thermally and photochemically stable [137–139]. The thin film structure and growth behavior of DNTT are well established and similar to DIP and PEN [136, 140]. The unit cell parameters of DNTT are shown in Table 3.3.

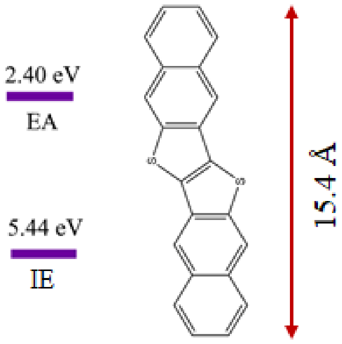

Figure 3.7: *Schematic structure of the donor molecule DNTT with the electron affinity (EA) and ionization energy (IE) [141].*

For DNTT a layer-by-layer growth is detected where almost planar molecules are arranged in a 2D herringbone structure [134]. DNTT is showing an interfacial wetting layer on various substrates and de-wetting effects after growth. It was shown that breaking-up of the layers, island formation, and wedding-cake island structures can be established [127, 135]. The molecules are oriented upright standing when growing under suitable conditions on for example SiO_2 substrates [135, 136]. The TDM of DNTT is oriented along the long molecular axis.

With its structure and size, the donor molecules fit perfectly to the PDI core and do not contain any sterically hindering side groups. DIP and DNTT are with their energy levels perfect donor molecules for the different PDI derivatives. DIP is bought from Stephan Hirschmann, University of Stuttgart, DNTT is purchased from Sigma Aldrich (purity of 98 %) and used as received.

3.3 Silicon and glass substrates

For preparing thin films in this thesis, different substrates were used. *P*-type Silicon (100) wafers with a diameter of 6 inch (15.24 cm) and a thickness of 675 ± 25 μm were purchased from Micro Chemicals GmbH. The wafers are covered with a 2 nm thick native Silicon oxide (SiO_2) layer under ambient conditions (with constant diffusion of O_2 in the silicon surface). Additionally, fused Silica glasses with a size of 4 inch (10.16 cm) and a thickness of 500 ± 25 μm were also needed and bought from Micro Chemicals GmbH. The nominal transmittance of these wafers is approximately 90 % in the range of λ = 270 nm - 2000 nm. The advantages of both substrates are that they have amorphous surface structures and interact only weakly with the organic molecules used in this thesis in contrast to metal surfaces. Furthermore, Silicon wafers are also used as gate dielectric in

OFETs with a passivation layer on top [142, 143]. Silicon substrates are suitable for the various necessary characterization methods such as X-ray scattering (Section 4.2) and together with the glass substrates, also essential for multi-sample analyses required for example for ellipsometry measurements (Section 4.4.4). The fused Silica glass substrates have a surface roughness ≤ 1 mm and similar surface properties as the Silicon wafers. This leads presumably to similar structure and morphology of the deposited thin films and therefore, both wafers are suitable for the usage as substrates for the thin film characterizations and investigations in this thesis.

Chapter 4

Experimental methods

4.1 Organic molecular beam deposition

Organic molecular beam deposition (OMBD) is a common technique to prepare thin films of organic semiconductors under ultra-high vacuum (UHV) conditions. For the fundamentals of OMBD in general it is referred to Refs. [26, 27, 61].

4.1.1 Ultra-high vacuum technique

In this thesis, UHV conditions which are by definition pressures of $p < 10^{-7}$ mbar are used to prepare thin films in a UHV chamber. For more details on vacuum techniques, it is referred to Refs. [144, 145].

To connect the pressure p and the number of particles in a specific volume, the ideal gas law has to be taken into account (Eq. 4.1)

$$p \cdot V = n \cdot R \cdot T = n \cdot k_B \cdot N_A \cdot T \tag{4.1}$$

with the volume V, the amount of substance n, the temperature T, and the Boltzmann constant k_B. The Avogadro constant with $N_A = 6.022 \cdot 10^{23}$ mol^{-1} and the ideal gas constant with $R = 8.3145$ J mol^{-1} K^{-1} have also to be considered. The particle density of an ideal gas at standard temperature and pressure is about $2.688 \cdot 10^{25}$ m^{-3} [144].

The advantages of UHV conditions are to establish thin films with low density of impurities. Additionally, the surfaces of the substrates, are kept free of contaminants such as residues of organic solvents, remaining gases in the chamber, or water. Particles can travel a specific path and time before they collide and the distances are called mean free paths. Ultra-high vacuum ensures large mean free paths, in the range of $\lambda > 10^3$ m (longer than the respective chamber diameter). This avoids interaction of the molecules before they can reach the substrate in the respective vacuum chamber. Another suitable property is the large monolayer time for UHV conditions. It is the time molecules, in this case, contaminant molecules, are adsorbed at the substrate surface to form a monolayer. To reach the suitable pressure and to get rid of further contaminations, a *bake-out* procedure for the respective UHV chamber is essential. This is achieved by heating the whole chamber walls, the substrates, and the organic compounds to reasonable temperatures for the respective material.

Several different pumps (such as pre-vacuum, turbomolecular, ion getting, and titanium sublimation pumps) which can be coupled together are used to maintain UHV conditions. One basic pump is the pre-vacuum pump which creates an initial vacuum down to $\sim\ 10^{-3}$ mbar. There are different types of oil or membrane pre-vacuum pumps which can be used. To get a high vacuum, turbomolecular pumps (TMP) can be coupled to pre-vacuum pumps. TMPs are pumps with rotating turbines to compress gas and the pump principle is established on the transfer of the kinetic energy from the rotating blades to the residual gas molecules. This forces the gas molecules away from the respective chamber.

The ion getting and the titanium sublimation pump are both capture pumps. Here, the pump principle is achieved because molecules are bound to the surfaces of the pump walls by physical and chemical forces. It is necessary to couple two different capture processes because of the different types and sensitivity of the gases. The titanium sublimation pump is a getter pump where Titanium is the active surface of the vacuum pump. In principle, the Titanium will be deposited on the pump wall through heating and sublimation of the respective filament. On the new surface of Titanium, the remaining gas molecules are trapped. For heavy organic contamination, the ion getting pump is used instead. The concept is the ionization of the contaminant gas molecules employing electric and magnetic fields because ions instead of neutral molecules are pumped much easier and are more reactive with the surfaces of the pump walls. This forces the gas ions to embed themselves into the pump walls. The setup of a UHV chamber and the thin film growth procedure are described in the next section.

4.1.2 Setup of the stationary UHV chamber

The preparation of thin films by OMBD takes place inside a stationary UHV chamber under pressure of $p \approx 2 \cdot 10^{-10}$ mbar. The principle of such a UHV system is shown in Figure 4.1. A powder of organic material is installed inside a ceramic crucible of a Knudsen cell. The cell is heated to the respective temperature so that the material can sublime. When the cell shutter is opened, a flux of the molecules can be emitted and hit the substrate on the sample holder if it is installed in the way of the flux and aligned in the right position. For co-evaporation, several Knudsen cells can be used. The molecules can be deposited as thin films on the respective substrate.

Through the cell temperature, the flux can be varied and the respective growth rate can be adjusted. The growth rate and the film thickness can be controlled by a quartz-crystal microbalance (QCM). The quartz crystal oscillates with a high frequency which will change by arriving molecules due to the modified mass of the crystal. Through a correction factor which is depending on the organic material and the position of the Knudsen cell in the chamber, the real thickness and growth rate of the thin films can be determined.

The samples can be transferred in and out of the main chamber through the load lock which can be separated from the main chamber and vented independently. The suitable pressure in the main chamber is maintained and is achieved by an ion getting, a titanium sublimation, and a TMP. There are several windows installed in the main chamber for *in-situ* measurements during the growth procedure for example *in-situ* differential reflectance spectroscopy (DRS) or variable angle spectroscopic ellipsometry (VASE).

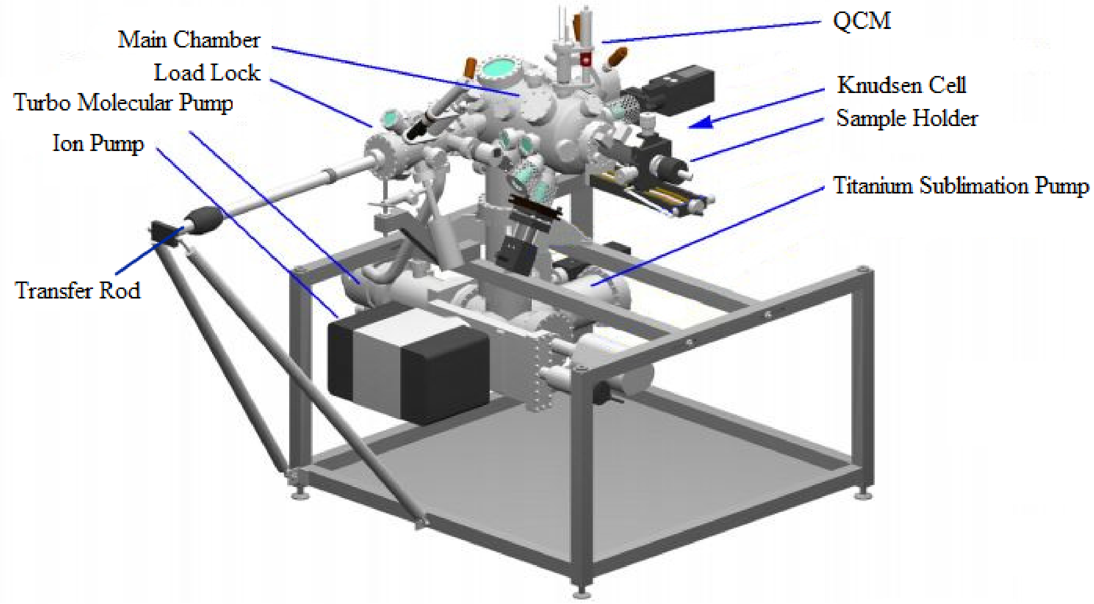

Figure 4.1: *Drawing of the stationary UHV chamber used for the thin film preparation by OMBD in this thesis. Picture is taken from Ref. [146].*

4.1.3 Sample preparation and growth procedure

For the preparation of the thin films, three different substrates were used for the various structural and optical investigations: 5 x 10 mm pieces of a Silicon (100) wafer with a native oxide layer of 2 nm, a transparent glass wafer, and a glass wafer roughened at the backside (for more details of the substrates see Section 3.3). For Fourier-transform infrared (FTIR) spectroscopy measurements, Silicon substrates that are polished on both sides are used. The substrates were cleaned with Acetone and Isopropyl Alcohol in an ultrasonic bath each for 10 min and dried with gaseous Nitrogen. They were glued with a silver paste on the sample holder and degassed overnight in the chamber before film preparation. The substrates were kept at constant temperatures of 293 K, 373 K, and 423 K during film growth. Mixed thin films were prepared by co-evaporation of the donor and acceptor molecules with molecular mixing ratios of 3:1, 2:1, 1:1, 1:2, and 1:3. The nominal thicknesses of about 20 nm and growth rates of about 0.2 nm min^{-1} in total were controlled by a QCM during film growth and calibrated by X-ray reflectivity (XRR). For each organic material, calibration curves have to be made to achieve suitable cell temperatures and growth rates. The thin film samples are stored after growth under rough vacuum conditions. In Table 4.1 an overview of the differently prepared donor-acceptor thin films and the respective growth conditions is shown.

Table 4.1: *Overview of the differently prepared donor-acceptor thin films and the respective growth conditions: different substrate temperatures and mixing ratios.*

	Pure film	DIP	DNTT
Pure film		150 °C	100 °C
PDIC$_1$	25 °C, 150 °C	25 °C & 150 °C 1:1	
PDIC$_3$	25 °C, 150 °C	25 °C & 150 °C 3:1, 1:1, 1:3	
PDIC$_5$	25 °C, 150 °C	25 °C & 150 °C 1:1	
PDIC$_8$	25 °C, 150 °C	25 °C & 150 °C 2:1, 1:1, 1:2	
PDIC$_8$-CN$_2$	25 °C, 150 °C	25 °C & 150 °C 2:1, 1:1, 1:2	25 °C & 150 °C 2:1, 1:1, 1:2
PDIC$_2$F$_3$	25 °C, 100 °C, 150 °C, 165 °C	100 °C & 150 °C 2:1, 1:1, 1:2	100 °C & 150 °C 2:1, 1:1, 1:2
PDIF-CN$_2$	150 °C		25 °C & 150 °C 3:1, 2:1, 1:1, 1:2, 1:3

4.1.4 Sample preparation for mixed layer devices

For the mixed layer devices, Indium-tin oxide (ITO) coated glass substrates are used. On top, a polymeric hole injection layer (HIL 1.3) was spin-coated from an aqueous solution and annealed at 398 K for 30 min. As active layer, the organic molecules were evaporated under vacuum (20 nm donor / 50 nm equimolar mixed film / 20 nm acceptor). Onto an exciton blocking layer of Bathocuproine (BCP, 5 nm), Aluminium (100 nm) was thermally deposited through a shadow mask.

4.2 X-Ray diffraction techniques

X-ray diffraction techniques are sensitive methods to investigate structural properties of organic thin films at molecular and atomic level. In this section, the theory of X-ray diffraction techniques within different experimental geometries is described.

4.2.1 X-ray reflectivity

X-ray reflectivity (XRR) is a very surface sensitive and precise method to structurally analyze crystalline materials or layered structures. Here, only the basic concepts are described and for more details, it is referred to Refs. [147–149]. With this technique, information about the electron-density profile, the thickness, the roughness of thin films, or the out-of-plane lattice spacing in crystalline samples are obtained. Figure 4.2a shows the scattering geometry for XRR measurements. The specular condition indicates that the incoming and outcoming beam have the same angle. During a scan, the source and the detector move simultaneously. The complete momentum transfer Q has therefore only a non-zero component perpendicular to the substrate and can be described with Eq. 4.2

$$Q_z = \frac{4\pi}{\lambda} \cdot sin\ \theta \tag{4.2}$$

with the wavelength λ and θ as the angle of incidence.

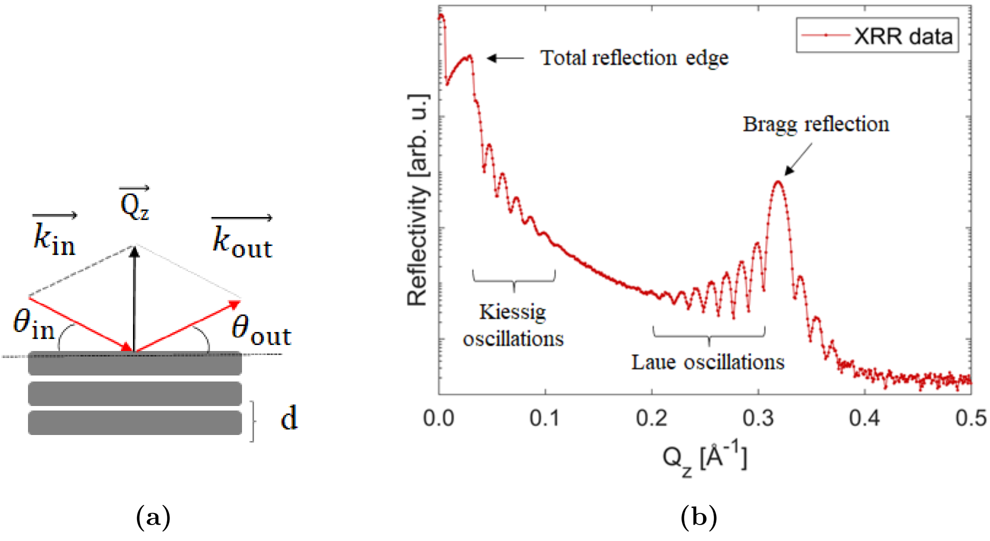

(a) **(b)**

Figure 4.2: *a) Scattering geometry for an XRR measurement on a thin film and b) exemplary XRR data from a 30 nm* $PDIC_8$*-*CN_2 *thin film grown on* SiO_2*.*

With the XRR only information about the out-of-plane structure is obtained. In Figure 4.2b a typical XRR dataset of a PDI thin film is shown with its characteristic features. The total reflection edge is directly connected to the average electron density of a thin film sample. The edge appears because the refractive index for X-rays inside the material is lower than one and therefore total reflection occurs. Kiessig oscillations can emerge from interferences of reflections from the bottom and the top interface of the thin film. From the periodicity and the dampening of the Kiessig oscillations, the average thickness and the roughness of a thin film can be determined. Regarding ordered out-of-plane crystalline structures in thin films, Bragg reflections can occur at certain angles due to constructive interference from waves scattered at the crystal planes. This can be described by the Braggs' law

$$n\lambda = 2d\ sin\ \theta \tag{4.3}$$

with the lattice spacing d of the thin film and n as an integer number.

From the periodicity of the side fringes of the Bragg peak, the so-called Laue oscillations, the size of the coherent crystalline domains can be obtained. If both Kiessig and Laue oscillations are in the same range, the thin film is crystalline ordered over the whole thickness. The out-of-plane lattice spacing d_z can be obtained using Q_z of a Bragg reflection via:

$$d_z = \frac{2\pi}{Q_z} \tag{4.4}$$

XRR was measured with a GE Inspection Technologies XRD 3003 TT X-ray diffraction system using Cu $K_{\alpha 1}$-radiation (λ = 1.5406 Å) and the data is fitted with GenX [150] by means of the Parratt formalism [151].

4.2.2 Grazing incidence X-ray diffraction and grazing incidence wide angle X-ray scattering

To gain knowledge about the in-plane structure of thin film samples, grazing incidence X-ray diffraction (GIXD) can be applied. By the usage of a 2D detector, information about the in-plane and the out-of-plane structure of the sample can be obtained simultaneously by using grazing incidence wide angle X-ray scattering (GIWAXS). Only the general concepts are discussed and for more insights, it is referred to Refs. [152–155].

For GIXD, the angle of incidence is kept constant near the total reflection edge (critical angle) which leads to a finite penetration depth of the beam within the thin film. The out-of-plane angle is in the same range as the incidence angle and the in-plane angle 2ϕ is varying to get insights into the in-plane structure of the sample (Figure 4.3). Therefore, the in-plane momentum transfer Q_{xy} is almost parallel to the surface and can be described as follows:

$$Q_{xy} = \frac{4\pi}{\lambda} \cdot sin\ \phi \tag{4.5}$$

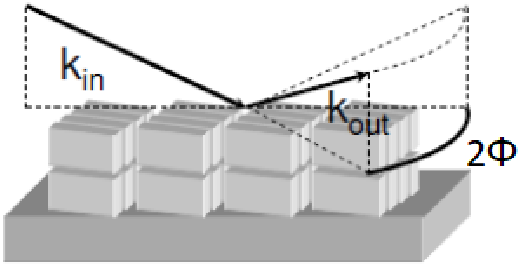

Figure 4.3: *Scattering geometry for a GIXD measurement on a thin film. Picture is taken from Ref. [156].*

To get information about the whole sample, GIWAXS measurements on the thin film can be performed. With a 2D area detector, the in-plane and the out-of-plane structure of the thin film can be determined simultaneously which results in a two-dimensional reciprocal scattering pattern. Details about the crystal unit cell and the quality of the crystal order can be obtained.

Figure 4.4 shows different GIWAXS sketches for three different cases of poly-crystalline thin film samples with different degrees of crystallite ordering and misalignment along the Q_z direction. Precise Bragg peaks occur for highly ordered crystalline samples with a vertical orientation of the crystalline domains. For samples where the crystallites are oriented with an angular distribution along the Q_z direction, the Bragg peaks will be broadened and Debye-Scherrer-like rings will be obtained if the crystallites are randomly oriented in the thin film sample [154].

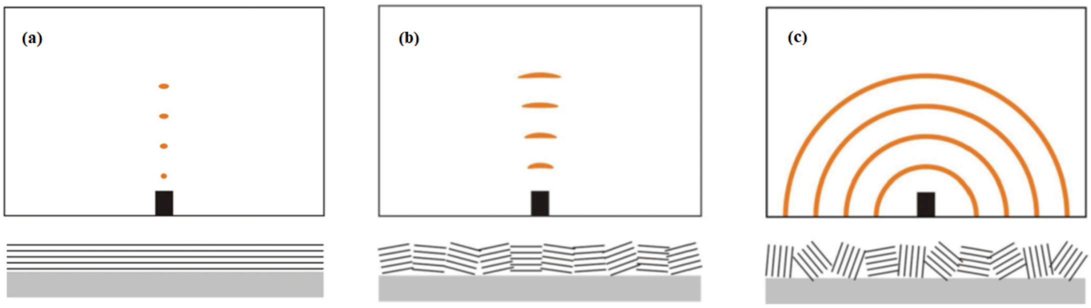

Figure 4.4: *Different scenarios of crystalline ordering and misalignment along the Q_z direction in thin films and the respective GIWAXS pattern: a) highly ordered crystalline domains parallel to the substrate, b) slightly misoriented crystalline domains and c) randomly oriented crystallites. Picture is taken from Ref. [154].*

Especially for performing GIWAXS measurements, synchrotron facilities are used. The great advantage is the higher flux and the higher brilliance (which is the flux normalized by its emittance). They can reach brilliance up to 10^{21} (photons per second) / (0.1% bandwidth mm^2 mrad^2). Additionally, shorter acquisition times are required and better signal-to-noise ratios are achieved. It should be considered that organic films may be affected by radiation damage. GIWAXS measurements are recorded at the beamlines P03, P08 of DESY (Hamburg, Germany) using a focused beam with a wavelength of 0.9686 Å and 0.6888 Å and at the beamlines ID03, ID10 of ESRF (Grenoble, France) using a focused beam with a wavelength of 0.992 Å and 1.2398 Å.

4.3 Atomic force microscopy

Atomic force microscopy (AFM) is a scanning probe microscopic method to characterize the surface morphology of a thin film sample with subnanometer resolution. The schematic setup of an AFM measurement is shown in Figure 4.5. The sample is scanned line-by-line and a topographic image of the surface is recorded by using the short range interaction forces between the analyzed surface and the sharp tip attached to a cantilever. The cantilever oscillates by means of a piezoelectric element in several scanning modes and the displacement of the cantilever is proportional to the attractive or repulsive forces between the tip and the surface to get a height profile of the sample. A laser is focused on the backside of the cantilever and is reflected to the detector.

For soft materials like organic molecules, mostly the intermittent contact or tapping mode is used as the imaging method. The tip is here periodically driven in contact with the film surface with a given frequency and a target amplitude of this oscillation is set. The deflection from the forces between the tip and the surface is compensated by a voltage signal and the recorded feedback parameters during the scan provide the data for the height profile of the sample. With this imaging mode, the contact time between tip and surface is minimized, and like this, a damage of the film is reduced [157, 158].

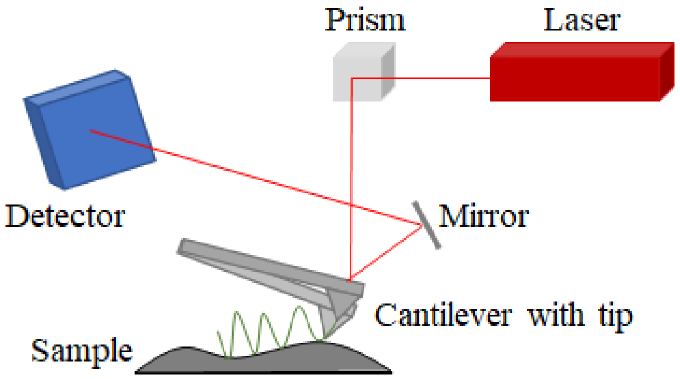

Figure 4.5: *Schematic setup of an AFM measurement with the optical pathway showing the imaging tapping mode. Picture is modified from Ref. [158].*

Atomic force microscopy was measured using a JPK NanoWizard II in tapping mode and the image analysis was performed with Gwyddion [159].

4.4 Optical spectroscopy

4.4.1 UV/vis/NIR spectroscopy

UV/vis/NIR spectroscopy is a non-invasive spectroscopic method. In this thesis, absorption measurements are performed of thin films in the wavelength range of 200 nm to 1100 nm using normal incidence. With this technique, only the in-plane absorption is received. The underlying principle for absorption is the Lambert-Beer law with the measured transmittance T which is the ratio of transmitted radiation $I(d)$ to incident radiation I_0 through a sample:

$$T = \frac{I(d)}{I_0} = e^{-\alpha d} \tag{4.6}$$

The absorption coefficient α can be calculated for thin films if the thickness d of the samples is known measured through other methods such as ellipsometry (VASE) or scattering techniques (XRR). With the following Equation 4.7 the respective component of the extinction coefficient (in-plane component k_{xy}) which is related to the absorption coefficient and the wavelength λ can be determined:

$$k \equiv k_{xy} = \frac{\alpha \lambda}{4\pi} \tag{4.7}$$

A bare glass substrate was measured as a reference and subtracted as a baseline to minimize errors from radiation scattering and to take fluctuations into account. UV/vis/NIR spectra were acquired using a Varian Cary 50 spectrometer in the wavelength range of 200 nm to 1100 nm at normal incidence.

4.4.2 Temperature-dependent photoluminescence spectroscopy

Photoluminescence (PL) spectroscopy is a very sensitive technique. A sample is irradiated with laser light and the light emission of the thin film is measured. Intermolecular interactions of the sample especially from the solid-state arrangement within the organic film can be probed [87, 88]. This technique is also very promising to detect and estimate the CT states which are the lowest lying excited-states [160]. Temperature-dependent PL is performed at low temperatures to get more precise and sharper resolved peaks in the PL spectra of organic thin films due to the reduced amount of possible relaxation pathways or thermal broadening. Information about CT states is also expected in PL spectra at lower temperatures [74, 161].

The optical pathway of a PL spectrometer is shown in Figure 4.6. The laser beam is irradiated through optical components and focused on the sample by an objective. The intensity of the laser light can be reduced through density filters and therefore also the damage of the sample can be minimized. With the help of a video camera and different objectives, the sample can also be investigated by use of the spectrometer as a microscope. The emitted light from the sample is guided through optical compounds to changeable gratings (150 or 1800 lines) to define the desired resolution of the diffracted light on the charge-coupled device (CCD) detector [82].

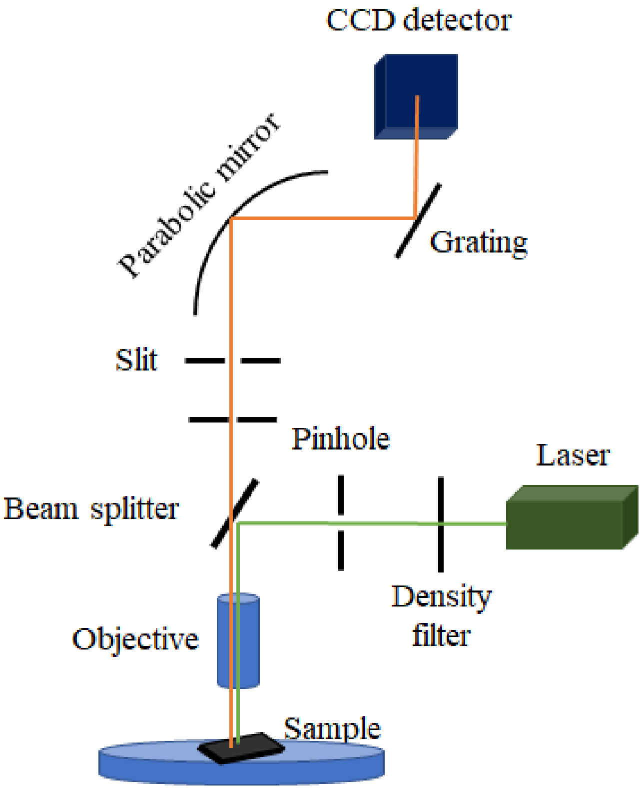

Figure 4.6: *Schematic setup and optical pathway of a photoluminescence spectrometer. The laser beam (green line) is irradiated and focused on the sample. The emitted light (orange line) of the sample leads from the beam splitter through a grating to the CCD detector.*

PL spectra were gained using a Horiba Jobin Yvon Labram HR 800 spectrometer with a Nitrogen cooled CCD 1024x256 detector. For PL excitation an Nd:YAG laser with a wavelength of 532 nm was used. Temperature-dependent PL spectra were determined with a CryoVac cooling system with liquid Nitrogen or liquid Helium in the range from 293 K to 77 K or 15 K.

4.4.3 Fourier-transform infrared spectroscopy

Fourier-transform infrared spectroscopy (FTIR) is used to earn information about the vibrational modes of a molecule. The sensitive stretching mode of the nitrile group (CN-group) of the molecules used in this thesis is located around $\sim 2200\ \mathrm{cm}^{-1}$ and is very suitable to estimate ground-state CT effects [78, 79].

With this method, GS-CT effects can be detected and also quantified. Based on an analysis similar to Ref. [78], the degree of a CT can be calculated when comparing the shift of the CN-group with the difference between the pure and the fully ionized CN-mode of the respective molecule. In Figure 4.7 the schematic setup of an FTIR spectrometer is shown.

The main component of an FTIR spectrometer is a Michelson interferometer. The IR beam from the light source is guided into the Michelson interferometer and split into two equal beams. They are both reflected, one from a fixed and the other one from a moving mirror. Through the different paths, the reflected beams have different phase shifts and through the recombination at the beam splitter, the outgoing beam has a relative phase depending on the mirror displacement. Now, the beam is focused on the sample and afterwards on the detector. A laser is used to precisely detect the path difference. The laser is modulated several times during one movement cycle of the operating mirror. The spectrum in frequency is required by evaluating a discrete Fourier transform of the recorded raw data in form of an interferogram [162].

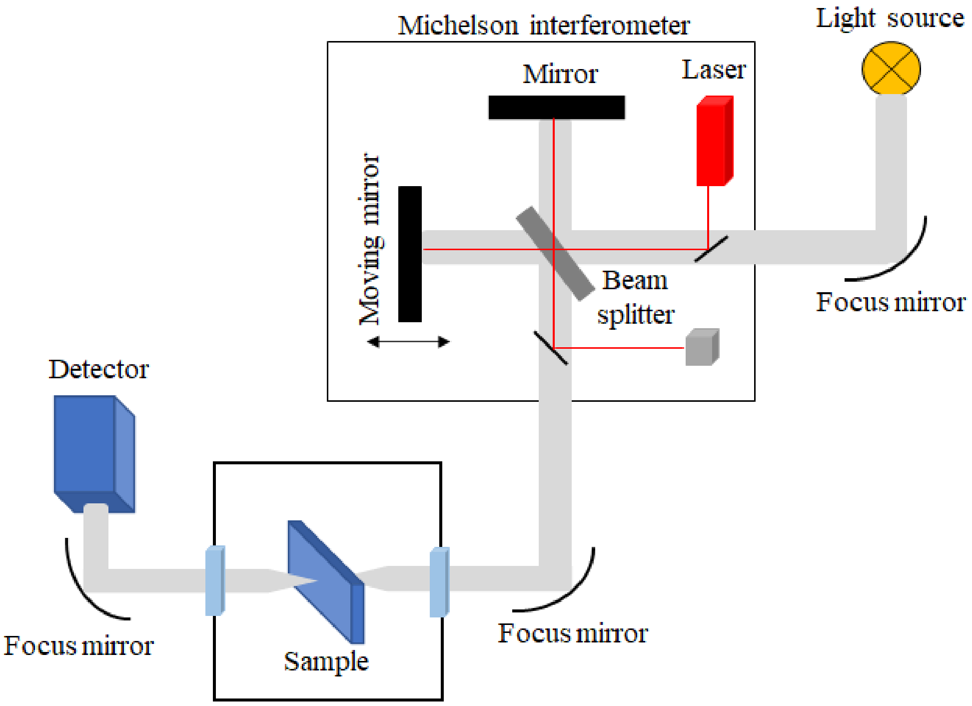

Figure 4.7: *Schematic setup and optical pathway of an FTIR spectrometer based on a Michelson interferometer. Picture is modified from Ref. [162].*

Infrared spectra were acquired using a Vertex 70 FTIR spectrometer by Bruker in transmission mode.

4.4.4 Variable angle spectroscopic ellipsometry

Variable angle spectroscopic ellipsometry (VASE) is a sensitive technique to probe optical anisotropy of organic molecules in thin films. In particular, the optical functions of the in-plane and the out-of-plane component can be determined for the respective molecule or thin film [163]. With this method also film properties such as film thicknesses can be obtained.

In Figure 4.8 the schematic setup of an ellipsometric measurement is shown. The ellipsometer is installed on a Woollam goniometer so that the angle of incidence relative to the surface normal can be changed. The light passes from the light source through a fixed polarizer and is linearly polarized. Through the next optical component, a rotating compensator, the polarization of the light beam is changed from linear to elliptical. When the light is reflected by or transmitted through the sample, it interacts with the sample and the polarization is varied with respect to the incoming beam and the optical properties of the investigated sample. Afterwards the beam passes the analyzer, which is again a fixed polarizer before it reaches the CCD detector [66].

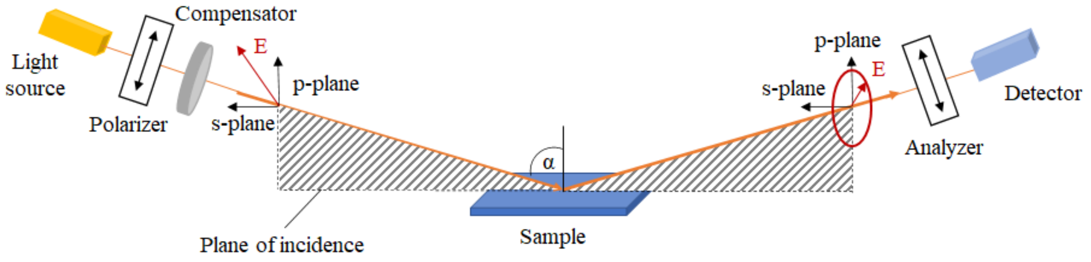

Figure 4.8: *Schematic setup of an ellipsometric measurement. Picture is modified from Ref. [66].*

The light beam interacts with the sample in transmission or reflection mode. The polarization state is changed with respect to the incoming beam and the optical properties of the investigated thin film. The optical constants of the thin film are obtained from the measured ellipsometric parameters Ψ and Δ. They are related to the ratio of the Fresnel reflection coefficients $\tilde{R}_s$ and $\tilde{R}_p$ for s- and p-polarized light (more details on the theory of Fresnel coefficients in Section 2.2.1) [66]. The ratio of $\tilde{R}_p$ and $\tilde{R}_s$ is defined as the complex ellipsometric parameter ρ as:

$$\rho = \frac{\tilde{R}_p}{\tilde{R}_s} = tan(\Psi) \cdot e^{i\Delta} \tag{4.8}$$

The optical constants and film properties are not measured directly, only reflected and transmitted beam intensities and polarization states are detected. Therefore, a model and a multisample analysis are needed to obtain the anisotropic optical properties of the investigated sample. In this thesis, thin films on three different substrates were investigated. Reflection measurements on Silicon substrates with a native oxide layer and glass roughened at the backside are performed as well as measurements in transmission mode with glass substrates. For all films on the substrates, the same optical properties are assumed and models for all substrates are coupled together and fitted simultaneously. In the model, two layers are applied for the in-plane and out-of-plane structures. For rough films, also an EMA (effective medium approximation) layer was taken into account including a fixed 50 % / 50 % void-to-full ratio with different thicknesses [164].

The VASE measurements were performed with a Woollam M-2000 ellipsometer in reflection with incidence angles of 45° to 80° in 5° steps and in transmission mode with incidence angles of 0° to 70° in 10° steps. The spectrometer is controlled by EASE software and analyzed by WVASE32 software from Woollam [66].

4.5 Electroluminescence spectroscopy and incident photon-to-current efficiency

The incident monochromatic photon-to-current efficiency (IPCE) is an essential characterization tool to estimate the photoelectrical performance of solar cells. This method is used to understand optoelectronic processes such as current generation, recombination, and diffusion mechanism in the solar cell. The prepared layer device is continuously irradiated with monochromatic light under working conditions, so that the short-circuit photocurrent I_{SC} can be measured in the spectral response range [165, 166].

Electroluminescence (EL) is a method that is used in this thesis similar to PL spectroscopy to detect and determine the CT states. Electrons and holes are injected into a mixed layer device. The first state of recombination which is the lowest energetic state, the CT state, can be determined without the presence of signals from the pure materials. This is an advantage compared to PL spectroscopy [167]. To estimate the CT energy E_{CT} in organic photovoltaic materials the methodology refined by Vandewal et al. [168], on how EL and IPCE spectra can be analyzed in the framework of Marcus theory is used.

EL measurements were carried out on the prepared mixed layer devices by using a CCD camera (PyLoN:100BR eXcelon, Princeton Instruments) coupled with a spectrometer (SP2300i, Princeton Instruments) under a DC voltage driven by a Keithley source meter (applied bias voltage of 3.5 V). IPCE was performed using a halogen lamp and a monochromator (Omni-λ300, Zoliz Instruments Co., Ltd.), which allows measurements in the range from 350 to 1100 nm in steps of 1 nm.

4.6 Theoretical calculations

In the following, the theoretical calculations performed in this thesis are discussed based on Ref. [169]. Ground- and excited-state properties of the donor-acceptor organic small molecule systems considered in this thesis are computed from density-functional theory (DFT) [170, 171] and many-body perturbation theory (MBPT) [172], including the single-shot G_0W_0 approximation [173] and the solution of the Bethe-Salpeter equation (BSE) [174]. Equilibrium geometries of the individual donor and acceptor molecules as well as of the complexes are computed with the all-electron code FHI-aims [175], adopting tight integration grids and TIER2 basis sets [176]. The generalized-gradient approximation for the exchange-correlation potential is adopted in the Perdew-Burke-Ernzerhof [177] parameterization. Van der Waals interactions are accounted for by the Tkatchenko-Scheffler scheme [178]. Atomic positions are relaxed until the Hellmann-Feynman forces are smaller than 10^3 eV/Å. From these calculations, we estimate the CT using the Hirshfeld partition scheme [179].

The MOLGW code [180] is employed to compute the electronic and optical properties of all systems. Gaussian-type cc-pVDZ basis sets [181] are adopted including the frozen-core approximation. The resolution-of-identity approximation is also employed [182]. The hybrid functional PBE0 [183] is used to provide an enhanced starting point for the G_0W_0 calculations in the considered π-conjugated molecules [184, 185]. The BSE is solved in the Tamm-Dancoff approximation [186] including in the transition space all the occupied and unoccupied states available from the basis set. To evaluate the character and the spatial distribution of the excitons, we compute the hole and electron density [187, 188], which defined the λ^{th} excitation as

$$\rho_h^\lambda(\mathbf{r}) = \sum_{\alpha\beta} A_{\alpha\beta}^\lambda |\phi_\alpha(\mathbf{r})|^2 \tag{4.9}$$

and

$$\rho_e^\lambda(\mathbf{r}) = \sum_{\alpha\beta} A_{\alpha\beta}^\lambda |\phi_\beta(\mathbf{r})|^2, \tag{4.10}$$

respectively. The coefficients $A_{\alpha\beta}^\lambda$ are the square of the normalized BSE eigenvectors and weight each transition between occupied (ϕ_α) and unoccupied (ϕ_β) states.

Part II

Results and discussion

In this chapter, the experimental results of this thesis are presented and discussed. This thesis is focused on the structural morphology and charge transfer effects of organic binary bulk heterojunctions. An overview of the experimental results with the different donor and acceptor molecules is shown in Figure 4.9. The different donors DIP and DNTT used in this thesis are listed in this tabular format as a row and the respective acceptors are displayed as a column. The details of the individual molecules are described in the Chapter 3. The different mixing scenarios (details described in Section 2.1.3) are schematically presented for the various investigated donor-acceptor systems and the respective degrees of charge transfer effects are described by the actual transition dipole moment of the CT (Fig. 4.9). The investigated donor-acceptor thin film systems which are examined together are marked by different grey colors and are therefore split into three parts.

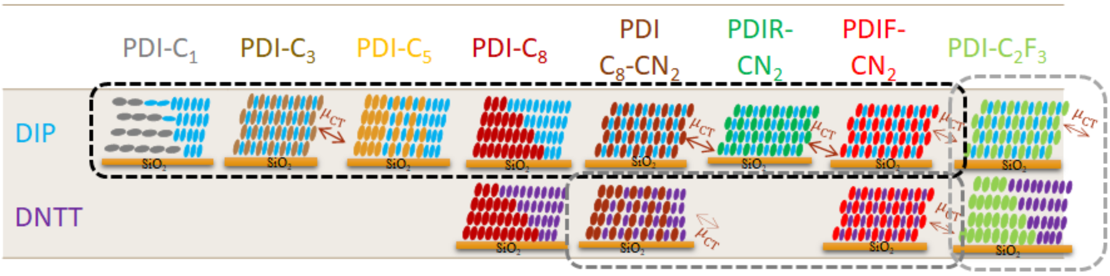

Figure 4.9: *Schematic representation of the investigated organic binary bulk heterojunctions. The donor molecules are listed as a row and the respective acceptor molecules as a column. The different schematic scenarios are describing the mixing behavior and the charge transfer effects of the individual systems. Systems that are investigated together are marked by different grey colors.*

The first part includes the influences of the different n-alkyl side chains and cyano groups of the different PDI acceptors with the donor molecule DIP on structural morphology and mixing behavior as well as CT effects in these thin film systems (the responding systems are marked with a black color in Fig. 4.9). The second part characterizes the molecular CT of two different PDI:DNTT systems in regards to mixing behavior as well as theoretical calculations on energy levels and optical absorption spectroscopy (the responding systems are marked with a dark grey color in Fig. 4.9). The third part deals with the question of the influences of different donor molecules. The synthesized PDI acceptor with a different side chain is investigated with the two donor molecules DIP and DNTT related to mixing behavior and CT effects (the corresponding systems are marked with a light grey color in Fig. 4.9).

Chapter 5

Influence of the PDI alkyl chain length on co-crystal formation and charge transfer effects with the donor DIP

The results presented in this chapter will be published in Ref. [189] and they are based on bulk heterojunction thin films. Here, a comprehensive investigation on co-crystal formation and charge transfer effects in weakly interacting organic semiconductor mixtures is performed. As a donor molecule DIP is chosen and as acceptors several PDI derivatives are selected which differ in the n-alkyl side chain in the imide position and in the cyano (CN) group in the bay position (Fig. 5.1). In previous studies, it was shown that alkyl, branched, and fluorinated side chains and electron-withdrawing side groups can alter molecular packing and morphology of the deposited thin films [19, 20, 23]. By varying the n-alkyl side chain and by incorporation of cyano groups, the different mixing behavior and the influence on possible CT effects can be investigated in such systems. Therefore, the mixing behavior and CT effects for the various PDI:DIP thin film systems are characterized in this chapter.

The growth and mixing behavior as well as the structural morphology of the pristine PDI as well as the mixed thin films are investigated by X-ray scattering (GIWAXS and XRR). The optimization of intermixing and co-crystal formation regarding different side chains of the acceptor molecules is examined. Combining these structural analyses with optical spectroscopy, the different mixed films are studied regarding ES-CT effects by absorption and photoluminescence spectroscopy. Besides, the CT energies of the different thin film systems are calculated by means of electroluminescence and incident-photon-to-current efficiency in cooperation with Hongwon Kim and Wolfgang Brütting, University of Augsburg. Additionally, correlations between structural morphology and CT effects were established depending on the chain length and their configuration within the different perylene diimide:DIP mixed systems.

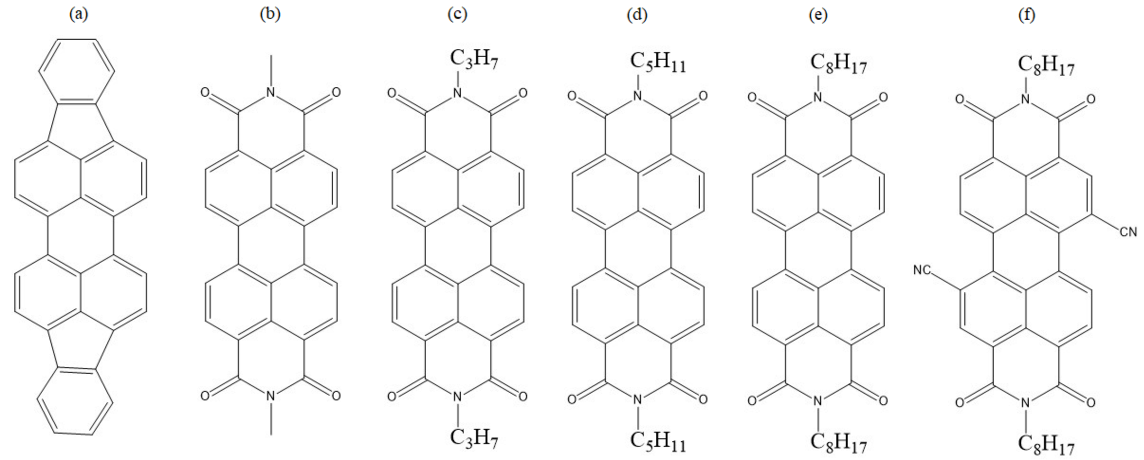

Figure 5.1: *Overview of the studied compounds: a) donor DIP, different perylene diimide acceptors b) PDIC*$_1$*, c) PDIC*$_3$*, d) PDIC*$_5$*, e) PDIC*$_8$ *and f) PDIC*$_8$*-CN*$_2$*.*

5.1 Structural investigations by X-ray scattering

First, the thin film structure and mixing behavior of PDI:DIP mixtures and its dependence on the side chain length in the imide position as well as the incorporation of cyano groups in the bay position of the acceptor molecules will be discussed. Therefore, the thin film structures and growth behaviors of the pure PDI derivatives are essential, especially in regards to the various incorporated side groups in the imide and bay position of the acceptor molecules.

5.1.1 Structural investigations by grazing incidence wide angle X-ray scattering

An overview of the GIWAXS data of the different pristine perylene diimide derivatives and the mixtures with the donor DIP is shown in Figure 5.2 and in Figures 9.1 and 9.2 in the Appendixes.

Depending on the length of the n-alkyl chains in the imide position, the various pristine perylene derivatives create different thin film structures, as shown in the GIWAXS patterns (Fig. 5.2a-e) [92, 190]. For short alkyl chains (up to three C-atoms), the molecules lie down with their long molecular axes close to parallel to the substrate surface (Fig. 5.2a) and form the well-known herringbone structure [104, 105]. With increasing length of the n-alkyl side chain, the orientation changes to a more upright conformation, and the molecules assume the offset-stacked geometry, where neighboring molecules are shifted relative to each other (Fig. 5.2c-e) [91, 101, 107, 110]. An outlier to this is the acceptor PDIC$_3$. The molecules seem to grow in an intermediate form between the aforementioned orientations and geometries in thin films [106]. With this alkyl chain length, the perylene diimide molecules are oriented to a more standing-up conformation on

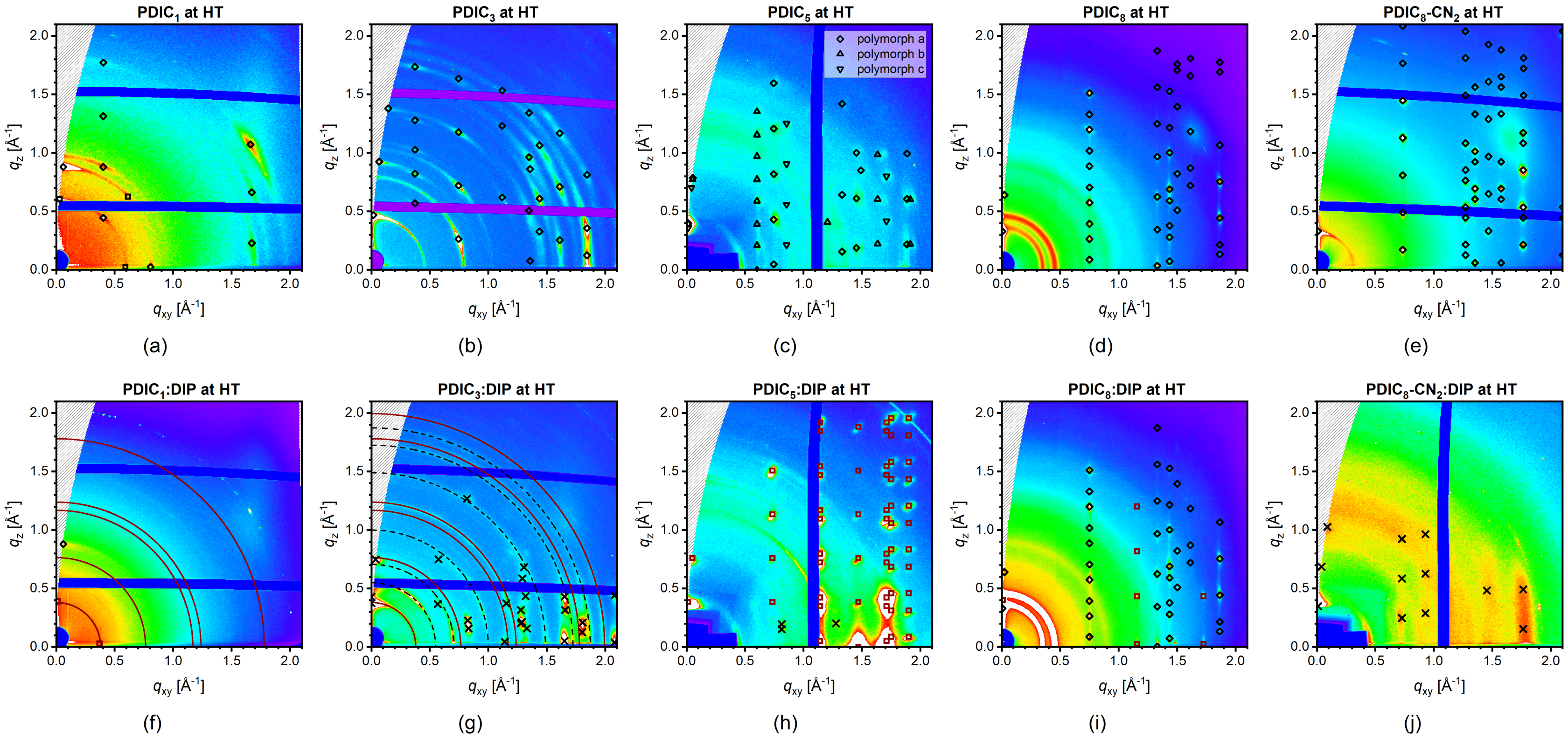

Figure 5.2: *GIWAXS data (150 °C deposition temperature): a) PDIC$_1$, b) PDIC$_3$, c) PDIC$_5$, d) PDIC$_8$, e) PDIC$_8$-CN$_2$, f) DIP 1:1 PDIC$_1$, g) DIP 1:1 PDIC$_3$, h) DIP 1:1 PDIC$_5$, i) DIP 1:1 PDIC$_8$ and j) DIP 1:1 PDIC$_8$-CN$_2$ (the donor is marked in violet, the acceptor is marked with black triangles or squares for the different phases, and black crosses indicate the mixed phase).*

the Silicon substrate, and a more offset-stacked orientation is established (Fig. 5.2b).

Important for the comparison of these pristine films is the increasing crystallinity with increased n-alkyl chain length in the imide position, since the longer n-alkyl chain can be arranged in an energetically favorable orientation with a higher packing density. It can be speculated that the additional van der Waals forces between the longer n-alkyl side chains lead to more favorable intermolecular $\pi-\pi$ stacking between the perylene diimide molecules, the so-called fastener effect [191–194]. This implies that the orientation of the perylene diimide derivative molecules in the thin film structure depends on the n-alkyl chain length and also influences the mixing behavior with the donor molecule DIP.

Two different PDI derivatives with an n-octyl side chain are examined in this thesis (PDIC$_8$ and PDIC$_8$-CN$_2$), they differ in the cyano-groups in the imide position. Through the incorporation of this side group, the electron density of the aromatic backbone is reduced and the $\pi-\pi$ stacking is weaker due to steric hindrance of these side groups [19, 23, 95, 195]. This leads to a lower crystallinity of the pure compound with incorporated cyano groups (PDIC$_8$-CN$_2$, Fig. 5.2e) compared to the respective counterpart (PDIC$_8$, Fig. 5.2d).

The different unit cell parameters of the various pure acceptor molecules are depicted in Table 5.1. For comparison, the unit cell parameters of two PDI derivatives with two different kinds of side chains (no n-alkyl side chains) in the imide position and incorporated cyano-groups are shown. The thin film structures and the growth behaviors of these PDI molecules were already examined [49]. The calculated unit cell parameters feature the unit cell orientations for the various PDI molecules as described above. To complete, PDIC$_5$ is known to create numerous polymorphs when deposited at high substrate temperatures [103]. The reciprocal space map of pristine PDIC$_5$ (Fig. 5.2c) shows reflections arising from three different unit cell structures consistent with previously observed polymorphs. The various calculated parameters of these orientations are also given in Table 5.1.

Table 5.1: *Calculated thin film unit cell parameters of the pristine PDI derivatives based on the respective references if available.*

	a [Å]	b [Å]	c [Å]	α [°]	β [°]	γ [°]
PDIC$_1$ [102]	3.867	15.571	14.587	90	97.71	90
PDIC$_3$ [102]	4.689	18.077	14.258	104.24	89.93	111.30
PDIC$_5$ Polymorph A [103]	4.754	8.479	16.30	86.88	93.50	83.68
PDIC$_5$ Polymorph B [103]	11.624	11.617	17.415	98.21	71.25	116.06
PDIC$_5$ Polymorph C	-	7.35	18.4	80.5	90	90
PDIC$_8$	8.45	4.77	21.49	99.7	106.4	97.8
PDIC$_8$-CN$_2$	5.0	8.7	20.3	100.78	96.94	100.1
PDIR-CN$_2$ [49]	9.33	12.07	16.93	105.2	90	90
PDIF-CN$_2$ [49]	5.53	7.52	20.4	87.12	101.5	106.3

The mixing behavior of the organic small molecules in this thesis is considered in terms of a nearest-neighbor interaction model (Eq. 5.1) [25]. The main driving force is the difference between the intermolecular interaction of similar (W_{AA} or W_{BB}) and dissimilar molecules (W_{AB}). This is also explained in more detail in Section 2.1.3.

$$\chi = \frac{Z}{k_B T} \cdot (W_{AA} + W_{BB} - 2W_{AB}) \tag{5.1}$$

Here, χ is the interaction parameter, Z is the coordination number, k_B is the Boltzmann constant, and T is the temperature. In the total free energy, the direct interactions represented by the interaction parameter compete with the entropy of the system, so if the interaction energy W_{AA} or W_{BB} is similar to W_{AB}, no preferred interaction occurs ($\chi \approx 0$) and a statistical mixing is observed. The system of A and B tends to mix ($\chi < 0$) or phase-separate into the pure components ($\chi > 2$) if one of the interaction energy terms dominates. It is emphasized that this is of course a simplified description. More complex scenarios involve the consideration of orientational order [57] and depth-dependent structural order in thin films [196].

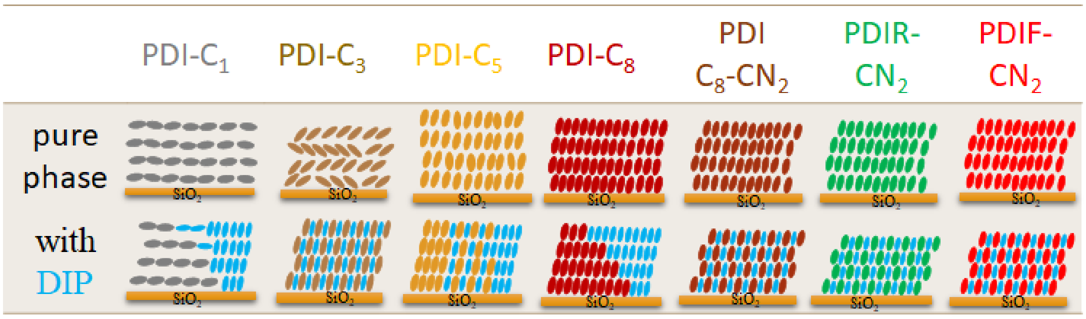

Figure 5.3: *Schematic overview of the growth behavior for the different pure PDI derivatives and the mixing behavior with the donor DIP at high substrate temperature (the donor is colored in blue and the acceptors in the respective colors of their pure phases).*

An overview of the growth behavior for the individual pure PDI derivatives as well as the mixing behavior with DIP at high substrate temperature is shown in Fig. 5.3. Regarding the different mixed systems, the equimolar films of PDIC$_1$ and DIP do not form a co-crystal. Instead, the compounds tend to phase-separate. In the reciprocal space map in Figure 5.2f of the equimolar thin film, all visible peaks can be assigned to either pristine DIP or PDIC$_1$ domains. No new phase is observed even at a higher substrate temperature that should favor the mixing behavior [25]. Here, the energy term of the pure compounds seems to dominate ($W_{\mathrm{DIP/DIP}} + W_{\mathrm{PDIC_1/PDIC_1}} > 2\ W_{\mathrm{DIP/PDIC_1}}$) because the lying-down conformation of the phase-separated PDIC$_1$ [105] and the standing-up orientation of the phase-separated DIP [123, 124, 129] seem to be energetically more favorable than a co-crystal. Interestingly, a small amount of DIP domains with a lying-down conformation as well as a random orientation is also observed. A possible explanation for a lying-down conformation is that DIP domains that nucleate on top of already present $\mathrm{PDIC_1}$ domains crystallize with their long molecular axis parallel to lying-down molecules of $\mathrm{PDIC_1}$, while DIP crystallizes in the standing-up conformation on the Silicon substrate.

A different picture arises for the mixing behavior of DIP and $\mathrm{PDIC_3}$ deposited at higher substrate temperature. The GIWAXS pattern (Fig. 5.2g) shows a number of phases, however, none of them can be assigned to pristine $\mathrm{PDIC_3}$ shown in Fig. 5.2b, suggesting the formation of a $\mathrm{PDIC_3}$:DIP co-crystal. Two distinct co-crystal phases with slightly different out-of-plane stacking can be distinguished based on the presence of two sets of peaks in the Q_z direction. Both phases of the co-crystals show a high degree of ordering and a well-defined thin film structure in both in-plane and out-of-plane directions as evidenced by the presence of pronounced reflection spots. Finally, several Debye-Scherrer ring features observed in the pattern can be attributed to a small amount of phase-separated DIP domains with a random orientation [154, 197, 198]. Here, the co-crystal formed partially overcomes the energy term of the pure compounds ($2\ W_{\mathrm{DIP/PDIC_3}} > W_{\mathrm{DIP/DIP}} + W_{\mathrm{PDIC_3/PDIC_3}}$) which seems to be an energetically favorable orientation for both molecules.

The DIP:$\mathrm{PDIC_5}$ system is significantly more complex, as pristine $\mathrm{PDIC_5}$ creates three different polymorphs when deposited at high substrate temperatures and in contrast, shows only signals from one polymorph when grown at room substrate temperature (Fig.5.2c and Fig. 9.1c in the Appendixes). The reciprocal space map (Fig. 5.2h) of the equimolar thin film shows that $\mathrm{PDIC_5}$ and DIP phase-separate. Most of the observed reflections arise from DIP domains with an exceptionally long-range ordering at both room and high substrate temperatures. This supports the observation that longer side chains promote higher crystallinity and therefore: $W_{\mathrm{DIP/DIP}} + W_{\mathrm{PDIC_5/PDIC_5}} > 2\ W_{\mathrm{DIP/PDIC_5}}$. On the other hand, $\mathrm{PDIC_5}$ reflections are barely visible and generally lack any preferential orientation. The only hint of a possible co-crystal formation is a set of weak but well-defined peaks at $Q_{xy} = 0.8\ \text{Å}^{-1}$ and $1.28\ \text{Å}^{-1}$, that can not be attributed to any of the phases observed in the pristine films. It can be generally concluded that the attraction between similar molecules ($\mathrm{PDIC_5}$) is larger.

Two different PDI derivatives with an *n*-octyl side chain are examined in this thesis, which differ in the cyano-groups in the imide position. The mixing behavior of DIP and $\mathrm{PDIC_8}$ shows a complete phase-separation. Only peaks from both pure compounds are visible in the reciprocal space map of the equimolar thin film (Fig. 5.2i) which are showing long-range ordering in the xy-direction and indicating a high crystallinity of the phase-separated pure compounds ($W_{\mathrm{DIP/DIP}} + W_{\mathrm{PDIC_8/PDIC_8}} > 2\ W_{\mathrm{DIP/PDIC_8}}$). In comparison, the reciprocal space map of the equimolar mixed thin film of DIP and $\mathrm{PDIC_8\text{-}CN_2}$ shows only reflections from a formed co-crystal (Fig. 5.2j). No peaks from pristine DIP or $\mathrm{PDIC_8\text{-}CN_2}$ are visible. This highlights a significant influence of the cyano-groups on packing and mixing behavior within these systems. Through the incorporated groups, the energy term 2 $W_{\mathrm{DIP/PDIC_8CN_2}}$ becomes dominant compared to $W_{\mathrm{DIP/DIP}}$ + $W_{\mathrm{PDIC_8CN_2/PDIC_8CN_2}}$, so that a co-crystal can be formed. In Table 5.2 the thin film unit cell parameters of both pure compounds and the equimolar mixed co-crystal are depicted.

Table 5.2: *Calculated thin film unit cell parameters of pristine DIP, pure PDIC$_8$-CN$_2$, and the mixed co-crystal.*

	a [Å]	b [Å]	c [Å]	α [°]	β [°]	γ [°]	V [Å^3]
PDIC$_8$-CN$_2$	5.0	8.7	20.3	100.78	96.94	100.1	843.18
PDIC$_8$-CN$_2$ 1:1 DIP	8.8	6.8	18.7	89.2	82.7	85.8	1106.9
DIP [133]	7.171	8.550	16.798	90	92.416	90	1029

When comparing the different perylene diimide acceptors, the mixing behavior with DIP is strongly influenced by the structure of these molecules and therefore easily chemically tunable in the desired way. For additional structural information on growth and mixing behavior, X-ray reflectivity data of the various mixed PDI:DIP thin film systems are acquired.

5.1.2 Structural investigations by X-ray reflectivity

In Figures 5.4 - 5.8 the XRR data of the several PDI:DIP mixed thin films are shown.

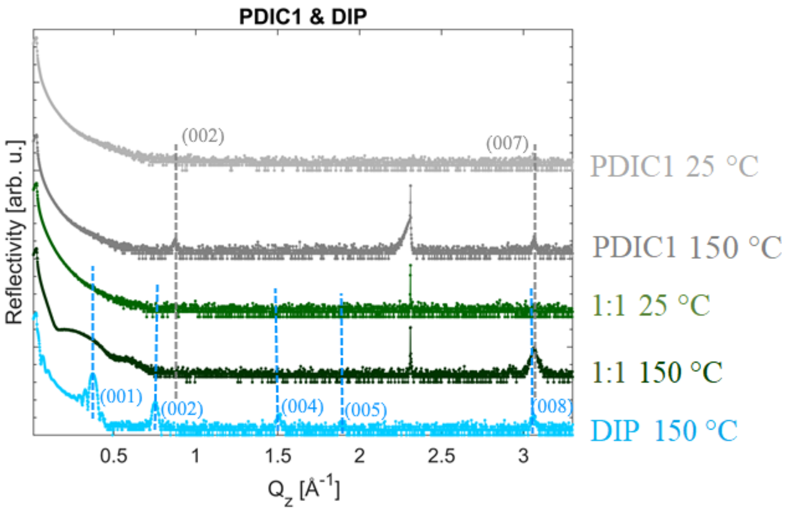

Figure 5.4: *XRR spectra of PDIC$_1$ and DIP equimolar mixed films deposited at 25 °C and 150 °C (blue dashed lines indicate peaks of the donor and grey of the acceptor with the respective Miller indices of the Bragg peaks, all spectra are vertically offset for better clarity).*

The out-of-plane Bragg reflections of the two pristine materials DIP and PDIC$_1$ indicate crystalline formed thin films agreeing with the GIWAXS pattern of the acceptor. In the X-ray reflectivity data of the equimolar thin films, all visible peaks can be assigned to either pristine DIP or PDIC$_1$ domains (Fig. 5.4) and suggest the phase-separation into the pristine donor and acceptor compounds as explained above with the GIWAXS pattern.

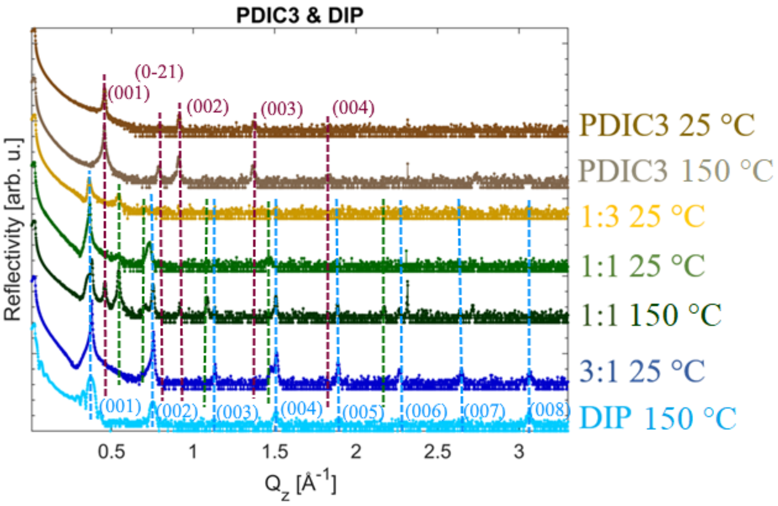

Figure 5.5: *XRR spectra of PDIC$_3$ and DIP mixed films deposited at $25\,^\circ C$ and $150\,^\circ C$ (blue dashed lines indicate peaks of the donor, dark purple of the acceptor, and green for the mixed phase with the respective Miller indices of the Bragg peaks, all spectra are vertically offset for better clarity).*

DIP and PDIC$_3$ form crystalline thin films shown also by the estimated Bragg reflections in the XRR data (Fig. 5.5). In the equimolar film deposited at high substrate temperature, peaks assigned to the co-crystal phases can be distinguished as also reported above by means of the GIWAXS pattern. Additionally, there are also signals visible attributed to pristine DIP or PDIC$_3$. This is in contrast to the equimolar thin film grown at room temperature, where DIP and PDIC$_3$ almost completely phase-separate. The XRR data of this film show mainly peaks of pure materials and very weak signals of a formed co-crystal. Besides, the thin film with excess of PDIC$_3$ show also only very weak peaks of a formed co-crystal whereas the thin film with excess of DIP shows only signals from the phase-separated pristine compounds.

As mentioned above, the GIWAXS pattern of pristine PDIC$_5$ suggests three phases of the thin film deposited at high and only one unit cell orientation for the film grown at room substrate temperature. The XRR data of the pure acceptor show signals assigned to two of these polymorphs for the thin film deposited at $T_{sub} = 150\,^\circ\mathrm{C}$ and almost only one phase for the thin film grown at $T_{sub} = 25\,^\circ\mathrm{C}$ (Fig. 5.6). The X-ray reflectivity scans of the equimolar thin films confirm the observation of phase-separated PDIC$_5$ and DIP domains.

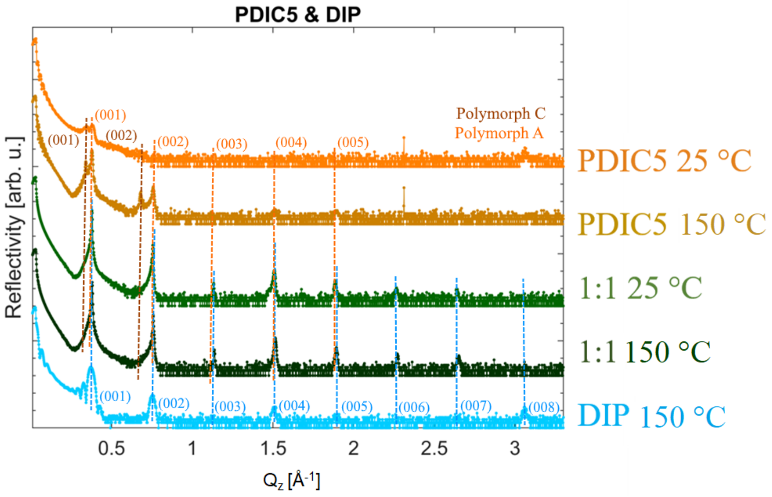

Figure 5.6: *XRR spectra of PDIC$_5$ and DIP equimolar mixed films deposited at 25 °C and 150 °C (blue dashed lines indicate peaks of the donor and orange of the acceptor with the respective Miller indices of the Bragg peaks, all spectra are vertically offset for better clarity).*

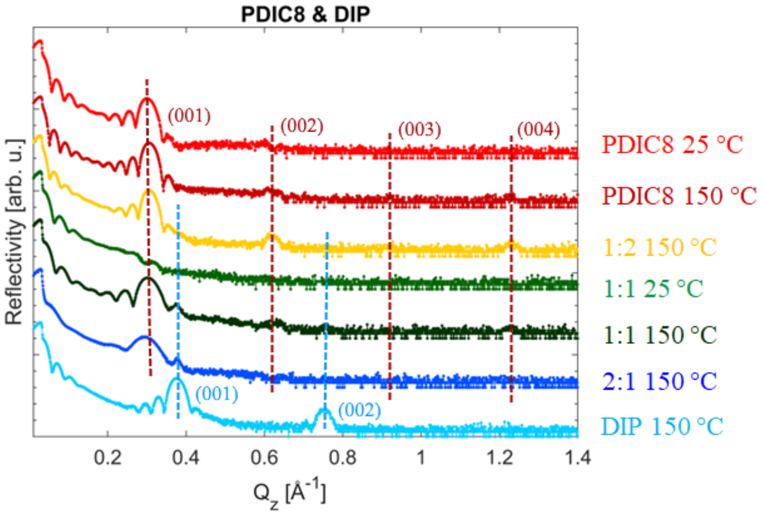

Figure 5.7: *XRR spectra of PDIC$_8$ and DIP mixed films deposited at 25 °C and 150 °C (blue dashed lines indicate peaks of the donor and red of the acceptor with the respective Miller indices of the Bragg peaks, all spectra are vertically offset for better clarity).*

The out-of-plane Bragg reflections of the two pristine materials DIP and PDIC$_8$ indicate crystalline formed thin films agreeing with the GIWAXS pattern of the acceptor (Fig. 5.7). The XRR data of the equimolar thin films support the examination of the phase-separation into both pristine materials. For the thin films with excess of DIP or PDIC$_8$, the signals of the respective excess pristine materials are getting more pronounced.

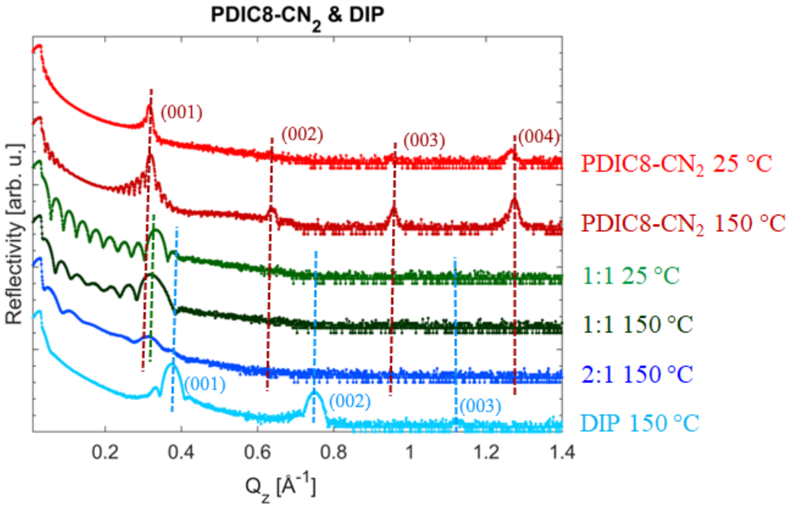

Figure 5.8: *XRR spectra of PDIC$_8$-CN$_2$ and DIP mixed films deposited at 25°C and 150°C (blue dashed lines indicate peaks of the donor, red of the acceptor, and green for the mixed phase with the respective Miller indices of the Bragg peaks, all spectra are vertically offset for better clarity).*

DIP and PDIC$_8$-CN$_2$ form crystalline thin films shown also by the estimated Bragg reflections in the XRR data (Fig. 5.8). An out-of-plane Bragg peak of a newly formed co-crystal can be observed of the equimolar thin films. The co-crystal formation was also visible in the GIWAXS pattern of the respective films.

The XRR data confirm in more detail the different growth and mixing behaviors depicted in Figure 5.3 as explained above by means of the GIWAXS examinations for the different PDI:DIP mixed thin film systems. In the following, the optical properties of the different PDI:DIP mixed films are investigated regarding the different PDI acceptors with various incorporated side groups in the imide and bay positions.

5.2 Excited-state properties: Photoluminescence spectroscopy

The different mixing behavior of the DIP:PDI systems indicates that the alkyl chain variation also influences the optical properties and the charge transfer effects. Figure 5.9 shows the emission spectra for the different DIP:PDI systems.

The various pure PDI derivatives show slightly different emission features. The temperature-dependent PL data for the pure PDI derivatives are shown in Fig. 9.5 in the Appendixes. In Fig. 5.9 the pure PDI emission spectra at a measurement temperature of 15 K are presented. For PDIC$_1$, PDIC$_5$, and PDIC$_8$ three dominant peaks are visible which are sharper at low measuring temperatures. For PDIC$_3$ and PDIC$_8$-CN$_2$ only a broad emission feature is observed for all measure-

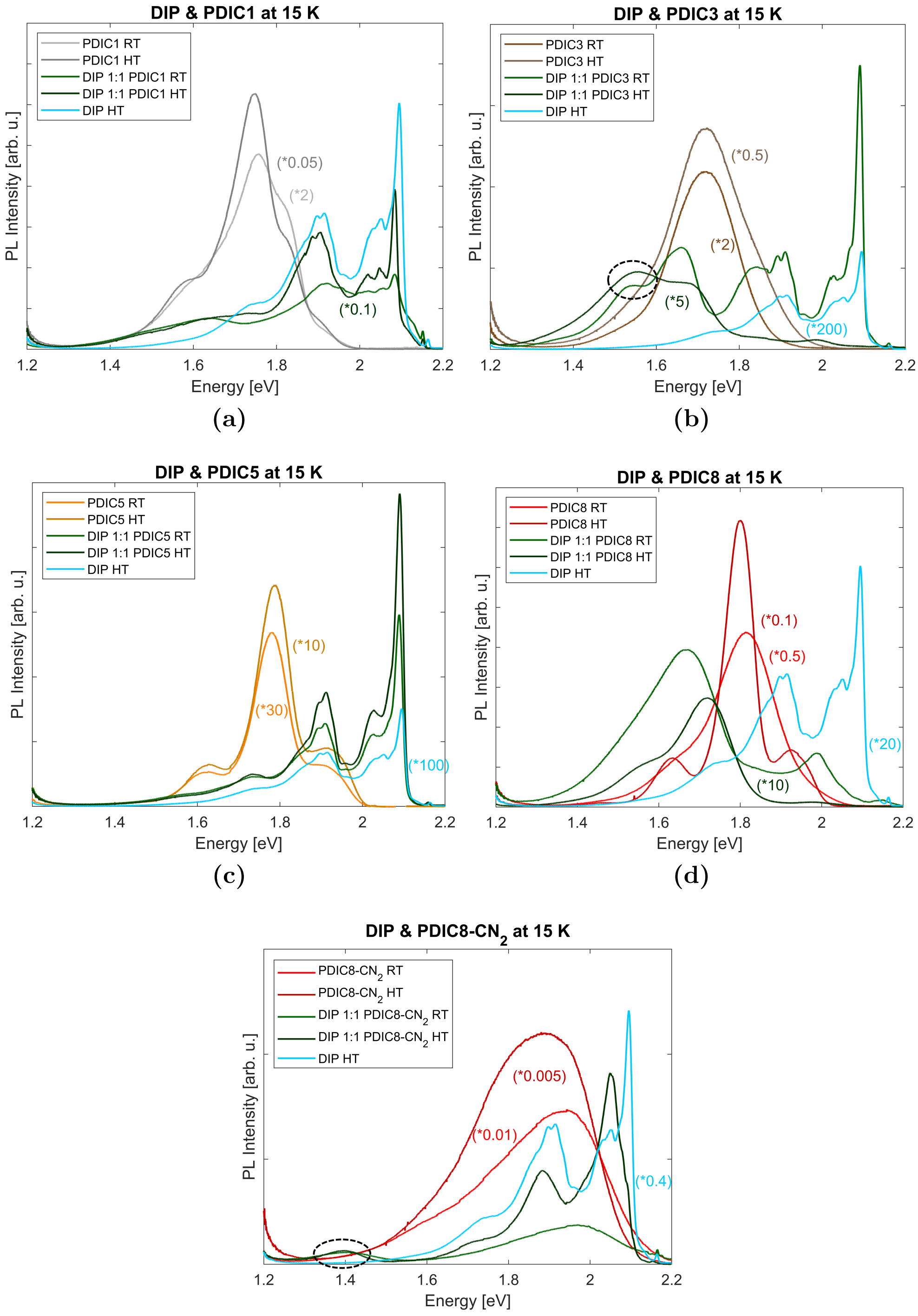

(a) (b)

(c) (d)

(e)

Figure 5.9: *Photoluminescence spectra (measured at 15 K) of equimolar mixed films deposited at 25 °C and 150 °C: a) DIP and PDIC$_1$, b) DIP and PDIC$_3$, c) DIP and PDIC$_5$, d) DIP and PDIC$_8$ and e) DIP and PDIC$_8$-CN$_2$ (CT peaks are marked in black). The spectra are scaled for clarity based on the respective equimolar mixed film grown at 25 °C and the signals at about 2.1 and 2.2 eV are background PL signals of the SiO$_2$ substrate [199]. Note that the apparent sharp peaks at 2.1 eV originate from the cut-off filter of the laser.*

ment temperatures. It is possible that for the PDIs with strong intermolecular interactions defined emission features are visible whereas for the other compounds only one broad peak is observed [200].

Regarding the mixed films of DIP and PDIC$_1$, the PL spectra (Figure 5.9a) show for both equimolar films a broad peak at 1.6 eV which can be assigned to the pure acceptor molecule. The emission features of the equimolar films are superpositions of the two pure components DIP and PDIC$_1$. As shown by the X-ray scattering data, donor-acceptor thin films of DIP and perylene diimide with an *n*-methyl alkyl chain cannot mix, forming no co-crystal and showing no CT effects.

Perylene diimide acceptor molecules with *n*-propyl chains favor the intermixing with the donor molecule DIP as demonstrated by the X-ray scattering evaluation of the mixed thin films. In the emission spectra, a peak at 1.70 eV originating from the pure PDIC$_3$ molecule and a peak at 1.55 eV assigned to the mixed co-crystal are visible for the equimolar thin films. The ES-CT peak is marked in Figure 5.9b in black and signals of both pristine materials are also detected for the equimolar thin films. This indicates that for DIP:PDIC$_3$ mixed films ES-CT effects occur in emission which have to be examined in more detail.

In the emission spectra (Figure 5.9c) of the PDIC$_5$:DIP system, peaks of the pure donor are well resolved for the equimolar thin films and there is only a small peak at 1.62 eV from the pure acceptor molecule. PDIC$_5$ and DIP show only limited intermixing with no degree of charge transfer presumably due to the higher attraction forces between similar PDIC$_5$ molecules. The system PDIC$_8$:DIP shows also phase-separating into both pristine materials determined by X-ray scattering and in the emission spectra also only peaks of the two pure compounds DIP and PDIC$_8$ are visible (Figure 5.9d). This means mixed PDIC$_8$:DIP films present also phase-separation with no degree of CT effects.

In contrast to DIP:PDIC$_8$, PDIC$_8$-CN$_2$ and DIP form a mixed co-crystal examined by the X-ray scattering data. In the emission spectra, there is a CT peak for both DIP:PDIC$_8$-CN$_2$ equimolar thin films (Figure 5.9e). Here, a peak maximum of the CT band at 1.33 eV is visible for the film grown at room temperature and at 1.37 eV for the film prepared at higher substrate temperature. Signals of both pristine materials, DIP and PDIC$_8$-CN$_2$, are also shown in the data, but they are slightly quenched. DIP and PDIC$_8$-CN$_2$ form an ordered mixed co-crystal with possibly two CT states which should be also evaluated more precisely.

5.3 Excited-state properties: Absorption

To analyze the optical properties and the ES-CT effects of the various PDI:DIP mixed films in more detail, absorption data of the various systems are recorded, visible in Figures 5.10 and 5.11.

Figure 5.10 shows the absorption spectra of the three perylene diimide systems mixed with the donor DIP which show no ES-CT effects in the emission spectra

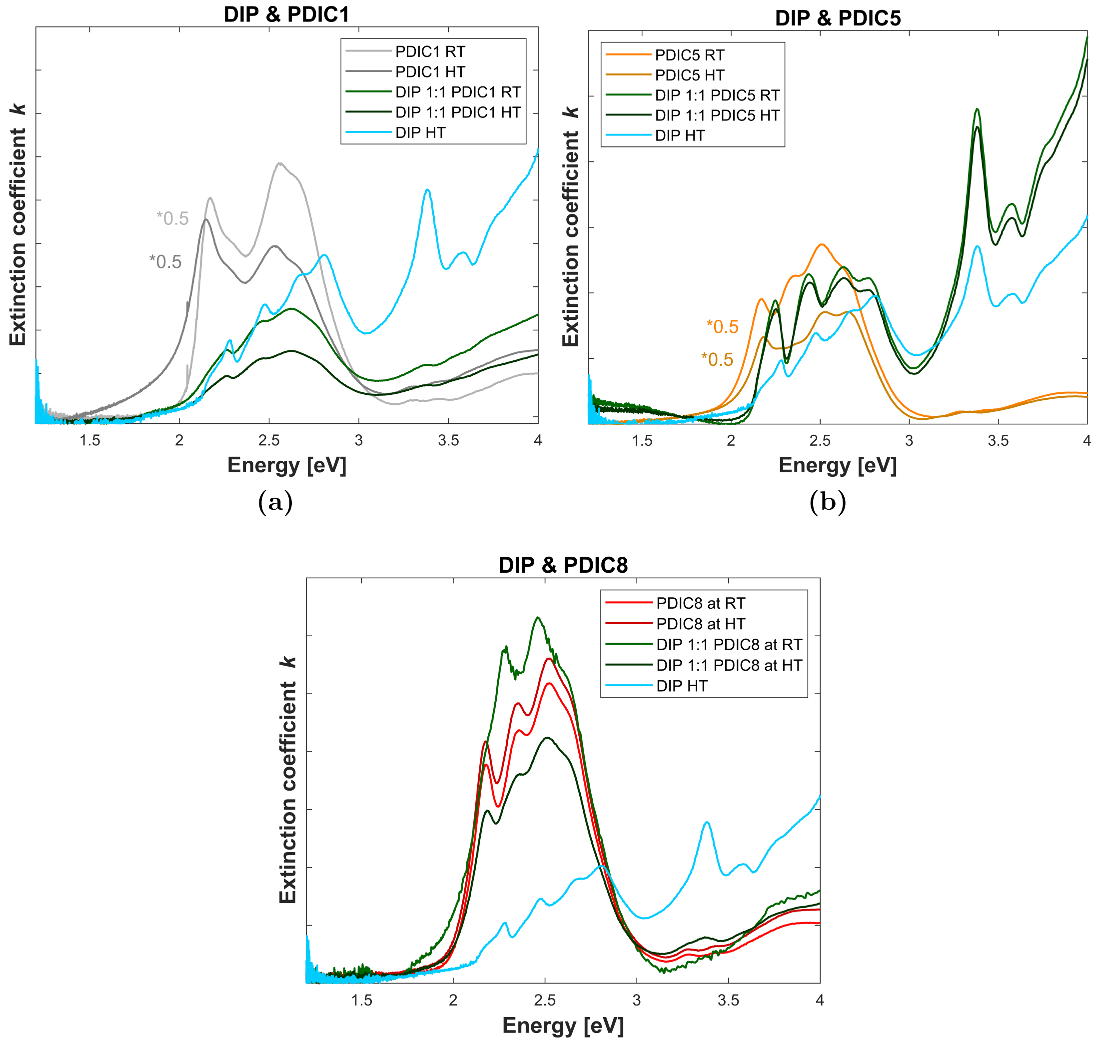

(a) (b)

(c)

Figure 5.10: *Absorption spectra of equimolar mixed films deposited at 25 °C and 150 °C: a) DIP and PDIC$_1$, b) DIP and PDIC$_5$ and c) DIP and PDIC$_8$. The spectra are scaled for clarity based on the respective equimolar mixed film grown at 25 °C.*

(DIP:PDIC$_1$, DIP:PDIC$_5$, and DIP:PDIC$_8$). In the absorption spectra of the equimolar thin films for all three different DIP:PDI systems, superpositions of the respective two pristine materials are detectable. All systems show in the absorption as well as in the emission no degree of an excited-state charge transfer effect. That is also in agreement with the results of the X-ray scattering evaluation where the various mixed films of these systems suggest phase-separation into both pure compounds.

In contrast, Figure 5.11 shows the absorption spectra of the two perylene diimide systems mixed with the donor DIP which show ES-CT effects in the emission spec-

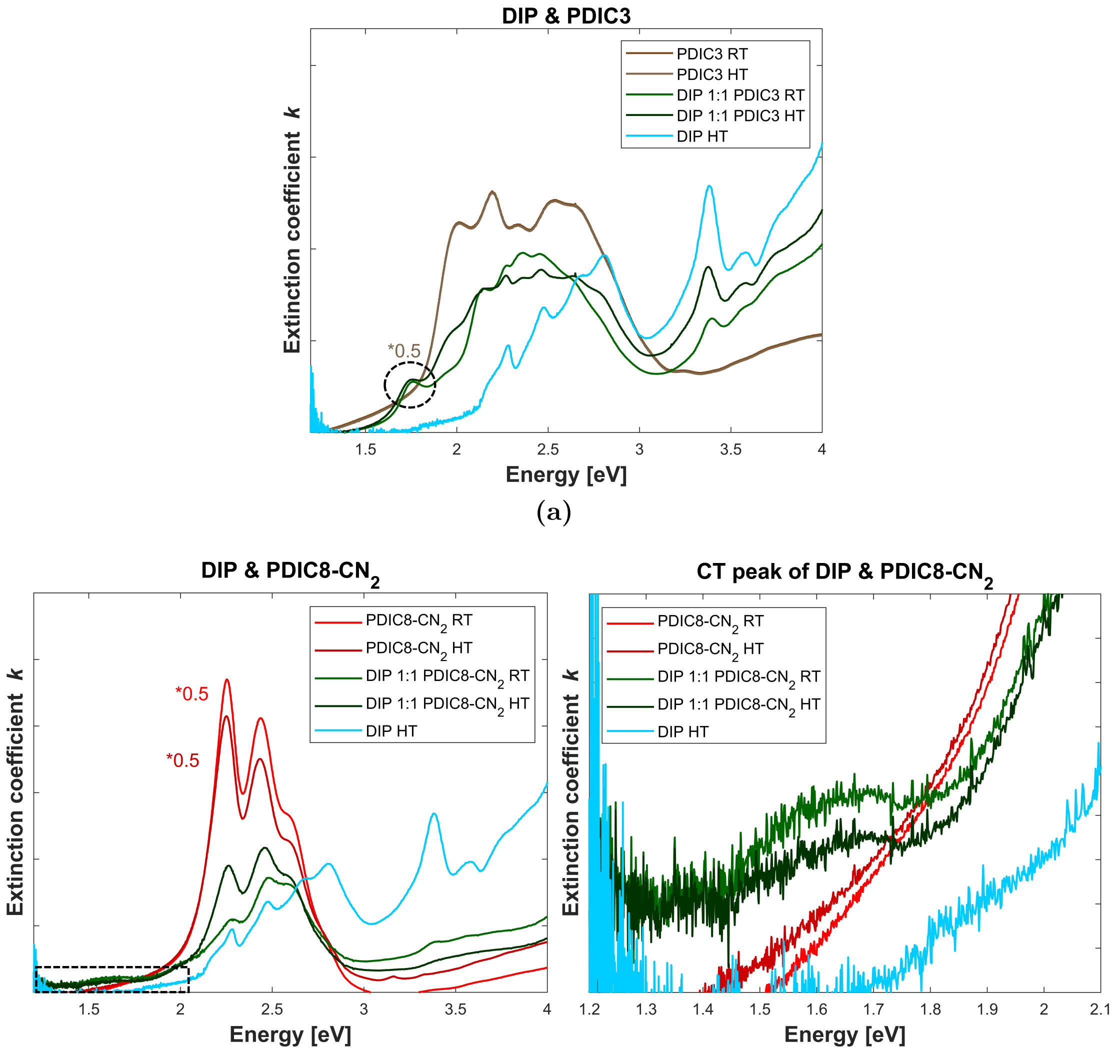

(a)

(b)

(c)

Figure 5.11: *Absorption spectra of equimolar mixed films deposited at 25 °C and 150 °C: a) DIP and PDIC$_3$ (CT peaks are marked in black), b) DIP and PDIC$_8$-CN$_2$ and c) enlarged section of the CT peak (black marked area of (b)). The spectra are scaled for clarity.*

tra (DIP:PDIC$_3$ and DIP:PDIC$_8$-CN$_2$). In the absorption spectra of the equimolar DIP:PDIC$_3$ thin films a sharp peak at 1.75 eV indicates a charge transfer effect between the donor and the acceptor molecule (Figure 5.11a). Additionally, the signals of both pristine materials are also observed in the absorption data of the equimolar thin films. For comparison, a very broad CT band with an onset at 1.55 eV is visible for the equimolar thin films of DIP and PDIC$_8$-CN$_2$ (Figure 5.11c). The degree of the ES-CT is the same for the equimolar thin films of both systems grown at different substrate temperatures. For the mixed films of DIP:PDIC$_3$ a defined CT state is detectable whereas for the PDIC$_8$-CN$_2$ and DIP several CT states are observed as shown in emission and a broad band is visible in the absorption spectra. The detected peaks in the low energy region in absorption and emission for the two equimolar mixed film systems indicate different ES-CT effects. The CT energies can be calculated for the equimolar PDI:DIP thin films by means of a mixed layer device structure and electrical and optical characterization methods.

5.4 Excited-state properties: Electroluminescence and photocurrent spectra

To complete the optical characterization regarding CT effects, electroluminescence and photocurrent spectra (expressed here as incident-photon-to-current efficiency) with the solar cell devices of DIP:PDIC$_3$ and DIP:PDIC$_8$-CN$_2$ mixture layers were also measured in cooperation by Hongwon Kim and Wolfgang Brütting, University of Augsburg. Figure 5.12 shows the reduced EL and IPCE spectra for the two DIP:PDIC$_3$ and DIP:PDIC$_8$-CN$_2$ mixed layer devices on a logarithmic scale.

The IPCE spectra correlate well with the absorption spectra for both equimolar thin films. The CT emission bands observed in the PL spectra for both systems are also visible in the two EL spectra, but, in contrast to the PL spectra, only a weak signal of the pristine materials (peak at 1.85 eV) can be observed in the DIP:PDIC$_3$ EL spectra, which indicates that nearly all injected electron-hole pairs recombine. The methodology introduced by Vandewal et al. is used [168] on adjustment for the crossing regime between reduced EL as well as the reduced IPCE spectra originating from CT states, following Marcus theory to estimate the CT energy E_{CT} in organic photovoltaic materials. The normalized reduced emission $\tilde{I}_{\mathrm{EL}}(E)$ and absorption $\tilde{\eta}_{\mathrm{IPCE}}(E)$ spectra are fitted by Gaussian functions (Eq. 5.2,5.3) [168, 201]:

$$\tilde{I}_{EL}(E) \quad \equiv \quad \frac{I_{EL}(E)}{E} \quad \propto \quad \frac{1}{\sqrt{4\pi\lambda_{DA}k_BT}} \cdot exp(-\frac{[E-(E_{CT}-\lambda_{DA})]^2}{4\lambda_{DA}k_BT}) \quad (5.2)$$

$$\tilde{\eta}_{IPCE}(E) \equiv \eta_{IPCE}(E)\cdot E \propto \frac{1}{\sqrt{4\pi\lambda_{DA}k_BT}} \cdot exp(-\frac{[E-(E_{CT}+\lambda_{DA})]^2}{4\lambda_{DA}k_BT}) \quad (5.3)$$

Here, λ_{DA} represents the reorganization energy related to the Stokes shift in the CT manifold. The CT energy is the crossing point of the fitted reduced EL and IPCE curves. For the DIP:PDIC$_3$ system a CT energy of E_{CT} = 1.77 eV is obtained, in contrast to DIP:PDIC$_8$-CN$_2$ where two CT energies: $E_{CT,1}$ = 1.51 eV and $E_{CT,2}$ = 1.61 eV are observed. When subtracting the λ parameters

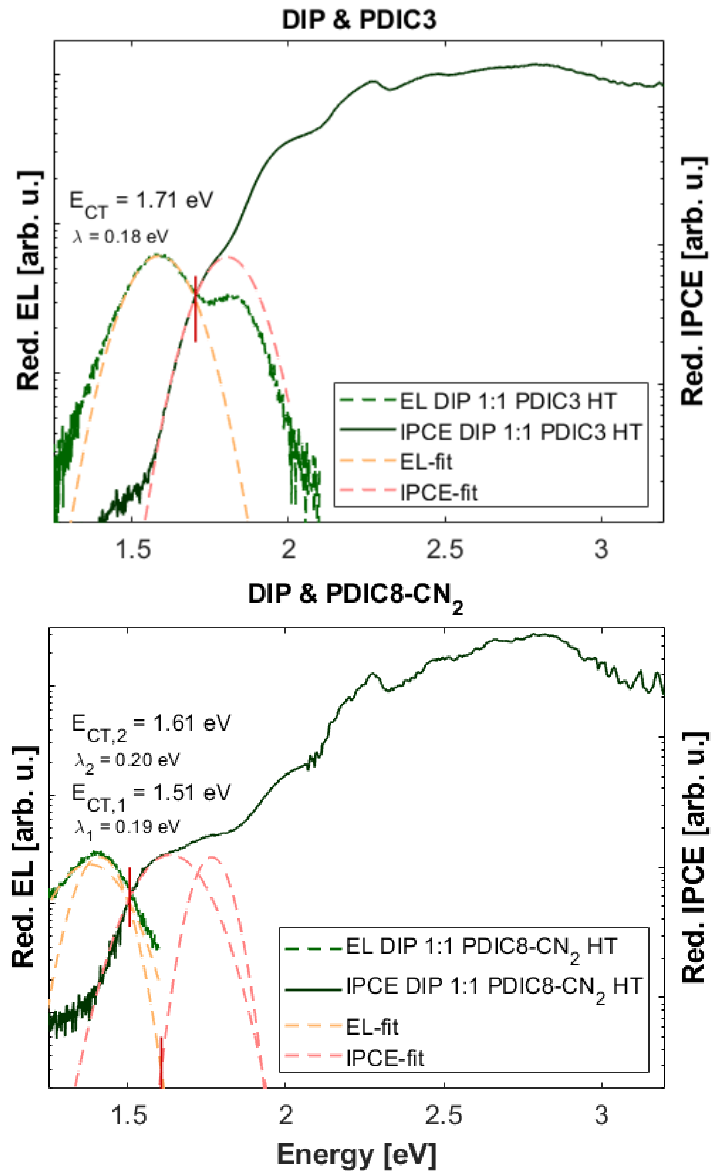

Figure 5.12: *Reduced EL and IPCE spectra of DIP:PDIC$_3$ and DIP:PDIC$_8$-CN$_2$ mixed layer devices with the architecture ITO/HIL 1.3/organic mixed thin film (50 nm)/BCP (5 nm)/Al, with the respectively Gaussian fits and the CT energies (marked by the red lines) as well as the λ parameters.*

from the CT energies (crossing points), we receive the maxima of the EL curves. These values are in good agreement with the PL results where one sharp CT state for DIP:PDIC$_3$ and two different CT peaks for the other DIP:PDI system are obtained. The ES-CT effects and the calculated CT energies if applicable, will be discussed in the following section for the different DIP:PDI mixed films in consideration of the various incorporated side group in the imide and bay position of the respective acceptor molecules.

5.5 Discussion and conclusions

In Figure 5.13 an overview of the excited-state CT effects for the different PDI derivatives in mixed thin films with DIP is shown. Here, the CT energies are calculated based on EL and IPCE measurements for the different PDI derivatives and are presented with the resulting features in the absorption data. For the DIP:PDIC$_3$ system, the co-crystal formation leads to a sharp CT peak in absorption and a defined CT energy. In contrast, the DIP:PDIC$_8$-CN$_2$ mixed films show a broad CT band in absorption and two different CT energies. The threefold broadening of the Bragg peaks in the GIWAXS pattern of the DIP:PDIC$_8$-CN$_2$ equimolar films compared to the DIP:PDIC$_3$ system (see Fig. 5.2g and 5.2j) might suggest more crystal defects in the equimolar thin films and therefore more conformations to nearest-neighbor molecules [148, 202] which could explain the various CT energies for the co-crystal phase of DIP and PDIC$_8$-CN$_2$.

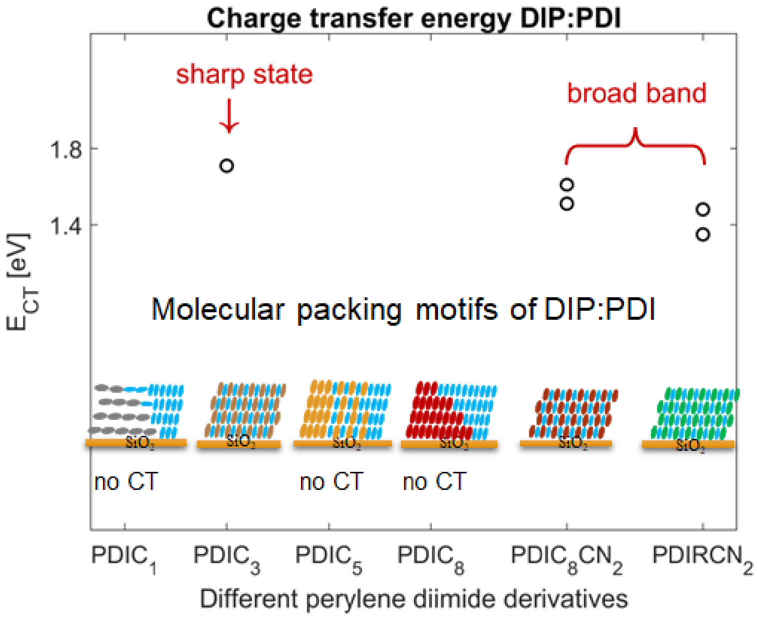

Figure 5.13: *Schematic representation of the results for the ES-CT effects. The calculated CT energies by EL and IPCE data are presented for the different PDI derivatives with the respective CT peak features in the absorption data and the molecular packing motifs of the various DIP:PDI thin film systems [49].*

The PDI acceptors with a small n-alkyl side chain in the imide position phase-separate and show no excited-state CT effect in absorption or emission with the donor DIP. A surprising exception is the DIP:PDIC$_3$ mixed films where the co-crystal phases lead to a sharp CT energy in absorption. In contrast, longer n-alkyl or branched side chains of the PDI derivatives with incorporated cyano-groups in the bay position show a different behavior with DIP. Here, two CT energies can be calculated and a broad band in the absorption is visible for the mixed films.

The co-crystal phase of these mixed films induces two different CT conformations with different CT energies.

In summary, a comprehensive study on mixing behavior and charge transfer effects of different donor-acceptor (DIP:PDI) molecular systems prepared by OMBD was performed. The acceptor molecules differ in the n-alkyl side chain of the imide position and in the cyano-groups of the bay position. In Figure 5.14 (as part of Fig. 4.9) the respective results of the DIP:PDI mixed film systems are schematically shown. Here, the mixing behavior and the degree of ES-CT effects are illustrated for the five investigated thin film systems in this thesis and in addition also compared with two other DIP:PDI derivatives which were also investigated regarding mixing behavior and CT effects with the donor DIP [49].

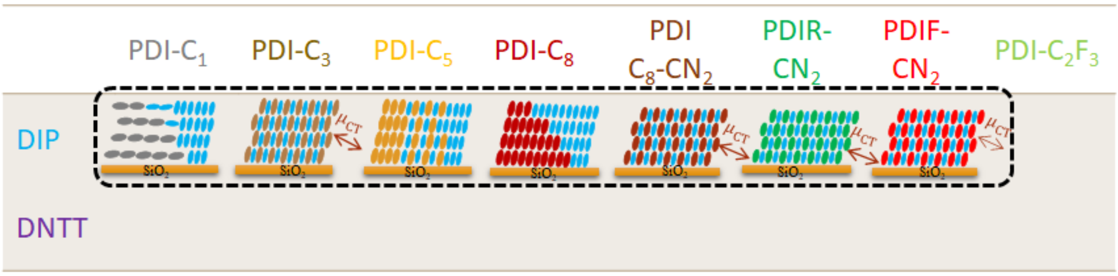

Figure 5.14: *Schematic results of the investigated mixed film DIP:PDI systems. The different schematic scenarios are describing the mixing behavior and the degree of the charge transfer effects of the individual systems. This illustration is part of Fig. 4.9.*

The optimized n-alkyl side chain length of the perylene diimide acceptors was found for the mixing behavior with DIP. With increasing chain length in the imide position of the acceptors, a strong CT effect as well as a strong mixing for the system DIP:PDIC$_3$ is detected. The acceptor molecule with n-propyl side chains forms a well-defined co-crystal with DIP and shows a sharp ES-CT state. Different factors play a role and influence the mixing behavior and CT effects. The increased intermolecular interactions of the pure acceptor molecules with longer n-alkyl side chains appear to disfavor the mixing and the CT effects. However, the orientation of the acceptor molecules on the substrate (SiO$_2$) is changing with longer n-alkyl side chains which favor the mixing and the CT effects. Strong CT and intermixing are also shown for systems of DIP and perylene diimide derivatives with cyano groups in the bay position. PDIC$_8$-CN$_2$:DIP forms also a well-ordered co-crystal, but with two ES-CT states. The incorporated cyano groups influence the aromatic backbone of the perylene diimide derivatives and favor the CT effects as well as the mixing behavior. This was also shown for the two examined thin film systems PDIR-CN$_2$:DIP and PDIF-CN$_2$:DIP with incorporated cyano groups in the bay position of the acceptors. Both molecule combinations form a well-defined co-crystal and show a broad ES-CT band in absorption as well as two defined CT energies (for equimolar thin films of PDIR-CN$_2$:DIP) [49].

Through the influence of the different side chains of the acceptor molecules on the mixing behavior and CT effects with DIP, it is possible to control mixing behavior and CT effects using suitable perylene diimide molecules. A key to this is the structure of these acceptor molecules, which can be modified easily in the desired way.

Chapter 6

Molecule charge transfer effects in $PDIC_8$-CN_2:DNTT and PDIF-CN_2:DNTT systems

The results presented in this chapter have been recently published in Ref. [169]. They are based on binary organic bulk heterojunction thin films. The focus was set on weakly interacting organic semiconductive mixtures with DNTT as donor molecule and two different PDI derivatives as acceptors ($PDIC_8$-CN_2 and PDIF-CN_2) which differ in the fluorination of the side chains (Fig. 6.1). For organic optoelectronics, the interactions between donor and acceptor molecules and the related CT effects are very important. The microscopic details of CT, in particular for the different strengths of interactions, are still not fully understood [41, 42, 49].

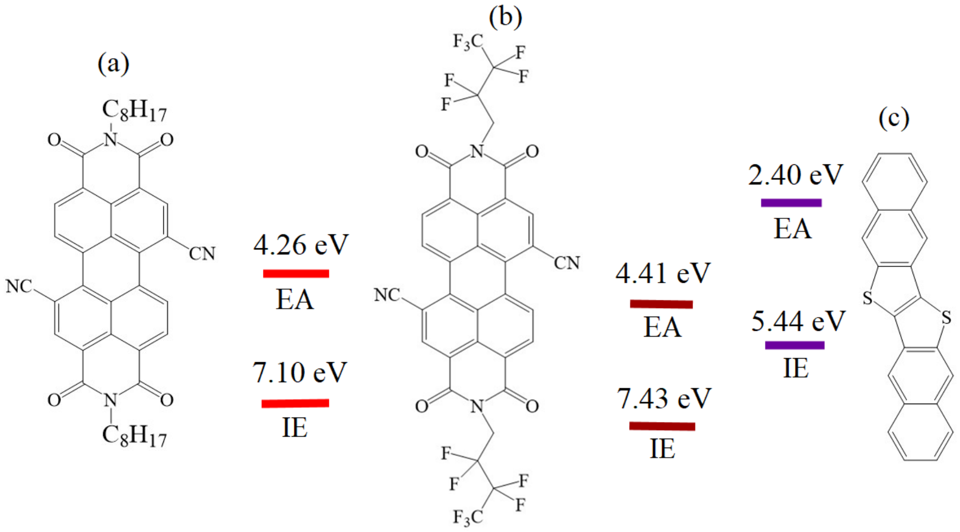

Figure 6.1: *Overview of the studied perylene diimide acceptor molecules with the different electron affinities (EA) and ionization energies (IE). The IEs levels are determined by ultraviolet photoelectron spectroscopy (UPS) of the thin films, [49, 113, 141] and the EAs are calculated with the IEs, the optical band gaps and the exciton binding energies: a)* $PDIC_8$-CN_2 *b) PDIF-*CN_2 *and c) donor molecule DNTT.*

Therefore, the molecular CT of two different PDI:DNTT thin film systems is characterized in this chapter. The co-crystal formation and structural morphology of the thin films are investigated by GIWAXS and XRR and combined with a comprehensive experimental and first-principles study of CT effects based on density-functional theory and many-body perturbation theory performed in cooperation by Ana M. Valencia and Caterina Cocchi, University of Oldenburg. The GS-CT effects are examined by infrared spectroscopy, followed by energy level calculations and the comparison of the calculated and experimental absorption spectroscopy to describe the ES-CT properties. Other different optical methods such as PL and ellipsometry are used to examine inter alia the anisotropy of the CT effect. Additionally, the general impact of localized HOMO and LUMO levels on optoelectronic properties in CT complexes will be discussed.

6.1 Structural investigations by X-ray scattering

The morphology and the intermixing in bulk heterojunction thin films on the molecular level has a great impact on the microscopic details of charge transfer effects [25, 30–33]. As described in Sec. 3.1 and the results Chap. 5, the alkyl, branched, and fluorinated side chains and the electron-withdrawing side groups of the respective PDI derivatives can alter molecular packing and morphology of the deposited films [19, 20, 23]. Therefore, they influence also the co-crystal formation with suitable donor molecules, and therefore the growth and mixing behavior has to be clarified. The structure of the mixed DNTT:PDI thin films depending on the different side chains in the imide position of the acceptor molecules will be discussed first. An overview of the measured GIWAXS diffraction patterns from both pure perylene diimide derivatives and the donor molecule DNTT as well as the equimolar donor acceptor mixtures is shown in Figure 6.2. All three pure compounds form crystalline thin films with Bragg reflections belonging to known crystal structures (Fig. 6.2a, 6.2c, 6.2d) [154, 197, 198]. All molecules are oriented with their longest axis almost normal to the substrate surface. The tilt angles of the respective molecules to the Silicon substrate are 68.11° for PDIC$_8$-CN$_2$, 85.47° for DNTT, and 73.92° for PDIF-CN$_2$ assuming the known crystal structures. The crystal quality of the acceptors depends strongly on the substrate temperature during deposition. In thin films, PDIF-CN$_2$ is only crystalline on SiO$_2$ (and not on the other substrates employed) at a deposition temperature higher than 120 °C in contrast to PDIC$_8$-CN$_2$, which forms crystalline films already at room temperature [117].

Figure 6.2b and 6.2e show GIWAXS data of the equimolar DNTT:PDIC$_8$-CN$_2$ and DNTT:PDIF-CN$_2$ mixed films. In both reciprocal space maps only signals from the mixed co-crystals are visible (marked by dashed green lines). The donor DNTT has roughly the size of the PDI core and exhibits different mixing behavior with the two acceptor compounds. PDIC$_8$-CN$_2$ forms a co-crystal with DNTT when co-deposited at room temperature, however, it tends to phase-separate at

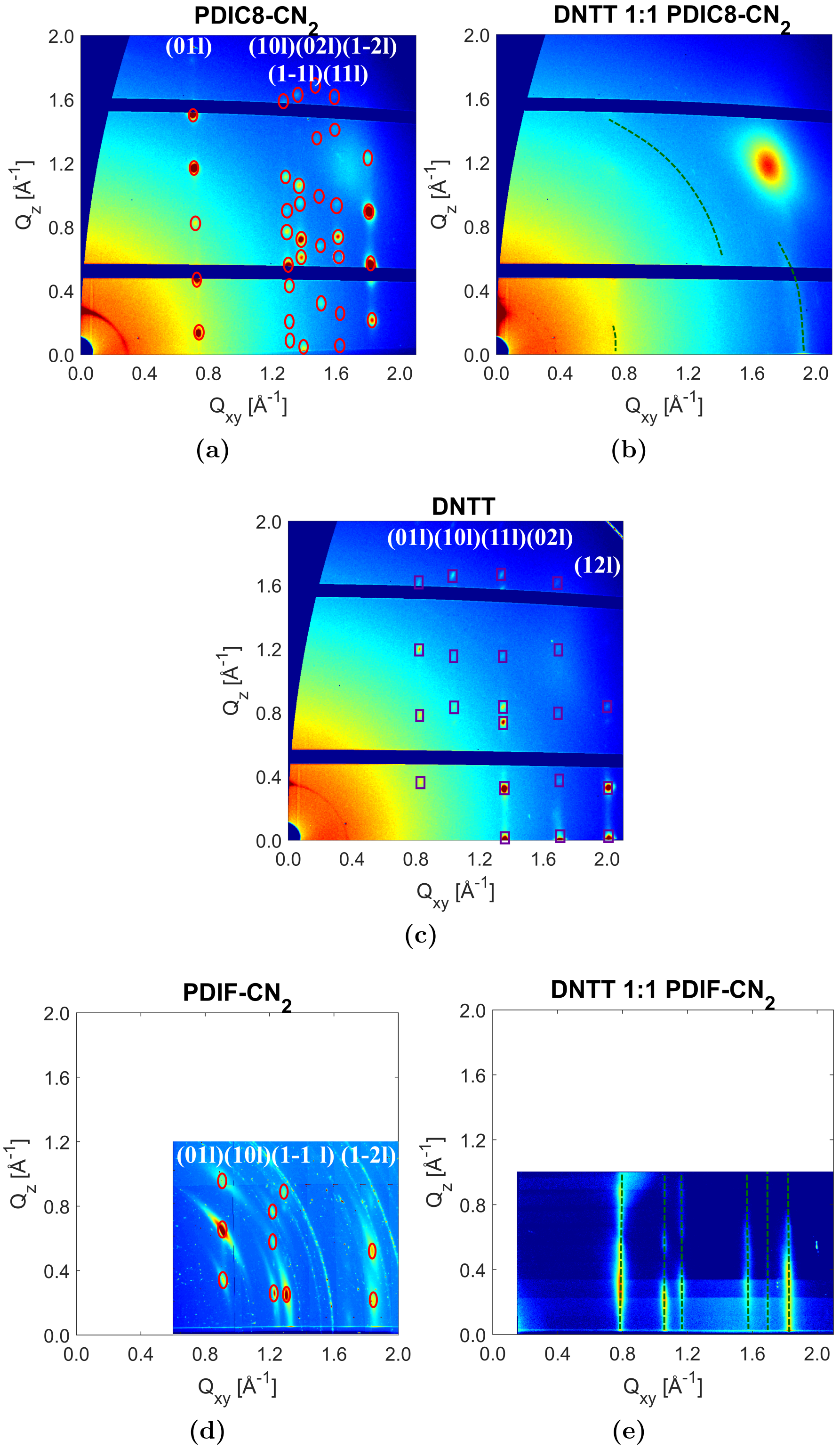

(a) **(b)**

(c)

(d) **(e)**

Figure 6.2: *GIWAXS data of a) PDIC$_8$-CN$_2$ (T_{sub} = 150 °C), b) DNTT 1:1 PDIC$_8$-CN$_2$ (T_{sub} = 25 °C), c) DNTT (T_{sub} = 100 °C), d) PDIF-CN$_2$ (T_{sub} = 150 °C) and e) DNTT 1:1 PDIF-CN$_2$ (T_{sub} = 150 °C) (squares indicate peaks of the donor, circles of the acceptor, and dashed green lines for the mixed phase, the same q-ranges were taken for clarity).*

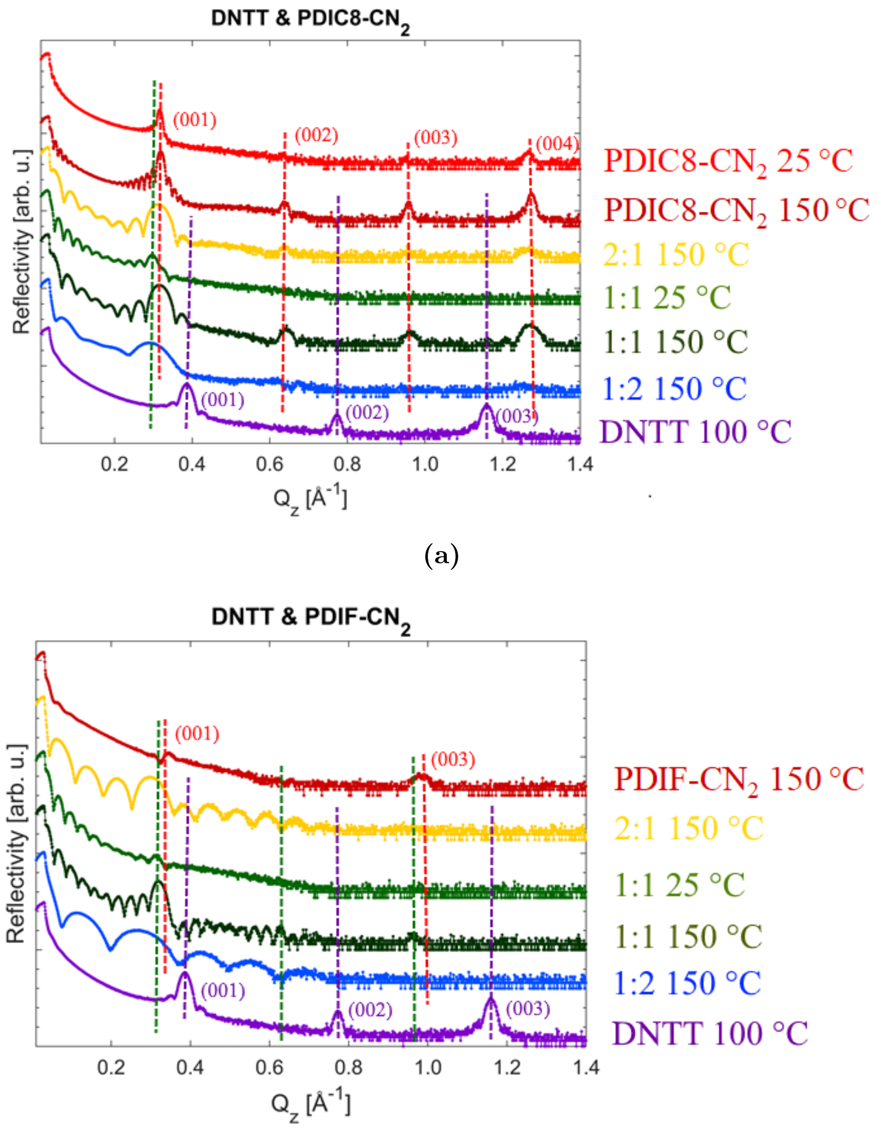

(a)

(b)

Figure 6.3: *XRR data of mixed films deposited at 25 °C and 150 °C: a) DNTT and PDIC$_8$-CN$_2$ and b) DNTT and PDIF-CN$_2$ (violet dashed lines indicate peaks of the donor, red of the acceptor, and green for the mixed phase with the respective Miller indices of the Bragg peaks, all spectra are vertically offset for better clarity).*

higher substrate temperatures. Figure 6.2b shows GIWAXS data of a PDIC$_8$-CN$_2$:DNTT 1:1 mixed film deposited at 25 °C. The weak ring-shaped features indicate the formation of 1:1 co-crystalline grains without preferred orientation. In contrast, the donor DNTT and the acceptor PDIF-CN$_2$ form a well-defined highly ordered co-crystal visible in the GIWAXS data in Figure 6.2e. In the reciprocal space map of the equimolar thin film only signals from the co-crystal and no signals of the pure compounds are visible. Furthermore, the crystallinity of the co-crystal for the equimolar thin films is increasing with higher film thickness and with higher deposition temperature.

Figure 6.3 shows the X-ray reflectivity scans for both DNTT:PDIC$_8$-CN$_2$ and DNTT:PDIF-CN$_2$ thin film systems. Here, the out-of-plane Bragg reflections of the three pure compounds indicate, as mentioned before for the GIWAXS patterns, crystalline formed thin films. For the pure PDIF-CN$_2$ thin film deposited at high substrate temperature, the first two reflections are suppressed due to the high electron negativity of the fluorinated side chain as common for this PDI derivative [117]. The XRR scans for the equimolar films of both systems show, as the GIWAXS patterns, Bragg reflections from the mixed co-crystals (marked by green lines). Signals of the pure PDIC$_8$-CN$_2$ are visible for both equimolar thin films in the X-ray reflectivity scans (Fig. 6.3a), but only the equimolar film deposited at room temperature presents a Bragg peak from the mixed co-crystal showing that at higher substrate temperature phase-separating into the pure compounds occurs. In the XRR spectra of the DNTT:PDIF-CN$_2$ system, the equimolar and the PDIF-CN$_2$ 2:1 DNTT thin films are presenting only Bragg signals from the co-crystal and no signals of the pure compounds (Fig. 6.3b) which indicates a highly defined co-crystal.

When comparing the mixing behavior of the two acceptor perylene diimide derivatives with the donor molecule DNTT, the acceptor PDIF-CN$_2$ with the fluorinated side chain favors the mixing and forms with DNTT a highly defined co-crystal with long-range ordering.

6.2 Ground-state CT properties: Infrared spectroscopy

It was shown for the two DNTT:PDIC$_8$-CN$_2$ and DNTT:PDIF-CN$_2$ thin film systems that the donor is intermixing with different strengths with both acceptor molecules at suitable growth conditions. The electronic interaction between the donor and the acceptor molecule is therefore not inhibited by phase-separation of both organic compounds. So, the electronic interaction and the charge transfer effects can be examined by applying different spectroscopic methods and the optical properties of the thin films can be investigated. At first, the CT between donor and acceptor in absence of electronic excitations, the electronic ground-state CT properties of the investigated films are of high interest. To study a possible ground-state CT, the highly sensitive stretching mode of the nitrile group (CN-group) is probed by IR spectroscopy [78, 79].

In Figure 6.4 the infrared spectra for the two PDI:DNTT systems are shown. The donor molecule DNTT shows no IR active vibration mode in this range, showing that the stretching mode of the nitrile group is ideal for GS-CT investigations. A shift of 2.1 ± 0.5 cm^{-1} of the CN-group is visible for the equimolar DNTT:PDIF-CN$_2$ mixed film at high deposition temperature. For the equimolar

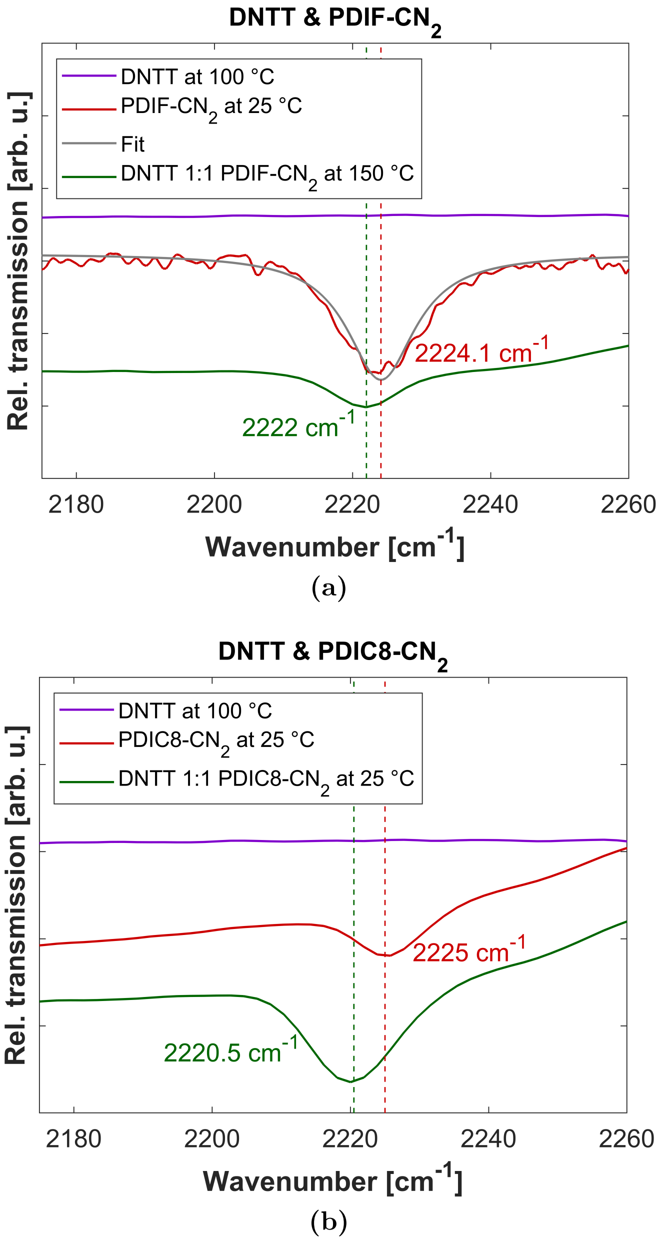

(a)

(b)

Figure 6.4: *Infrared spectra of a) DNTT:PDIF-CN$_2$ equimolar mixed film deposited at 150 °C and b) DNTT:PDIC$_8$-CN$_2$ equimolar mixed film deposited at 25 °C.*

DNTT:PDIC$_8$-CN$_2$ mixed film grown at 25 °C the corresponding shift amounts to 4.5 ± 0.4 cm^{-1}. These results indicate a weak partial ground-state charge transfer of 0.08 or 0.17 e$^-$, respectively, based on an analysis similar to Ref. [78]. In the following section, the ES-CT effects and the comparison with the theoretical investigations for both systems will be examined.

6.3 Calculated energy levels in CT complexes

The experimental analysis is complemented with the results of first-principles calculations based on density-functional theory and many-body perturbation theory performed in cooperation by Ana M. Valencia and Caterina Cocchi, University of Oldenburg. The DNTT:PDIC$_8$-CN$_2$ and DNTT:PDIF-CN$_2$ mixtures are modeled as bimolecular clusters *in vacuo*. Both structures are constructed assuming a co-facial arrangement of the two constituting molecules, which remains present also after structural optimization. In the relaxed complexes, as a result of the interactions with the donor, the acceptor molecules show a slight bending of their backbone, as visible in Figure 6.5.

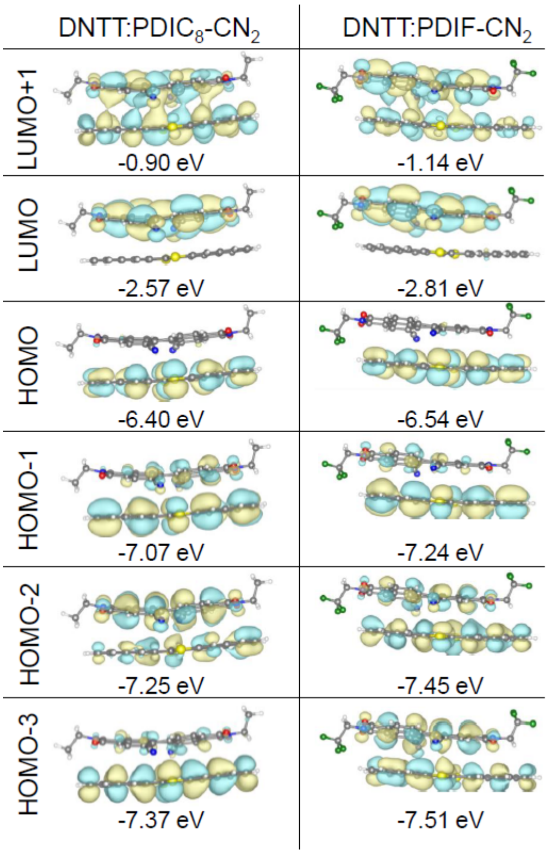

Figure 6.5: *Molecular orbitals of DNTT:PDIC$_8$-CN$_2$ and DNTT:PDIF-CN$_2$ accompanied by their respective energy eigenvalues computed from G_0W_0.*

Inspecting the energy levels of the isolated donor and acceptor molecules (Figure 6.6), they form in both cases a type-II level alignment, with the LUMO of the acceptor lying within the gap of the donor [203]. In DNTT:PDIC$_8$-CN$_2$ and DNTT:PDIF-CN$_2$, the HOMO is energetically lower than the HOMO of the donor, whereas the LUMO is higher than the LUMO of the acceptor. The energy gap of the complexes is therefore about 0.2 eV and 0.3 eV larger than the energy differ-

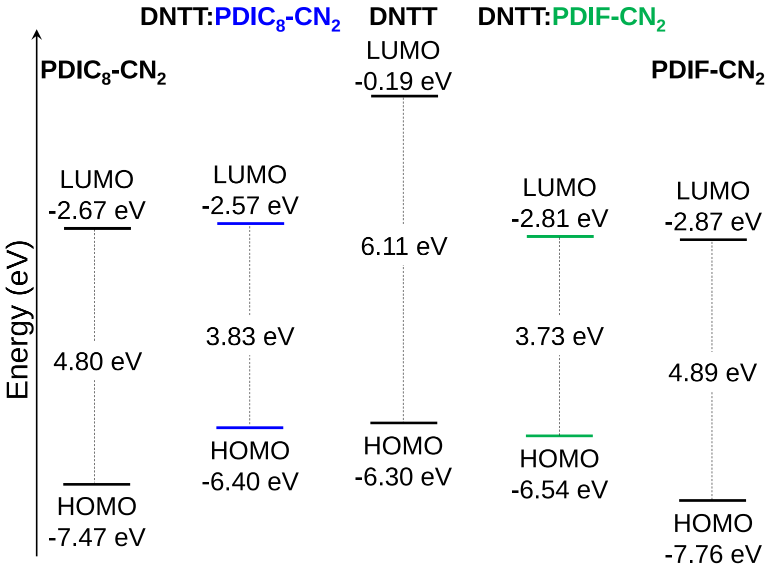

Figure 6.6: *Energy level alignment for both DNTT:PDIC$_8$-CN$_2$ and DNTT:PDIF-CN$_2$ complexes computed from G_0W_0 on top of DFT (PBE0 functional).*

ence between the HOMO of DNTT and the LUMO of PDIC$_8$-CN$_2$ and PDIF-CN$_2$, respectively.

As a result, the HOMO and the LUMO of the complexes are localized on the donor and on the acceptor molecule, respectively (Figure 6.5). Hybridization effects appear in lower (higher) occupied (unoccupied) states. This scenario is compatible with the GS-CT, $\delta = 0.11$ e, obtained for both systems in agreement with the experimental result for DNTT:PDIF-CN$_2$ ($\delta = 0.08$ e, Section 6.2).

In summary, both systems DNTT:PDIC$_8$-CN$_2$ and DNTT:PDIF-CN$_2$ show a small GS-CT governed by hybridized HOMO-1 and LUMO+1 levels. In contrast, the respective HOMO and LUMO energy levels of the complexes are localized on the acceptor and donor molecule. This leads to the estimation of a nearly pure charge transfer from the acceptor to the donor and the ES-CT effects and optical properties are examined for both systems in the following section.

6.4 Excited-state CT properties

For both systems, DNTT:PDIC$_8$-CN$_2$ and DNTT:PDIF-CN$_2$, a weak CT in the ground-state is presented. Next, the CT effects upon excitation are of high interest. So, Es-CT effects and optical properties of the thin films of the two molecule combinations are examined by emission and absorption spectroscopy.

6.4.1 Excited-state CT properties: Absorption

In the absorption spectra of both DNTT:PDIC$_8$-CN$_2$ and DNTT:PDIF-CN$_2$ systems (Fig. 6.7), excited-state CT peaks are visible at low energy below the HOMO-LUMO transition of the pure compounds. For thin films with PDIC$_8$-CN$_2$, only a weak CT peak is detected, which is most intense for the equimolar film deposited at room temperature with an onset of a maximum at 1.55 eV (Fig. 6.7b). The weak excited-state CT peak is additionally only visible for the equimolar film deposited at higher temperature and for the 1:2 thin film with excess of the pure acceptor.

In contrast, for thin films with PDIF-CN$_2$ a strong excited-state CT peak with an onset of a maximum at 1.58 eV is visible (Fig. 6.7d). The intensity of the CT peak is increasing with higher deposition temperature. All thin films present only peaks of the formed co-crystal in the absorption spectra. For the thin films with excess of one pure compound, only the 1:2 thin film with excess of PDIF-CN$_2$ shows the strong ES-CT peak. The equimolar 80 nm film of DNTT:PDIF-CN$_2$ shows two CT states in the absorption spectrum at 1.58 eV and 1.73 eV.

6.4.2 Excited-state CT properties: Photoluminescence

Figure 6.8 shows the photoluminescence spectra for DNTT:PDIC$_8$-CN$_2$ and DNTT: PDIF-CN$_2$ measured at 77 K. A well-defined CT peak is visible at 1.37 eV of the equimolar PDIC$_8$-CN$_2$:DNTT mixed film deposited at 25 °C (Fig. 6.8b). This CT peak is related to the absorption band at 1.55 eV. A shift in PL to lower energy of $\sim$ 0.2 eV is common for related mixed systems [74]. Features of the pure PDIC$_8$-CN$_2$ are also visible for the mixed thin films. The PL signals of the pure acceptor thin films are much more intense than those of the pure DNTT thin film. Broad and intense emission spectra are very common for PDI derivatives [115, 117, 204]. Therefore, in the mixed films the emission signals of the acceptor are dominating.

A strong excited-state CT effect is detected for all DNTT:PDIF-CN$_2$ mixed thin films (Fig. 6.8c). The CT leads to quenching of the signals of the pure compounds [205, 206]. The intensity of the CT peak is the largest for the equimolar thin films and decreases with an excess of one of the pure materials. The mixed thin films with excess of the donor molecule have here the lowest CT intensities that was also shown for both systems in the absorption data. This indicates that the co-crystal formation and CT effects are favored with the excess of the acceptor and disfavored with more DNTT in the mixed thin films. As described for the absorption data, the ES-CT of the equimolar thin film is increasing with the deposition temperature and is the highest for the equimolar 80 nm thick film (Fig. 6.8d). High temperature and film thickness favor therefore the intermixing and the charge transfer effects of PDIF-CN$_2$ and DNTT [25].

To summarize, the acceptor PDIF-CN$_2$ with the DNTT donor forms a highly defined co-crystal with long-range order exhibiting a weak ground-state and strong excited-state charge transfer which is increasing with higher substrate temperature

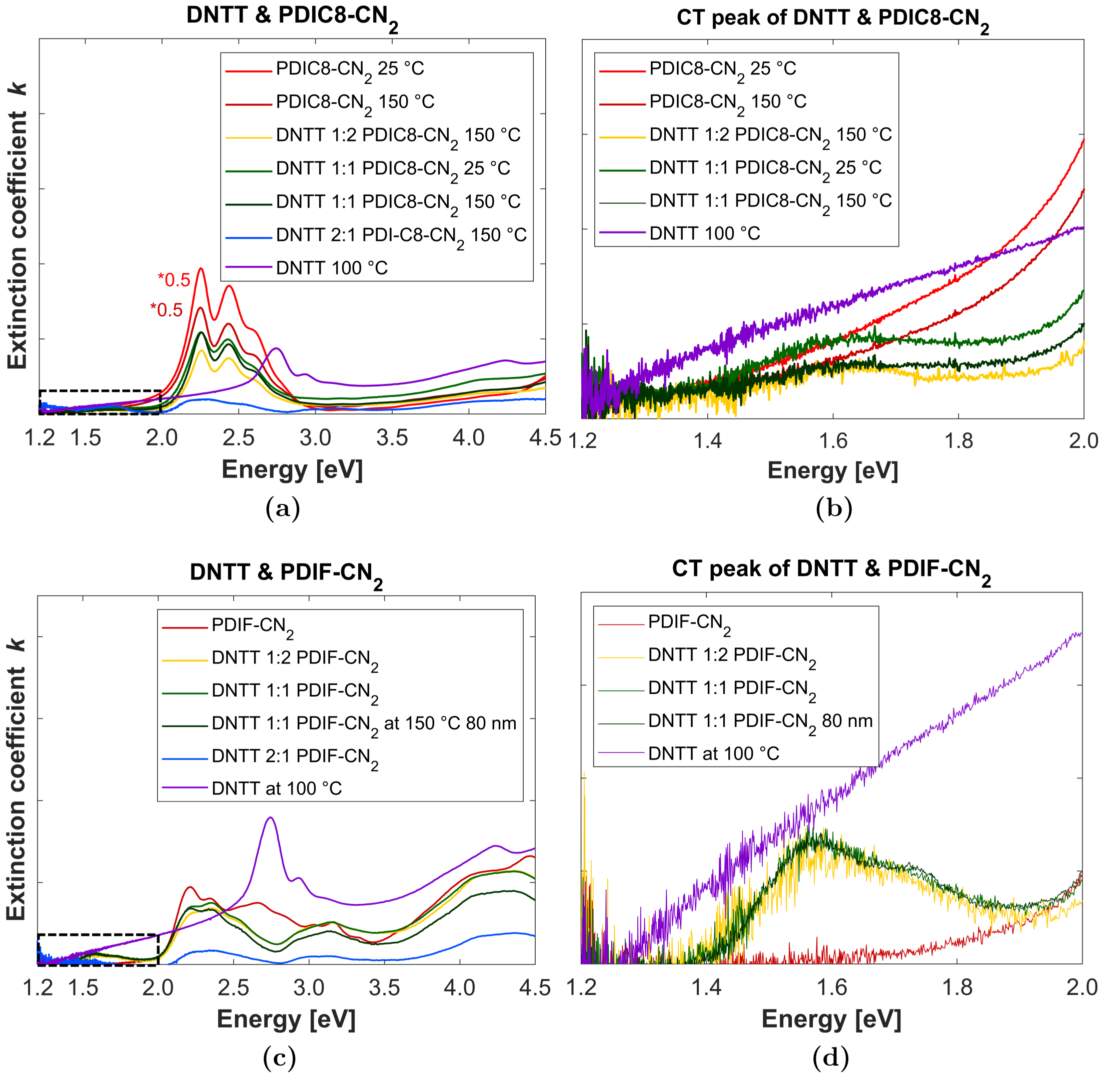

(a) (b)

(c) (d)

Figure 6.7: *Absorption spectra of a) DNTT and PDIC$_8$-CN$_2$ mixed films deposited at 25 °C and 150 °C, b) enlarged section of the CT peak (black marked area of (a)), c) DNTT and PDIF-CN$_2$ mixed films deposited at 150 °C and d) enlarged section of the CT peak (black marked area of (c)). The spectra are scaled for clarity.*

and higher film thickness. In contrast, PDIC$_8$-CN$_2$ forms a co-crystal with DNTT in particular for the substrate at room temperature during growth, showing only weak ES-CT and GS-CT.

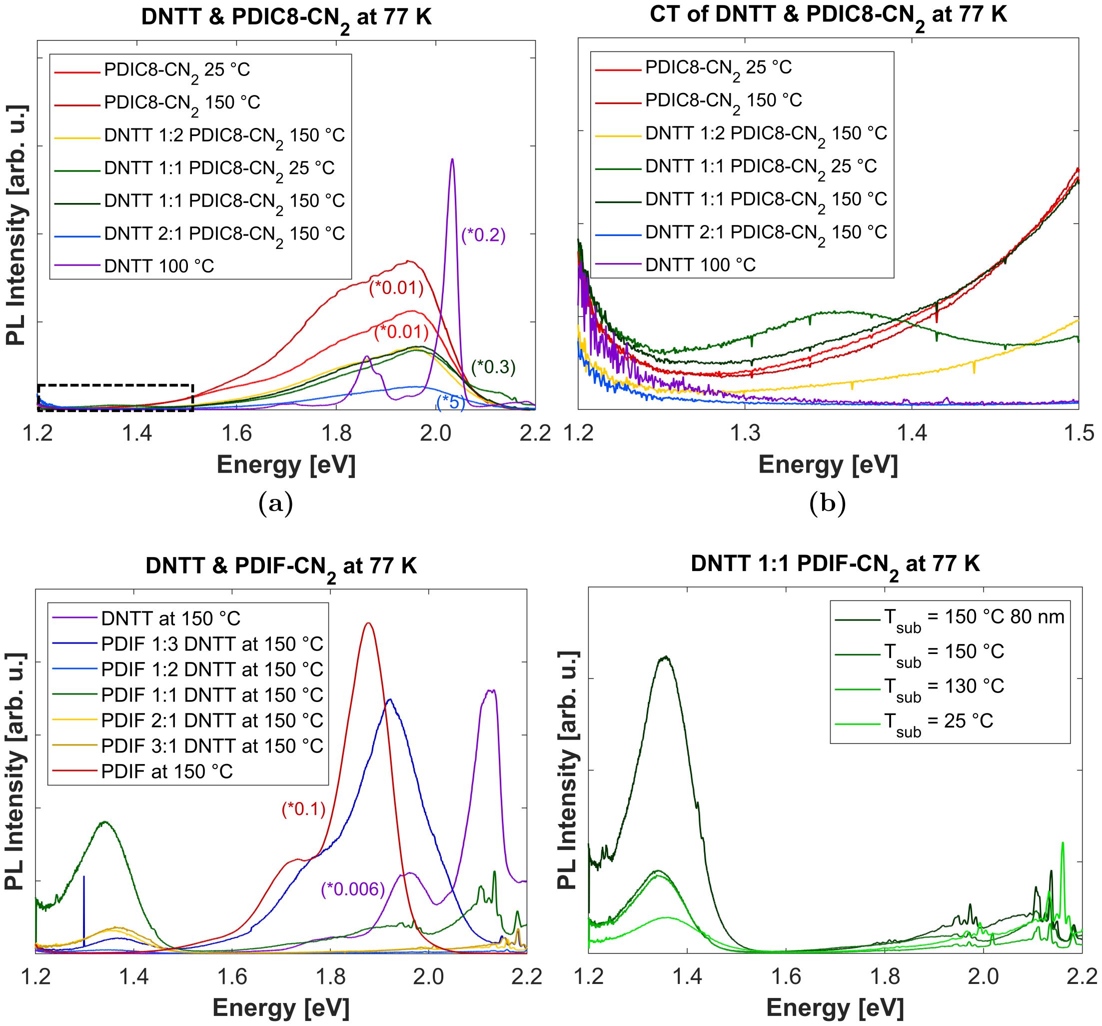

(a) (b)

(c) (d)

Figure 6.8: *Photoluminescence spectra of a) DNTT and PDIC$_8$-CN$_2$ mixed films deposited at 25 °C and 150 °C, b) enlarged section of the CT peak (black marked area of (a)), c) DNTT and PDIF-CN$_2$ mixed films deposited at 150 °C and d) equimolar DNTT and PDIF-CN$_2$ films at different deposition temperatures. The spectra are scaled for clarity and the signals at about 2.1 and 2.2 eV are background PL signals of the SiO$_2$ substrate [199].*

6.5 Calculated optical absorption spectroscopy

The experimental results of the optical absorption spectra for DNTT:PDIC$_8$-CN$_2$ and DNTT:PDIF-CN$_2$ are compared with first-principles calculations based on density-functional theory and many-body perturbation theory performed in cooperation by Ana M. Valencia and Caterina Cocchi, University of Oldenburg. The calculated absorption spectra for both systems are in agreement with the exper-

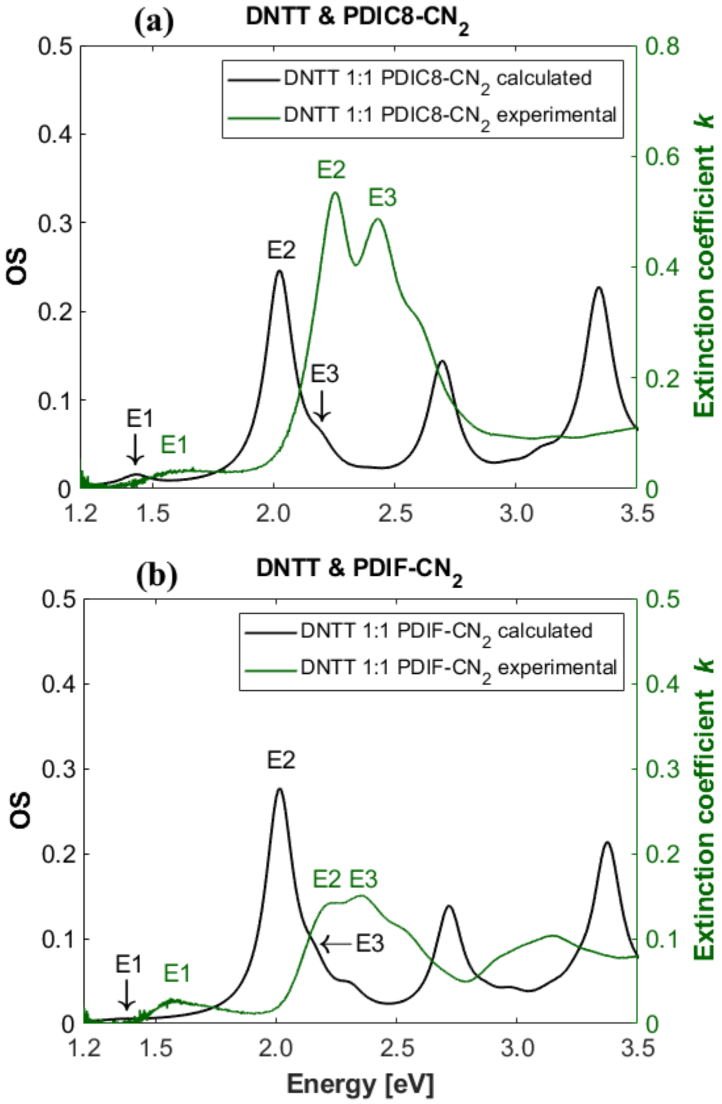

Figure 6.9: *Experimental and computed optical absorption spectra of the complexes: a) DNTT:PDIC$_8$-CN$_2$ and b) DNTT:PDIF-CN$_2$. The first three excitations are labeled as E_1, E_2, and E_3. OS stands for oscillator strength.*

iments (Figure 6.9). The computed absorption peaks are in the same range as the experimental ones although slightly shifted by 0.2 eV, possibly, due to solid state solvation [207–209]. Differences can be also ascribed to the missing vibronic effects in the calculations. The spectra of the two complexes are very similar. The first excitation (E_1) is found at 1.43 eV in the spectrum of DNTT:PDIC$_8$-CN$_2$ and at 1.36 eV in the one of DNTT:PDIF-CN$_2$. In both cases, its oscillator strength is extremely weak, compatible with the negligible overlap between the wave-functions associated with the HOMO and the LUMO in the two complexes (see Figure 6.5 in Sec. 6.3): As reported in Table 6.1, the transition between the frontier orbitals contributes almost entirely to E_1. As a result, the hole and the

Table 6.1: *Energies, oscillator strength (OS), and composition in terms of single-quasiparticle transitions of the first three excitations in DNTT:PDIC$_8$-CN$_2$ and DNTT:PDIF-CN$_2$ complexes. HOMO and LUMO are abbreviated by H and L, respectively.*

	Excitation	Energy [eV]	OS	Composition
DNTT:PDIC$_8$-CN$_2$	E$_1$	1.429	0.011	H → L (95%)
	E$_2$	2.023	0.240	H-1 → L (48%) H-3 → L (47%)
	E$_3$	2.193	0.026	H-1 → L (50%) H-2 → L (47%)
DNTT:PDIF-CN$_2$	E$_1$	1.356	0.001	H → L (95%)
	E$_2$	2.013	0.266	H-1 → L (42%) H-2 → L (31%) H-3 → L (24%)
	E$_3$	2.156	0.035	H-1 → L (50%) H-3 → L (34%) H-2 → L (11%)

electron densities are fully segregated on the donor and on the acceptor molecule, respectively (Figure 6.10).

The strongest maximum (E_2) is found at approximately 2.0 eV and stems from various orbital transitions between occupied orbitals below the HOMO and the LUMO (Table 6.1). This feature is reflected in the distribution of the hole and the electron densities: the latter remains localized on the acceptor molecules, while the former is now spread over the whole complex. Analogous behavior pertains also to the third excitation (E_3), which appears as a shoulder above the first peak (see Figure 6.9). Again, a number of transitions between lower occupied levels and the LUMO characterize its composition in both complexes. Hence, also for E_3, the hole is delocalized on the entire complex while the electron sits solely on the acceptor. The fact that all transitions contributing to the first three excitations target only the LUMO can be understood considering the energy separation of more than 1.6 eV between the lowest unoccupied level and the next one (see Figure 6.5 in Sec. 6.3). Conversely, occupied states are energetically much closer to each other. In the calculated spectra, two additional maxima are visible at higher energies, around 2.6 eV and 3.4 eV. Both peaks, analyzed in detail in Figure 9.8 in the Appendixes, target higher unoccupied orbitals than the LUMO and correspond to delocalized excitations within the complex.

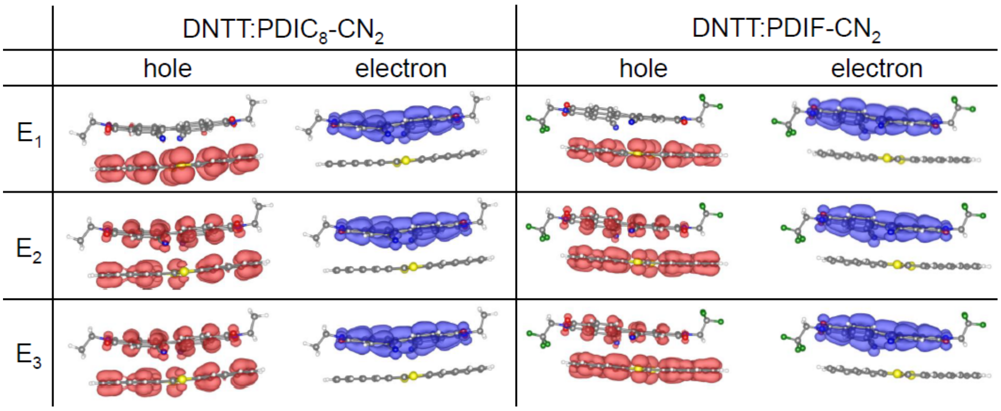

Figure 6.10: *Hole and electron densities calculated for E_1, E_2, and E_3 in the DNTT:PDIC$_8$-CN$_2$ and DNTT:PDIF-CN$_2$ complexes. Isosurfaces plotted with a cutoff of 0.002 Å^{-3}.*

6.6 Anisotropic excited-state CT properties

The anisotropy of the excited-state CT peak is examined for the mixed films of DNTT:PDIC$_8$-CN$_2$ and DNTT:PDIF-CN$_2$ by using ellipsometry data and evaluating the dielectric function of the thin films. The results for the in-plane ϵ_{xy} and the out-of-plane ϵ_z components of the dielectric functions for the different mixed films are shown in Figure 6.11. Here, the in-plane component is parallel, and the out-of-plane component is perpendicular to the substrate plane. For the different molecules used in this thesis, the TDMs are oriented along the longest molecule axis. The spectral shapes of the in- and out-of-plane components of the dielectric functions are similar for both donor-acceptor mixed films however the overall intensities and the low energy region between 1.3 and 2.1 eV are different for these two plane directions. The shape of the in-plane components ϵ_{xy} are comparable with the absorption data (Fig. 6.7 in Sec. 6.4.1). Only in the in-plane spectra of the DNTT:PDIC$_8$-CN$_2$ and DNTT:PDIF-CN$_2$ mixed films, excited-state CT peaks are visible at low energy below the HOMO-LUMO transition of the pure compounds (Fig. 6.11a and 6.11c) which are also observed in the absorption data (Fig. 6.7 in Sec. 6.4.1).

For PDIC$_8$-CN$_2$ and DNTT mixed films, only a weak excited-state CT is shown in the xy-direction with an onset of a maximum at 1.55 eV in Fig. 6.11a. The ES-CT effect is also visible in absorption and emission and is the highest for the equimolar film deposited at room temperature. The in-plane components of the dielectric functions are higher than the out-of-plane components which indicates a stronger tilted co-crystal of DNTT and PDIC$_8$-CN$_2$ molecules.

In Figure 6.11c, a strong excited-state CT peak is detected in the in-plane direction with an onset of a maximum at 1.58 eV for the PDIF-CN$_2$:DNTT mixed thin films. The ES-CT is also observed in the absorption data, the highest for the equimolar films and slightly lower for the mixed films with excess of one pure

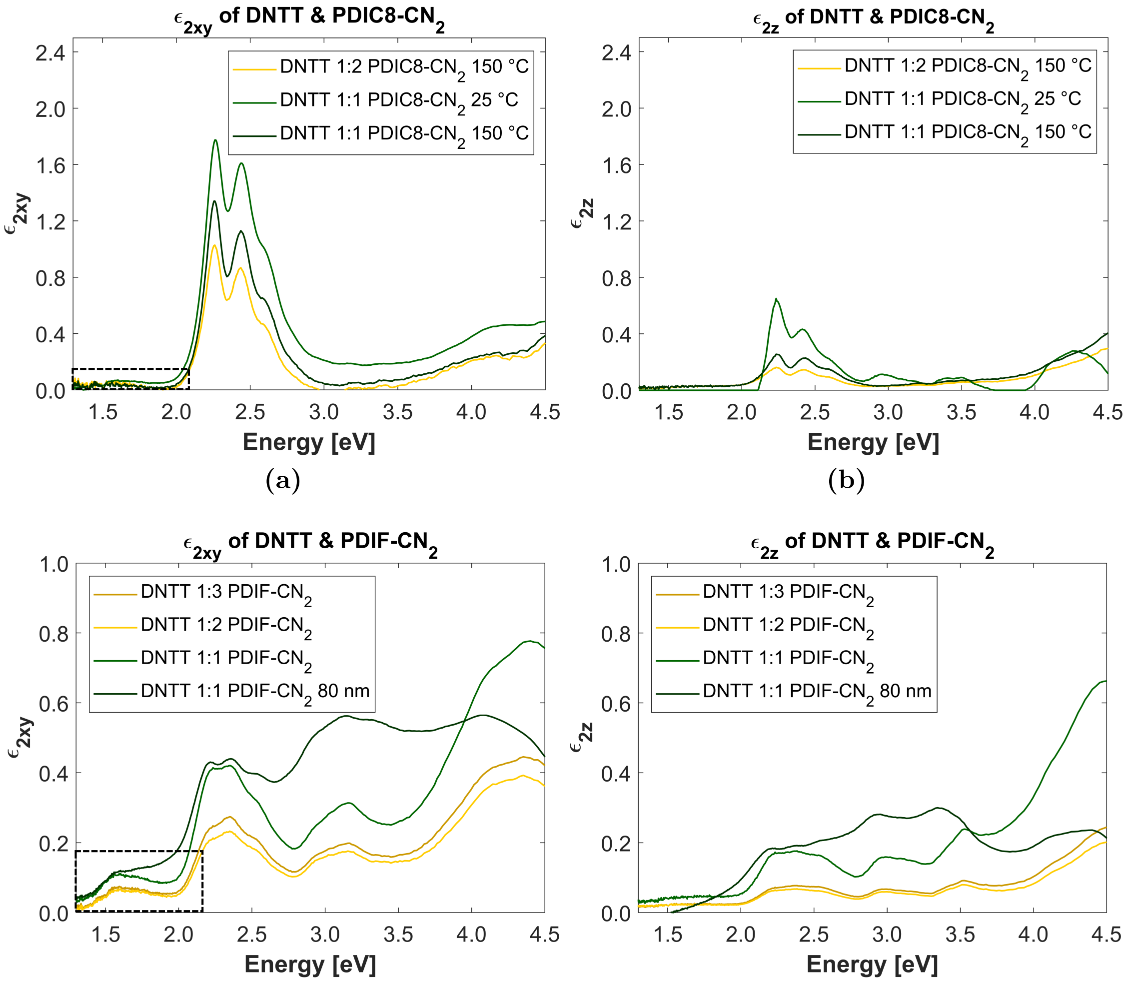

(a) (b)

(c) (d)

Figure 6.11: *Dielectric function determined by ellipsometry of a) the in-plane ϵ_{xy} and b) the out-of-plane ϵ_z components of DNTT and PDIC$_8$-CN$_2$ mixed films deposited at 25 °C and 150 °C, c) the in-plane ϵ_{xy} and d) the out-of-plane ϵ_z components of DNTT and PDIF-CN$_2$ mixed films deposited at 150 °C.*

compound. Here, the in-plane intensities of the dielectric functions for the mixed thin films are only slightly higher than the out-of-plane intensities. This results in a tilted co-crystal of DNTT and PDIF-CN$_2$ molecules.

For both molecule combinations, an anisotropic nature of the excited-state CT peak is obtained. The ES-CT effect is only visible in the in-plane direction of the film, parallel to the substrate plane. In Figure 6.12 the orientation of the ES-CT is illustrated for the tilted molecules with a standing-up conformation and the TDM oriented along the longest axis. The TDM of the CT is observed between the molecules, in the in-plane direction. To summarize, the acceptor PDIF-CN$_2$ and the donor DNTT exhibit a strong ES-CT in the in-plane direction which is

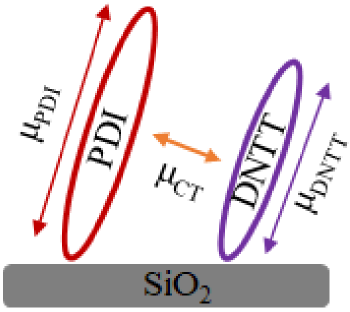

Figure 6.12: *Schematic illustration of the donor (TDM of DNTT marked in violet) and acceptor (TDM of PDI marked in red) π-stacking and the orientation of the TDM (marked in orange) of the excited-state CT.*

increasing with higher substrate temperature. In contrast, $PDIC_8$-CN_2 shows only a weak ES-CT with DNTT in particular for the equimolar film deposited at room temperature.

6.7 Discussion

There are different approaches to categorizing the possible CT scenarios. In a rather common one, molecular charge transfer can be divided roughly into three different cases depending on the degree the molecules interact with each other (Figure 6.13) [41, 42, 49]. Systems of organic small molecules, in which the intermolecular energy gap ΔE_{DA} between the HOMO of the donor and the LUMO of the acceptor is similar to the individual energy gaps of the donor (ΔE_D) or acceptor (ΔE_A) molecule, are assigned to the first category (Figure 6.13a). In this case, charges are only transferred through molecular excitations (D^* or A^* states), and no CT effects in the ground-state are detectable. Weakly bound acceptor and donor molecules belong to the second category. Here, the individual gaps are larger than the intermolecular energy gap ($\Delta E_{DA} < \Delta E_D$ or ΔE_A, Figure 6.13b). This results in weak GS-CT and strong ES-CT effects shown through a peak that can be seen in the absorption or PL spectra. ES-CT either takes place under direct excitation or via exciton dissociation. Molecular orbitals are only slightly shifted compared to the pure compounds. The last category concerns molecular systems which are strongly bound to each other. The intermolecular energy gap is much smaller than the individual ones ($\Delta E_{DA} \ll \Delta E_D$ or ΔE_A, Figure 6.13c). Here, hybridized molecular orbitals are formed with the energy of the CT complex ΔE_{CT}. For these systems, strong GS-CT effects are detectable by IR spectroscopy.

In the two considered systems (DNTT:$PDIC_8$-CN_2 and DNTT:PDIF-CN_2), the donor and the two acceptor molecules are weakly bound. This corresponds to the second scenario illustrated above and leads to a partial charge transfer from

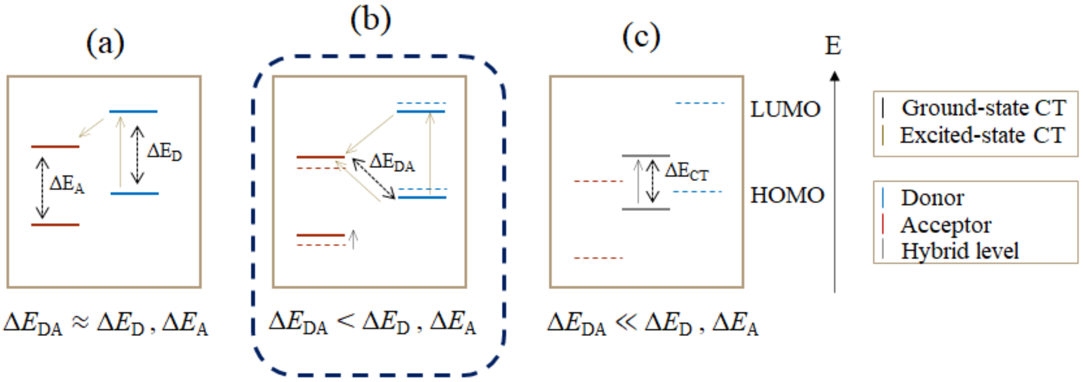

Figure 6.13: *Schematic illustration of possible charge transfer mechanisms for different energy level alignments.*

the donor to the acceptor molecule. This is also supported by experiments and calculations. In the optical spectra of the two investigated mixed co-crystals (Figure 6.9), a strong ES-CT band is shown at lower energy in the absorption ($\sim$ 1.6 eV) and in the emission spectra ($\sim$ 1.4 eV). Additionally, weak partial GS-CT effects are identified through infrared spectroscopy (Figure 6.4), and the amount of partially transferred electron matches with the related calculation.

The interaction between donor and acceptor molecules is affected by molecular packing and structural disorder [209]. Through the design of the acceptor and donor molecules, the positions of the HOMO and LUMO levels can be tuned independently [79]. The physical properties of these compounds are *inter alia* defined by the structure of the resulting donor-acceptor compounds and by the amount of transferred electrons. The required properties, therefore, can be adjusted through the tuned degree of charge transfer [79].

The localized character of HOMO and LUMO leads to CT effects from the donor to the acceptor as illustrated for the two binary systems in this thesis. Similar electronic structure and physical properties are also common for other weakly bound acceptor-donor systems [210–213]. A deeper insight into the underlying mechanism is important to understand the fundamental structure-properties relations [79].

One example for such localized HOMO/LUMO levels and hybridized LUMO+1/HOMO-1 etc. is the co-crystal of the organic small molecules bisdimethylstyrylbenzene : phenylene bis(bis(trifluoromethyl)phenyl)acrylonitrile (4M-DSB:CN-TFPA). The large molecular orbital offset between the designed molecules implies the localized HOMO and LUMO level of the donor-acceptor complex. Through the pronounced localized character of the FMOs, the HOMO-LUMO transition reveals a strong CT character. For this co-crystal also CT effects were investigated [210]. Another example is the system tetracyanoquinodimethane : meso-diphenyltetrathia[22]annulene (TCNQ:DPTTA), in this case, the formed co-crystal shows no CT effects [212]. For the system quarterthiophene : tris(pentafluorophenyl)borane (4T:BCF) only ES-CT effects are detectable clearly related to polaron formation [213, 214]. This implies that different CT properties are observed and that GS-CT and ES-CT can occur independently. There are also other organic small molecule combinations (for example PTCDI-C6:Coronene) which show strong CT effects but with slightly different electronic structure of the energy levels. Here, the LUMO and HOMO-1 levels are localized [97]. There are different physical properties favored through the electronic structure which are important for such binary systems. Localized FMOs are, for example, an important prerequisite for ambipolar CT [210–212]. These systems favor optical or electrical properties such as high conductivity, ambipolar carrier transport, and tuneable luminescence [97].

To classify the systems, DNTT:PDIC$_8$-CN$_2$ and DNTT:PDIF-CN$_2$, in the possible CT cases, they can be compared with strongly bound acceptor and donor molecules showing a small intermolecular energy gap. For a well investigated system such as 4T:F4-TCNQ (2,3,5,6-tetrafluoro-7,7,8,8-tetracyano-quinodimethane), the energy levels of the CT complex and its optical properties were calculated and examined [31, 188, 215, 216]. In contrast to the systems in this thesis, the energy levels of the HOMO LUMO transition are hybridized. 4T:F4-TCNQ shows strong ES-CT effects in absorption and emission and strong GS-CT effects visible by IR spectroscopy. These energy level calculations and optical properties are also common for other strongly bound acceptor-donor systems [217, 218]. In contrast, they are favored for very efficient electrical doping effects [31, 216].

With the adopted theoretical and experimental methods, the systems in this thesis can be classified in the second scenario illustrated above belonging to weakly bound molecules where the respective HOMO and LUMO levels are localized.

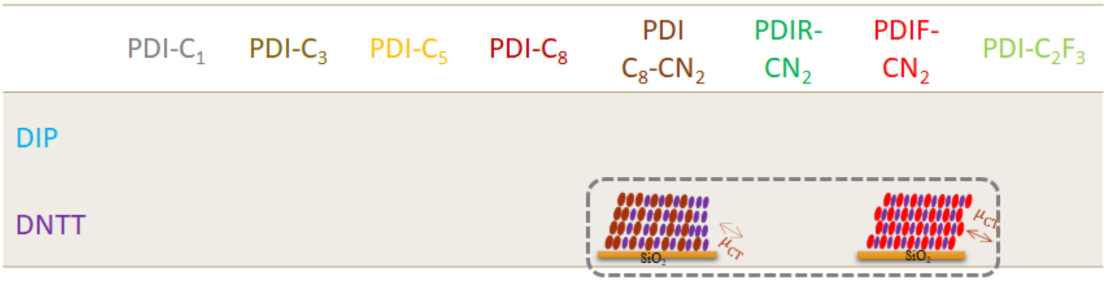

Figure 6.14: *Schematic results for the investigated mixed films of DNTT:PDIC*$_8$*-CN*$_2$ *and DNTT:PDIF-CN*$_2$*. The different schematic scenarios are describing the mixing behavior and the degree of the CT effects. This illustration is part of Fig. 4.9.*

In summary, a comprehensive study on mixing behavior and charge transfer effects of the two donor-acceptor (DNTT:PDI) molecular systems prepared by OMBD has been performed. The two considered acceptor molecules differ in the fluorination of the side chain in the imide position. The results are schematically shown in Figure 6.14 (as part of Fig. 4.9). Here, the respective mixing behavior and degree of CT effects are illustrated. The influence of the side chain variation of the acceptor molecules was investigated by obtaining a favored mixing behavior and stronger ES-CT effects in the in-plane direction for the system DNTT:PDIF-CN_2. CT effects of the mixed thin films increase with raising deposition temperature for the acceptor with fluorinated side chain and decrease for the acceptor with n-alkyl side chain. Both systems show a small ground-state CT governed by hybridized HOMO-1 and LUMO+1 levels, while the frontier orbitals are segregated on the donor and acceptor molecule. The calculated optical spectra show similar visible absorption peaks for both systems in agreement with the experimental results. The aforementioned localization for the frontier orbitals leads to a nearly pure charge transfer exciton in the absorption spectra.

With these results, it is possible to make a comparison with other weakly bound donor-acceptor molecules depending on their optical properties and to classify the two PDI:DNTT systems in different CT scenarios.

Chapter 7

Comparison of growth behavior and molecular charge transfer for the $PDIC_2F_3$:DNTT/DIP thin film systems

In this chapter, the mixing behavior and intermolecular coupling of several donors and a synthesized acceptor molecule in binary organic bulk heterojunction thin films prepared by organic molecular beam deposition are examined based on Ref. [219]. The focus lies on weakly interacting organic semiconductive mixtures with DIP and DNTT as donor molecules and the synthesized PDI derivative $PDIC_2F_3$, with a short fluorinated side chain in the imide position, as acceptor (Fig. 7.1).

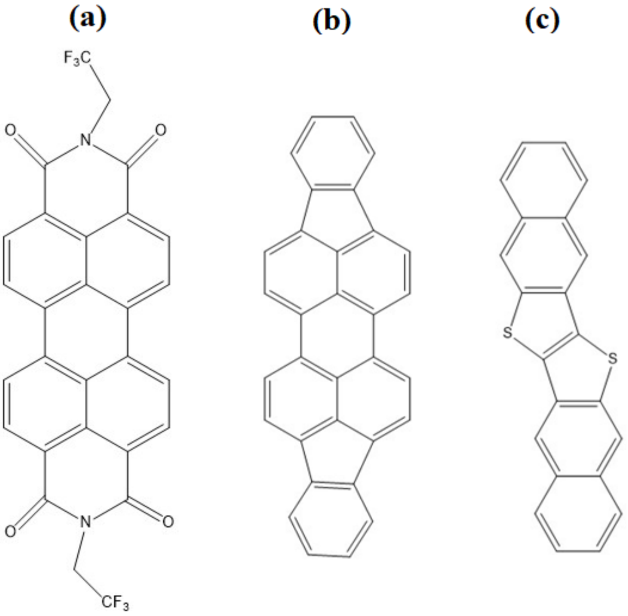

Figure 7.1: *Sketch of the synthesized PDI derivative a) $PDIC_2F_3$ and the two donor molecules b) DIP and c) DNTT.*

For organic optoelectronics, the interactions between donor and acceptor molecules and the related CT effects are very important [41, 42]. A great impact on charge transfer effects is given by the morphology and intermixing on the molecular level in bulk heterojunction thin films [25, 30]. Therefore, the influences of two different donor molecules with the fluorinated PDI derivative on structural morphology and CT effects in thin films are determined. At first, the growth behavior and molecular packing of pure thin films from the synthesized PDIC$_2$F$_3$ molecule are investigated by GIWAXS, XRR, and AFM. The comprehensive structural characterization of thin films with this acceptor molecule is not described in the literature and was performed for the first time in this work. Additionally, the optical properties of the pure thin films are examined by absorption and emission spectroscopy. The co-crystal formation and structural morphology of the mixed thin films with their respective donors are investigated by X-ray scattering. The excited-state CT effects are investigated by different optical methods such as absorption and PL spectroscopy.

7.1 Growth behavior and optical properties of pure PDIC$_2$F$_3$ thin films

7.1.1 Characterization of the synthesized powder PDIC$_2$F$_3$

To investigate the influences of different PDI derivatives with suitable donor molecules on mixing behavior and CT, a PDI derivative was synthesized with appropriate side chains in the imide positions. To compare this material with the other PDI derivatives examined in this thesis, short fluorinated side chains in the imide position of this acceptor molecule were chosen. The synthesis of the PDIC$_2$F$_3$ powder, also known as N,N'-bis(2,2,2-Trisfluoroethyl)-perylene-3,4:9,10-bis(dicarboxyimide), is described in Section 3.1.3. With the synthesized powder, thin films were grown under various conditions and with different donor molecules. The growth and optical properties of the pure and mixed thin films will be investigated in the following chapter. First, the PDIC$_2$F$_3$ powder is characterized by mass spectrometry (MS) to identify the material. Furthermore, an absorption spectrum of the powder in solution as well as a powder PL spectrum was examined.

In Figure 7.2 the mass spectrum of the purified PDIC$_2$F$_3$ powder is shown. Here, the relative intensity is a function of the mass-to-charge ratio. The investigated material as well as possible side products can be identified with this analytic technique. The powder of the examined material is sublimed, electrically ionized by impact ionization, and the ions or fragments are then separated according to their mass-to-charge ratio [53, 220]. The purified PDIC$_2$F$_3$ powder was measured with a mass spectrometer MAT 95, Finnigan by the MS department of the organic chemistry at the University of Tuebingen. The main peak reveals a mass-to-charge ratio of 554 g mol^{-1}. This is in agreement with the molecular weight of PDIC$_2$F$_3$ (554 g mol^{-1}) and the molecular formula of $C_{28}H_{12}N_2O_4F_6$. Because of carbon isotopes, fragments or ions with m carbon atoms show added to the main peak

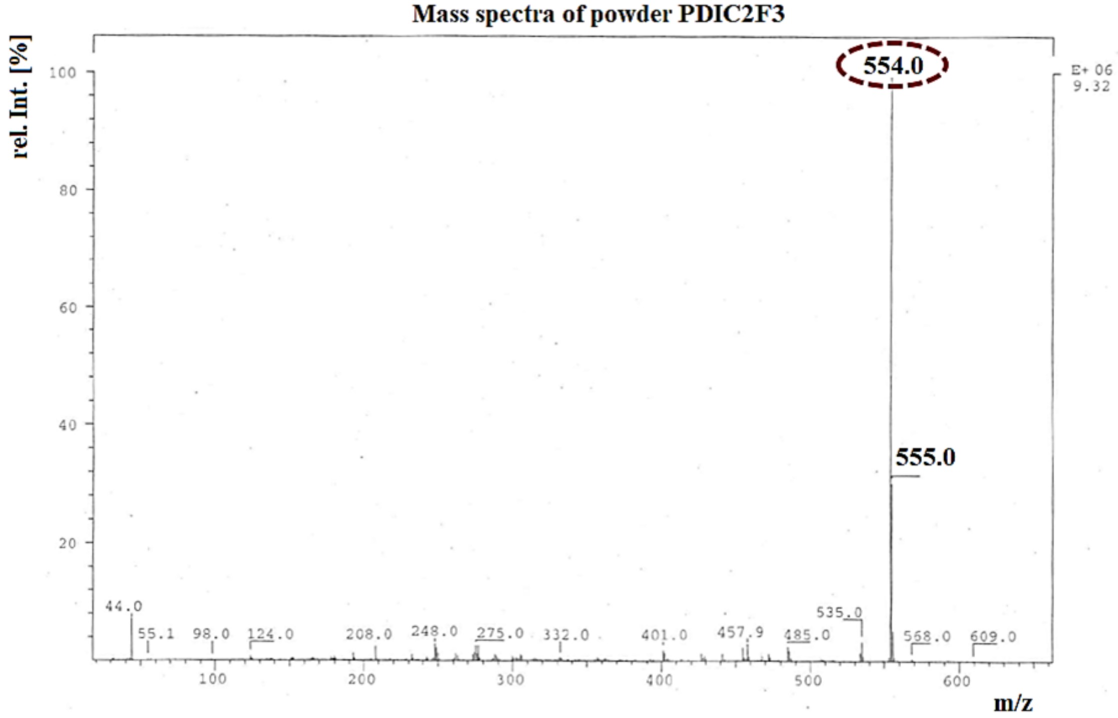

Figure 7.2: *Measured mass spectrum of the purified powder PDIC$_2$F$_3$ by gradient sublimation.*

(C^{12}-peak) also an (m+1) peak whose intensity is the number of carbon atoms (m) x 1.1 %, related to the C^{12}-peak [220]. In this spectrum, a peak with the mass-to-charge ratio of 555 g mol^{-1} and the intensity of 30.8 % is shown which also agrees with the amount of carbon atoms in the molecular formula and the weight of PDIC$_2$F$_3$. There are only minor other residuals so this powder was used as starting material for the thin film preparation.

Figure 7.3 shows a microscope image of the powder with a 50-times magnification, the absorption in solution, and the powder PL spectrum. In the microscope image, needlelike grains are visible. The absorption spectrum of the PDIC$_2$F$_3$ solution and the PL spectrum are similar to the absorption and emission spectra of other PDI derivatives with fluorinated side chains [117]. In Section 7.1.3 the absorption spectrum of the solution is compared to the thin film optical properties of PDIC$_2$F$_3$.

7.1.2 Structural investigations of pure PDIC$_2$F$_3$ thin films

At first, the growth behavior and structural morphology of pure PDIC$_2$F$_3$ thin films are examined by X-ray scattering and AFM, before the mixing and growth behavior of the mixed films with the donors DIP and DNTT are investigated.

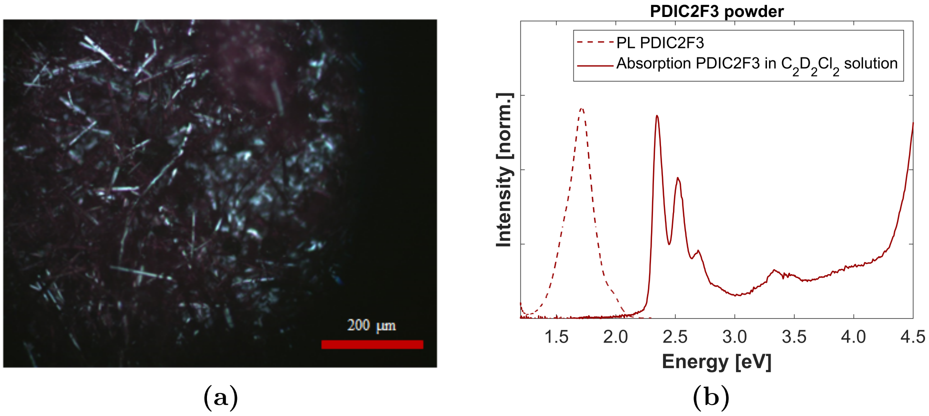

Figure 7.3: *Powder characterization of* $PDIC_2F_3$*: a) microscope image with a 50-times magnification and b) absorption spectrum in* $C_2D_2Cl_2$ *solution and PL spectrum.*

X-ray scattering of pure $PDIC_2F_3$ thin films

Figure 7.4 shows the diffraction patterns of the pure $PDIC_2F_3$ thin films grown at different deposition temperatures. Here, the thin pure films are grown at various substrate temperatures, and the different structural morphologies depending on the temperature are presented. Parameters of two unit cells can be calculated for the pure $PDIC_2F_3$ films grown at lower deposition temperatures (LT-phase, T_{sub} between 25 °C and 150 °C) and at higher temperature (HT-phase, $T_{sub} = 165\,°C$), shown in Table 7.1. The orientation of the acceptor molecules changes from a lying-down to a more standing-up conformation. For the pure films deposited at substrate temperatures of up to 150 °C, a unit cell is tilted with respect to the surface normal, so that the molecules with the short fluorinated side chains are lying on the Silicon substrate. For a higher growth temperature, a unit cell has its longest axis c perpendicular to the substrate plane. Additionally, the crystallinity of the films is increased with the substrate temperature which is evident from the change of the Debye-Scherrer rings into sharper Bragg peaks. This is also common for other fluorinated PDI derivatives where a higher deposition temperature is needed to form a smooth crystalline thin film [117].

In the GIWAXS data of the pure film deposited at 100 °C (Fig. 7.4b) the Bragg peaks of the calculated unit cell are marked by black crosses. The crystallinity of this crystal structure for the thin films increases with higher substrate temperature, visible when comparing the GIWAXS pattern of the thin films grown at 25 °C and 100 °C. The $PDIC_2F_3$ film deposited at 150 °C presents blurry Bragg peaks of the lying-down and standing-up conformations. The latter orientation is dominant in the thin film grown at 165 °C (Fig. 7.4d). The Bragg peaks, corresponding to the standing-up conformation, are marked with red crosses. Additionally, also peaks from the lying-down conformation are shown in this GIWAXS pattern, la-

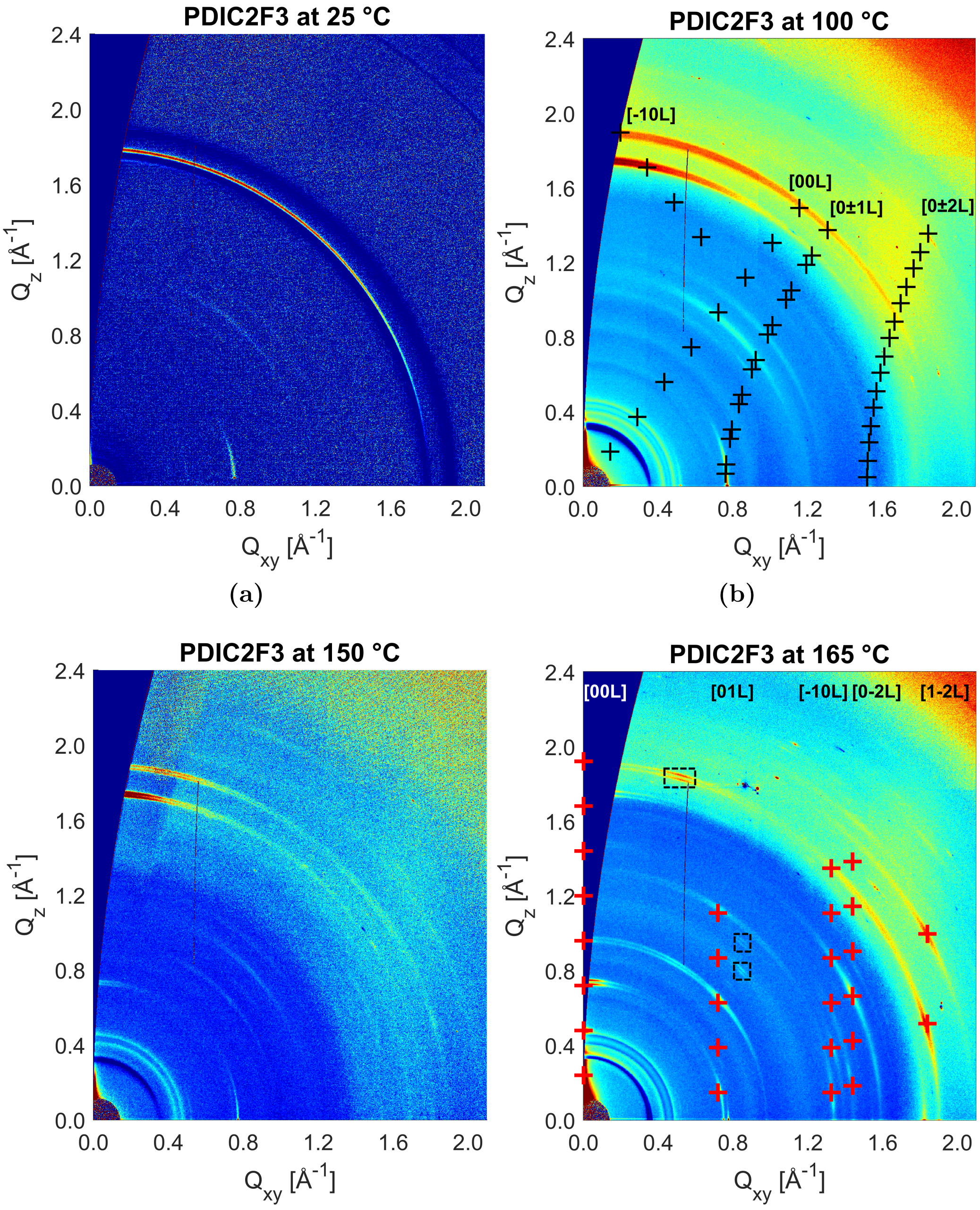
PDIC2F3 at 25 °C

PDIC2F3 at 100 °C

PDIC2F3 at 150 °C

PDIC2F3 at 165 °C

(a) (b)

(c) (d)

Figure 7.4: *GIWAXS data of PDIC$_2$F$_3$ deposited at a) 25 °C, b) 100 °C, c) 150 °C and d) 165 °C (with calculated Bragg peak positions, black and red crosses correspond to the unit cells of PDIC$_2$F$_3$ listed in Table 7.1).*

beled with black rectangles. Comparing the thin films deposited at 150 °C and 165 °C, a crystalline thin film is formed and the standing-up conformation of the

$PDIC_2F_3$ molecules is established at a substrate temperature of 165 °C.

Table 7.1: *Calculated unit cell parameters of* $PDIC_2F_3$ *thin films (with* a *and* b *parallel to the substrate surface (for* $\delta = 0$*) and the angle* δ *between the normal of the surface and the unit cell).*

	a [Å]	b [Å]	c [Å]	α [°]	β [°]	γ [°]	δ [°]	V [Å^3]
$PDIC_2F_3$ LT-phase	4.77	8.27	26.8	83.54	91.5	88.7	37.8	1049.78
$PDIC_2F_3$ HT-phase	4.77	8.79	26.5	83.45	84.5	96.7	~0	1089.58

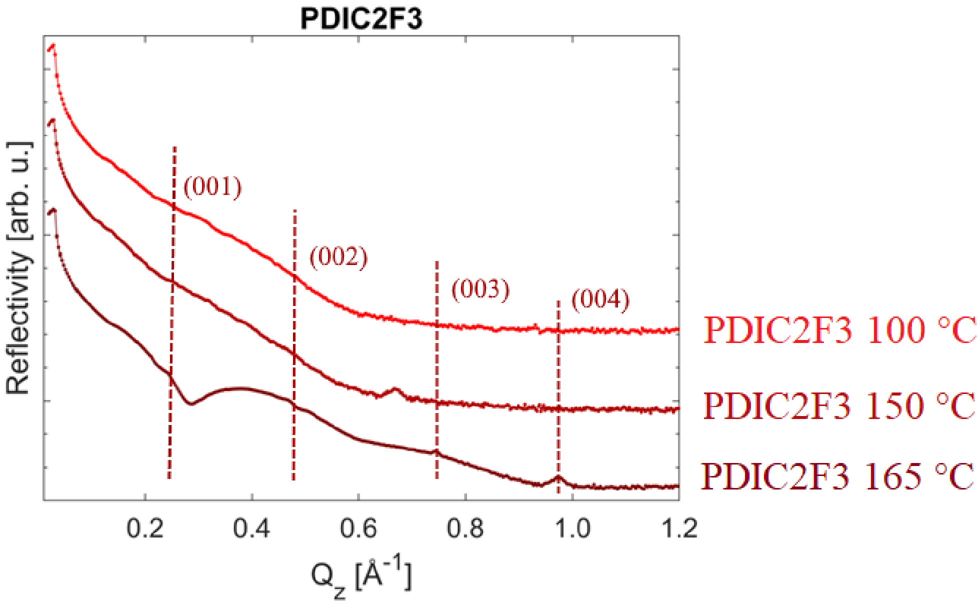

Figure 7.5: *XRR data of* $PDIC_2F_3$ *thin films deposited at* 100 °*C*, 150 °*C, and* 165 °*C.*

In Figure 7.5 the XRR data of the pure $PDIC_2F_3$ thin films deposited at various substrate temperatures are shown. In these spectra, several Bragg reflections for the film grown at higher substrate temperature are shown. As in the GIWAXS pattern, only the film deposited at 165 °C shows Bragg peaks belonging to the standing-up conformation. The first Bragg reflections are suppressed due to the electron density of the fluorinated side chains and only the fourth Bragg peak is the most intense one. For the other films grown at substrate temperatures below 165 °C, the molecules are mostly oriented in a lying-down conformation, observed by the GIWAXS patterns, where the Bragg reflections in Q_z direction are at much higher values. Only for the film grown at a substrate temperature of 150 °C and unlike the GIWAXS pattern (Fig. 7.4c), there is a peak at $Q_z = 0.66$ Å^{-1} which is assumed to be either from another polymorph or from a contamination. All thin films seem to be rough which leads to the absence of the Kiessig oscillations.

Thin films of pure PDIF-CN_2, a PDI derivative with a longer fluorinated side chain in the imide position which is also used in this thesis, show similar growth behavior (Figures 6.3b and 6.2d in the results Chapter 6) [117]. A higher deposition temperature is needed to grow crystalline thin films of PDIF-CN$_2$, where the molecules are oriented in a standing-up conformation. In the XRR spectra (Figure 6.3b in the results Chapter 6), also the first two Bragg peaks are suppressed and the third one is the most intense.

Morphology study by AFM of pure PDIC$_2$F$_3$ thin films

Moreover, the morphology of the pure PDIC$_2$F$_3$ films deposited at various substrate temperatures is investigated in more detail. The AFM images of the pure thin films are provided in Figure 7.6. The morphology is different for the film deposited at room temperature and the films grown at higher substrate temperatures.

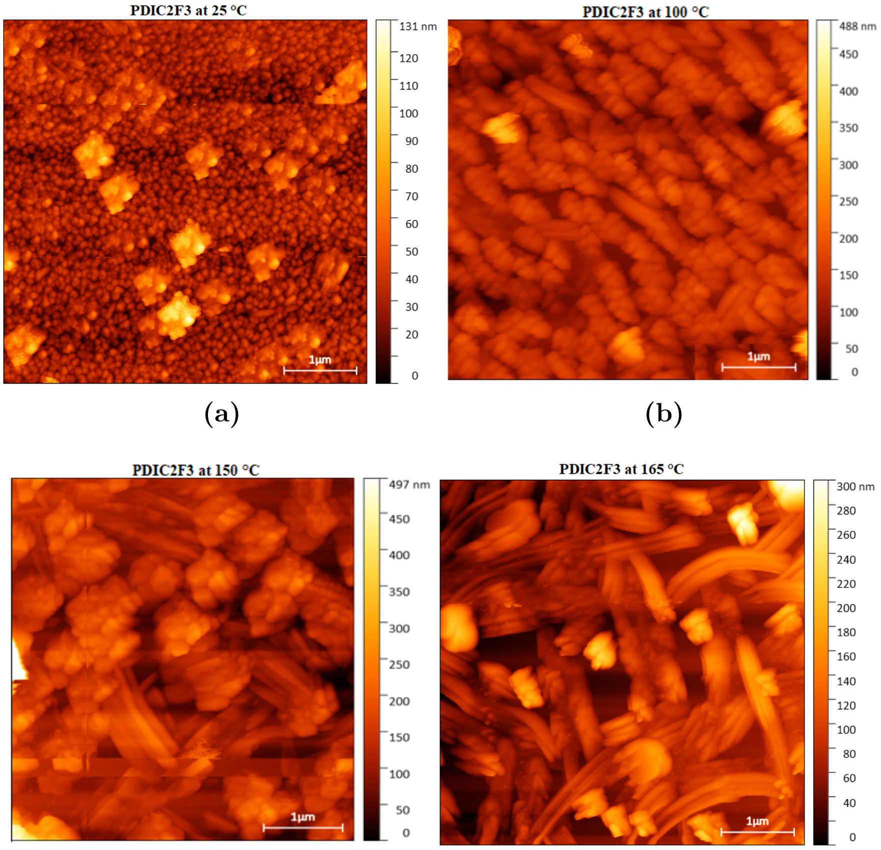

(a) (b)

(c) (d)

Figure 7.6: *AFM images (5 x 5 µm) of PDIC$_2$F$_3$ deposited at a) 25°C, b) 100°C, c) 150°C and d) 165°C (Length of the scale bar is 1 µm and artifacts in the images are visible due to measurement difficulties of the rough thin films).*

The film grown at 25 °C shows a homogenous surface that consists of small grains and a high islands density (Fig. 7.6a). With a substrate temperature of

100 °C, the molecules form larger grains and the overall islands density gets lower (Fig. 7.6b). A visible change in the morphology is shown for the thin film grown at 150 °C. A mixture of elongated islands and grains is formed and a change to an anisotropic 2D growth is established (Fig. 7.6c). The elongated islands consist probably of molecules with a standing-up conformation whereas the grains comprise lying-down molecules. However, only a needlelike texture with elongated islands appears for the thin film deposited at 165 °C substrate temperature (Fig. 7.6d). This indicates a temperature-dependent structural and morphology change, from small grains to a needlelike texture which is also in agreement with the X-ray scattering data. The roughness of the pure $PDIC_2F_3$ films changes with the growth regime and is thus also temperature-dependent. A low roughness can be observed for the film grown at room temperature which can be explained by the low crystallinity of this film. With increasing temperature, the roughness increased ($T_{sub} = 100\,°C$) and is smoother at higher substrate temperatures due to the formation of flatter domains.

To summarize, the growth behavior and morphology of $PDIC_2F_3$ on SiO_2 substrates are temperature-dependent. The orientation varies from a lying-down to a standing-up conformation and the crystallinity increases with the substrate temperature. The surface morphology of the pure thin films modifies from small grains at low to a needlelike texture at high substrate temperature.

7.1.3 Optical properties of pure $PDIC_2F_3$ thin films

Before describing the CT effects of the mixed films with both donor molecules, the optical properties of the pure $PDIC_2F_3$ thin films are examined by absorption and emission spectroscopy.

Figure 7.7 shows the absorption spectra of $PDIC_2F_3$ thin films grown at various temperatures in comparison with the spectrum in solution. The spectral shape of the absorption of the $PDIC_2F_3$ thin films deviates only slightly from the solution spectrum. Two peaks at about 2.2 eV and 2.4 eV with a shoulder at 2.6 eV are common for PDI derivatives especially for the absorption spectra of PDIF-CN_2 thin films [117]. In the absorption spectra of the pristine films grown at higher deposition temperatures, a peak, instead of a shoulder, is visible at 2.6 eV which is possible due to a more ordered structure at higher growth temperatures. Due to the solvatochromic effect, the three peaks in the solution spectrum are blue-shifted by 0.15 eV compared to the thin film absorption spectra. The shift is common for absorption spectra of organic molecules in thin films [61, 221]. The relative intensities of the peaks are changing slightly for the thin films grown at different temperatures with the most pronounced changes for the film deposited at room temperature. This implies an orientational change depending on the growth temperature which was also shown by the structural characterization.

Figure 7.8 shows the temperature-dependent emission spectra of the $PDIC_2F_3$ film deposited at 165 °C substrate temperature (from 250 K to 15 K measurement temperature). The temperature-dependent PL data of the other pristine $PDIC_2F_3$

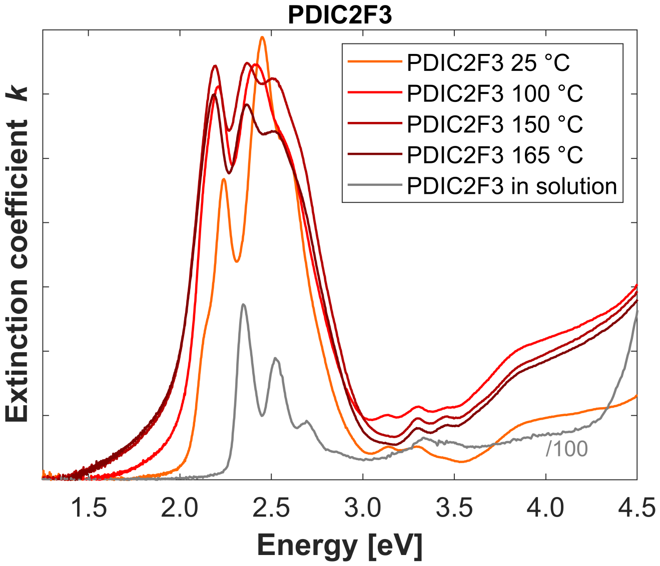

Figure 7.7: *Absorption spectra of $PDIC_2F_3$ thin films on a glass substrate, deposited at different temperatures, and in solution ($C_2D_2Cl_2$).*

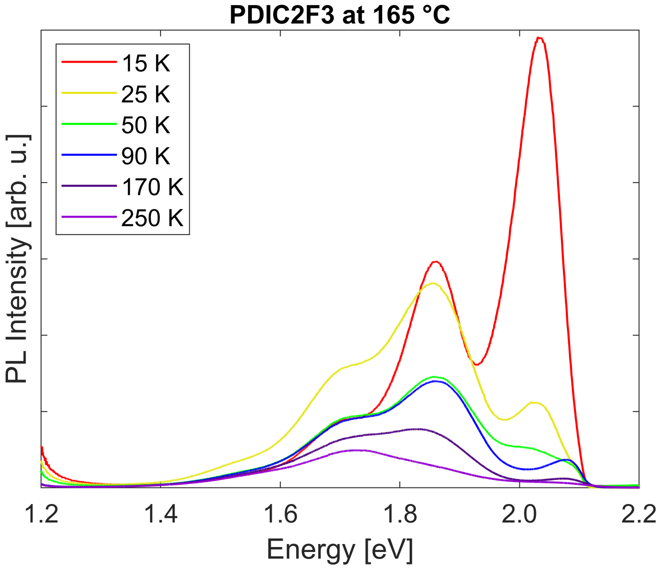

Figure 7.8: *Temperature-dependent photoluminescence spectra of $PDIC_2F_3$ thin films deposited at 165 °C. Measurements were performed in the range from 250 K to 15 K.*

films are shown in Fig. 9.10 in the Appendixes. Common for temperature-dependent emission data, the overall photoluminescence intensities of the pristine $PDIC_2F_3$ film are increasing with lower measurement temperatures due to suppression of non-radiative relaxations. At low measurement temperatures, possible relaxation paths are minimized leading to sharper and distinct peaks [161]. At 15 K, three distinct peaks are detectable that are very similar in shape and have an

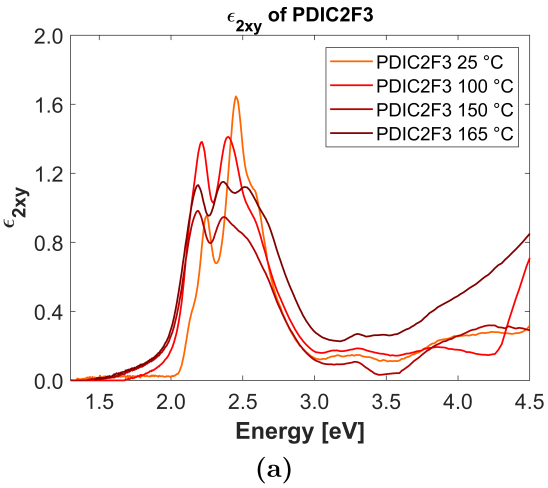

Figure 7.9: *Dielectric function determined by ellipsometry of a) the in-plane ϵ_{xy} and b) the out-of-plane ϵ_z components of PDIC$_2$F$_3$ thin films deposited at 25 °C, 100 °C, 150 °C, and 165 °C. For the calculation of the dielectric function, different EMA layers were taken into account in the models for the films grown on Silicon and glass substrates.*

equidistant energy spacing of 0.17 eV which suggests that the peaks belong to a vibronic progression [88].

Figure 7.9 shows the results for the in-plane ϵ_{xy} and the out-of-plane ϵ_z components of the dielectric functions for the different pristine PDIC$_2$F$_3$ films grown at various temperatures. Here, the in-plane component is parallel to the substrate plane, and the out-of-plane component is perpendicular to it. Similar to the other PDI derivatives, the TDM is oriented along the longest molecular axis [117]. The spectral shapes of the in-plane components ϵ_{xy} are comparable with the absorption data with some deviations (Fig. 7.7). The spectral shape of the in- and out-of-plane components of the dielectric functions are similar, however, the overall intensities are different for these two directions. The intensities of the in-plane components of the dielectric functions are moderately higher than the out-of-plane components. The differences between the two components are higher for the films deposited at 25 °C and 100 °C, which is possible to a more tilted conformation, a more lying-down conformation compared to the molecule orientation in the other pure films grown at higher temperatures. This indicates slightly tilted PDIC$_2$F$_3$ molecules instead of a complete standing-up orientation for the thin films deposited at high growth temperatures.

7.2 Growth behavior and CT effects of $PDIC_2F_3$:DIP/DNTT mixed films

7.2.1 Structural characterization

Prior to CT examination, the structure and mixing behavior of the mixed films with the acceptor $PDIC_2F_3$ and the two donors DIP and DNTT are investigated. The mixed thin films are examined by X-ray scattering (XRR and GIWAXS) and AFM.

X-ray scattering

Figure 7.10 shows the reciprocal space maps of the equimolar $PDIC_2F_3$:DIP and $PDIC_2F_3$:DNTT mixed films and the respective pure materials (DIP, $PDIC_2F_3$, and DNTT). Both donor molecules fit with their molecule sizes to the perylene diimide core and form crystalline thin films with Bragg reflections belonging to known crystal structures (Fig. 7.10b and 7.10e). The molecules are both oriented with their longest axis almost normal to the substrate surface. For completion, the GIWAXS pattern (Fig. 7.10c) of the pure acceptor $PDIC_2F_3$ film deposited at 165 °C is also shown. The molecules form a crystalline thin film at this growth temperature with the crystal structure calculated in Table 7.1 in Sec. 7.1.2. As shown before, the alkyl, branched, and fluorinated side chains in the imide position of the PDI acceptor molecules can alter molecular packing and morphology of the deposited thin films [19, 20, 23]. The different morphology and growth behavior also influence the co-crystal formation and the mixing and growth behavior with different donor materials. Based on this, the structure of the mixed $PDIC_2F_3$:DIP and $PDIC_2F_3$:DNTT thin films will be discussed depending on the different donors. The equimolar mixed films are investigated at the optimized substrate temperatures for the respective system ($T_{sub} = 150\,°\mathrm{C}$ for $PDIC_2F_3$:DIP and $T_{sub} = 100\,°\mathrm{C}$ for $PDIC_2F_3$:DNTT).

$PDIC_2F_3$ forms with the donor DIP a co-crystal with Bragg reflections at $Q_{xy} = 1.88$ Å^{-1} marked with yellow squares in the reciprocal space map (Fig. 7.10a). Here, also signals from the pure compounds, especially from the acceptor, are visible. The expected Bragg peaks of the two pristine materials are also featured in this image. The equimolar mixed film grown at 150 °C shows a crystalline structure and well ordering in the xy-direction observed by precisely aligned Bragg peaks.

In contrast, $PDIC_2F_3$ does not form a co-crystal with the donor DNTT, instead, the molecules tend to phase-separate. In the GIWAXS data (Fig. 7.10d), only Bragg reflections from both pure materials, especially from $PDIC_2F_3$, are detectable. Here, also the different expected Bragg peaks of the two pristine materials are visible. The Bragg peaks are slightly blurred out, indicating a less ordered crystallinity in the equimolar mixed film. For more structural details, the X-ray reflectivity data of the different mixed thin films have to be examined.

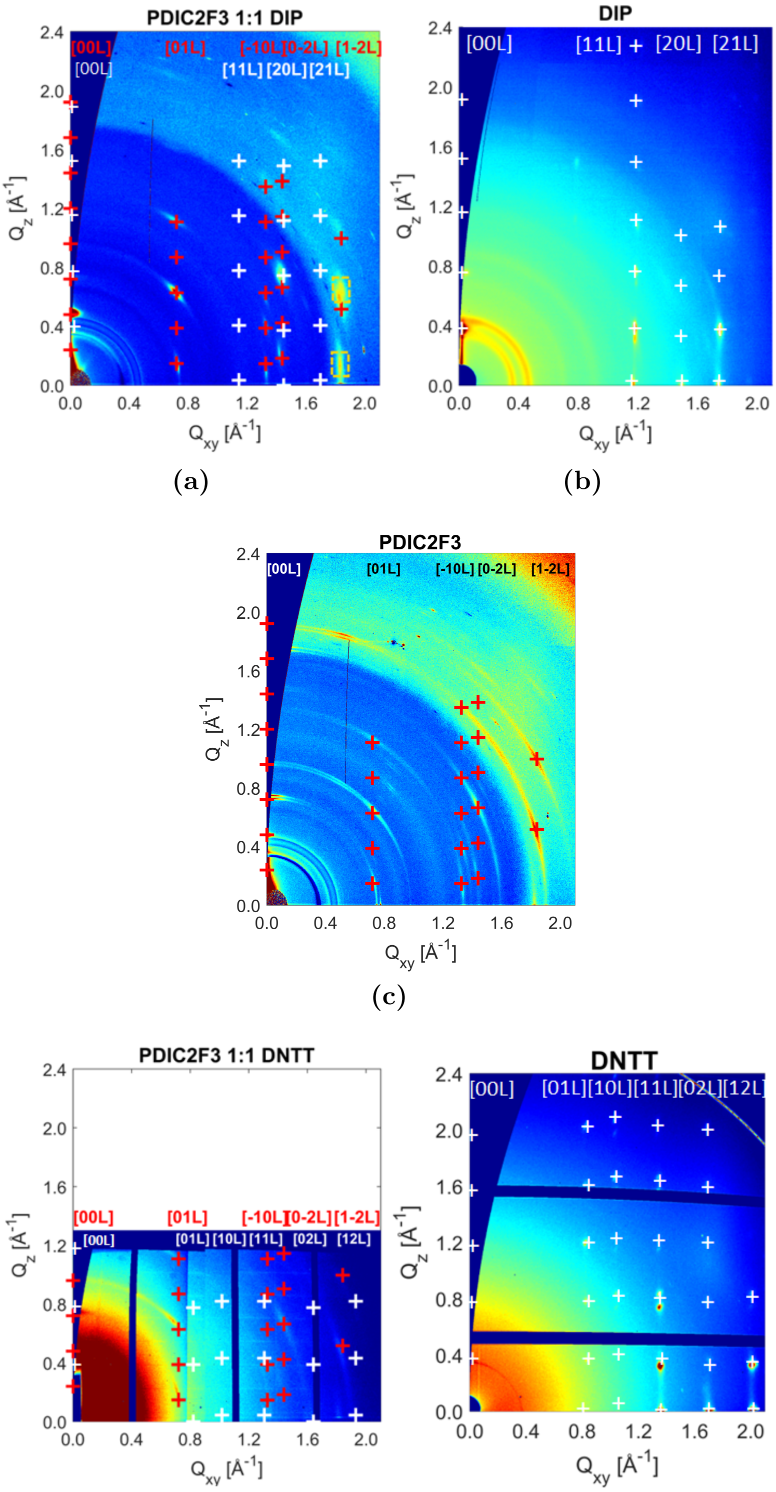

(a) (b) (c) (d) (e)

Figure 7.10: *GIWAXS data: a) PDIC$_2$F$_3$ 1:1 DIP (T_{sub} = 150 °C), b) DIP (T_{sub} = 150 °C), c) PDIC$_2$F$_3$ (T_{sub} = 165 °C), d) PDIC$_2$F$_3$ 1:1 DNTT (T_{sub} = 100 °C) and e) DNTT (T_{sub} = 100 °C) (white crosses indicate peaks of the donor, red crosses of the acceptor, and yellow squares for the mixed phase).*

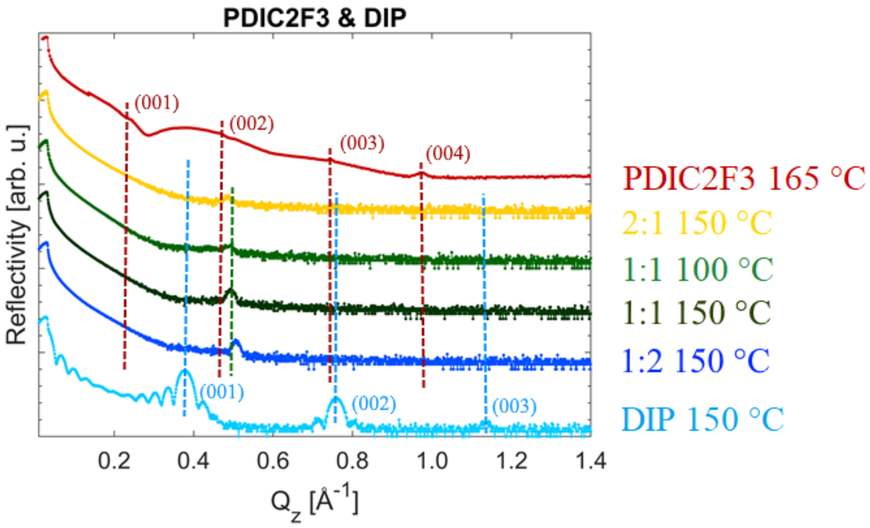

(a)

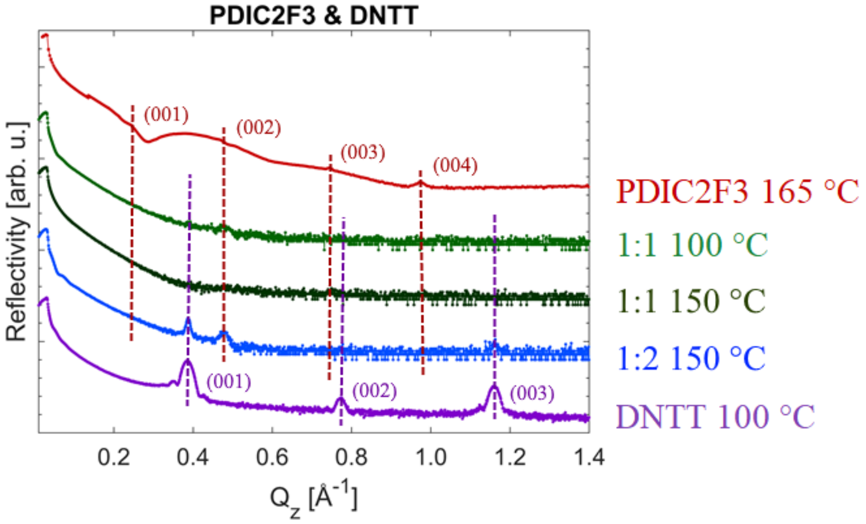

(b)

Figure 7.11: *XRR data of mixed films deposited at 100 °C and 150 °C: a) PDIC$_2$F$_3$ and DIP and b) PDIC$_2$F$_3$ and DNTT (violet and blue dashed lines indicate peaks of the respective donor, red of the acceptor, and green for the mixed phase with the respective Miller indices of the Bragg peaks, all spectra are vertically offset for better clarity).*

Figure 7.11 shows the XRR data of both PDIC$_2$F$_3$:DIP and PDIC$_2$F$_3$:DNTT thin film binary systems. In both data sets, the XRR curves of the pristine materials are also depicted for comparison with the mixed films. The out-of-plane Bragg reflections of the three pristine compounds indicate, as mentioned for the GIWAXS patterns, crystalline formed thin films.

One Bragg peak of the co-crystal is at $Q_z = 0.49$ Å^{-1} for all PDIC$_2$F$_3$:DIP mixed films in the XRR spectra (Fig. 7.11a). The Bragg peak is the most intense for the equimolar film deposited at $T_{sub} = 150\,°\mathrm{C}$ which indicates that with increasing substrate temperature the crystallinity of the equimolar mixed films increases. The Bragg peak of the formed co-crystal is the weakest for the mixed film with excess of the acceptor. However, with excess of the donor DIP, the co-crystal formation is favored. All films except the pristine DIP film show no Kiessig oscillations which suggests rough mixed thin films.

In the XRR spectra of the PDIC$_2$F$_3$:DNTT mixed films, only Bragg reflections from both pure materials are detectable (Fig. 7.11b). For the 1:2 mixed film with excess of the donor DNTT, Bragg peaks of pure PDIC$_2$F$_3$ and DNTT are visible. This indicates that a phase-separation into the pure compounds PDIC$_2$F$_3$ and DNTT occurs. These different films also show no Kiessig oscillations assuming rough mixed thin films.

The results obtained by the XRR data are consistent with the GIWAXS data. When comparing the mixing behavior of PDIC$_2$F$_3$ with both donors, DIP which has a similar structure to the perylene diimide core favors the mixing and forms a well-defined co-crystal with long-range ordering with PDIC$_2$F$_3$. The morphology of the equimolar mixed films will be investigated in more detail by means of AFM measurements.

Morphology study by AFM

Figure 7.12 shows the AFM images of the mixed DIP:PDIC$_2$F$_3$ and DNTT: PDIC$_2$F$_3$ thin films to investigate the surface morphology of the equimolar mixed films. The morphology of the three pristine films has to be considered to compare the surface structure with the equimolar mixed films (Fig.7.12a-7.12c).

The two donor molecules, DIP and DNTT, are establishing wedding-cake structures visible through the density of islands and plateaus on top of each other. However, DNTT forms no closed wetting layer due to the depressions visible in the AFM image which is an indication of de-wetting and also common for this material [135]. The surface morphology of pure PDIC$_2$F$_3$ thin films grown at higher deposition temperature has already been discussed in Sec. 7.1.2. DIP forms crystalline smooth films, while DNTT and PDIC$_2$F$_3$ establish also crystalline, but rougher films. The root mean square roughness values of the pristine compounds and the equimolar mixed films are given in Table 7.2.

Table 7.2: *Roughness values σ_{RMS} of pristine DNTT, DIP, PDIC$_2$F$_3$, and the respective equimolar mixed films (determined by AFM).*

	DIP	DNTT	PDIC$_2$F$_3$	DIP:PDIC$_2$F$_3$	DNTT:PDIC$_2$F$_3$
σ_{RMS} [nm]	2.8 ± 0.2	8.4 ± 1.0	27.3 ± 2.3	12.6 ± 1.7	17.6 ± 0.7

The surface structure of the equimolar mixed PDIC$_2$F$_3$:DIP thin film is shown

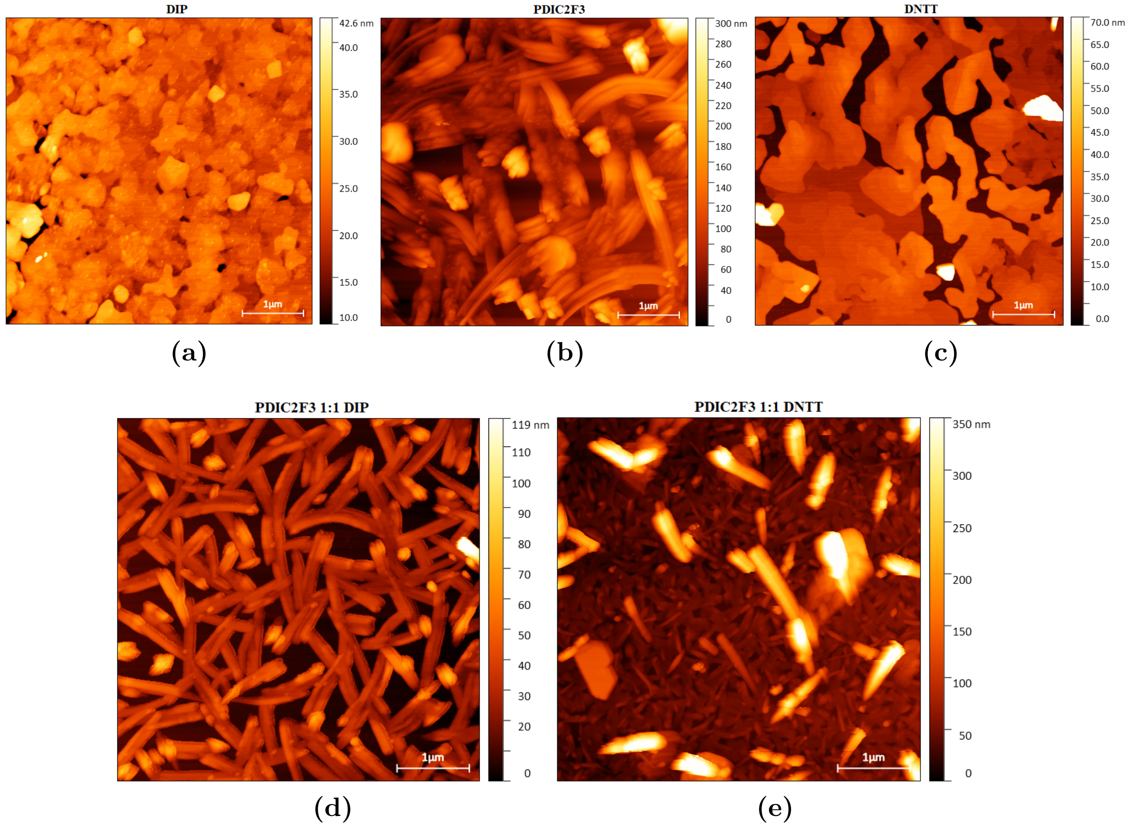

(a) **(b)** **(c)**

(d) **(e)**

Figure 7.12: *AFM images (5 x 5 μm) of pure and mixed films: a) DIP (T_{sub} = 150 °C), b) PDIC$_2$F$_3$ (T_{sub} = 165 °C), c) DNTT (T_{sub} = 100 °C), d) PDIC$_2$F$_3$ 1:1 DIP (T_{sub} = 150 °C) and e) PDIC$_2$F$_3$ 1:1 DNTT (T_{sub} = 100 °C) (Length of the scale bar is 1 μm).*

in Fig. 7.12d. Here, needlelike features with a length of 0.7 - 1 μm are visible. The structure differs from both pristine materials and the thin film seems to be very homogenous which indicates the formation of a co-crystal between PDIC$_2$F$_3$ and DIP. This is also in agreement with the X-ray scattering data. The thin film is smoother than the pristine PDIC$_2$F$_3$ film. A preferred 1D growth of the needles possibly occurs in the direction of the donor/ acceptor $\pi - \pi$- stacking [222].

In contrast, the equimolar mixed film of PDIC$_2$F$_3$ and DNTT reveals a different surface morphology (Fig. 7.12e). Smaller and elongated islands with sizes between 0.3 - 1 μm and islands on top are shown. This film seems to be rougher than the equimolar mixed film with DIP. This structure possibly suggests phase-separated DNTT and PDIC$_2$F$_3$. The surface morphology together with the X-ray scattering data indicates different mixing and growth behavior for the two PDIC$_2$F$_3$ systems which reveals the formation of a co-crystal for the mixed films with DIP and phase-separation into the pure materials for the mixed films with DNTT.

7.2.2 Excited CT properties

The optical properties and the CT effects of the mixed thin films with $PDIC_2F_3$ and the two donors DIP and DNTT are investigated. The influences of the different donor molecules on excited-state CT effects in thin films are examined by absorption and emission spectroscopy.

Absorption spectroscopy

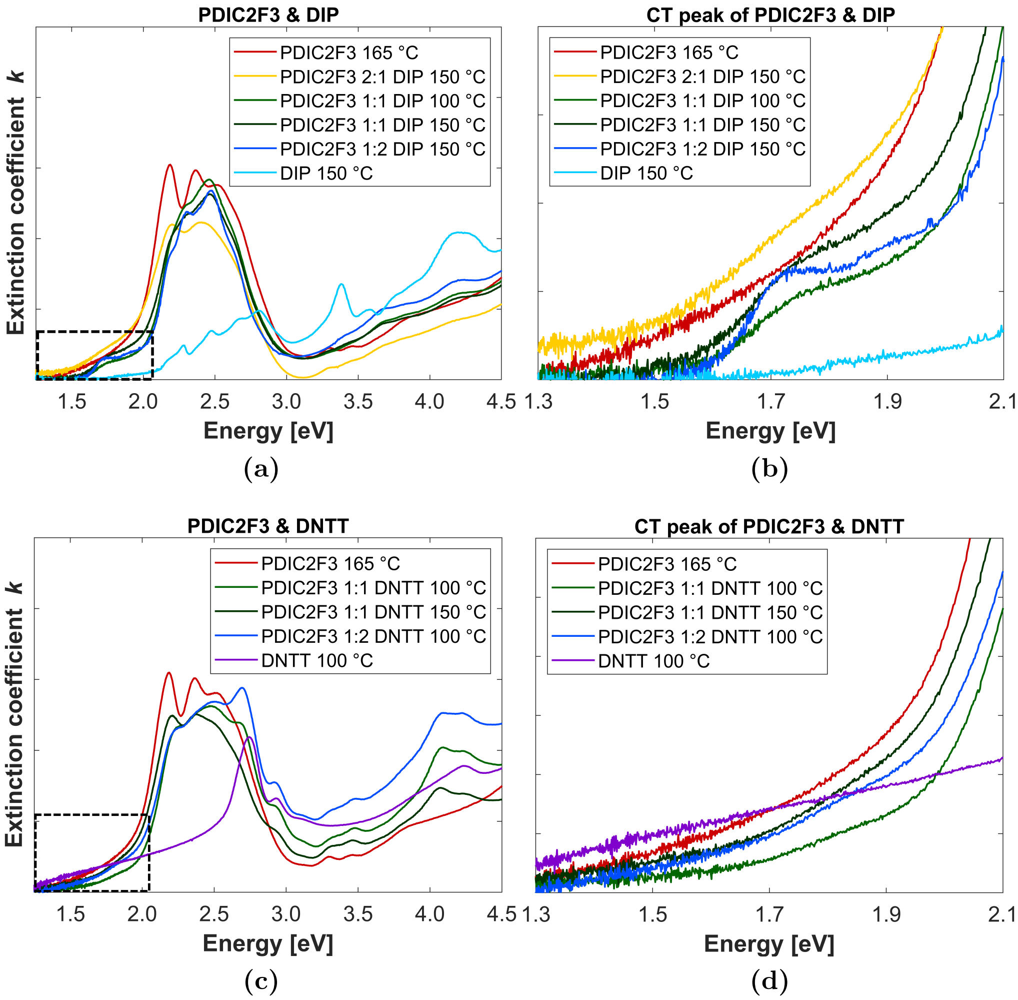

(a) (b)

(c) (d)

Figure 7.13: *Absorption spectra of a) $PDIC_2F_3$:DIP mixed films deposited at 100 °C and 150 °C, b) enlarged section of CT peak (black marked area of (a)), c) $PDIC_2F_3$:DNTT mixed films deposited at 100 °C and 150 °C and d) enlarged section of CT peak (black marked area of (c)).*

In Figure 7.13 the absorption spectra of the two mixed $PDIC_2F_3$:DIP and $PDIC_2F_3$:DNTT thin film systems are shown. The CT effect upon excitation of the different mixed films is of high interest. The low energy region (1.3 eV -

2.0 eV) below the HOMO-LUMO transition of the pristine materials is examined in more detail.

For all mixed films of $PDIC_2F_3$ and DIP, an excited-state CT peak below the HOMO-LUMO transition of the pure compounds with a maximum at 1.73 eV is detected (Fig. 7.13b). For the thin films with excess of one pure compound, the CT peak is the most intense for the 1:2 mixed film with DIP excess. In contrast, for the 2:1 thin film with $PDIC_2F_3$ excess the ES-CT peak is the weakest. In agreement with the XRR data of these films (see Fig. 7.11 in Sec. 7.2.1), it is shown that the excess of DIP favors the co-crystal formation and thus the CT effects whereas the excess of the acceptor hinders the mixing and the excited-state CT effects.

In the absorption spectra of $PDIC_2F_3$:DNTT mixed films, almost no CT peak is shown (Fig. 7.13d). The mixed thin films only show peaks of both pure compounds. In the absorption spectra of the 1:2 thin film with excess of DNTT, peaks of $PDIC_2F_3$ are visible and the remarkable peak of the pure DNTT at 2.7 eV dominates. This indicates a superposition of DNTT and $PDIC_2F_3$ which is shown in the absorption spectra of the mixed films. As a result, a phase-separation into both pristine materials is observed and no ES-CT effects are identified for these mixed thin films.

Photoluminescence spectroscopy

Figure 7.14 shows the emission spectra of the mixed $PDIC_2F_3$:DIP and $PDIC_2F_3$: DNTT thin films. As mentioned for the absorption spectra, peaks in the emission spectra located at the low energy region below the HOMO-LUMO transition of the pure compounds belonging to the ES-CT effects are investigated for both compound combinations. The emission spectra are recorded at a measurement temperature of 25 K with liquid Helium.

For all DIP:$PDIC_2F_3$ mixed films, a shoulder at 1.4 eV originates from an excited-state charge transfer (Fig. 7.14a). This peak emerges only at measurement temperatures lower than 90 K in temperature-dependent PL data (see Fig. 9.11a in the Appendixes). It is related to the absorption band at 1.73 eV (Fig. 7.13b). In a PL spectrum, a shift of ~ 0.3 eV to lower energy is common for related mixed systems [74]. The other peaks shown in the emission data are either from pure DIP or $PDIC_2F_3$ which may be slightly shifted due to solid state solvation [207–209]. The PL signals of the pure $PDIC_2F_3$ are much more intense than those of pristine DIP. In the spectra of the equimolar mixed films, the CT leads to a slight quenching of the signals of the pristine materials [205, 206].

In contrast, the emission spectra of mixed DNTT and $PDIC_2F_3$ films show only signals of both pure compounds (Fig. 7.14b). The PL signals of the pure $PDIC_2F_3$ are much more intense than those of pristine DNTT. The peak at 1.5 eV possibly originates from the pure acceptor molecule, potentially in a different orientation due to the DNTT molecule. In the temperature-dependent PL data of the pure $PDIC_2F_3$ (see Fig. 7.8 in Sec. 7.1.3), there is only a weak shoulder at 1.5 eV.

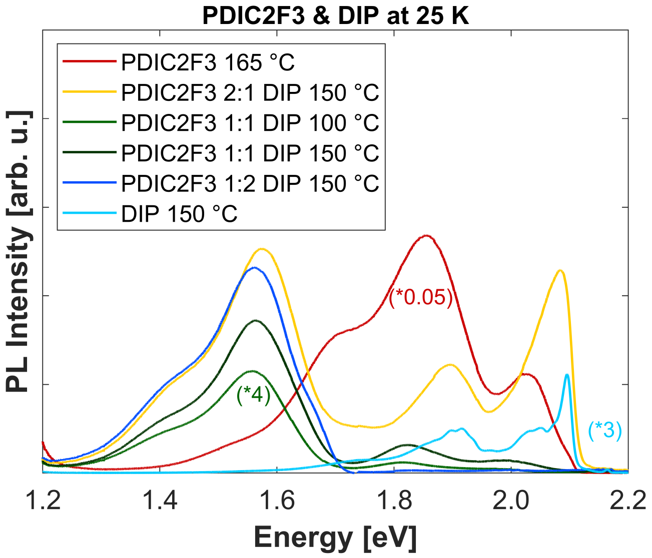

(a)

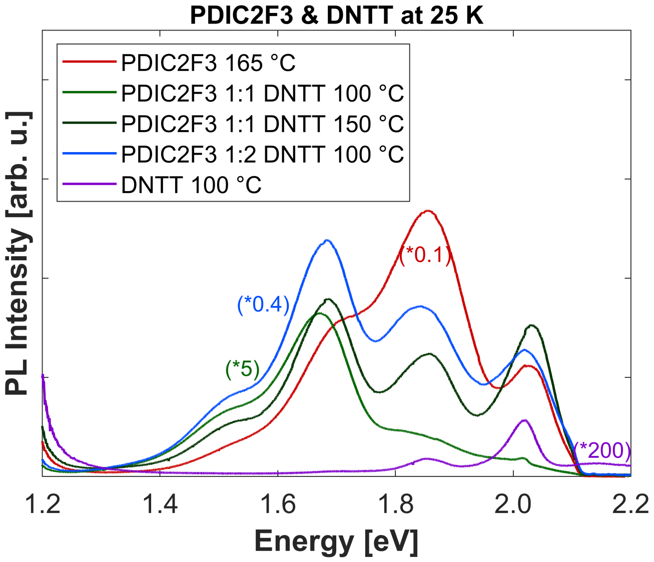

(b)

Figure 7.14: *Photoluminescence spectra of mixed films deposited at 100 °C and 150°C: a) PDIC$_2$F$_3$:DIP and b) PDIC$_2$F$_3$:DNTT. The spectra are scaled for clarity based on the respective equimolar mixed film grown at 150 °C.*

Compared with the other results (especially GIWAXS and absorption data), it appears that PDIC$_2$F$_3$ and DNTT, in contrast to thin films with DIP, tend to phase-separate.

To summarize, PDIC$_2$F$_3$ has different mixing and CT behavior with the two donor molecules DIP and DNTT. PDIC$_2$F$_3$ forms a well-defined co-crystal with strong ES-CT effects with DIP. In contrast, the acceptor tends to phase-separate with the donor DNTT with almost no ES-CT effects.

7.3 Discussion and conclusions

A comprehensive study on mixing behavior and charge transfer effects of the two donor-acceptor (DIP/DNTT:PDIC_2F_3) molecular systems prepared by OMBD has been performed. The thin films consist of the two different donor molecules, DIP and DNTT, and one PDI derivative with a short fluorinated side chain in the imide position as acceptor. Pristine and mixed thin films of PDIC_2F_3 and the two donors DIP and DNTT are prepared at different conditions (T_{sub} and mixing ratios) which results in different molecular order, mixing behavior, and CT effects. The structure and morphology of these thin films are investigated by GIWAXS, XRR, and AFM measurements, whereas optical properties are examined for both thin film systems by absorption and emission spectroscopy.

For the pure acceptor, PDIC_2F_3, the structure of the thin films is schematically shown in Figure 7.15. An orientational change from a lying-down to a standing-up conformation of the PDIC_2F_3 molecules and a higher crystallinity of the pristine thin films with increasing substrate temperature are shown.

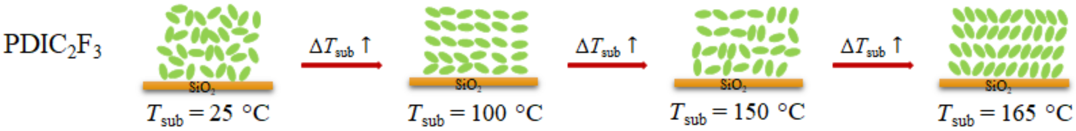

Figure 7.15: *Schematic results for the investigated pristine films of PDIC_2F_3. The different schematic scenarios are describing the temperature-dependent growth behavior (T_{sub} = 25 °C - 165 °C).*

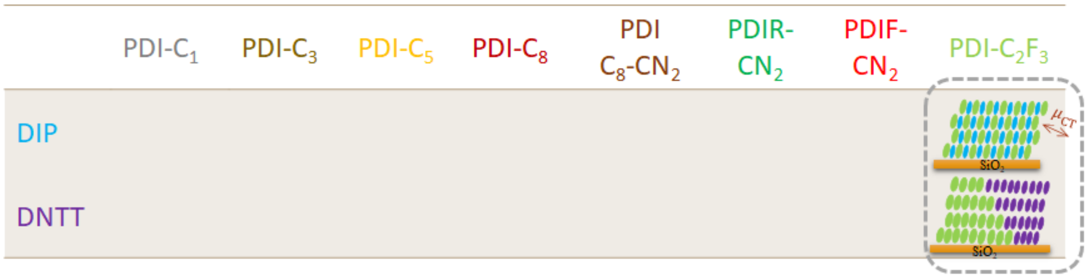

Figure 7.16: *Schematic results for the investigated mixed films of PDIC_2F_3:DIP and PDIC_2F_3: DNTT. The different schematic scenarios are describing the mixing behavior and the degree of the CT effects. This illustration is part of Fig. 4.9.*

The results of the mixed films with DIP and DNTT are schematically shown in Figure 7.16 (as part of Fig. 4.9). Here, the respective mixing behavior and the degree of ES-CT effects are illustrated for both thin film systems. For PDIC_2F_3:DIP mixed films, a donor/acceptor co-crystal formation is detected. For the equimolar mixed films, a well-defined co-crystal with long-range order and strong ES-CT effects is observed. The excess of DIP in the mixed films favors the co-crystal formation and CT effects, while the excess of the acceptor hinders both effects. For the mixed films with $PDIC_2F_3$ and DNTT, an opposite behavior regarding mixing and CT effects is noticed. For these thin films, there is almost no indication of a co-crystal formation or ES-CT effects. This suggests phase-separation into both pure compounds.

These results show the influence of the donor on the mixing behavior and CT effects. The donor molecule DIP possibly fits better with its structure and size to the $PDIC_2F_3$ molecule than the donor DNTT molecule which could explain the favored mixing and CT effects of DIP and $PDIC_2F_3$ in the mixed thin films.

Part III

Conclusions and outlook

Chapter 8

Conclusions and outlook

The main topics of this thesis are the structural morphology and charge transfer effects of organic binary bulk heterojunctions studied by structural and optical characterization methods like X-ray scattering and absorption as well as emission spectroscopy. Knowledge of growth and mixing behavior as well as molecular CT were applied and are also closely related to organic optoelectronic applications. An overview of the experimental results with the different donor and acceptor molecules is shown in Figure 8.1 as described at the beginning of Part II.

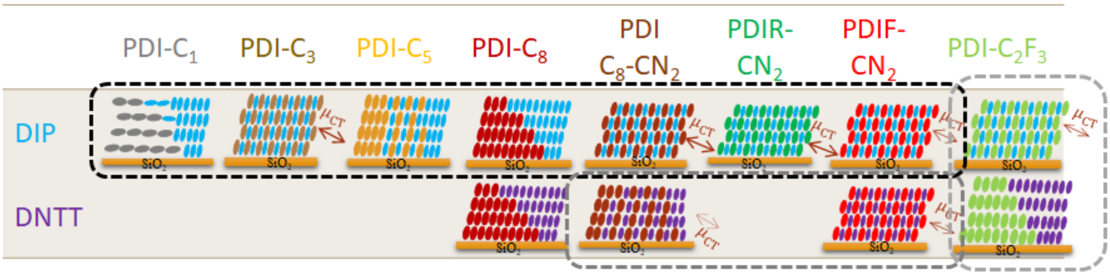

Figure 8.1: *Schematic representation of the investigated organic binary bulk heterojunctions. The donor molecules are listed as a row and the respective acceptor molecules as a column. The different schematic scenarios are describing the mixing behavior and the charge transfer effects of the individual systems. Systems that are investigated together are marked by different grey colors.*

The different mixing scenarios are schematically presented for the various investigated donor-acceptor systems and the respective degrees of charge transfer effects are described by the actual transition dipole moment of the CT. More details are summarized separately for the respective parts of investigated donor-acceptor thin film systems. Afterward, possible future projects as an outlook are discussed.

8.1 Results on PDI:DIP mixed films

The various n-alkyl side chains and cyano groups of the different PDI acceptors influence the structural morphology and mixing behavior as well as the charge transfer effects with the donor molecule DIP in these thin film systems. Thereby, two thin film systems show strong mixing and excited-state CT effects which are schematically presented in Figure 8.2. The different influences and aspects are illustrated below:

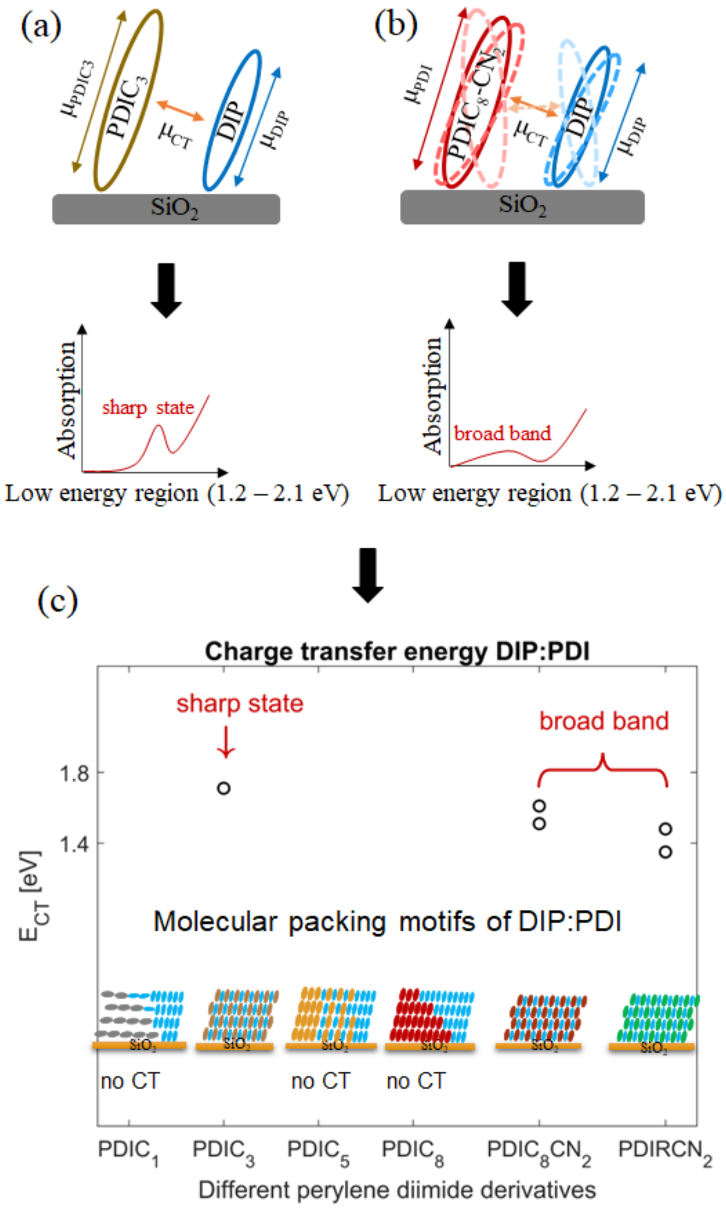

Figure 8.2: *Schematic representation of donor-acceptor π-stacking with the orientation of the TDMs and the illustrated absorption spectra in the low energy region for the thin film system: a) PDIC$_3$:DIP, b) PDIC$_8$-CN$_2$:DIP and c) sketch of the calculated CT energies by EL and IPCE data presented for the various PDI derivatives with DIP, the respective CT peak features in the absorption data and the molecular packing motifs of the various DIP:PDI thin film systems.*

- A strong CT effect, as well as a strong mixing, is detected for the system DIP:PDIC$_3$. The acceptor molecule has an optimal length of n-alkyl side chains in the imide position to form a well-defined co-crystal with DIP which shows a sharp ES-CT peak in absorption as well as one defined charge transfer energy (Fig. 8.2a and 8.2c).
- Strong CT and intermixing exist also for systems of DIP and perylene diimide derivatives with cyano groups in the bay position. These side groups influence the aromatic backbone of the PDIs. PDIC$_8$-CN$_2$ and DIP form also in thin films a well-ordered co-crystal but show a broad ES-CT band in absorption as well as two defined charge transfer energies (Fig. 8.2b and 8.2c). The same behavior was observed for the investigated system of PDIR-CN$_2$:DIP [49].
- The increased intermolecular interactions of the pure acceptor molecules with longer n-alkyl side chains appear to disfavor the mixing and the CT effects. However, the orientation of the acceptor molecules on the substrate (SiO$_2$) is changing with longer n-alkyl side chains which favor the mixing and the CT effects.

It is possible to control mixing behavior and CT effects by using suitable perylene diimide molecules. An important aspect is the structure of these acceptor molecules which can be modified easily in the desired way.

8.2 Results on molecular CT of PDI:DNTT mixed films

The molecular charge transfer effects of the two different DNTT:PDIF-CN$_2$ and DNTT:PDIC$_8$-CN$_2$ systems were characterized in regards to mixing behavior as well as theoretical calculations on energy levels and optical absorption spectroscopy. The two considered acceptor molecules differ in the fluorination of the side chain in the imide position. The main points of the results are illustrated in Figure 8.3 and summarized in the following:

- The influences of the different side chains of the acceptor molecules were investigated by obtaining a favored mixing behavior and stronger ES-CT effects for the system DNTT:PDIF-CN$_2$ (Fig. 8.3b).
- CT effects as well as co-crystal formation of the mixed thin films increase with raising deposition temperature and thickness for the acceptor with fluorinated side chains (PDIF-CN$_2$) and decrease for the acceptor with n-alkyl side chains (PDIC$_8$-CN$_2$).

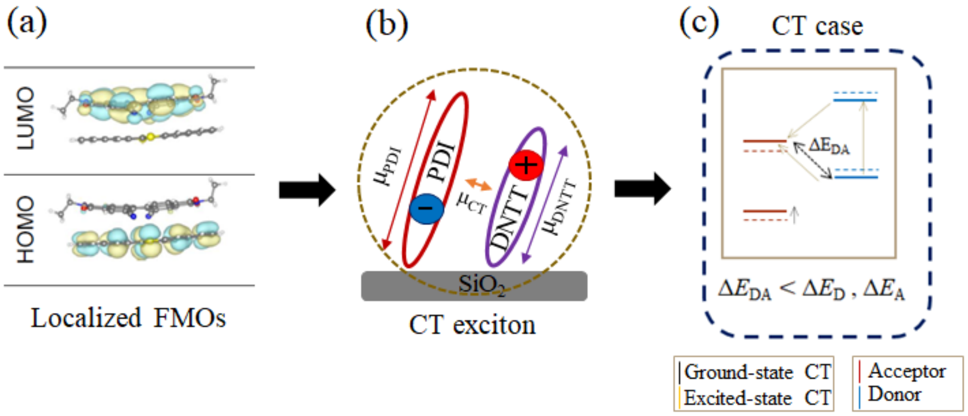

Figure 8.3: *Representation for both DNTT 1:1 PDI thin films of a) the localized HOMO and LUMO level of the CT complex, b) the schematical CT exciton formation with the respective TDMs and c) the charge transfer case indicating a small GS-CT and a strong ES-CT effect.*

- For both mixed thin film combinations an anisotropic nature of the excited-state CT is obtained. The ES-CT effect occurs only in the in-plane direction, parallel to the substrate plane (Fig. 8.3b).
- Both systems show a small ground-state CT governed by hybridized HOMO-1 and LUMO+1 levels, while the frontier orbitals are segregated on the donor and acceptor molecule (Fig. 8.3a).
- The calculated optical spectra show similar visible absorption peaks for both systems in agreement with the experimental results. The aforementioned localization for the frontier orbitals leads to a nearly pure charge transfer exciton visible in the absorption spectra.
- With these results it is possible to make a comparison with other weakly bound donor-acceptor molecules depending on their optical properties and to classify the two PDI:DNTT systems in different CT scenarios (Fig. 8.3c).

8.3 Results on $PDIC_2F_3$:DNTT/DIP mixed films

The influence of two donor molecules on mixing behavior and charge transfer effects with a PDI derivative is characterized in mixed thin film systems. The synthesized PDI acceptor with a short fluorinated side chain in the imide position is investigated with the two donor molecules DIP and DNTT. The main results are presented schematically in Figure 8.4. They are illustrated in the following:

- An orientational change from a lying-down to a standing-up conformation

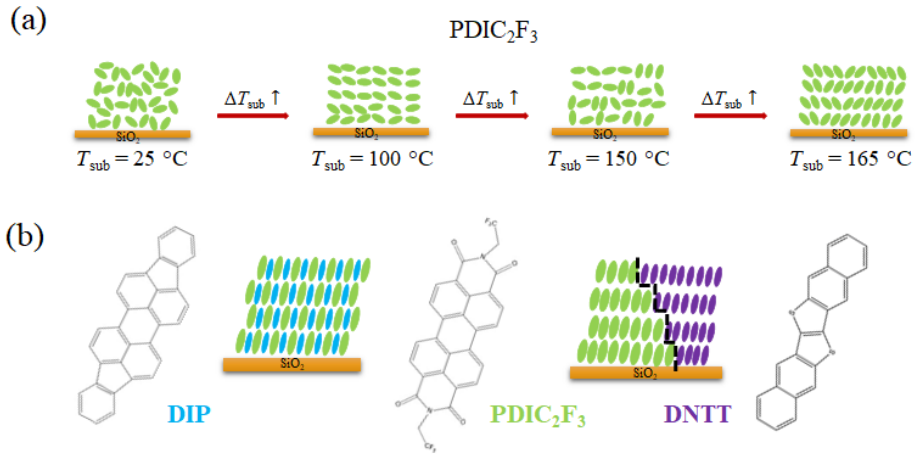

Figure 8.4: *Schematic illustration of a) the temperature-dependent growth behavior (T_{sub} = 25 °C - 165 °C) for the investigated pristine films of PDIC$_2$F$_3$ and b) the mixing behavior and molecule structure of DIP:PDIC$_2$F$_3$ and DNTT:PDI-C$_2$F$_3$ mixed thin films.*

of the PDIC$_2$F$_3$ molecules and higher crystallinity of the pristine thin films with increasing substrate temperature is observed (Fig 8.4a).

- For PDIC$_2$F$_3$:DIP mixed films a donor/acceptor co-crystal formation is obtained. For the equimolar mixed films, a well-defined co-crystal with long-range order and strong ES-CT effects is observed. The excess of the donor in the mixed films favors the co-crystal formation and CT effects and the excess of the acceptor disfavors both (Fig 8.4b).
- For the mixed films with PDIC$_2$F$_3$ and DNTT, there is almost no indication of a co-crystal formation or ES-CT effects. This suggests phase-separation into both pure compounds (Fig 8.4b).
- The donor molecule DIP possibly matches better with its structure and size the PDIC$_2$F$_3$ molecule, than the donor DNTT, which could explain the favored mixing and CT effects of DIP and PDIC$_2$F$_3$ in the mixed thin films.

8.4 Outlook

The presented results offered insights into the interplay between structural morphology and charge transfer effects in donor-acceptor thin films. These results in this thesis raise new questions and ideas which are considered in the following future projects:

- For a better understanding of the influences of the various PDI derivatives with different donor molecules on mixing behavior and CT effects in weakly bound donor-acceptor thin film systems, the different trends of the various PDI derivatives (see Chapter 5) can be tested with another donor molecule with similar structure, size, and energy levels such as Anthradithiophene (ADT). Another interesting aspect could be to compare one PDI derivative with suitable other donor molecules (f. ex. PEN, ADT, etc.) regarding the mixing behavior and the CT effects.

- First-principle calculations based on DFT and many-body perturbation theory could also be performed on other donor-acceptor molecule combinations (PDI:DNTT/DIP) to combine them with the experimental results on thin film systems. The calculations could be achieved before, choosing suitable donor and acceptor molecules with the desired optical properties (desired CT effects).

- Other PDI derivatives such as PDIC$_5$-CN$_2$ (PDIC$_5$ with incorporated cyano groups) can be synthesized and are likely to exhibit co-crystal formation or CT effects with suitable donor molecules based on the insights gained with this thesis. So, more details regarding the influences of the different side chains could be obtained.

- UPS measurements can be performed for the thin film systems where GS-CT effects were investigated (such as PDIC$_8$-CN$_2$:DNTT and PDIF-CN$_2$:DNTT) to gain knowledge about GS-CT properties.

- *In-situ* experiments regarding the structural morphology (for instance *in-situ* XRR and *in-situ* GIWAXS) and the CT effects (such as *in-situ* DRS and *in-situ* VASE spectroscopy) can be considered to study transient or thickness-dependent properties during growth.

Chapter 9

Appendixes

9.1 Additional data and comments on the comparative study of PDI:DIP mixed films

This section covers the supplementary data of the results in Chapter 5 based on the comparative study of PDI:DIP mixed films (Ref. [189]). Additional GIWAXS patterns, AFM images, temperature-dependent PL spectra, and VASE data of the various mixed thin films are presented below.

9.1.1 GIWAXS data

In Figures 9.1 and 9.2 the GIWAXS data of the various PDI:DIP mixed thin films are shown. In addition, the growth and mixing behavior of the various PDI:DIP mixed films deposited at a substrate temperature of $T_{sub} = 25\,^{\circ}\mathrm{C}$ is examined by the various GIWAXS patterns of the pristine PDI derivatives and their equimolar mixed thin films with DIP. The thin film structure of the donor molecule DIP (Fig. 9.2a) and the formed co-crystal phases of the two DIP:PDIF-CN$_2$ (9.2b) and DIP:PDIR-CN$_2$ (9.2c) equimolar thin films are shown in the GIWAXS patterns. Well-defined co-crystal phases of DIP:PDIF-CN$_2$ and DIP:PDIR-CN$_2$ were already investigated and strong ES-CT effects for these thin film systems were analyzed [49]. Therefore, they serve as a good comparison model.

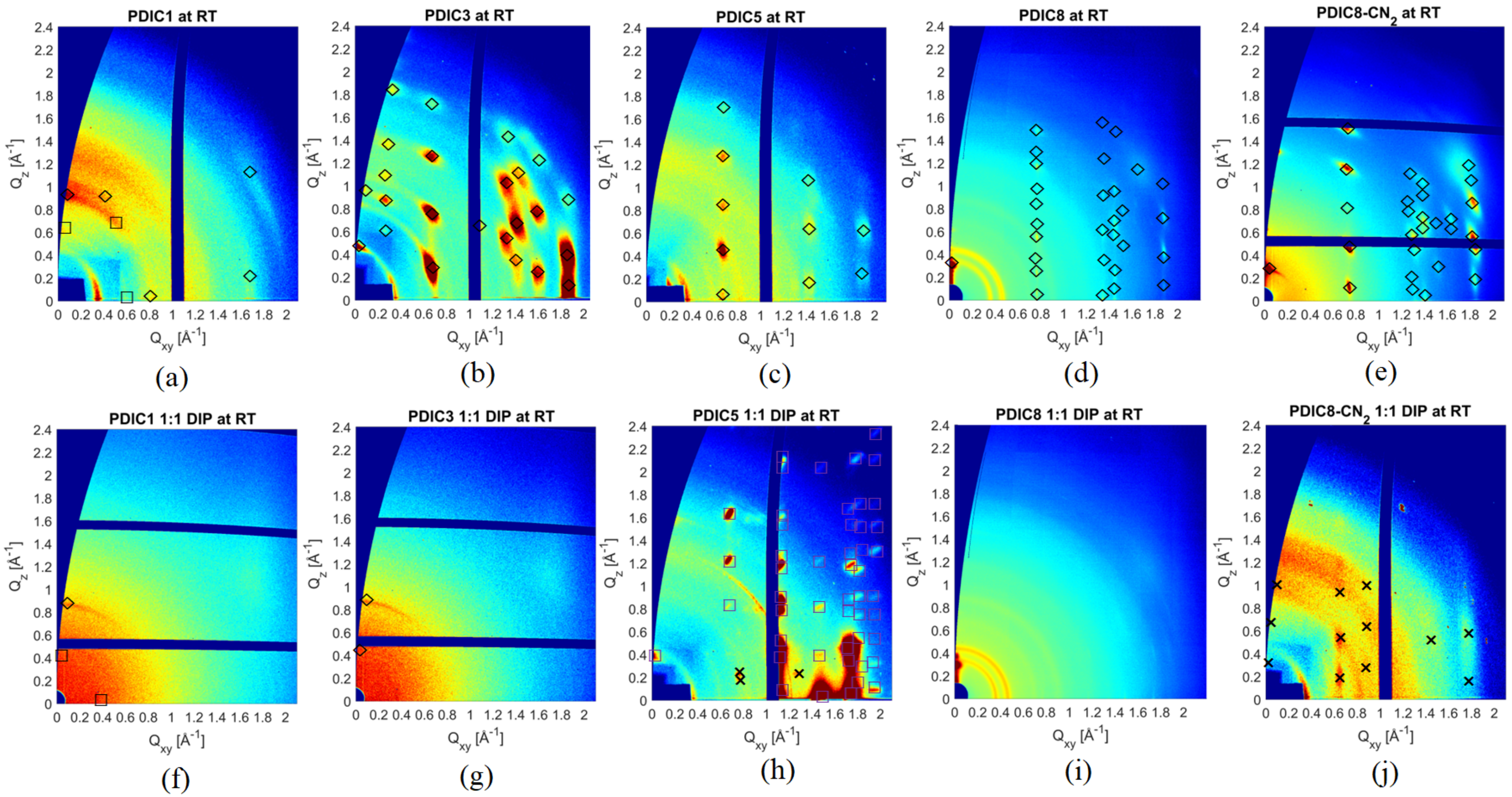

Figure 9.1: *GIWAXS data (25 °C deposition temperature): a) PDIC*$_1$*, b) PDIC*$_3$*, c) PDIC*$_5$*, d) PDIC*$_8$*, e) PDIC*$_8$*-CN*$_2$*, f) DIP 1:1 PDIC*$_1$*, g) DIP 1:1 PDIC*$_3$*, h) DIP 1:1 PDIC*$_5$*, i) DIP 1:1 PDIC*$_8$ *and j) DIP 1:1 PDIC*$_8$*-CN*$_2$ *(the donor is marked in violet, the acceptor is marked with black squares, and black crosses indicate the mixed phase).*

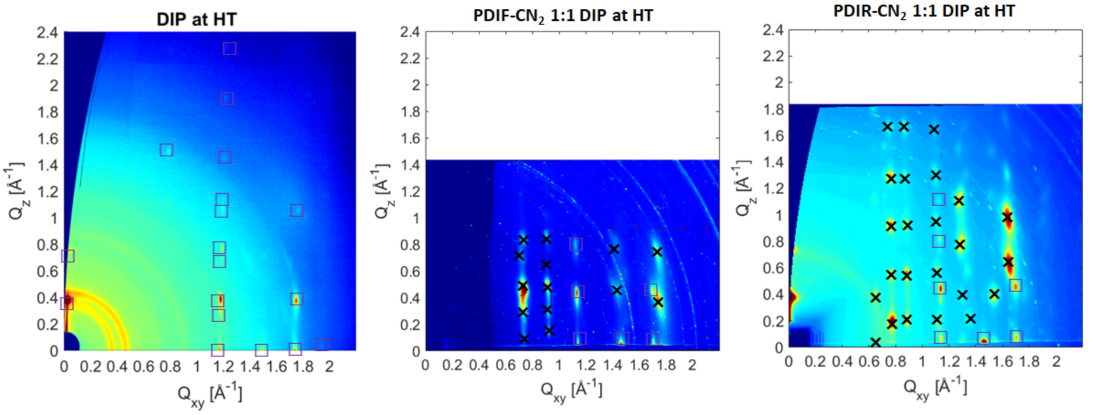

(a) (b) (c)

Figure 9.2: *GIWAXS data (150 °C deposition temperature): a) DIP, b) PDIF-CN$_2$ 1:1 DIP and c) PDIR-CN$_2$ 1:1 DIP (the donor is marked in violet and black crosses indicate the mixed phase).*

9.1.2 AFM images

AFM images of the pristine PDI thin films and the equimolar mixed films with the donor DIP which are grown at room and high substrate temperatures are shown in Figures 9.3 and 9.4. The morphology of the pristine PDI derivatives can be compared with the thin film structures of the 1:1 mixed films with DIP. All PDI derivatives show homogenous surfaces with small grains for the thin films grown at room temperature and elongated islands for the thin films deposited at high substrate temperature.

Especially, the PDI derivatives with longer n-alkyl side chains (PDIC$_5$, PDIC$_8$, and PDIC$_8$-CN$_2$) form smooth thin films at both substrate temperatures. The equimolar mixed films are forming all rougher films except for the equimolar thin films of DIP 1:1 PDIC$_8$-CN$_2$. The co-crystal phase forms smooth films with small grains or needlelike features at the respective growth substrate temperature. For DIP 1:1 PDIC$_3$, rougher thin films with a different morphology compared to the pure PDI derivative can be established which can indicate the co-crystal phases.

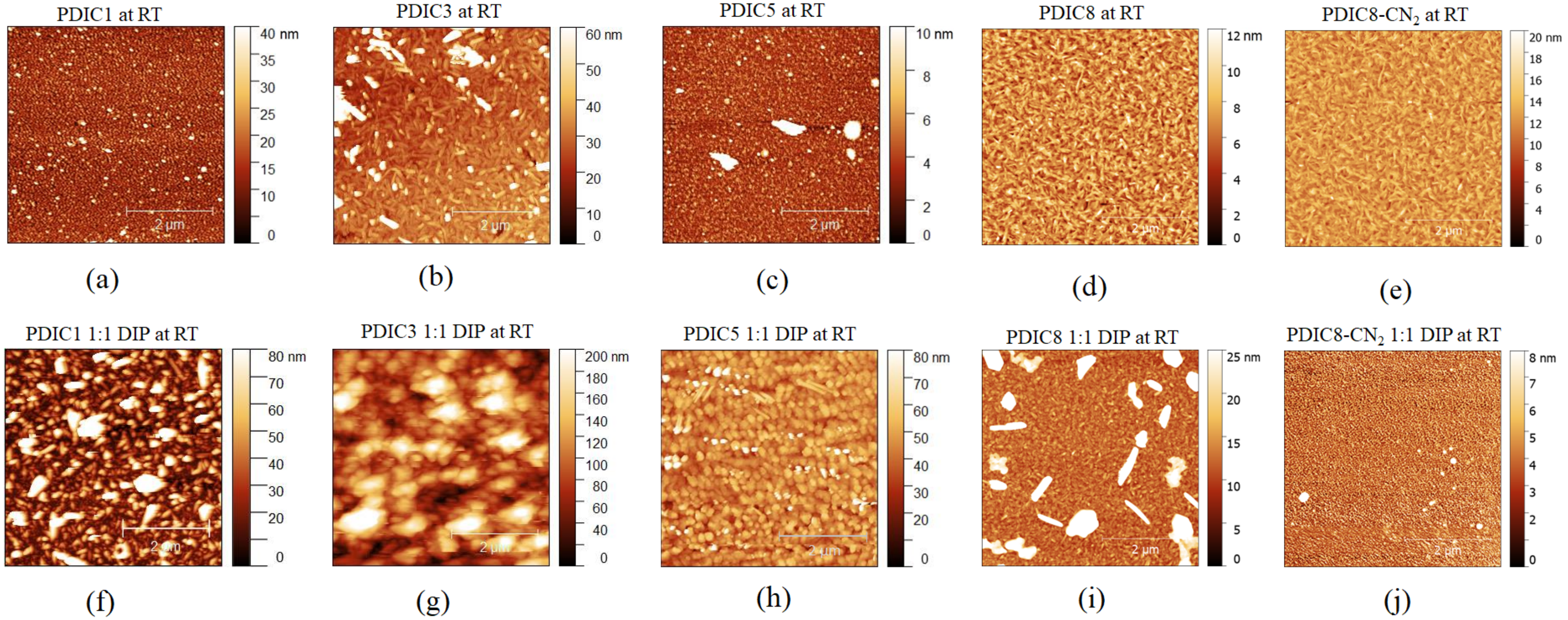

Figure 9.3: *AFM images (5 x 5 µm) of pristine and equimolar thin films (25 °C deposition temperature): a) PDIC$_1$, b) PDIC$_3$, c) PDIC$_5$, d) PDIC$_8$, e) PDIC$_8$-CN$_2$, f) DIP 1:1 PDIC$_1$, g) DIP 1:1 PDIC$_3$, h) DIP 1:1 PDIC$_5$, i) DIP 1:1 PDIC$_8$ and j) DIP 1:1 PDIC$_8$-CN$_2$ (Length of the scale bar is 2 µm).*

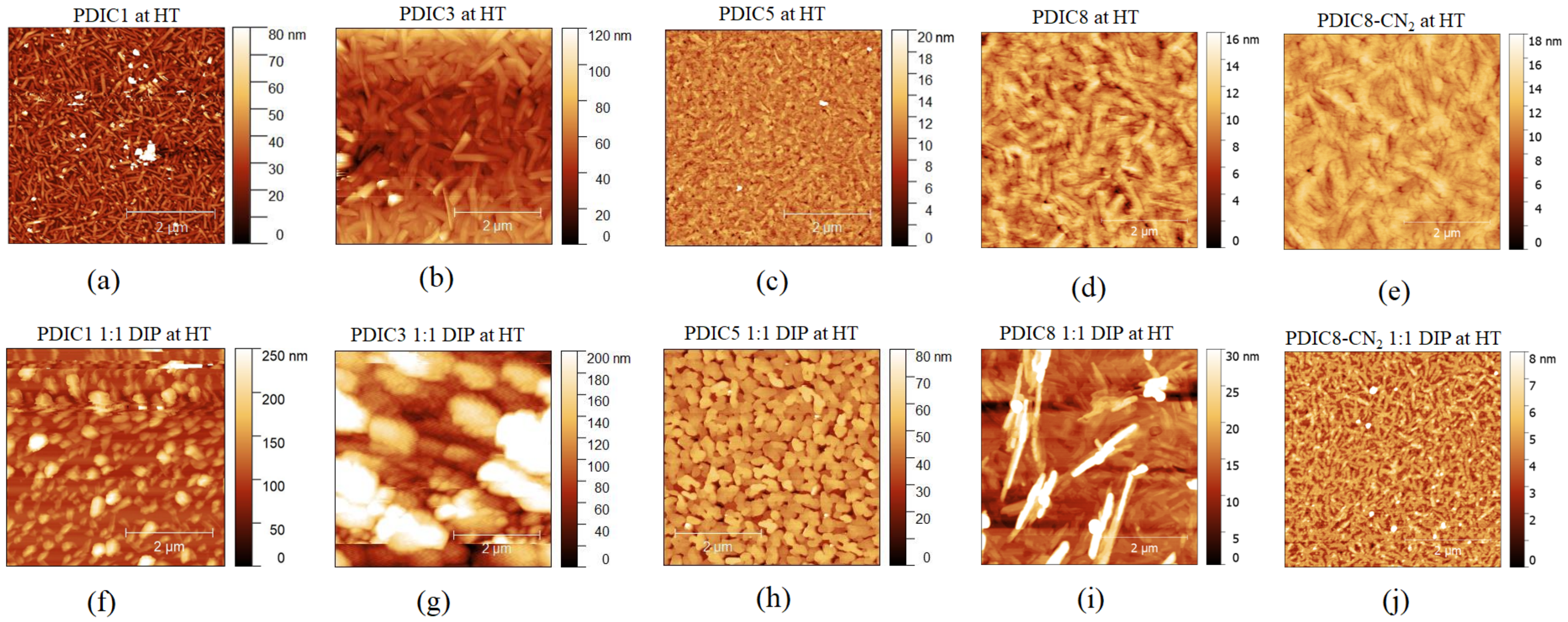

Figure 9.4: *AFM images (5 x 5 µm) of pristine and equimolar thin films (150 °C deposition temperature): a) PDIC*$_1$*, b) PDIC*$_3$*, c) PDIC*$_5$*, d) PDIC*$_8$*, e) PDIC*$_8$*-CN*$_2$*, f) DIP 1:1 PDIC*$_1$*, g) DIP 1:1 PDIC*$_3$*, h) DIP 1:1 PDIC*$_5$*, i) DIP 1:1 PDIC*$_8$ *and j) DIP 1:1 PDIC*$_8$*-CN*$_2$ *(Length of the scale bar is 2 µm).*

9.1.3 PL temperature-dependent data

In Figure 9.5 the temperature-dependent PL data is shown of the pristine PDI derivatives. The PL spectra are measured from 250 K to 15 K. For PDIC$_1$, PDIC$_5$, and PDIC$_8$ three dominant peaks are visible which are sharper at low measuring temperatures. For PDIC$_3$ and PDIC$_8$-CN$_2$ only a broad emission feature is shown for all measurement temperatures. It is possible that for the PDIs with strong intermolecular interactions defined emission features are visible whereas for the other compounds only one broad peak is presented [200].

9.1.4 Ellipsometry data

The results of the in-plane ϵ_{xy} and the out-of-plane ϵ_z components of the dielectric functions for the various equimolar DIP:PDI thin films are shown in Figure 9.6. The shape of the in-plane components is comparable with the absorption data (see Figures 5.10 and 5.11 in Sec. 5.3). Only in the in-plane spectra of DIP 1:1 PDIC$_3$ and DIP 1:1 PDIC$_8$-CN$_2$ excited-state CT peaks are visible at low energy below the HOMO-LUMO transition of the pure materials. The ES-CT effects for these mixed films are also observed in the absorption data.

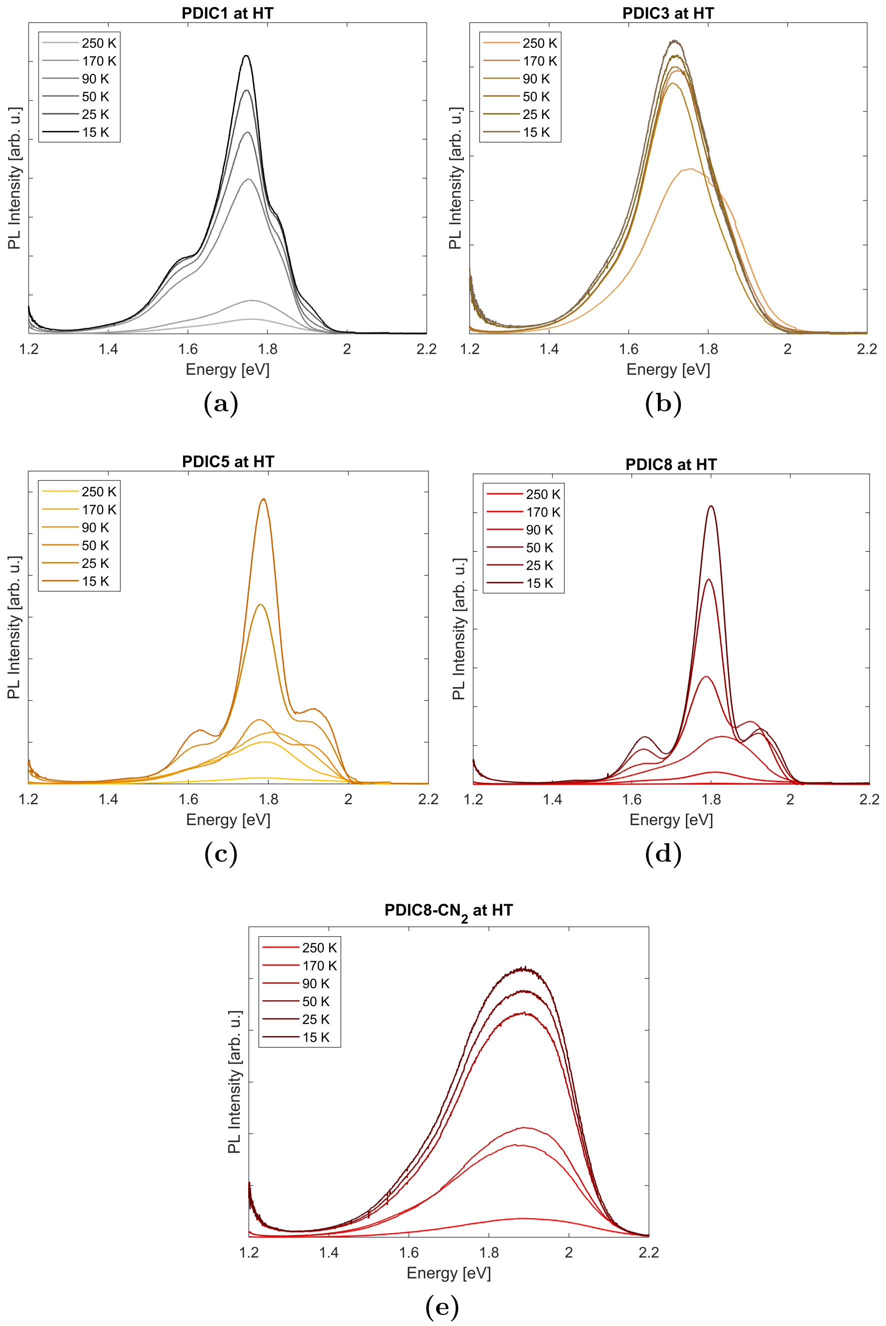

(a)

(b)

(c)

(d)

(e)

Figure 9.5: *Temperature-dependent photoluminescence spectra (measured from 250 K (light color) to 15 K (dark color)) of the pure PDI films deposited at 150°C: a) PDIC$_1$, b) PDIC$_3$, c) PDIC$_5$, d) PDIC$_8$ and e) PDIC$_8$-CN$_2$.*

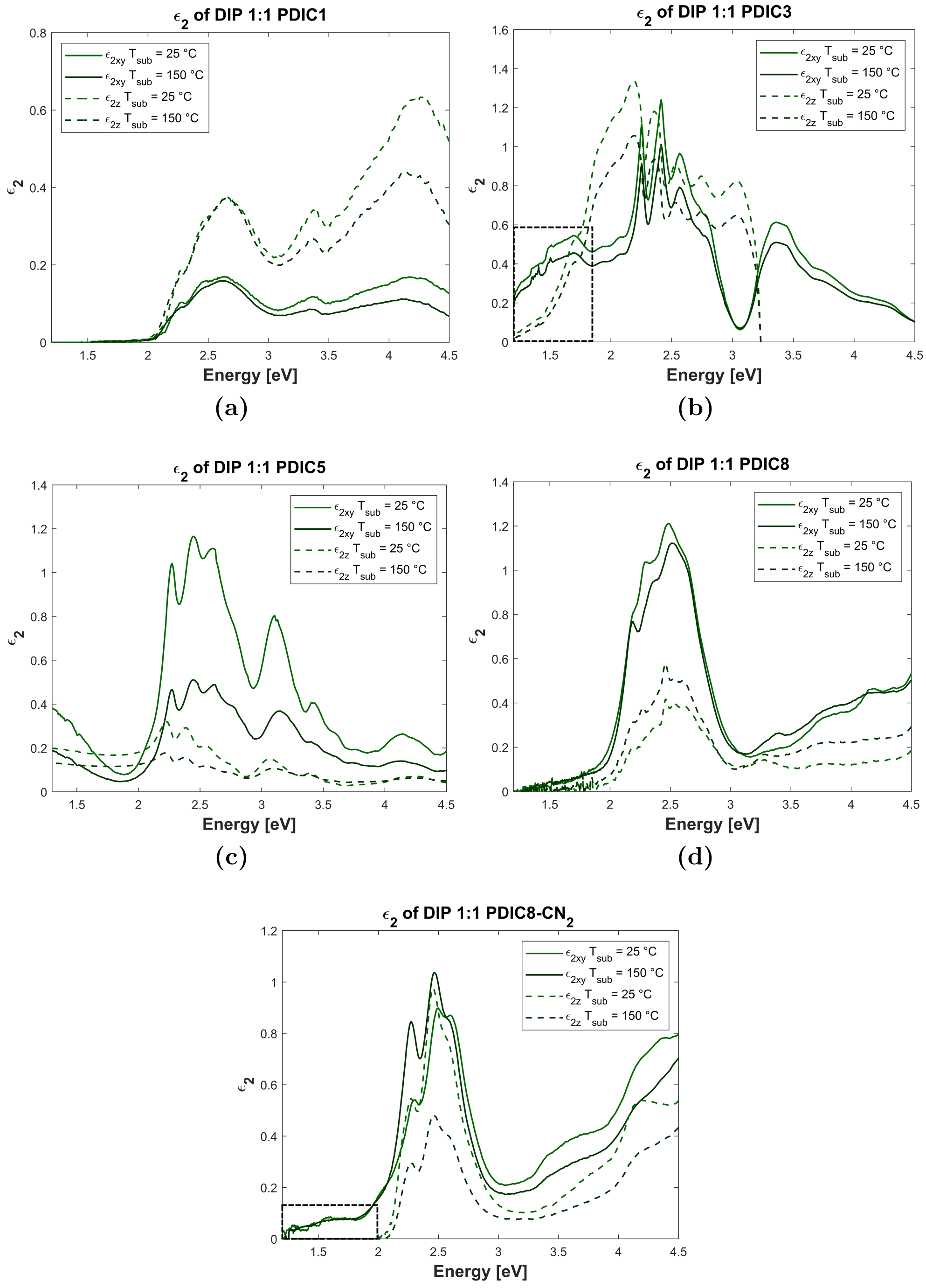

(a) (b) (c) (d) (e)

Figure 9.6: *Dielecrtic function with the in-plane ϵ_{xy} and out-of-plane ϵ_z components of the equimolar thin films deposited at 25 °C and 150 °C: a) DIP 1:1 PDIC$_1$, b) DIP 1:1 PDIC$_3$, c) DIP 1:1 PDIC$_5$, d) DIP 1:1 PDIC$_8$ and e) DIP 1:1 PDIC$_8$-CN$_2$. CT peaks are marked in black.*

9.2 Additional data and comments on molecule charge transfer effects of PDI:DNTT mixed films

This section covers the supplementary data of the results in Chapter 6 based on the recent publication [169]. Additional calculated molecular orbitals and optical spectra are presented below.

9.2.1 Calculated molecular orbitals

In Figure 9.7 the frontier orbitals and the respective energy levels are shown for both DNTT:PDIC$_8$-CN$_2$ and DNTT:PDIF-CN$_2$ complexes computed from DFT. The long alkyl side chains in the imide position of the PDI acceptors do not influence the calculated frontier orbitals or the respective energy values. So, for the calculations, the side chains can be reduced to the important groups.

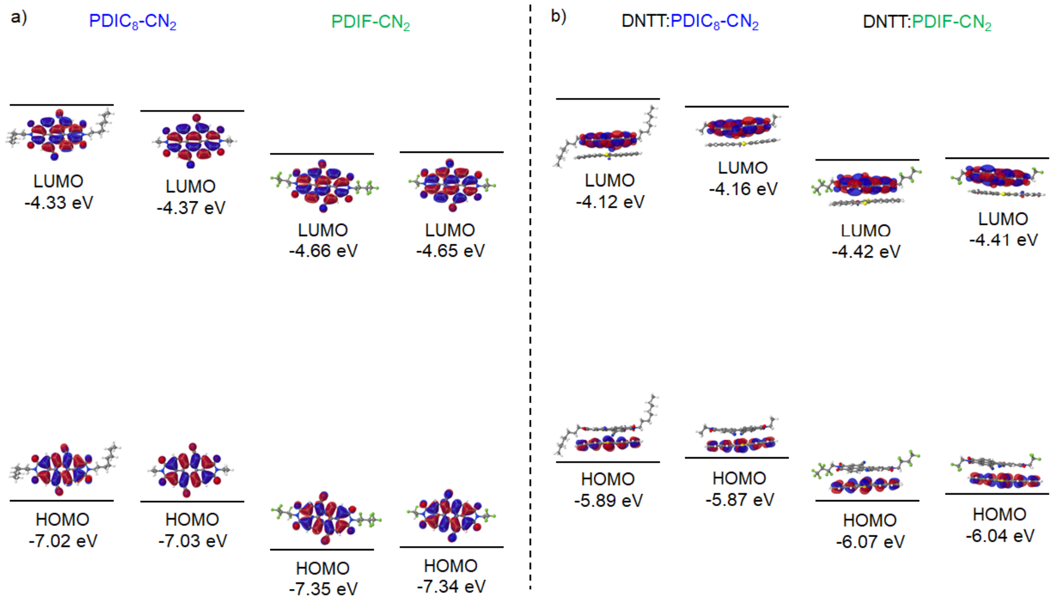

Figure 9.7: *Frontier orbitals and respective energy levels calculated for a) the individual acceptor molecules and b) the complexes with the donor DNTT. Values computed from DFT (PBE0 functional).*

9.2.2 Additional details on the computed optical spectra

The analysis of the optical absorption spectra of the DNTT:PDIC$_8$-CN$_2$ and DNTT:PDIF-CN$_2$ complexes is complemented by considering the character of the high-energy excitations labeled as E_4 and E_5 in Figure 9.8. E_4 appears at 2.70 eV (2.72 eV) in the spectrum of DNTT:PDIC$_8$-CN$_2$ (DNTT:PDIF-CN$_2$). In both complexes, it exhibits similar composition and oscillation strength, corresponding to transitions from the HOMO to higher unoccupied orbitals (Table 9.1). E_5 appears at 3.34 eV (3.37 eV) in the spectrum of DNTT:PDIC$_8$-CN$_2$ (DNTT:PDIF-CN$_2$), again with comparable oscillator strength in the spectra of the two complexes. It is composed by a manifold of transitions mainly from occupied orbitals below the HOMO and unoccupied ones above the LUMO. The hole and electron densities plotted for these two excitations reveal that in both cases the electron is delocalized over the whole complex. On the other hand, the hole of E_4 sits on the donor while in E_5 it is delocalized over both constituents (Figure 9.9).

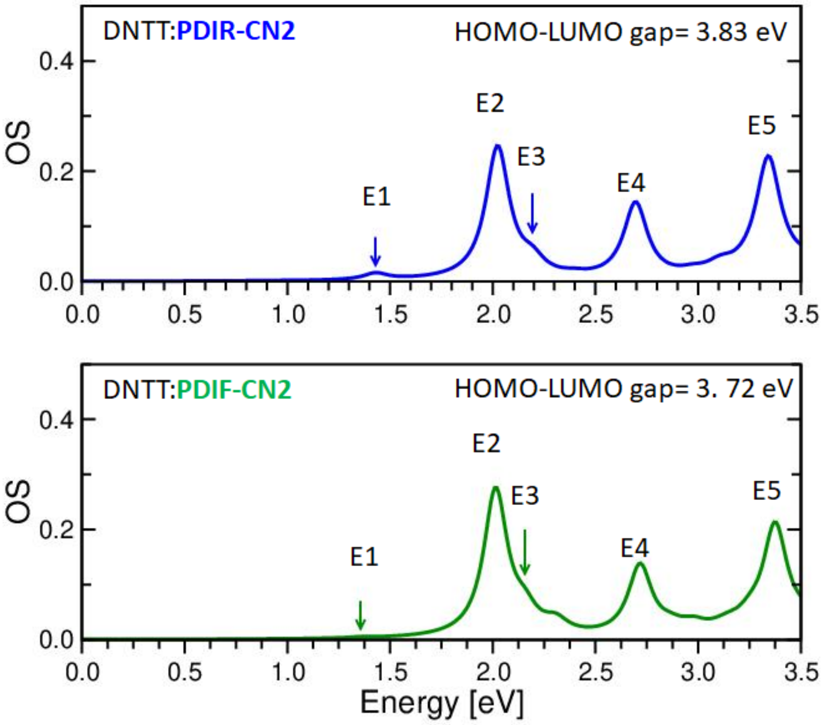

Figure 9.8: *Optical absorption spectra of the DNTT:PDIC$_8$-CN$_2$ and DNTT:PDIF-CN$_2$ complexes computed from GW/BSE. The excitations are labeled as E_1, E_2, E_3, E_4, and E_5. The energy of the quasi-particle gaps (E_{gap}) is reported in each panel. OS denotes the oscillator strength.*

Table 9.1: *Energies, oscillator strength (OS), and composition in terms of single-quasi-particle transitions of the high-energy excitations in the DNTT:PDIC$_8$-CN$_2$ and DNTT:PDIF-CN$_2$ complexes. HOMO and LUMO are abbreviated by H and L, respectively.*

	Excitation	Energy [eV]	OS	Composition
DNTT:PDIC$_8$-CN$_2$	E$_4$	2.70	0.136	H → L+1 (59%) H → L+4 (33%)
	E$_5$	3.34	0.183	H-3 → L+1 (31%) H-3 → L+4 (20%) H → L+7 (14%) H-2 → L (3%) H-2 → L+1 (3%)
DNTT:PDIF-CN$_2$	E$_4$	2.72	0.127	H → L+1 (51%) H → L+3 (29%) H → L+2 (11%)
	E$_5$	3.37	0.175	H-2 → L+3 (17%) H → L+8 (15%) H-2 → L+1 (14%) H-3 → L+1 (12%) H-3 → L+3 (9%) H → L+4 (8%)

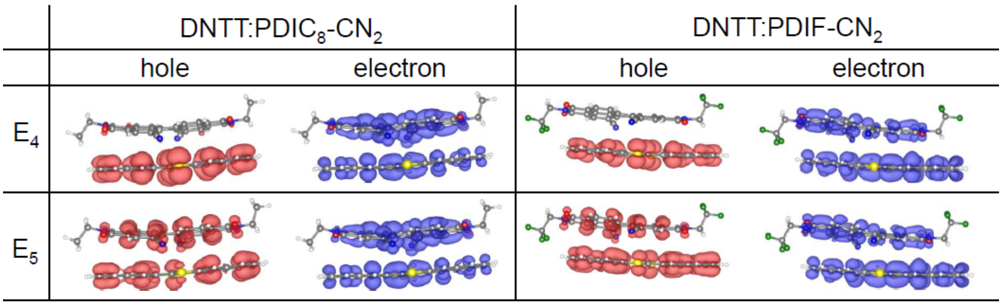

Figure 9.9: *Hole and electron densities calculated for E$_4$ and E$_5$ in the DNTT:PDIC$_8$-CN$_2$ and DNTT:PDIF-CN$_2$ complexes. Isosurfaces plotted with a cutoff of 0.002 Å^{-3}.*

9.3 Additional data and comments on the comparative study of PDIC$_2$F$_3$: DNTT/DIP mixed films

This section covers the supplementary data of the results in Chapter 7 based on the comparative study of PDIC$_2$F$_3$:DNTT/DIP mixed films (Ref. [219]). Additional temperature-dependent PL spectra as well as VASE data of the pure and mixed films are presented below.

9.3.1 Temperature-dependent PL spectra of pure $PDIC_2F_3$ thin films

In Figure 9.10 the temperature-dependent emission data are shown of the pristine $PDIC_2F_3$ thin films which are grown at substrate deposition temperatures of 25°C, 100 °C, and 150 °C.

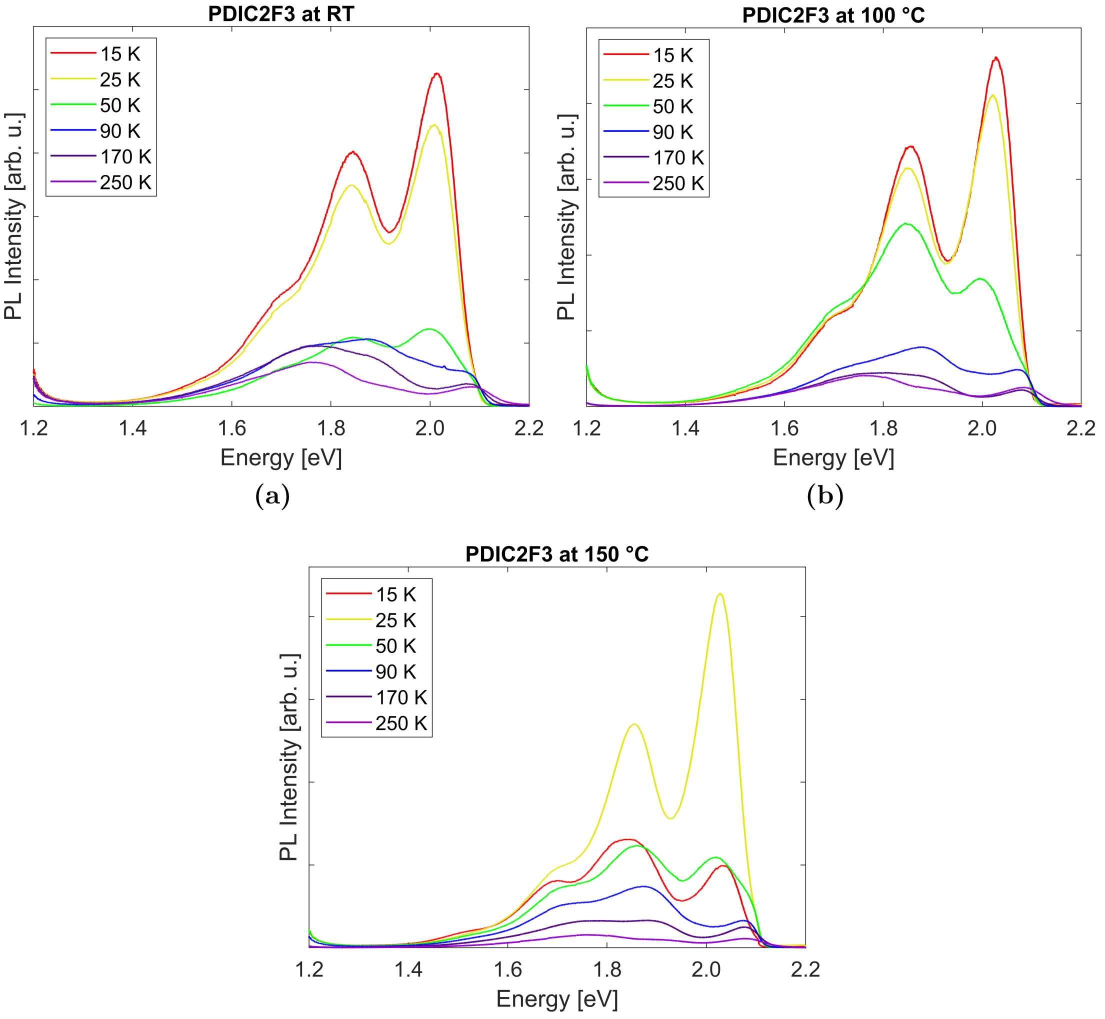

(a)

(b)

(c)

Figure 9.10: *Temperature-dependent photoluminescence spectra of* $PDIC_2F_3$ *thin films deposited at a) 25 °C, b) 100 °C and c) 150 °C. Measurement temperatures in the range from 250 K to 15 K.*

The spectral shape and temperature dependency are similar to the PL spectra in Fig. 7.8 in Sec. 7.1.3. These spectra show the temperature-dependent PL data of the pure film grown at 165 °C to compare the spectra with the data of the mixed films. The slight variations of the spectra at the various measurement temperatures are possible due to the different measurement spots and the different orientations of the $PDIC_2F_3$ molecules.

9.3.2 Temperature-dependent PL spectra of DIP/DNTT:$PDIC_2F_3$ mixed films

In Figure 9.11 the temperature-dependent emission data are shown of the equimolar DIP:$PDIC_2F_3$ and DNTT:$PDIC_2F_3$ mixed thin films.

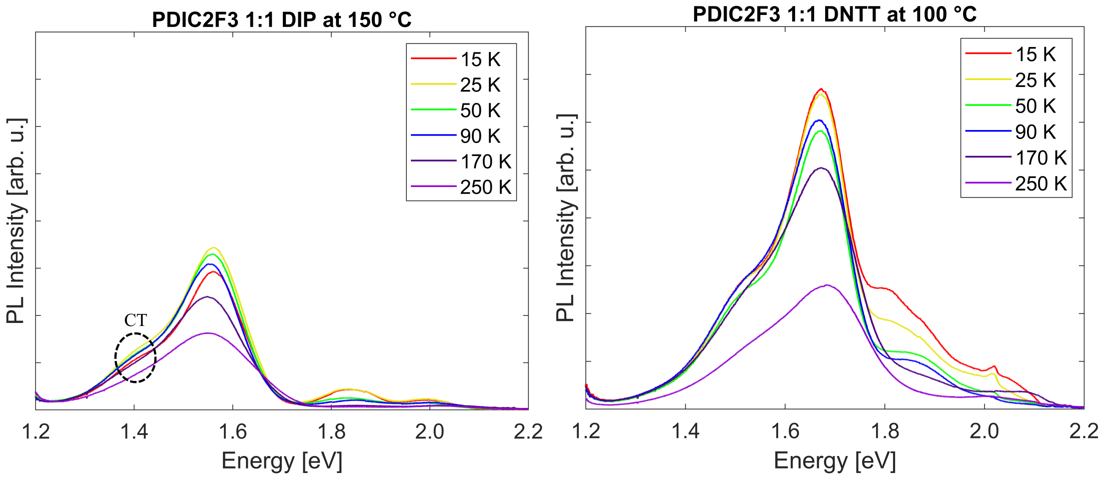

(a) (b)

Figure 9.11: *Temperature-dependent photoluminescence spectra of equimolar mixed thin films: a) DIP:$PDIC_2F_3$ deposited at 150 °C and b) DNTT:$PDIC_2F_3$ deposited at 100 °C. Measurement temperatures in the range from 250 K to 15 K and the ES-CT peak is marked in black.*

9.3.3 Ellipsometry data of DIP/DNTT:PDIC$_2$F$_3$ mixed films

The results of the in-plane ϵ_{xy} and the out-of-plane ϵ_z components of the dielectric functions for the equimolar DNTT/DIP:PDIC$_2$F$_3$ thin films are shown in Figure 9.12. The shape of the in-plane components is comparable with the absorption data (see Figure 7.13 in Sec. 7.2.2). Only in the in-plane spectra of DIP 1:1 PDIC$_2$F$_3$ an excited-state CT peak is visible at low energy below the HOMO-LUMO transition of the pure materials. The ES-CT effects for these mixed films are also observed in the absorption data. The out-of-plane components of the dielectric functions are moderately higher than the in-plane components for the films of the pure donors which indicates a standing-up orientation of these molecules. The molecules of the pure acceptor (for more details see Sec. 7.1.3) and the equimolar mixed films present possibly a more tilted orientation.

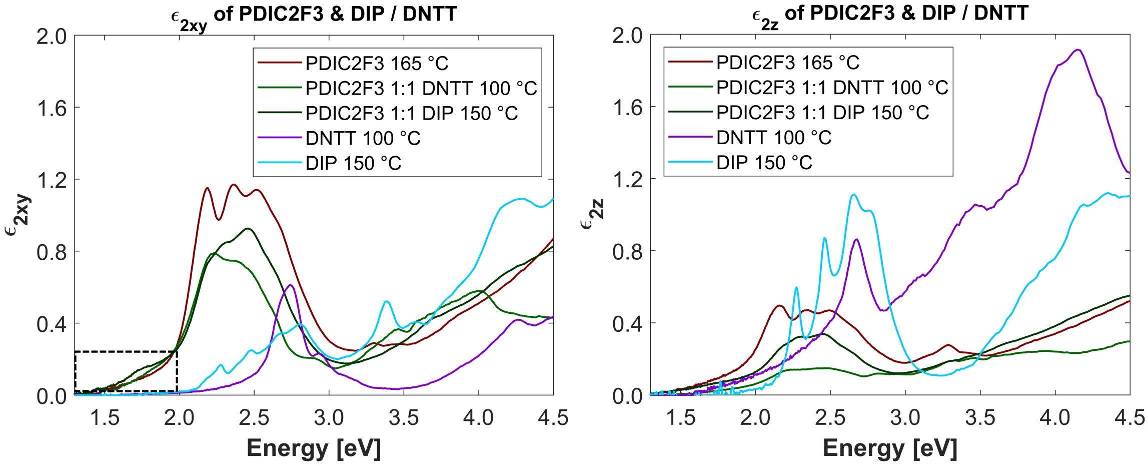

(a) (b)

Figure 9.12: *Dielectric function of a) the in-plane ϵ_{xy} and b) the out-of-plane ϵ_z components of PDIC$_2$F$_3$:DIP/DNTT equimolar thin films deposited at 100 °C and 150 °C. The CT peak is marked in black.*

List of abbreviations

Miscellaneous:

BHJ	Bulk heterojunctions
CS	Charge-separated
CT	Charge transfer
EA	Electron affnity
ES	Excited-state
ETL	Electron transporting layer
FMO	Frontier molecular orbital
GS	Ground-state
HOMO	Highest occupied molecule orbital
HTL	Hole transporting layer
IC	Internal conversation
IE	Ionization energy
ISC	Intersystem crossing
LCAO	Linear combination of atomic orbitals
LUMO	Lowest unoccupied molecule orbital
OFET	Organic field-effect transistor
OLED	Organic light emitting diode
OPVC	Organic photovoltaic cell
OS	Oscillator strength
PHJ	Planar heterojunction
TDM	Transition dipole moment
TMP	Turbomolecular pump
T_{sub}	Substrate temperature

Materials:

ADT	Anthradithiophene
BCP	Bathocuproine
DIP	Diindenoperylene
DNTT	Dinaphtothienothiophene
HIL 1.3	Hole injection layer 1.3
HMDS	Hexamethyldisilazane

ITO	Indium-tin oxide
NMP	N-methyl-2-pyrrolidone
PDI	Perylene diimide
PDIC$_2$F$_3$	N,N'-bis(2,2,2-Trisfluoroethyl)-perylene-3,4:9,10-bis(dicarboxyimide)
PDIF-CN$_2$	N,N'-1H,1H-perfluorobutyl-dicyanoperylene-3,4:9,10-bis(dicarboxyimide)
PDIR-CN$_2$	N,N'-bis-(2-ethylhexyl)-1,7-dicyanoperylene-3,4:9,10-bis(dicarboxyimide)
PEN	Pentacene
PTCDA	Perylenetetracarboxylic anhydride
PTCDI-C$_1$	N,N'-dimethyl-3,4:9,10-perylenedicarboxyimide
PTCDI-C$_3$	2,9-Dipropylanthra[2,1,9-def:6,5,10-d'e'f']diisoquinoline-1,3,8,10(2H,9H)tetrone
PTCDI-C$_5$	N,N'-dipentyl-3,4:9,10-perylenedicarboxyimide
PTCDI-C$_8$	N,N'-dioctyl-3,4:9,10-perylenedicarboxyimide
PTCDI-C$_8$-CN$_2$	N,N'-bis(n-octyl)-dicyanoperylene-3,4:9,10-bis-(dicarboxyimide)
SiO$_2$	Silicon oxide

Experimental techniques:

AFM	Atomic force microscopy
BSE	Bethe-Salpeter equation
CCD	Charge-coupled device
DFT	Density-functional theory
DRS	Differential reflectance spectroscopy
EL	Electroluminescence
EMA	Effective medium approximation
FTIR	Fourier-transform infrared
GIWAXS	Grazing incidence wide angle X-ray scattering
GIXD	Grazing incidence X-ray diffraction
IPCE	Incident photon-to-current efficiency
MBPT	Many-body perturbation theory
MS	Mass spectrometer
OMBD	Organic molecular beam deposition
PL	Photoluminescence
QCM	Quartz-crystal microbalance
UHV	Ultra-high vacuum
UV/vis/NIR	Ultraviolet/visible/near-infrared
UPS	Ultraviolet photoelectron spectroscopy
VASE	Variable angle spectroscopic ellipsometry
XRR	X-ray reflectivity

Bibliography

[1] W. Brütting, *Physics of Organic Semiconductors.* Wiley, 2005.

[2] K. Leo, "Organic photovoltaics," *Nature Reviews Materials*, vol. 1, no. 8, pp. 1–2, 2016.

[3] O. Inganäs, "Organic photovoltaics over three decades," *Advanced Materials*, vol. 30, no. 35, p. 1800388, 2018.

[4] F. Liscio, S. Milita, C. Albonetti, P. D'Angelo, A. Guagliardi, N. Masciocchi, R. G. D. Valle, E. Venuti, A. Brillante, and F. Biscarini, "Structure and morphology of PDI8-CN2 for n-type thin-film transistors," *Advanced Functional Materials*, vol. 22, no. 5, pp. 943–953, 2011.

[5] Y. Sun, Y. Liu, and D. Zhu, "Advances in organic field-effect transistors," *Journal of Materials Chemistry*, vol. 15, no. 1, pp. 53–65, 2005.

[6] C. Dimitrakopoulos and P. Malenfant, "Organic thin film transistors for large area electronics," *Advanced Materials*, vol. 14, no. 2, pp. 99–117, 2002.

[7] G. Horowitz, "Organic field-effect transistors," *Advanced Materials*, vol. 10, no. 5, pp. 365–377, 1998.

[8] J. Yoon, H. Kwon, M. Lee, Y. y. Yu, N. Cheong, S. Min, J. Choi, H. Im, K. Lee, J. Jo, *et al.*, "65.1: invited paper: world 1st large size 18-inch flexible oled display and the key technologies," *SID Symposium Digest of Technical Papers*, vol. 46, no. 1, pp. 962–965, 2015.

[9] C. W. Tang and S. A. VanSlyke, "Organic electroluminescent diodes," *Applied Physics Letters*, vol. 51, no. 12, pp. 913–915, 1987.

[10] C. Deibel and V. Dyakonov, "Polymer–fullerene bulk heterojunction solar cells," *Reports on Progress in Physics*, vol. 73, no. 9, p. 096401, 2010.

[11] P. Peumans, A. Yakimov, and S. R. Forrest, "Small molecular weight organic thin-film photodetectors and solar cells," *Journal of Applied Physics*, vol. 93, no. 7, pp. 3693–3723, 2003.

[12] A. Opitz, J. Wagner, W. Brütting, I. Salzmann, N. Koch, J. Manara, J. Pflaum, A. Hinderhofer, and F. Schreiber, "Charge separation at molecular donor–acceptor interfaces: Correlation between morphology and solar

cell performance," *IEEE Journal of Selected Topics in Quantum Electronics*, vol. 16, no. 6, pp. 1707–1717, 2010.

[13] J. E. Anthony, "Small-molecule, nonfullerene acceptors for polymer bulk heterojunction organic photovoltaics," *Chemistry of Materials*, vol. 23, no. 3, pp. 583–590, 2010.

[14] S. R. Forrest, "The path to ubiquitous and low-cost organic electronic appliances on plastic," *Nature*, vol. 428, pp. 911–918, 2004.

[15] B. Ecker, "Flexibel, leicht und durchsichtig," *Physik in unserer Zeit*, vol. 44, no. 2, pp. 84–91, 2013.

[16] R. Gaudiana and C. Brabec, "Fantastic plastic," *Nature Photonics*, vol. 2, no. 5, pp. 287–289, 2008.

[17] C. J. Brabec, "Organic photovoltaics: technology and market," *Solar Energy Materials and Solar Cells*, vol. 83, no. 2-3, pp. 273–292, 2004.

[18] G. P. Neupane, W. Ma, T. Yildirim, Y. Tang, L. Zhang, and Y. Lu, "2d organic semiconductors, the future of green nanotechnology," *Nano Materials Science*, vol. 1, no. 4, pp. 246–259, 2019.

[19] A. Pron, P. Gawrys, M. Zagorska, D. Djurado, and R. Demadrille, "Electroactive materials for organic electronics: preparation strategies, structural aspects and characterization techniques," *Chemical Society Reviews*, vol. 39, no. 7, pp. 2577–2632, 2010.

[20] B. J. Jung, N. J. Tremblay, M.-L. Yeh, and H. E. Katz, "Molecular design and synthetic approaches to electron-transporting organic transistor semiconductors," *Chemistry of Materials*, vol. 23, no. 3, pp. 568–582, 2011.

[21] A. R. Murphy and J. M. J. Fréchet, "Organic semiconducting oligomers for use in thin film transistors," *Chemical Reviews*, vol. 107, no. 4, pp. 1066–1096, 2007.

[22] Y. Wen and Y. Liu, "Recent progress in n-channel organic thin-film transistors," *Advanced Materials*, vol. 22, no. 12, pp. 1331–1345, 2010.

[23] B. A. Jones, A. Facchetti, M. R. Wasielewski, and T. J. Marks, "Tuning orbital energetics in arylene diimide semiconductors. Materials design for ambient stability of n-type charge transport," *Journal of the American Chemical Society*, vol. 129, no. 49, pp. 15259–15278, 2007.

[24] W. Chen, D.-C. Qi, H. Huang, X. Gao, and A. T. S. Wee, "Organic-organic heterojunction interfaces: Effect of molecular orientation," *Advanced Functional Materials*, vol. 21, no. 3, pp. 410–424, 2010.

[25] A. Hinderhofer and F. Schreiber, "Organic-organic heterostructures: Concepts and applications," *ChemPhysChem*, vol. 13, no. 3, pp. 628–643, 2012.

[26] F. Schreiber, "Organic molecular beam deposition: Growth studies beyond the first monolayer," *Physica Status Solidi A*, vol. 201, no. 6, pp. 1037–1054, 2004.

[27] S. Kowarik, A. Gerlach, and F. Schreiber, "Organic molecular beam deposition: fundamentals, growth dynamics, and in situ studies," *Journal of Physics: Condensed Matter*, vol. 20, no. 18, p. 184005, 2008.

[28] K. Vasseur, C. Rolin, S. Vandezande, K. Temst, L. Froyen, and P. Heremans, "A growth and morphology study of organic vapor phase deposited perylene diimide thin films for transistor applications," *The Journal of Physical Chemistry C*, vol. 114, no. 6, pp. 2730–2737, 2010.

[29] R. Ye, M. Baba, K. Suzuki, and K. Mori, "Structure and morphology of CuPc and F16CuPc pn heterojunction," *Applied Surface Science*, vol. 254, no. 23, pp. 7885–7888, 2008.

[30] M. A. Ruderer and P. Müller-Buschbaum, "Morphology of polymer-based bulk heterojunction films for organic photovoltaics," *Soft Matter*, vol. 7, no. 12, pp. 5482–5493, 2011.

[31] H. Méndez, G. Heimel, S. Winkler, J. Frisch, A. Opitz, K. Sauer, B. Wegner, M. Oehzelt, C. Röthel, S. Duhm, *et al.*, "Charge-transfer crystallites as molecular electrical dopants," *Nature Communications*, vol. 6, p. 8560, 2015.

[32] K. Broch, J. Dieterle, F. Branchi, N. J. Hestand, Y. Olivier, H. Tamura, C. Cruz, V. M. Nichols, A. Hinderhofer, D. Beljonne, *et al.*, "Robust singlet fission in pentacene thin films with tuned charge transfer interactions," *Nature Communications*, vol. 9, no. 1, p. 954, 2018.

[33] M. Schwarze, K. S. Schellhammer, K. Ortstein, J. Benduhn, C. Gaul, A. Hinderhofer, L. P. Toro, R. Scholz, J. Kublitski, S. Roland, *et al.*, "Impact of molecular quadrupole moments on the energy levels at organic heterojunctions," *Nature Communications*, vol. 10, no. 1, p. 2466, 2019.

[34] N. Koch, "Organic electronic devices and their functional interfaces," *ChemPhysChem*, vol. 8, no. 10, pp. 1438–1455, 2007.

[35] S. R. Forrest, "The limits to organic photovoltaic cell efficiency," *MRS Bulletin*, vol. 30, no. 1, pp. 28–32, 2005.

[36] B. A. Jones, M. J. Ahrens, M.-H. Yoon, A. Facchetti, T. J. Marks, and M. R. Wasielewski, "High-mobility air-stable n-type semiconductors with processing versatility: Dicyanoperylene-3,4:9,10-bis(dicarboximides)," *Angewandte Chemie*, vol. 116, no. 46, pp. 6523–6526, 2004.

[37] C. W. Tang, "Two-layer organic photovoltaic cell," *Applied Physics Letters*, vol. 48, no. 2, pp. 183–185, 1986.

[38] J.-L. Brédas, J. E. Norton, J. Cornil, and V. Coropceanu, "Molecular understanding of organic solar cells: The challenges," *Accounts of Chemical Research*, vol. 42, no. 11, pp. 1691–1699, 2009.

[39] R. S. Mulliken, "Molecular compounds and their spectra. III. The interaction of electron donors and acceptors," *The Journal of Physical Chemistry*, vol. 56, no. 7, pp. 801–822, 1952.

[40] N. J. Hestand, R. V. Kazantsev, A. S. Weingarten, L. C. Palmer, S. I. Stupp, and F. C. Spano, "Extended-charge-transfer excitons in crystalline supramolecular photocatalytic scaffolds," *Journal of the American Chemical Society*, vol. 138, no. 36, pp. 11762–11774, 2016.

[41] K. Vandewal, "Interfacial charge transfer states in condensed phase systems," *Annual Review of Physical Chemistry*, vol. 67, pp. 113–133, 2016.

[42] K. Vandewal, S. Albrecht, E. T. Hoke, K. R. Graham, J. Widmer, J. D. Douglas, M. Schubert, W. R. Mateker, J. T. Bloking, G. F. Burkhard, *et al.*, "Efficient charge generation by relaxed charge-transfer states at organic interfaces," *Nature Materials*, vol. 13, no. 1, pp. 63–68, 2014.

[43] C. Deibel, T. Strobel, and V. Dyakonov, "Role of the charge transfer state in organic donor–acceptor solar cells," *Advanced Materials*, vol. 22, no. 37, pp. 4097–4111, 2010.

[44] A. Babuji, A. Cazorla, E. Solano, C. Habenicht, H. Kleemann, C. Ocal, K. Leo, and E. Barrena, "Charge-transfer complexes in organic field-effect transistors: Superior suitability for surface doping," *ACS Applied Materials & Interfaces*, vol. 14, no. 39, pp. 44632–44641, 2022.

[45] M. Hallermann, E. D. Como, J. Feldmann, M. Izquierdo, S. Filippone, N. Martín, S. Jüchter, and E. von Hauff, "Correlation between charge transfer exciton recombination and photocurrent in polymer/fullerene solar cells," *Applied Physics Letters*, vol. 97, no. 2, p. 023301, 2010.

[46] K. Vandewal, K. Tvingstedt, A. Gadisa, O. Inganäs, and J. V. Manca, "Relating the open-circuit voltage to interface molecular properties of donor:acceptor bulk heterojunction solar cells," *Physical Review B*, vol. 81, no. 12, p. 125204, 2010.

[47] M. J. Kendrick, A. Neunzert, M. M. Payne, B. Purushothaman, B. D. Rose, J. E. Anthony, M. M. Haley, and O. Ostroverkhova, "Formation of the donor–acceptor charge-transfer exciton and its contribution to charge photogeneration and recombination in small-molecule bulk heterojunctions,"

The Journal of Physical Chemistry C, vol. 116, no. 34, pp. 18108–18116, 2012.

[48] X.-K. Chen, M. K. Ravva, H. Li, S. M. Ryno, and J.-L. Brédas, "Effect of molecular packing and charge delocalization on the nonradiative recombination of charge-transfer states in organic solar cells," *Advanced Energy Materials*, vol. 6, no. 24, p. 1601325, 2016.

[49] V. Belova, P. Beyer, E. Meister, T. Linderl, M.-U. Halbich, M. Gerhard, S. Schmidt, T. Zechel, T. Meisel, A. V. Generalov, *et al.*, "Evidence for anisotropic electronic coupling of charge transfer states in weakly interacting organic semiconductor mixtures," *Journal of the American Chemical Society*, vol. 139, no. 25, pp. 8474–8486, 2017.

[50] A. Köhler and H. Bässler, *Electronic Processes in Organic Semiconductors: An Introduction.* John Wiley & Sons, 2015.

[51] M. Schwoerer and H. C. Wolf, *Organic Molecular Solids.* John Wiley & Sons, 2007.

[52] E. Breitmaier and G. Jung, *Organische Chemie Grundlagen, Verbindungsklassen, Reaktionen, Konzepte, Molekülstruktur, Naturstoffe.* Thieme, 2009.

[53] C. E. Mortimer and U. Müller, *Chemie das Basiswissen der Chemie.* Thieme, 2007.

[54] E. A. Meyer, R. K. Castellano, and F. Diederich, "Interactions with aromatic rings in chemical and biological recognition," *Angewandte Chemie International Edition*, vol. 42, no. 11, pp. 1210–1250, 2003.

[55] C. R. Martinez and B. L. Iverson, "Rethinking the term "pi-stacking"," *Chemical Science*, vol. 3, no. 7, pp. 2191–2201, 2012.

[56] S. Grimme, "Do special noncovalent π–π stacking interactions really exist?," *Angewandte Chemie International Edition*, vol. 47, no. 18, pp. 3430–3434, 2008.

[57] A. Aufderheide, K. Broch, J. Novák, A. Hinderhofer, R. Nervo, A. Gerlach, R. Banerjee, and F. Schreiber, "Mixing-induced anisotropic correlations in molecular crystalline systems," *Physical Review Letters*, vol. 109, no. 15, p. 156102, 2012.

[58] A. I. Kitaigorodsky, *Mixed Crystals.* Springer Berlin Heidelberg, 1984.

[59] B. Lewis and J. C. Anderson, *Nucleation and growth of thin films.* Academic Press, 1978.

[60] I. Markov and S. Stoyanov, “Mechanisms of epitaxial growth,” *Contemporary Physics*, vol. 28, no. 3, pp. 267–320, 1987.

[61] S. R. Forrest, “Ultrathin organic films grown by organic molecular beam deposition and related techniques,” *Chemical Reviews*, vol. 97, no. 6, pp. 1793–1896, 1997.

[62] I. V. Markov, *Crystal growth for beginners: fundamentals of nucleation, crystal growth and epitaxy.* World scientific, 2016.

[63] A. Pimpinelli, *Physics of Crystal Growth.* Cambridge University Press, 2011.

[64] G. Hlawacek and C. Teichert, “Nucleation and growth of thin films of rod-like conjugated molecules,” *Journal of Physics: Condensed Matter*, vol. 25, no. 14, p. 143202, 2013.

[65] M. Born and E. Wolf, *Principles of optics: electromagnetic theory of propagation, interference and diffraction of light.* Pergamon Press, 1980.

[66] J. A. Woollam, *Guide to Using WVASE Spectroscopic Ellipsometry Data Acquisition and Analysis Software.* J. A. Woollam Co., Inc, 2012.

[67] B. H. Bransden and C. J. Joachain, *Physics of atoms and molecules.* Longman, 1983.

[68] E. Condon, “A theory of intensity distribution in band systems,” *Physical Review*, vol. 28, no. 6, pp. 1182–1201, 1926.

[69] G. Wedler, *Lehrbuch der physikalischen Chemie.* Wiley-VCH, 1997.

[70] M. de Jong, L. Seijo, A. Meijerink, and F. T. Rabouw, “Resolving the ambiguity in the relation between stokes shift and huang–rhys parameter,” *Physical Chemistry Chemical Physics*, vol. 17, no. 26, pp. 16959–16969, 2015.

[71] W. Y. Liang, “Excitons,” *Physics Education*, vol. 5, no. 4, pp. 226–228, 1970.

[72] G. H. Wannier, “The structure of electronic excitation levels in insulating crystals,” *Physical Review*, vol. 52, no. 3, pp. 191–197, 1937.

[73] S. Ullbrich, J. Benduhn, X. Jia, V. C. Nikolis, K. Tvingstedt, F. Piersimoni, S. Roland, Y. Liu, J. Wu, A. Fischer, *et al.*, “Emissive and charge-generating donor–acceptor interfaces for organic optoelectronics with low voltage losses,” *Nature Materials*, vol. 18, no. 5, pp. 459–464, 2019.

[74] F. Anger, J. O. Ossó, U. Heinemeyer, K. Broch, R. Scholz, A. Gerlach, and F. Schreiber, “Photoluminescence spectroscopy of pure pentacene, perfluoropentacene, and mixed thin films,” *The Journal of Chemical Physics*, vol. 136, no. 5, p. 054701, 2012.

[75] Q. Zhang, X. Liu, F. Jiao, S. Braun, M. J. Jafari, X. Crispin, T. Ederth, and M. Fahlman, "Ground-state charge transfer for NIR absorption with donor/acceptor molecules: interactions mediated via energetics and orbital symmetries," *Journal of Materials Chemistry C*, vol. 5, no. 2, pp. 275–281, 2017.

[76] S. Duhm, A. Gerlach, I. Salzmann, B. Bröker, R. Johnson, F. Schreiber, and N. Koch, "PTCDA on Au(111), Ag(111) and Cu(111): Correlation of interface charge transfer to bonding distance," *Organic Electronics*, vol. 9, no. 1, pp. 111–118, 2008.

[77] D. Nanova, S. Beck, A. Fuchs, T. Glaser, C. Lennartz, W. Kowalsky, A. Pucci, and M. Kroeger, "Charge transfer in thin films of donor–acceptor complexes studied by infrared spectroscopy," *Organic Electronics*, vol. 13, no. 7, pp. 1237–1244, 2012.

[78] J. Chappell, A. Bloch, W. Bryden, M. Maxfield, T. Poehler, and D. Cowan, "Degree of charge transfer in organic conductors by infrared absorption spectroscopy," *Journal of the American Chemical Society*, vol. 103, no. 9, pp. 2442–2443, 1981.

[79] H. Jiang, P. Hu, J. Ye, K. K. Zhang, Y. Long, W. Hu, and C. Kloc, "Tuning of the degree of charge transfer and the electronic properties in organic binary compounds by crystal engineering: a perspective," *Journal of Materials Chemistry C*, vol. 6, no. 8, pp. 1884–1902, 2018.

[80] H. Haken and H. C. Wolf, *Molekülphysik und Quantenchemie: Einführung in die experimentellen und theoretischen Grundlagen*. Springer-Verlag, 2013.

[81] A. S. Davydov, "The theory of molecular excitons," *Soviet Physics Uspekhi*, vol. 7, no. 2, pp. 145–178, 1964.

[82] M. Kasha, H. R. Rawls, and M. A. El-Bayoumi, "The exciton model in molecular spectroscopy," *Pure and Applied Chemistry*, vol. 11, no. 3-4, pp. 371–392, 1965.

[83] U. Heinemeyer, R. Scholz, L. Gisslén, M. I. Alonso, J. O. Ossó, M. Garriga, A. Hinderhofer, M. Kytka, S. Kowarik, A. Gerlach, *et al.*, "Exciton-phonon coupling in diindenoperylene thin films," *Physical Review B*, vol. 78, no. 8, p. 085210, 2008.

[84] N. J. Hestand, H. Yamagata, B. Xu, D. Sun, Y. Zhong, A. R. Harutyunyan, G. Chen, H.-L. Dai, Y. Rao, and F. C. Spano, "Polarized absorption in crystalline pentacene: Theory vs experiment," *The Journal of Physical Chemistry C*, vol. 119, no. 38, pp. 22137–22147, 2015.

[85] J. Megow, T. Körzdörfer, T. Renger, M. Sparenberg, S. Blumstengel, F. Henneberger, and V. May, "Calculating optical absorption spectra of thin polycrystalline organic films: Structural disorder and site-dependent van der waals interaction," *The Journal of Physical Chemistry C*, vol. 119, no. 10, pp. 5747–5751, 2015.

[86] K. A. Kistler, C. M. Pochas, H. Yamagata, S. Matsika, and F. C. Spano, "Absorption, circular dichroism, and photoluminescence in perylene diimide bichromophores: Polarization-dependent h- and j-aggregate behavior," *The Journal of Physical Chemistry B*, vol. 116, no. 1, pp. 77–86, 2011.

[87] M. Kasha, "Characterization of electronic transitions in complex molecules," *Discussions of the Faraday Society*, vol. 9, pp. 14–19, 1950.

[88] N. J. Hestand and F. C. Spano, "Expanded theory of h- and j-molecular aggregates: The effects of vibronic coupling and intermolecular charge transfer," *Chemical Reviews*, vol. 118, no. 15, pp. 7069–7163, 2018.

[89] F. C. Spano, "The spectral signatures of frenkel polarons in h- and j-aggregates," *Accounts of Chemical Research*, vol. 43, no. 3, pp. 429–439, 2009.

[90] B.-K. An, J. Gierschner, and S. Y. Park, "π-conjugated cyanostilbene derivatives: A unique self-assembly motif for molecular nanostructures with enhanced emission and transport," *Accounts of Chemical Research*, vol. 45, no. 4, pp. 544–554, 2011.

[91] R. Rahimi, V. Narang, and D. Korakakis, "Optical and morphological studies of thermally evaporated PTCDI-C8 thin films for organic solar cell applications," *International Journal of Photoenergy*, vol. 2013, pp. 1–7, 2013.

[92] A. Sugie, W. Han, N. Shioya, T. Hasegawa, and H. Yoshida, "Structure-dependent electron affinities of perylene diimide-based acceptors," *The Journal of Physical Chemistry C*, vol. 124, no. 18, pp. 9765–9773, 2020.

[93] A. S. Molinari, H. Alves, Z. Chen, A. Facchetti, and A. F. Morpurgo, "High electron mobility in vacuum and ambient for PDIF-CN2 single-crystal transistors," *Journal of the American Chemical Society*, vol. 131, no. 7, pp. 2462–2463, 2009.

[94] W.-Y. Chou, B.-L. Yeh, H.-L. Cheng, B.-Y. Sun, Y. C. Cheng, Y.-S. Lin, S.-J. Liu, F.-C. Tang, and C.-C. Chang, "Organic complementary inverters with polyimide films as the surface modification of dielectrics," *Organic Electronics*, vol. 10, no. 5, pp. 1001–1005, 2009.

[95] C. Huang, S. Barlow, and S. R. Marder, "Perylene-3,4,9,10-tetracarboxylic acid diimides: Synthesis, physical properties, and use in organic electronics," *The Journal of Organic Chemistry*, vol. 76, no. 8, pp. 2386–2407, 2011.

[96] J.-P. Sun, A. D. Hendsbee, A. J. Dobson, G. C. Welch, and I. G. Hill, "Perylene diimide based all small-molecule organic solar cells: Impact of branched-alkyl side chains on solubility, photophysics, self-assembly, and photovoltaic parameters," *Organic Electronics*, vol. 35, pp. 151–157, 2016.

[97] C. Wang, J. Wang, N. Wu, M. Xu, X. Yang, Y. Lu, and L. Zang, "Donor–acceptor single cocrystal of coronene and perylene diimide: molecular self-assembly and charge-transfer photoluminescence," *RSC Advances*, vol. 7, no. 4, pp. 2382–2387, 2017.

[98] H. Fan, W. Shi, X. Yu, and J. Yu, "High performance nitrogen dioxide sensor based on organic field-effect transistor utilizing ultrathin CuPc/PTCDI-C8 heterojunction," *Synthetic Metals*, vol. 211, pp. 161–166, 2016.

[99] M. Aghamohammadi, A. Fernández, M. Schmidt, A. Pérez-Rodríguez, A. R. Goñi, J. Fraxedas, G. Sauthier, M. Paradinas, C. Ocal, and E. Barrena, "Influence of the relative molecular orientation on interfacial charge-transfer excitons at donor/acceptor nanoscale heterojunctions," *The Journal of Physical Chemistry C*, vol. 118, no. 27, pp. 14833–14839, 2014.

[100] H. Méndez, I. Thurzo, and D. R. T. Zahn, "Experimental study of charge transport mechanisms in a hybrid metal/organic/inorganic device," *Physical Review B*, vol. 75, no. 4, p. 045321, 2007.

[101] T. N. Krauss, E. Barrena, D. G. de Oteyza, X. N. Zhang, J. Major, V. Dehm, F. Würthner, and H. Dosch, "X-ray/atomic force microscopy study of the temperature-dependent multilayer structure of PTCDI-C8 films on SiO2," *The Journal of Physical Chemistry C*, vol. 113, no. 11, pp. 4502–4506, 2009.

[102] E. Hädicke and F. Graser, "Structures of eleven perylene-3,4:9,10-bis(dicarboximide) pigments," *Acta Crystallographica Section C Crystal Structure Communications*, vol. 42, no. 2, pp. 189–195, 1986.

[103] F. Marin, S. Tombolesi, T. Salzillo, O. Yaffe, and L. Maini, "Thorough investigation on the high-temperature polymorphism of dipentyl-perylenediimide: thermal expansion vs. polymorphic transition," *Journal of Materials Chemistry C*, vol. 10, no. 20, pp. 8089–8100, 2022.

[104] A. J. Ferguson and T. S. Jones, "Photophysics of PTCDA and Me-PTCDI thin films: Effects of growth temperature," *The Journal of Physical Chemistry B*, vol. 110, no. 13, pp. 6891–6898, 2006.

[105] H. Yanagi, Y. Toda, and T. Noguchi, "Photoelectrochemical behaviors of orientation-controlled thin films of n,n'-substituted perylene-3,4:9,10-bis(dicarboximide)," *Japanese Journal of Applied Physics*, vol. 34, no. 7B, pp. 3808–3813, 1995.

[106] A. Kam, R. Aroca, J. Duff, and C. P. Tripp, "Evolution of the molecular organization in bis(n-propylimido)perylene films under thermal annealing," *Chemistry of Materials*, vol. 10, no. 1, pp. 172–176, 1998.

[107] M. Petit, R. Hayakawa, Y. Wakayama, and T. Chikyow, "Early stage of growth of a perylene diimide derivative thin film growth on various Si(001) substrates," *The Journal of Physical Chemistry C*, vol. 111, no. 34, pp. 12747–12751, 2007.

[108] M. Kurban and B. Gündüz, "Study of structural, optical properties and electronic structure of PTCDI-C5 organic nanostructure," *Chemical Physics Letters*, vol. 691, pp. 14–21, 2018.

[109] A. Zykov, S. Bommel, C. Wolf, L. Pithan, C. Weber, P. Beyer, G. Santoro, J. P. Rabe, and S. Kowarik, "Diffusion and nucleation in multilayer growth of PTCDI-C8 studied with in situ x-ray growth oscillations and real-time small angle x-ray scattering," *The Journal of Chemical Physics*, vol. 146, no. 5, p. 052803, 2017.

[110] T. N. Krauss, E. Barrena, X. N. Zhang, D. G. de Oteyza, J. Major, V. Dehm, F. Würthner, L. P. Cavalcanti, and H. Dosch, "Three-dimensional molecular packing of thin organic films of PTCDI-C8 determined by surface x-ray diffraction," *Langmuir*, vol. 24, no. 22, pp. 12742–12744, 2008.

[111] F. Chiarella, M. Barra, A. Cassinese, F. V. D. Girolamo, P. Maddalena, L. Santamaria, and S. Lettieri, "Dicyanoperylene-diimide thin-film growth: a combined optical and morphological study," *Applied Physics A*, vol. 104, no. 1, pp. 39–46, 2010.

[112] R. Buzio, A. Gerbi, M. Barra, F. Chiarella, E. Gnecco, and A. Cassinese, "Subnanometer resolution and enhanced friction contrast at the surface of perylene diimide PDI8-CN2 thin films in ambient conditions," *Langmuir*, vol. 34, no. 10, pp. 3207–3214, 2018.

[113] R. Buzio, A. Gerbi, D. Marrè, M. Barra, and A. Cassinese, "Electron injection barrier and energy-level alignment at the au/PDI8-CN2 interface via current–voltage measurements and ballistic emission microscopy," *Organic Electronics*, vol. 18, pp. 44–52, 2015.

[114] F. Liscio, C. Albonetti, K. Broch, A. Shehu, S. D. Quiroga, L. Ferlauto, C. Frank, S. Kowarik, R. Nervo, A. Gerlach, *et al.*, "Molecular reorganization in organic field-effect transistors and its effect on two-dimensional charge transport pathways," *ACS Nano*, vol. 7, no. 2, pp. 1257–1264, 2013.

[115] A. Brillante, T. Salzillo, R. G. D. Valle, E. Venuti, F. Borgatti, E. Lunedei, F. Liscio, S. Milita, and C. Albonetti, "Photoluminescence as a probe of

molecular organization in PDI8-CN2 ultra-thin films," *Journal of Luminescence*, vol. 187, pp. 403–409, 2017.

[116] C. Keil, H. Graaf, T. Baumgärtel, I. Trenkmann, and D. Schlettwein, "Intralayer vs. interlayer electronic coupling in perylene imide thin films," *Organic Electronics*, vol. 14, no. 11, pp. 2833–2839, 2013.

[117] V. Belova, B. Wagner, B. Reisz, C. Zeiser, G. Duva, J. Rozbořil, J. Novák, A. Gerlach, A. Hinderhofer, and F. Schreiber, "Real-time structural and optical study of growth and packing behavior of perylene diimide derivative thin films: Influence of side-chain modification," *The Journal of Physical Chemistry C*, vol. 122, no. 15, pp. 8589–8601, 2018.

[118] F. Chiarella, M. Barra, L. Ricciotti, A. Aloisio, and A. Cassinese, "Morphology, electrical performance and potentiometry of PDIF-CN2 thin-film transistors on HMDS-treated and bare silicon dioxide," *Electronics*, vol. 3, no. 1, pp. 76–86, 2014.

[119] R. Schmidt, J. H. Oh, Y.-S. Sun, M. Deppisch, A.-M. Krause, K. Radacki, H. Braunschweig, M. Könemann, P. Erk, Z. Bao, *et al.*, "High-performance air-stable n-channel organic thin film transistors based on halogenated perylene bisimide semiconductors," vol. 131, no. 17, pp. 6215–6228, 2009.

[120] A. Rademacher, S. Märkle, and H. Langhals, "Lösliche Perylen-Fluoreszenzfarbstoffe mit hoher Photostabilität," *Chemische Berichte*, vol. 115, no. 8, pp. 2927–2934, 1982.

[121] C. Yumusak, N. S. Sariciftci, and M. Irimia-Vladu, "Purity of organic semiconductors as a key factor for the performance of organic electronic devices," *Materials Chemistry Frontiers*, vol. 4, no. 12, pp. 3678–3689, 2020.

[122] R. T. Weitz, K. Amsharov, U. Zschieschang, E. B. Villas, D. K. Goswami, M. Burghard, H. Dosch, M. Jansen, K. Kern, and H. Klauk, "Organic n-channel transistors based on core-cyanated perylene carboxylic diimide derivatives," *Journal of the American Chemical Society*, vol. 130, no. 14, pp. 4637–4645, 2008.

[123] J. Wagner, M. Gruber, A. Hinderhofer, A. Wilke, B. Bröker, J. Frisch, P. Amsalem, A. Vollmer, A. Opitz, N. Koch, *et al.*, "High fill factor and open circuit voltage in organic photovoltaic cells with diindenoperylene as donor material," *Advanced Functional Materials*, vol. 20, no. 24, pp. 4295–4303, 2010.

[124] M. Gruber, M. Rawolle, J. Wagner, D. Magerl, U. Hörmann, J. Perlich, S. V. Roth, A. Opitz, F. Schreiber, P. Müller-Buschbaum, *et al.*, "Correlating structure and morphology to device performance of molecular organic donor-acceptor photovoltaic cells based on diindenoperylene (DIP) and C60," *Advanced Energy Materials*, vol. 3, no. 8, pp. 1075–1083, 2013.

[125] U. Kraft, K. Takimiya, M. J. Kang, R. Rödel, F. Letzkus, J. N. Burghartz, E. Weber, and H. Klauk, "Detailed analysis and contact properties of low-voltage organic thin-film transistors based on dinaphtho[2,3-b:2',3'-f]thieno[3,2-b]thiophene (DNTT) and its didecyl and diphenyl derivatives," *Organic Electronics*, vol. 35, pp. 33–40, 2016.

[126] S. Haas, Y. Takahashi, K. Takimiya, and T. Hasegawa, "High-performance dinaphtho-thieno-thiophene single crystal field-effect transistors," *Applied Physics Letters*, vol. 95, no. 2, p. 022111, 2009.

[127] H. Chang, Y. Deng, Y. Geng, T. Wang, and D. Yan, "Effect of the initial stage of film growth on device performance of organic transistors based on dinaphtho[2,3-b:2',3'-f]thieno[3,2-b]thiophene (DNTT)," *Organic Electronics*, vol. 22, pp. 86–91, 2015.

[128] S. Kowarik, A. Gerlach, S. Sellner, L. Cavalcanti, O. Konovalov, and F. Schreiber, "Real-time x-ray diffraction measurements of structural dynamics and polymorphism in diindenoperylene growth," *Applied Physics A*, vol. 95, no. 1, pp. 233–239, 2009.

[129] A. C. Dürr, F. Schreiber, K. A. Ritley, V. Kruppa, J. Krug, H. Dosch, and B. Struth, "Rapid roughening in thin film growth of an organic semiconductor (diindenoperylene)," *Physical Review Letters*, vol. 90, no. 1, p. 016104, 2003.

[130] M. Heilig, M. Domhan, and H. Port, "Optical properties and morphology of thin diindenoperylene films," *Journal of Luminescence*, vol. 110, no. 4, pp. 290–295, 2004.

[131] X. Zhang, E. Barrena, D. Goswami, D. G. de Oteyza, C. Weis, and H. Dosch, "Evidence for a layer-dependent ehrlich-schwöbel barrier in organic thin film growth," *Physical Review Letters*, vol. 103, no. 13, p. 136101, 2009.

[132] M. Mohamad, R. Ahmed, A. Shaari, and S. Goumri-Said, "Structure-dependent optoelectronic properties of perylene, di-indenoperylene (DIP) isolated molecule and DIP molecular crystal," *Chemistry Central Journal*, vol. 11, no. 1, pp. 1–9, 2017.

[133] M. A. Heinrich, J. Pflaum, A. K. Tripathi, W. Frey, M. L. Steigerwald, and T. Siegrist, "Enantiotropic polymorphism in di-indenoperylene," *The Journal of Physical Chemistry C*, vol. 111, no. 51, pp. 18878–18881, 2007.

[134] T. Yamamoto and K. Takimiya, "Facile synthesis of highly π-extended heteroarenes, dinaphtho[2,3-b:2',3'-f]chalcogenopheno[3,2-b]chalcogenophenes, and their application to field-effect transistors," *Journal of the American Chemical Society*, vol. 129, no. 8, pp. 2224–2225, 2007.

[135] T. Breuer, A. Karthäuser, H. Klemm, F. Genuzio, G. Peschel, A. Fuhrich, T. Schmidt, and G. Witte, "Exceptional dewetting of organic semiconductor films: The case of dinaphthothienothiophene (DNTT) at dielectric interfaces," *ACS Applied Materials & Interfaces*, vol. 9, no. 9, pp. 8384–8392, 2017.

[136] M.-C. Jung, M. R. Leyden, G. O. Nikiforov, M. V. Lee, H.-K. Lee, T. J. Shin, K. Takimiya, and Y. Qi, "Flat-lying semiconductor–insulator interfacial layer in DNTT thin films," *ACS Applied Materials & Interfaces*, vol. 7, no. 3, pp. 1833–1840, 2015.

[137] U. Zschieschang, F. Ante, D. Kälblein, T. Yamamoto, K. Takimiya, H. Kuwabara, M. Ikeda, T. Sekitani, T. Someya, J. Blochwitz-Nimoth, *et al.*, "Dinaphtho[2,3-b:2',3'-f]thieno[3,2-b]thiophene (DNTT) thin-film transistors with improved performance and stability," *Organic Electronics*, vol. 12, no. 8, pp. 1370–1375, 2011.

[138] K. Takimiya, Y. Kunugi, and T. Otsubo, "Development of new semiconducting materials for durable high-performance air-stable organic field-effect transistors," *Chemistry Letters*, vol. 36, no. 5, pp. 578–583, 2007.

[139] J. Gao, R. Li, L. Li, Q. Meng, H. Jiang, H. Li, and W. Hu, "High-performance field-effect transistor based on dibenzo[d,d']thieno[3,2-b;4,5-b']dithiophene, an easily synthesized semiconductor with high ionization potential," *Advanced Materials*, vol. 19, no. 19, pp. 3008–3011, 2007.

[140] W. Xie, K. Willa, Y. Wu, R. Häusermann, K. Takimiya, B. Batlogg, and C. D. Frisbie, "Temperature-independent transport in high-mobility dinaphtho-thieno-thiophene (DNTT) single crystal transistors," *Advanced Materials*, vol. 25, no. 25, pp. 3478–3484, 2013.

[141] H. Yagi, T. Miyazaki, Y. Tokumoto, Y. Aoki, M. Zenki, T. Zaima, S. Okita, T. Yamamoto, E. Miyazaki, K. Takimiya, *et al.*, "Ultraviolet photoelectron spectra of 2,7-diphenyl[1]benzothieno[3,2-b][1]benzothiophene and dinaphtho[2,3-b:2',3'-f]thieno[3,2-b]thiophene," *Chemical Physics Letters*, vol. 563, pp. 55–57, 2013.

[142] M. Kraus, S. Richler, A. Opitz, W. Brütting, S. Haas, T. Hasegawa, A. Hinderhofer, and F. Schreiber, "High-mobility copper-phthalocyanine field-effect transistors with tetratetracontane passivation layer and organic metal contacts," *Journal of Applied Physics*, vol. 107, no. 9, p. 094503, 2010.

[143] W. Shi, Y. Zheng, J. Yu, A. D. Taylor, and H. E. Katz, "Mobility enhancement of organic field-effect transistor based on guanine trap-neutralizing layer," *Applied Physics Letters*, vol. 109, no. 14, p. 143301, 2016.

[144] K. Jousten, *Wutz Handbuch Vakuumtechnik*. Springer Vieweg, 2018.

[145] O'Hanlon, *Vacuum Technology.* John Wiley & Sons, 2003.

[146] M. Kytka, *Characterization of rubrene thin films by optical techniques.* PhD thesis, Slovak University of Technology in Bratislava, 2008.

[147] J. Als-Nielsen and D. McMorrow, *Elements of Modern X-Ray Physics.* John Wiley & Sons, 2011.

[148] M. Birkholz, *Thin film analysis by X-ray scattering.* Wiley-VCH, 2006.

[149] M. Yasaka, "X-ray thin-film measurement techniques," *The Rigaku Journal*, vol. 26, no. 2, pp. 1–9, 2010.

[150] M. Björck and G. Andersson, "GenX: an extensible x-ray reflectivity refinement program utilizing differential evolution," *Journal of Applied Crystallography*, vol. 40, no. 6, pp. 1174–1178, 2007.

[151] L. G. Parratt, "Surface studies of solids by total reflection of x-rays," *Physical Review*, vol. 95, no. 2, pp. 359–369, 1954.

[152] H. Dosch, *Critical phenomena at surfaces and interfaces : evanescent X-ray and neutron scattering.* Springer-Verlag, 1992.

[153] R. Resel, M. Bainschab, A. Pichler, T. Dingemans, C. Simbrunner, J. Stangl, and I. Salzmann, "Multiple scattering in grazing-incidence x-ray diffraction: impact on lattice-constant determination in thin films," *Journal of Synchrotron Radiation*, vol. 23, no. 3, pp. 729–734, 2016.

[154] P. Müller-Buschbaum, "The active layer morphology of organic solar cells probed with grazing incidence scattering techniques," *Advanced Materials*, vol. 26, no. 46, pp. 7692–7709, 2014.

[155] P. Willmott, *An Introduction to Synchrotron Radiation.* John Wiley & Sons, 2019.

[156] S. M. Kowarik, *Real-time studies of thin film growth of orgnaic semiconductors.* PhD thesis, Wadham College, Oxford, 2006.

[157] D. Rugar and P. Hansma, "Atomic force microscopy," *Physics today*, vol. 43, no. 10, pp. 23–30, 1990.

[158] J. Instruments, *NanoWizard III AFM User Manual.* SPM Software Release 4.2, 2012.

[159] D. Nečas and P. Klapetek, "Gwyddion: an open-source software for SPM data analysis," *Open Physics*, vol. 10, no. 1, pp. 181–188, 2012.

[160] J. Gierschner, J. Shi, B. Milián-Medina, D. Roca-Sanjuán, S. Varghese, and S. Park, “Luminescence in crystalline organic materials: From molecules to molecular solids,” *Advanced Optical Materials*, vol. 9, no. 13, p. 2002251, 2021.

[161] S. M. Menke and R. J. Holmes, “Evaluating the role of energetic disorder and thermal activation in exciton transport,” *Journal of Materials Chemistry C*, vol. 4, no. 16, pp. 3437–3442, 2016.

[162] M. W. A. Skoda, *Interactions of Proteins with Oligo(ethylene glycol) Self-Assembled Monolayers*. PhD thesis, Wadham College, Oxford, 2007.

[163] M. Alonso, M. Garriga, N. Karl, J. Ossó, and F. Schreiber, “Anisotropic optical properties of single crystalline PTCDA studied by spectroscopic ellipsometry,” *Organic Electronics*, vol. 3, no. 1, pp. 23–31, 2002.

[164] D. A. G. Bruggeman, “Berechnung verschiedener physikalischer Konstanten von heterogenen Substanzen. I. Dielektrizitätskonstanten und Leitfähigkeiten der Mischkörper aus isotropen Substanzen,” *Annalen der Physik*, vol. 416, no. 7, pp. 636–664, 1935.

[165] X.-Z. Guo, Y.-H. Luo, Y.-D. Zhang, X.-C. Huang, D.-M. Li, and Q.-B. Meng, “Study on the effect of measuring methods on incident photon-to-electron conversion efficiency of dye-sensitized solar cells by home-made setup,” *Review of Scientific Instruments*, vol. 81, no. 10, p. 103106, 2010.

[166] G. Xue, X. Yu, T. Yu, C. Bao, J. Zhang, J. Guan, H. Huang, Z. Tang, and Z. Zou, “Understanding of the chopping frequency effect on IPCE measurements for dye-sensitized solar cells: from the viewpoint of electron transport and extinction spectrum,” *Journal of Physics D: Applied Physics*, vol. 45, no. 42, p. 425104, 2012.

[167] K. Tvingstedt, K. Vandewal, A. Gadisa, F. Zhang, J. Manca, and O. Inganäs, “Electroluminescence from charge transfer states in polymer solar cells,” *Journal of the American Chemical Society*, vol. 131, no. 33, pp. 11819–11824, 2009.

[168] K. Vandewal, J. Benduhn, and V. C. Nikolis, “How to determine optical gaps and voltage losses in organic photovoltaic materials,” *Sustainable Energy & Fuels*, vol. 2, no. 3, pp. 538–544, 2018.

[169] N. Rußegger, A. M. Valencia, L. Merten, M. Zwadlo, G. Duva, L. Pithan, A. Gerlach, A. Hinderhofer, C. Cocchi, and F. Schreiber, “Molecular charge transfer effects on perylene diimide acceptor and dinaphthothienothiophene donor systems,” *The Journal of Physical Chemistry C*, vol. 126, no. 8, pp. 4188–4198, 2022.

[170] P. Hohenberg and W. Kohn, “Inhomogeneous electron gas,” *Physical Review*, vol. 136, pp. B864–B871, 1964.

[171] W. Kohn and L. J. Sham, “Self-consistent equations including exchange and correlation effects,” *Physical Review*, vol. 140, pp. A1133–A1138, 1965.

[172] L. Hedin, “New method for calculating the one-particle green’s function with application to the electron-gas problem,” *Physical Review*, vol. 139, pp. A796–A823, 1965.

[173] M. S. Hybertsen and S. G. Louie, “Electron correlation in semiconductors and insulators: Band gaps and quasiparticle energies,” *Physical Review B*, vol. 34, no. 8, pp. 5390–5413, 1986.

[174] W. Hanke and L. J. Sham, “Many-particle effects in the optical spectrum of a semiconductor,” *Physical Review B*, vol. 21, pp. 4656–4673, 1980.

[175] V. Blum, R. Gehrke, F. Hanke, P. Havu, V. Havu, X. Ren, K. Reuter, and M. Scheffler, “Ab initio molecular simulations with numeric atom-centered orbitals,” *Computer Physics Communications*, vol. 180, pp. 2175–2196, 2009.

[176] V. Havu, V. Blum, P. Havu, and M. Scheffler, “Efficient O(N) integration for all-electron electronic structure calculation using numeric basis functions,” *Journal of Computational Physics*, vol. 228, no. 22, pp. 8367–8379, 2009.

[177] J. P. Perdew, K. Burke, and M. Ernzerhof, “Generalized gradient approximation made simple,” *Physical Review Letters*, vol. 77, pp. 3865–3868, 1996.

[178] A. Tkatchenko and M. Scheffler, “Accurate molecular van der waals interactions from ground-state electron density and free-atom reference data,” *Physical Review Letters*, vol. 102, p. 073005, 2009.

[179] F. L. Hirshfeld, “Bonded-atom fragments for describing molecular charge densities,” *Theoretica Chimica Acta*, vol. 44, no. 2, pp. 129–138, 1977.

[180] F. Bruneval, T. Rangel, S. M. Hamed, M. Shao, C. Yang, and J. B. Neaton, “Molgw 1: Many-body perturbation theory software for atoms, molecules, and clusters,” *Computer Physics Communications*, vol. 208, pp. 149–161, 2016.

[181] F. Bruneval, “Ionization energy of atoms obtained from GW self-energy or from random phase approximation total energies,” *The Journal of Chemical Physics*, vol. 136, no. 19, p. 194107, 2012.

[182] F. Weigend, A. Köhn, and C. Hättig, “Efficient use of the correlation consistent basis sets in resolution of the identity mp2 calculations,” *Journal of Chemical Physics*, vol. 116, no. 8, pp. 3175–3183, 2002.

[183] C. Adamo and V. Barone, "Toward reliable density functional methods without adjustable parameters: The PBE0 model," *Journal of Chemical Physics*, vol. 110, pp. 6158–6170, 1999.

[184] C. Faber, P. Boulanger, I. Duchemin, C. Attaccalite, and X. Blase, "Many-body green's function gw and bethe-salpeter study of the optical excitations in a paradigmatic model dipeptide," *Journal of Chemical Physics*, vol. 139, no. 19, p. 194308, 2013.

[185] F. Bruneval and M. A. L. Marques, "Benchmarking the starting points of the gw approximation for molecules," *Journal of Chemical Theory and Computation*, vol. 9, no. 1, pp. 324–329, 2013.

[186] T. Rangel, S. M. Hamed, F. Bruneval, and J. B. Neaton, "An assessment of low-lying excitation energies and triplet instabilities of organic molecules with an ab initio bethe-salpeter equation approach and the tamm-dancoff approximation," *Journal of Chemical Physics*, vol. 146, no. 19, p. 194108, 2017.

[187] C. Cocchi, D. Prezzi, A. Ruini, M. J. Caldas, and E. Molinari, "Optical properties and charge-transfer excitations in edge-functionalized all-graphene nanojunctions," *Journal of Physical Chemistry Letters*, vol. 2, no. 11, pp. 1315–1319, 2011.

[188] A. M. Valencia and C. Cocchi, "Electronic and optical properties of oligothiophene-F4TCNQ charge-transfer complexes: The role of the donor conjugation length," *The Journal of Physical Chemistry C*, vol. 123, no. 14, pp. 9617–9623, 2019.

[189] N. Rußegger, H. Kim, J. Hagara, O. Vladimirov, T. Eberle, I. Zalzhnyy, A. Gerlach, A. Hinderhofer, W. Brütting, and F. Schreiber, "Influence of alkyl chain variation on co-crystal formation and molecular charge transfer in dip:perylene diimide binary systems," *The Journal of Physical Chemistry C*, vol. 127, no. 23, pp. 11128–11137, 2023.

[190] A. K. Le, J. A. Bender, D. H. Arias, D. E. Cotton, J. C. Johnson, and S. T. Roberts, "Singlet fission involves an interplay between energetic driving force and electronic coupling in perylenediimide films," *Journal of the American Chemical Society*, vol. 140, no. 2, pp. 814–826, 2018.

[191] Y. Kubozono, K. Hyodo, H. Mori, S. Hamao, H. Goto, and Y. Nishihara, "Transistor application of new picene-type molecules, 2,9-dialkylated phenanthro[1,2-b:8,7-b']dithiophenes," *Journal of Materials Chemistry C*, vol. 3, no. 10, pp. 2413–2421, 2015.

[192] H. Inokuchi, G. Saito, P. Wu, K. Seki, T. B. Tang, T. Mori, K. Imaeda, T. Enoki, Y. Higuchi, K. Inaka, *et al.*, "A novel type of organic semiconductors. Molecular fastener," *Chemistry Letters*, vol. 15, no. 8, pp. 1263–1266, 1986.

[193] M. J. Kang, I. Doi, H. Mori, E. Miyazaki, K. Takimiya, M. Ikeda, and H. Kuwabara, "Alkylated dinaphtho[2,3-b:2',3'-f]thieno[3,2-b]thiophenes (Cn-DNTTs): Organic semiconductors for high-performance thin-film transistors," *Advanced Materials*, vol. 23, no. 10, pp. 1222–1225, 2010.

[194] S. Inoue, H. Minemawari, J. Tsutsumi, M. Chikamatsu, T. Yamada, S. Horiuchi, M. Tanaka, R. Kumai, M. Yoneya, and T. Hasegawa, "Effects of substituted alkyl chain length on solution-processable layered organic semiconductor crystals," *Chemistry of Materials*, vol. 27, no. 11, pp. 3809–3812, 2015.

[195] M. Barra, F. V. D. Girolamo, F. Chiarella, M. Salluzzo, Z. Chen, A. Facchetti, L. Anderson, and A. Cassinese, "Transport property and charge trap comparison for n-channel perylene diimide transistors with different air-stability," *The Journal of Physical Chemistry C*, vol. 114, no. 48, pp. 20387–20393, 2010.

[196] R. Banerjee, J. Novák, C. Frank, C. Lorch, A. Hinderhofer, A. Gerlach, and F. Schreiber, "Evidence for kinetically limited thickness dependent phase separation in organic thin film blends," *Physical Review Letters*, vol. 110, no. 18, p. 185506, 2013.

[197] J. Rivnay, S. C. B. Mannsfeld, C. E. Miller, A. Salleo, and M. F. Toney, "Quantitative determination of organic semiconductor microstructure from the molecular to device scale," *Chemical Reviews*, vol. 112, no. 10, pp. 5488–5519, 2012.

[198] W. Chen, M. P. Nikiforov, and S. B. Darling, "Morphology characterization in organic and hybrid solar cells," *Energy & Environmental Science*, vol. 5, no. 8, pp. 8045–8074, 2012.

[199] R. E. Hummel and S.-S. Chang, "Novel technique for preparing porous silicon," *Applied Physics Letters*, vol. 61, no. 16, pp. 1965–1967, 1992.

[200] E. Lifshitz, A. Kaplan, E. Ehrenfreund, and D. Meissner, "Optical and magnetooptical measurements of N,N'-dimethylperylene-3,4,9,10-tetracarboxylic acid diimide thin films," *The Journal of Physical Chemistry B*, vol. 102, no. 6, pp. 967–973, 1998.

[201] T. Linderl, T. Zechel, A. Hofmann, T. Sato, K. Shimizu, H. Ishii, and W. Brütting, "Crystalline versus amorphous donor-acceptor blends: Influence of layer morphology on the charge-transfer density of states," *Physical Review Applied*, vol. 13, no. 2, p. 024061, 2020.

[202] M. K. Huss-Hansen, J. Kjelstrup-Hansen, and M. Knaapila, “Structural effects of electrode proximity in vacuum-deposited organic semiconductors studied by microfocused x-ray scattering,” *Advanced Engineering Materials*, vol. 23, no. 11, p. 2100082, 2021.

[203] M. Oehzelt, K. Akaike, N. Koch, and G. Heimel, “Energy-level alignment at organic heterointerfaces,” *Science Advances*, vol. 1, no. 10, p. 1501127, 2015.

[204] M. Son, K. H. Park, C. Shao, F. Würthner, and D. Kim, “Spectroscopic demonstration of exciton dynamics and excimer formation in a sterically controlled perylene bisimide dimer aggregate,” *The Journal of Physical Chemistry Letters*, vol. 5, no. 20, pp. 3601–3607, 2014.

[205] J. Gierschner, H.-G. Mack, D. Oelkrug, I. Waldner, and H. Rau, “Modeling of the optical properties of cofacial chromophore pairs: stilbenophane,” *The Journal of Physical Chemistry A*, vol. 108, no. 2, pp. 257–263, 2004.

[206] J. Gierschner, M. Ehni, H.-J. Egelhaaf, B. M. Medina, D. Beljonne, H. Benmansour, and G. C. Bazan, “Solid-state optical properties of linear polyconjugated molecules: π-stack contra herringbone,” *The Journal of Chemical Physics*, vol. 123, no. 14, p. 144914, 2005.

[207] C. F. Madigan and V. Bulović, “Solid state solvation in amorphous organic thin films,” *Physical Review Letters*, vol. 91, no. 24, p. 247403, 2003.

[208] P. Imbrasas, R. Lygaitis, P. Kleine, R. Scholz, C. Hänisch, S. Buchholtz, K. Ortstein, F. Talnack, S. C. B. Mannsfeld, S. Lenk, *et al.*, “Dimers or solid-state solvation? Intermolecular effects of multiple donor–acceptor thermally activated delayed fluorescence emitter determining organic light-emitting diode performance,” *Advanced Optical Materials*, vol. 9, no. 14, p. 2002153, 2021.

[209] M. Guerrini, A. M. Valencia, and C. Cocchi, “Long-range order promotes charge-transfer excitations in donor/acceptor co-crystals,” *The Journal of Physical Chemistry C*, vol. 125, no. 38, pp. 20821–20830, 2021.

[210] S. K. Park, S. Varghese, J. H. Kim, S.-J. Yoon, O. K. Kwon, B.-K. An, J. Gierschner, and S. Y. Park, “Tailor-made highly luminescent and ambipolar transporting organic mixed stacked charge-transfer crystals: An isometric donor–acceptor approach,” *Journal of the American Chemical Society*, vol. 135, no. 12, pp. 4757–4764, 2013.

[211] H. Geng, L. Zhu, Y. Yi, D. Zhu, and Z. Shuai, “Superexchange induced charge transport in organic donor–acceptor cocrystals and copolymers: A theoretical perspective,” *Chemistry of Materials*, vol. 31, no. 17, pp. 6424–6434, 2019.

[212] J. Zhang, H. Geng, T. S. Virk, Y. Zhao, J. Tan, C. a. Di, W. Xu, K. Singh, W. Hu, Z. Shuai, *et al.*, “Sulfur-bridged annulene-TCNQ co-crystal: A self-assembled “molecular level heterojunction” with air stable ambipolar charge transport behavior,” *Advanced Materials*, vol. 24, no. 19, pp. 2603–2607, 2012.

[213] R. Schier, A. M. Valencia, and C. Cocchi, “Microscopic insight into the electronic structure of bcf-doped oligothiophenes from ab initio many-body theory,” *The Journal of Physical Chemistry C*, vol. 124, no. 26, pp. 14363–14370, 2020.

[214] A. E. Mansour, D. Lungwitz, T. Schultz, M. Arvind, A. M. Valencia, C. Cocchi, A. Opitz, D. Neher, and N. Koch, “The optical signatures of molecular-doping induced polarons in poly (3-hexylthiophene-2, 5-diyl): individual polymer chains versus aggregates,” *Journal of Materials Chemistry C*, vol. 8, no. 8, pp. 2870–2879, 2020.

[215] A. M. Valencia, M. Guerrini, and C. Cocchi, “Ab initio modelling of local interfaces in doped organic semiconductors,” *Physical Chemistry Chemical Physics*, vol. 22, pp. 3527–3538, 2020.

[216] L. Zhu, E.-G. Kim, Y. Yi, and J.-L. Brédas, “Charge transfer in molecular complexes with 2,3,5,6-tetrafluoro-7,7,8,8-tetracyanoquinodimethane (F4-TCNQ): A density functional theory study,” *Chemistry of Materials*, vol. 23, no. 23, pp. 5149–5159, 2011.

[217] B. Mahns, O. Kataeva, D. Islamov, S. Hampel, F. Steckel, C. Hess, M. Knupfer, B. Büchner, C. Himcinschi, T. Hahn, *et al.*, “Crystal growth, structure, and transport properties of the charge-transfer salt picene/2,3,5,6-tetrafluoro-7,7,8,8-tetracyanoquinodimethane,” *Crystal Growth & Design*, vol. 14, no. 3, pp. 1338–1346, 2014.

[218] I. Salzmann, G. Heimel, S. Duhm, M. Oehzelt, P. Pingel, B. M. George, A. Schnegg, K. Lips, R.-P. Blum, A. Vollmer, *et al.*, “Intermolecular hybridization governs molecular electrical doping,” *Physical Review Letters*, vol. 108, no. 3, p. 035502, 2012.

[219] N. Rußegger, R. Nasro, J. Hagara, F. Bertram, A. Gerlach, A. Hinderhofer, and F. Schreiber, “Co-crystal formation and molecular charge transfer in fluorinated perylene diimide binary systems,” *submitted.*

[220] E. Breitmaier and G. Jung, *Organische Chemie: Grundlagen, Verbindungsklassen, Reaktionen, Konzepte, Molekülstruktur, Naturstoffe, Syntheseplanung, Nachhaltigkeit.* Thieme, 2012.

[221] T. Storzer, A. Hinderhofer, C. Zeiser, J. Novák, Z. Fišer, V. Belova, B. Reisz, S. Maiti, G. Duva, R. K. Hallani, *et al.*, “Growth, structure, and anisotropic

optical properties of difluoro-anthradithiophene thin films," *The Journal of Physical Chemistry C*, vol. 121, no. 38, pp. 21011–21017, 2017.

[222] A. Hinderhofer, C. Frank, T. Hosokai, A. Resta, A. Gerlach, and F. Schreiber, "Structure and morphology of coevaporated pentacene-perfluoropentacene thin films," *The Journal of Chemical Physics*, vol. 134, no. 10, p. 104702, 2011.

List of publications

- N. Rußegger, R. Nasro, J. Hagara, F. Bertram, A. Gerlach, A. Hinderhofer, and F. Schreiber, ”Co-crystal formation and molecular charge transfer in fluorinated perylene diimide binary systems”, 2024, *submitted.*
- N. Rußegger, H. Kim, J. Hagara, O. Vladimirov, T. Eberle, I. Zalzhnyy, A. Gerlach, A. Hinderhofer, W. Brütting, and F. Schreiber, ”Influence of alkyl chain variation on co-crystal formation and molecular charge transfer in DIP:Perylene diimide binary systems”, *J. Phys. Chem. C*, vol. 127, no. 23, pp. 11128-11137, 2023.
- N. Rußegger, A. M. Valencia, L. Merten, M. Zwadlo, G. Duva, L. Pithan, A. Gerlach, A. Hinderhofer, C. Cocchi, and F. Schreiber, ”Molecular charge transfer effects on perylene diimide acceptor and dinapthothienothiophene donor systems”, *J. Phys. Chem. C*, vol. 126, no. 8, pp. 4188-4198, 2022.
- C. Wang, N. Rußegger, G. Duva, O. Konovalov, M. Jankowski, A. Gerlach, A. Hinderhofer, and F. Schreiber, ”Growth, structure and templating of anthradithiophene and its β-methylthiolated derivative”, *Mater. Chem. Front.*, vol. 6, pp. 3422-3430, 2022.
- A. Greco, V. Starostin, E. Edel, V. Munteanu, N. Rußegger, I. Dax, C. Shen, F. Bertram, A. Hinderhofer, A. Gerlach, and F. Schreiber, ”Neural network analysis of neutron and X-ray reflectivity data: automated analysis using mlreflect, experimental errors and feature engineering”, *J. Appl. Cryst.*, vol. 55, no. 2, pp. 362-369, 2022.
- J. Hagenlocher, N. Scheffczyk, K. Broch, G. Duva, N. Rußegger, L. Egenberger, R. Banerjee, S. Kera, F. Schreiber, and A. Hinderhofer, ”On the origin of gap states in molecular semiconductors - a combined UPS, AFM and X-ray diffraction study”, *J. Phys. Chem. C*, vol. 125, no. 32, pp. 17929-17938, 2021.
- J. Hagara, N. Mrkyvkova, L. Feriancová, M. Putala, P. Nádaždy, M. Hodas, A. Shaji, V. Nádazdy, M. Huss-Hansen, M. Knaapila, J. Hagenlocher, N. Rußegger, M. Zwadlo, L. Merten, M. Sojková, M. Hulman, A. Vlad, P. Pandit, S. Roth, M. Jergel, E. Majková, A. Hinderhofer, P. Siffalovic, and F. Schreiber, ”Novel highly substituted thiophene-based n-type organic semiconductor: Structural study, optical anisotropy and molecular control”, *CrystEngComm*, vol. 22, no. 42, pp. 7095-7103, 2020.
- M. Kern, L. Tesi, D. Neusser, N. Rußegger, M. Winkler, A. Allgaier, Y. M. Gross, S. Bechler, H. S. Funk, L.-T. Chang, J. Schulze, S. Ludwigs, and J. v. Slageren,

”Hybrid spintronic materials from conducting polymers with molecular quantum bits”, *Adv. Funct. Mater.*, vol. 31, no. 7, p. 2006882, 2021.

- A. V. Funes, M. Perfetti, M. Kern, N. Rußegger, L. Carrella, E. Rentschler, J. v. Slageren, and P. Alborés, ”Single molecule magnet features in the butterfly [Co$_2^{III}$Ln$_2^{III}$] pivalate family with alcohol-amine ligands”, *Eur. J. Inorg. Chem.*, vol. 31, pp. 3191-3210, 2021.

Acknowledgments

At the end of this thesis, I would like to express my gratitude to everyone who supported me during the years of my Ph.D. study. First of all, I would like to thank Prof. Dr. Dr. h.c. Frank Schreiber for the opportunity to be part of this group, to participate in this exciting project, and for all of his scientific guidance and advice.

I would strongly like to thank Dr. Alexander Hinderhofer for his tireless support and supervision through my whole Ph.D. study and for the long scientific discussions, for his patience, his motivation, and his immense knowledge in every situation. I would also like to thank Dr. Alexander Gerlach for his scientific support and for answering every question I had in the last few years.

I have to acknowledge that this research was financially supported by the German Research Foundation (Deutsche Forschungsgemeinschaft, DFG, SCHR 700/20-2).

I am very grateful to Dr. Ana M. Valencia and Prof. Dr. Caterina Cocchi for providing the theoretical calculations for my experimental results and for their supporting help with this project. I would like to thank Hongwon Kim and Prof. Dr. Wolfgang Brütting for performing the EL and IPCE measurements and for this successful collaboration. Furthermore, I would also thank Stephan Hirschmann for the help and performing of the gradient sublimation of my material. I am also very grateful to Dr. Jakub Hagara for his support with the evaluation of my GIWAXS data.

I would like to acknowledge thanks to Matthias Zwadlo, Dr. Giuliano Duva, Dr. Linus Pithan, Dr. Jan Hagenlocher, Dr. Ivan Zaluzhnyy, Ekaterina Kneschaurek, and Dr. Alessandro Greco for the support and realization of the beamtime measurements. I would also acknowledge DESY and ESRF for providing excellent facilities and the staff of the beamlines P03, P08, ID03, and ID10 for their immense support.

I would like to thank all the bachelor and master students I worked together for the performing and assistance of several experimental measurements: Lena Merten, Oleg Vladimirov, Tom Stumpp, Timo Eberle, Michael Schlegel, and Roody Nasro.

I have to thank Alexander Rötschke and Susanne Kern for their careful assistance with all the organizational tasks and also Bernd Hofferberth and Ralph Zenke for their technical support in the laboratories.

I wish to express my sincere thanks to Matthias Zwadlo, Dr. Alexander Hinderhofer, Lena Merten, Ingrid Dax, Roody Nasro, Jakub Hagara, and Dr. Ivan Zaluzhnyy for proofreading parts of this thesis and the whole group for their continuous support and encouragement.

Finally, I want to thank my parents, my sister, and my friends for all their support and patience over the last few years which made all this work possible. I want also to thank Marc for his endless encouragement and indulgence.